Numerical and experimental study of creep of Grade 91 steel at high temperature

Rattanak Lim

To cite this version:

Rattanak Lim. Numerical and experimental study of creep of Grade 91 steel at high temperature. Materials. École Nationale Supérieure des Mines de Paris, 2011. English. NNT : 2011ENMP0083 . pastel-00687235

HAL Id: pastel-00687235
https://pastel.hal.science/pastel-00687235

Submitted on 12 Apr 2012

HAL is a multi-disciplinary open access archive for the deposit and dissemination of scientific research documents, whether they are published or not. The documents may come from teaching and research institutions in France or abroad, or from public or private research centers.

L'archive ouverte pluridisciplinaire HAL, est destinée au dépôt et à la diffusion de documents scientifiques de niveau recherche, publiés ou non, émanant des établissements d'enseignement et de recherche français ou étrangers, des laboratoires publics ou privés.

École doctorale n° 432 : Sciences des Métiers de l’Ingénieur

Doctorat ParisTech

THÈSE

pour obtenir le grade de docteur délivré par

l’École nationale supérieure des mines de Paris

Spécialité “ Sciences et Génie des Matériaux ”

présentée et soutenue publiquement par

Rattanak LIM

le 21 décembre 2011

Simulation numérique et étude expérimentale du fluage de l’acier Grade 91 à haute température

Numerical and experimental study of creep of Grade 91 steel at high temperature

Directeurs de thèse : **Maxime SAUZAY / Anne-Françoise GOURGUES-LORENZON**

Jury

M. Tanguy ROUXEL, Professeur, Laboratoire LARMAUR, Université de Rennes 1	Président
M. Laurent TABOUROT, Professeur, Laboratoire SYMME, Université de Savoie	Rapporteur
M. Alan COCKS, Professeur, Department of Engineering Science, University of Oxford	Rapporteur
M. Gunther EGGELER, Professeur, Institute of Materials, Ruhr-Universität Bochum	Examinateur
M. Maxime SAUZAY, Chercheur-Ingénieur, SRMA, CEA Saclay	Examinateur
Mme AF GOURGUES-LORENZON, Professeur, Centre des Matériaux, MINES ParisTech	Examinateur

THÈSE

MINES ParisTech
Centre des Matériaux
BP 87, 91003 Evry Cedex, France

Remerciements

En premier lieu, je souhaite adresser mes remerciements au **Commissariat à l'Energie Atomique et aux Energies Alternatives** pour m'avoir attribué un financement de thèse de doctorat.

J'exprime ma gratitude à mes deux directeurs de thèse, **Anne-Françoise Gourgues-Lorenzon** et **Maxime Sauzay** pour m'avoir encouragé tout au long de ma thèse. Ils m'ont transféré leurs connaissances et leur expérience de la recherche scientifique en Sciences de Matériaux. Leurs conseils souvent pertinents m'ont aidé à résoudre mes problèmes de façon pragmatique, dans le sens de l'avancement de la recherche.

Mes remerciements viennent ensuite aux deux rapporteurs, **Laurent Tabourot** et **Alan Cocks**, pour avoir accepté d'examiner mon manuscrit de thèse et pour m'avoir permis de soutenir ma thèse. Leurs commentaires pertinents m'ont apportés des compléments intéressants ainsi que des perspectives à long terme pour l'étude du fluage des matériaux.

Je tiens à remercier sincèrement les membres du jury pour avoir accepté d'examiner ma thèse. Des discussions et des échanges avec eux suite à mon exposé m'ont permis d'élargir ma vision du domaine des Sciences des Matériaux.

Mes remerciements s'adressent ensuite à mes collègues du SRMA du CEA Saclay pour leur collaboration tout au long de ma thèse : **Ivan Tournié** et **France Dalle** pour de nombreuses données de fluages, **Céline Bernard** pour m'avoir appris à maîtriser l'instrument de métrologie à laser, **Véronique Rabaut** pour ses conseils sur des polissages très fins des échantillons ainsi que **Patrick Bonnaillie** (service SRMP) pour son collaboration sur des mesures en microscopie MEB-FEG. Ces résultats expérimentaux ont été introduits dans les modélisations et utilisés pour des comparaisons importantes dans le cadre de ma thèse.

Je tiens à remercier également des collègues du Centre des Matériaux de MINES ParisTech pour leur accueil et leur collaboration sympathique. Ils m'ont accompagné afin de mener des mesures expérimentales fines avec des instruments tels que l'appareil de métrologie à laser et la microscopie électronique MEB-FEG.

J'adresse mes remerciements chaleureux au **Prof. Tanguy Rouxel**, mon ancien professeur en classe de Master à l'INSA Rennes, pour avoir accepté de faire partie de mon jury de thèse. Son enseignement lors des cours en Master m'a donné envie de faire un doctorat en Sciences des Matériaux.

Je n'oublie pas de remercier infiniment ma famille pour son soutien dans mes études supérieures au Cambodge grâce auquel j'ai pu venir étudier en France et finalement mener à terme ce doctorat.

Je tiens à mercier chaleureusement mes amis que je connais depuis le Cambodge qui m'ont encouragé et m'ont apporté des conseils importants tout au long de mon séjour en France.

Mes remerciements viennent ensuite à la **Cité Internationale Universitaire de Paris** pour m'avoir hébergé pendant trois années de ma thèse. Particulièrement, mon séjour à la **Fondation Bermans-Lapôtre** (des Belges et des Luxembourgeois) m'a donné une belle occasion de faire des échanges multiculturels dans la bonne humeur.

Je tiens à remercier spécialement **Charlotte Maire** pour son soutien et ses conseils durant la période de la rédaction et de la soutenance de ma thèse.

Enfin, mes remerciements viennent aux personnes que je n'ai pas citées, mais avec qui j'ai discuté et qui ont contribué à l'élaboration de cette thèse de doctorat.

Table des matières

List of notations 9

I Introduction 13

1 Contexte et démarche de thèse 15
- 1.1 Contexte industriel 15
- 1.2 Introduction au fluage des aciers martensitiques revenus 15
  - 1.2.1 Striction 17
  - 1.2.2 Adoucissement de l'acier Grade 91 en cours de fluage 18
  - 1.2.3 Cavitation induite par la diffusion des lacunes le long des joints polycristallins 19
- 1.3 Conclusions et démarche de thèse 19

2 Propriétés de l'acier martensitique revenu Grade 91 21
- 2.1 Evolution historique des aciers martensitiques revenus au chrome 21
- 2.2 Composition chimique 22
- 2.3 Elaboration 22
- 2.4 Microstructure à l'état de réception 24
  - 2.4.1 Tailles caractéristiques 24
  - 2.4.2 Relations entre orientations cristallographiques 24
  - 2.4.3 Dislocations 26
  - 2.4.4 Précipités 28
- 2.5 Traction simple 28

II Necking 31

Résumé 33

3 Modelling and experimental study of the tertiary creep stage of grade 91 steel 35
- 3.1 Introduction 35
- 3.2 Materials and experiments 37
  - 3.2.1 Materials 37
  - 3.2.2 Mechanical testing 37
  - 3.2.3 Measurements and observations of fractured specimens 38

3.2.4 Analysis of the creep curves 39
3.2.5 Results and discussion 39
3.3 Modelling of the tertiary creep stage 45
3.3.1 Viscoplastic flow law 45
3.3.2 First approach : homogeneous deformation (no localised necking) 46
3.3.3 Instability and necking evolution 49
3.4 Results and discussion 52
3.4.1 Lifetime predictions using necking modelling 52
3.4.2 Derivation of simple lower and upper bounds 55
3.5 Conclusions 56

III Creep cavitation induced by grain boundary diffusion 59

Résumé 61

Introduction 63

4 Literature review on creep cavitation induced by grain boundary diffusion 65
4.1 Observations of creep cavities in martensitic steels 65
4.2 Modelling of creep cavitation induced by grain boundary diffusion 70
4.2.1 Creep cavity nucleation 70
4.2.2 Creep cavity growth driven by vacancy diffusion 77
4.3 Discussion and choice of models 86

5 Observations and modelling of long-term creep cavitation in Grade 91 steel 87
5.1 Creep cavity observations in Grade 91 steel 87
5.1.1 Preparation of creep samples 87
5.1.2 Procedure used for quantitative measurements of cavitation . . . 88
5.1.3 Cavity characteristics with regards to creep lifetime 92
5.1.4 Location of creep cavities 93
5.1.5 Conclusions 95
5.2 Modelling of cavitation along matrix boundaries 97
5.2.1 Diffusion data of tempered martensitic chromium steels 97
5.2.2 Dominant mechanism predicted with Rice length 98
5.2.3 Diffusion growth of cavities 99
5.2.4 Sensitivity of model predictions of cavity growth to the values of model parameters 104
5.2.5 Nucleation of cavities 105
5.2.6 Effect of stress concentrations at precipitate-matrix interfaces on the adjusted value of F_v 107
5.3 Discussion 107

Conclusions 109

IV Contribution of Finite Elements Analysis 111

Résumé 113

Introduction 115

6 Literature review on polycrystal models 117
6.1 Stress and strain concentrations at polycrystalline grain boundaries . . . 117
6.2 Crystal elasto-viscoplasticity constitutive equations 120
6.2.1 Basic kinematics in the finite strain framework 120
6.2.2 Viscoplastic slip rate and thermal activation 121
6.3 Crystal viscoplasticity parameters 123
6.4 Conclusions 124

7 Finite element modelling of polycrystalline aggregates 127
7.1 Geometry description and meshing 127
7.2 Crystal elasto-viscoplasticity constitutive equations 128
7.3 Boundary conditions and creep loading 128
7.4 Adjustment of the crystal viscoplasticity parameters 129
7.4.1 Effect of mesh refinement 130
7.4.2 Effect of random crystal orientations 131
7.4.3 Effect of the number of blocks 132
7.4.4 Effect of the V^* parameter 132
7.4.5 Discussion 135
7.5 Analysis of the mean block stress and strain distributions 135
7.5.1 Analysis based on the reference choice of parameters 135
7.5.2 Effect of creep time 140
7.5.3 Effect of the number of blocks 143
7.5.4 Effect of mesh refinement 143
7.5.5 Effect of the choice of the V^* values 143
7.6 Conclusions 146

8 Finite element computations of normal stress fields close to polycrystalline triple junctions 147
8.1 Model of polycrystalline triple junctions 147
8.1.1 Microstructure geometry and meshing 147
8.1.2 Isotropic creep flow rule 149
8.1.3 Effect of mesh refinement on normal stress fields 150
8.1.4 Effect of the sets of random crystal orientations on normal stress fields 151
8.2 Normal stress fields computed using microstructures based on EBSD measurements 158
8.2.1 Meshing 158
8.2.2 Stress and strain distributions in the microstructures 162
8.2.3 Normal stress fields along block boundaries close to triple junctions 162
8.3 Discussion about assessment of normal stress fields at block boundaries . 164
8.4 Application to the prediction of cavity nucleation 165

8.5 Conclusions 165

V Conclusions and recommendations for future works 169

9 Conclusions 171
9.1 Necking and Softening 171
9.2 Cavitation induced by boundary diffusion 172
9.3 Finite element computations of stress concentrations at triple junctions and their effect on cavity nucleation 173
9.4 Criticism of the Raj model 174
9.5 Final predictions of creep lifetimes and extrapolation out of creep data domain 174

10 Recommendations for future works 177
10.1 Cavity nucleation equation 177
10.2 Mechanisms of cavity nucleation 177
10.3 Local stress concentration 177
10.4 Effect of material creep softening 178

References 179

List of Figures 191

List of Tables 199

List of notations

α	angle formed at the junction of a void and the grain boundary
α_{Ib}	angle formed at the junction of the inclusion and the grain boundary
α_I	angle formed at the junction of the void and the inclusion
ΔG_0	barrier energy of obstacles to dislocation gliding
ΔG_c	thermodynamic barrier to nucleation of a critical nucleus (cavity)
$\dot{\gamma}^s$	slip rate on slip system (s)
$\dot{\varepsilon}_{min}$	minimum creep true strain rate
$\dot{N}_0$	constant nucleation rate of cavities during creep tests suggested by Dyson
γ_b	grain boundary surface energy
γ_{Ib}	inclusion-matrix interface energy
γ_I	inclusion free surface energy
γ_s	free surface energy of a matrix
μ^{ch}	chemical potential
Ω	atomic volume, $1.18 \times 10^{-29}\mathrm{m}^3$ for Fe
$\overline{\mathbf{J}}_b$	diffusion flux of vacancies along grain boundaries
$\overline{\omega}_f$	critical area fraction of cavities in grain boundaries
σ^{eng}	uniaxial engineering stress
Σ_n	normal macroscopic stress to a grain boundary
σ_n	normal stress acting on the surrounding matrix of a grain boundary
τ^s	resolved shear stress on slip system (s) having normal unit vector $\underline{\mathbf{n}}^{*s}$ and slip unit vector $\underline{\mathbf{m}}^{*s}$
τ^{*s}	viscous shear stress on slip system (s)
τ_i	incubation time required to reach the steady-state nucleation rate

τ_0^s	athermal shear stress due to obstacles
θ	angle given as a function of α, α_I and α_{Ib} by $\frac{1}{2}(\alpha+\alpha_I-\alpha_{Ib})$
$\underset{\approx}{\mathcal{C}}$	fourth-order tensor of elastic moduli
$\underset{\sim}{\mathbf{E}}$	Green-Lagrange strain tensor
$\underset{\sim}{\mathbf{E}}^e$	elasticity decomposition of the Green-Lagrange strain tensor
$\underset{\sim}{\mathbf{F}}$	transformation gradient
$\underset{\sim}{\mathbf{F}}^e$	elastic decomposition of the transformation gradient
$\underset{\sim}{\mathbf{F}}^p$	viscoplastic sliding gradient
$\underset{\sim}{\mathbf{L}}$	velocity gradient tensor
$\underset{\sim}{\mathbf{L}}^e$	elasticity decomposition of the velocity gradient tensor
$\underset{\sim}{\mathbf{L}}^{*p}$	tensor of slip induced-viscoplastic velocity gradient
$\underset{\sim}{\boldsymbol{\sigma}}$	Cauchy stress tensor
ε	uniaxial logarithmic or true strain
ε^{eng}	uniaxial engineering strain or relative elongation
ε_{min}	uniaxial true strain at which the minimum true strain rate is reached
d_g	average diameter of prior or former austenitic grains
$D_b\delta$	self-diffusion coefficient in grain boundaries times the grain boundary thickness, δ
D_v	volume diffusion coefficient
F_b	ratio of the grain boundary area replaced by the cavity to r^2
F_s	ratio of the cavity free surface to r^2
F_v	ratio of the cavity volume to r^3
k	softening slope during the tertiary creep stage, $\frac{\partial \log(\dot{\varepsilon})}{\partial \varepsilon}$
k_b	Boltzmann constant, $1.3806488 \times 10^{-23}$ JK^{-1}
L	one half the average distance between cavities in grain boundaries
L_R	Rice length characterizing a transition between diffusion-induced and viscoplasticity-induced cavity growth mechanisms
n	stress exponent of the Norton flow rule
N_a	number of cavities per unit area of grain boundary

N_a^{max}	maximum density of critical nucleation sites of cavities in grain boundary
N_m	number of cavities per unit area of polished cross-section
r	curvature radius of a void with a spherical segment shape
r_b	radius of the circular area in grain boundary that a cavity with spherical-cap shape replaces
r_c	curvature radius of a critical nucleus with spherical-segment shape
T	temperature
t_f	creep lifetime
t_{min}	time at which the minimum creep strain rate is reached
V^*	activation volume of dislocation gliding

Première partie

Introduction

Chapitre 1

Contexte et démarche de thèse

1.1 Contexte industriel

L'acier martensitique Grade 91 présente une bonne résistance à la corrosion, de bonnes propriétés mécaniques, un faible coefficient de dilatation thermique mais une forte conductivité thermique [1]. Sa résistance en fluage à haute température a été améliorée durant de nombreuses années de recherche à partir des aciers martensitiques à 9%Cr par ajout des éléments Mo, Nd et V [1]. Cette nuance serait un candidat approprié pour des éléments de structures du circuit secondaire et des tubes de générateurs de vapeur du prototype de réacteur nucléaire SFR (Sodium-cooled Fast Reactor) [1]. L'acier Grade 91 est économiquement plus compétitif que les aciers austénitiques, car son coût de fabrication est nettement inférieur du fait que le chrome est moins cher que le nickel [1]. En plus, ses bonnes caractéristiques de conductivité et de dilatation nous permettent de raccourcir les tuyauteries, ce qui aboutit en fin à une réduction importante du volume d'acier nécessaire [1].

La durée de vie des réacteurs nucléaires de la génération IV, y compris le prototype SFR, serait prolongée jusqu'à 60 ans [1]. Cela nécessite de prendre en compte les mécanismes de fluage actifs durant de très longues durées de vie (Cocks et Ashby [2]), dans le cas de l'acier martensitique Grade 91.

1.2 Introduction au fluage des aciers martensitiques revenus

L'essai de fluage consiste à appliquer une contrainte d'ingénieur (σ^{eng}) constante à une éprouvette (certains auteurs imposent une contrainte vraie constante). La courbe de fluage typique des métaux et des alliages est représentée sur la Figure 1.1 [3]. La durée de fluage est conventionnellement divisée en trois stades. Durant le stade primaire (premier stade), la vitesse de déformation diminue due aux effets des grains voisins ou au durcissement intergranulaire. Pendant le stade secondaire, la vitesse de déformation est approximativement constante. Cette vitesse peut être appelée aussi la vitesse de déformation minimale ($\dot{\varepsilon}_{min}$). Durant le stade tertiaire, la vitesse de déformation accélère jusqu'à la rupture. Ces deux derniers stades seront explicités plus en détails dans le chapitre 3.

Une loi exprimant le temps à rupture (t_f) en fluage comme une fonction puissance d'un

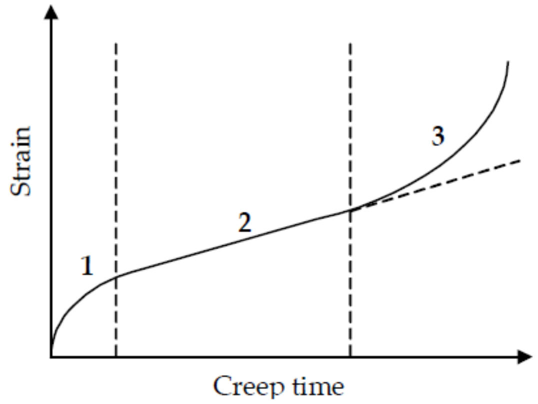

Figure 1.1 – Courbe de fluage des métaux (Figure issue de [4]).

exposant -1 de la vitesse de déformation minimale ($\dot{\varepsilon}_{min}$) a été proposée par Monkman et Grant [5]. Figure 1.2 montre que t_f et $\dot{\varepsilon}_{min}$ suivent une loi de type Monkman-Grant d'une puissance près de -1 jusqu'à des durées de vie de 200×10^3h, à des températures comprises entre 500 et 625°C pour l'acier Grade 91. Cette puissance est approximativement égale à celle trouvée par Abe [6] pour l'acier de la même nuance.

Cependant, la validité de la loi de Monkman-Grant au-delà de ces durées de vie n'est pas assurée. Ainsi, nous nous intéresserons à comprendre les différents mécanismes conduisant à la rupture du matériau en fluage. Cela nous permettra de les modéliser et de les valider pour les temps inférieurs à 200×10^3h à 500°C et 100×10^3h à 600°C, et surtout de proposer des extrapolations au-delà de ces durées.

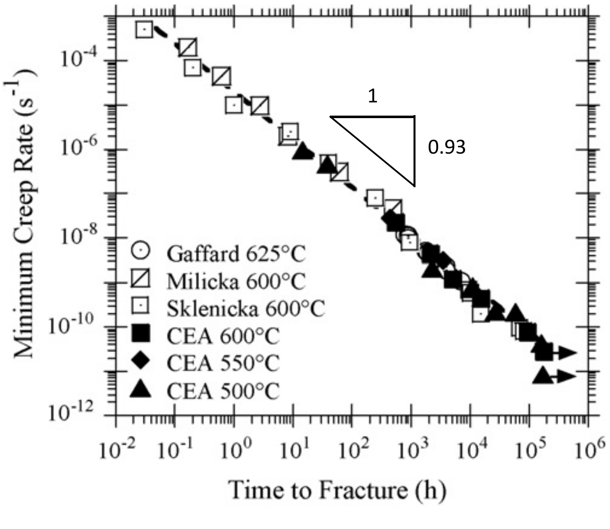

Figure 1.2 – Loi de Monkman-Grant pour l'acier Grade 91 à des températures comprises entre 500 et 625°C et pour des durées de vie jusqu'à 200×10^3h [7].

Les contraintes de fluage, σ^{eng}, sont tracées sur la Figure 1.3 en fonction des durées de vie à des températures entre 500 et 700°C. L'extrapolation des données obtenues à forte contrainte conduit à des surestimations notables des durées de vie à faible contrainte. Ces surestimations sont dues à l'adoucissement du matériau ainsi que la cavitation intergranulaire de fluage qui seront présentés par la suite. Avant de les aborder, la ruine par striction est présentée dans la section suivante afin de définir le domaine de durées de vie dans lequel est le mécanisme de ruine prépondérant.

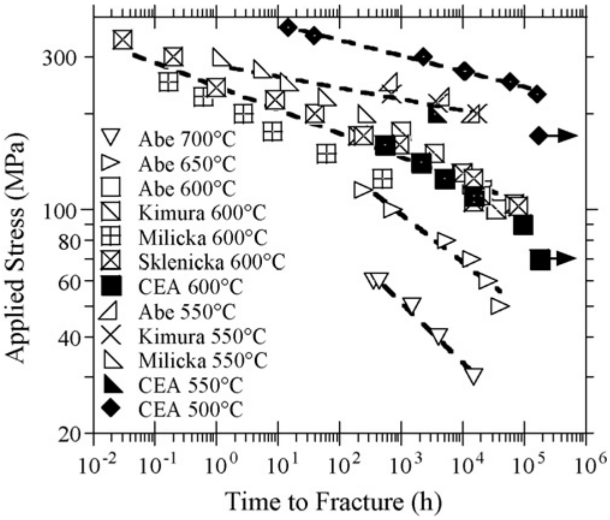

Figure 1.3 – Variation de contraintes de fluage (σ^{eng}) en fonction des durées de vie (t_f) d'après [7](CEA) et [8–11]. Figure issue de [7].

1.2.1 Striction

La striction durant des essais de traction a été étudiée il y a plus d'un siècle par Considère [12]. Elle est induite par une instabilité viscoplastique conduisant à une déformation localisée dans la longueur utile de l'éprouvette (Fig. 1.4). La déformation devient ensuite hétérogène.

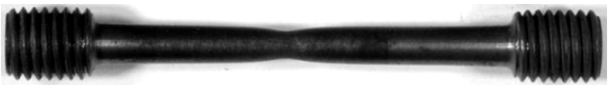

Figure 1.4 – Striction observée sur une éprouvette de Grade 92 à un instant précédant la rupture en traction monotone à la vitesse de déformation de 2.5×10^{-4}s^{-1} à 550°C [13].

Les réductions d'aire en zone de striction à la fin du fluage de l'acier Grade 91 sont reportées sur la Figure 1.5. A 500°C, la réduction d'aire finale est approximativement de 80% pour les durées de vie inférieures à 60×10^3h. A partir de la durée de vie de 160×10^3h, pour laquelle la réduction d'aire finale atteint 60%, la réduction d'aire commence à décroître en fonction de la durée de vie. A 600°C, la réduction est approximativement de 80% pour les durées de vie inférieures à 15×10^3h. Mais, la réduction d'aire est seulement de 20% pour la durée de vie de 94×10^3h à la même température.

Pendant les deux essais de fluage à 500°C et à 600°C dont les durées de vie sont respectivement de 160×10^3h et de 94×10^3h, l'adoucissement du matériau peut être important. Ils pourraient également avoir été affectées par la cavitation intergranulaire le long des anciens joints de grains austénitiques et des joints de blocs.

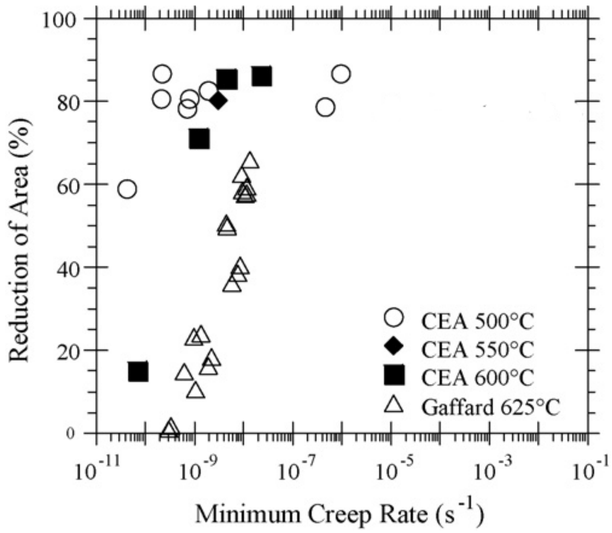

Figure 1.5 – Réduction de la section en zone de striction mesurée à la rupture pour l'acier Grade 91 d'après [4, 7]. Figure issue de [7].

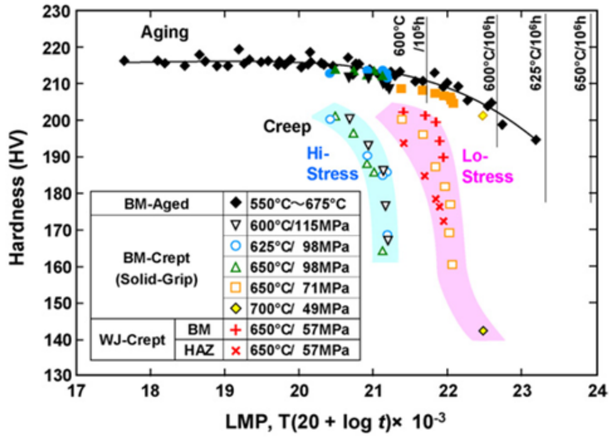

Figure 1.6 – Baisse de la dureté de l'acier Grade 91 (noté « BM-Crept ») selon la durée de vie et la température de fluage [14].

1.2.2 Adoucissement de l'acier Grade 91 en cours de fluage

A l'échelle macroscopique, l'adoucissement de l'acier Grade 91 est caractérisé par une baisse de dureté [14]. La Figure 1.6 montre que la dureté de cet acier baisse le long du temps de fluage. L'adoucissement de l'acier Grade 91 est dû à l'évolution métallurgique de sa microstructure. En effet, la taille des sous-grains croît le long d'un essai de fluage [15–17]. La densité de dislocations diminue aussi [18,19]. La taille des précipités de type $M_{23}C_6$ croît le long du fluage [16, 18, 20]. La croissance des phases de Laves dans l'acier Grade 91 a été observée à 600°C, ainsi que de manière limité une phase Z [20]. La croissance et la coalescence des précipités $M_{23}C_6$ induit une perte de l'ancrage des dislocations, alors que le grossissement des phases de Laves conduit à une réduction de la solution solide de Mo [4], et probablement à des sites de germination de cavités de fluage.

1.2.3 Cavitation induite par la diffusion des lacunes le long des joints polycristallins

Eggeler et al. [21] ont observé en microscopie optique des cavités de fluage dans un acier martensitique revenu à 12%Cr ayant une microstructure similaire à celle de l'acier Grade 91. Cette étude concerne un essai de fluage de durée de vie de 270 h. La déformation d'ingénieur à la rupture est de 12%. La réduction d'aire est de 10%, ce qui signifie que la striction est réduite. Ces auteurs ont constaté une rupture essentiellement d'origine intergranulaire dans le matériau. Des cavités de fluage situées le long des anciens joints de grains austénitiques et des joints de blocs ont été observées à une déformation d'ingénieur de 5% (réduction d'aire de 5%). Des observations similaires ont été rapportées concernant l'acier Grade 91 [4,22].

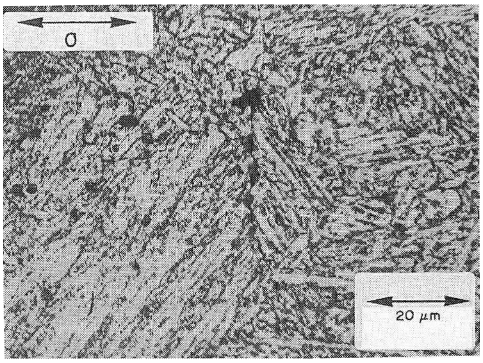

Figure 1.7 – Cavités de fluage intergranulaires observées en microscopie optique dans un acier martensitique à 12%Cr pour une déformation $\varepsilon^{eng} = 5\%$ durant un essai de fluage à 650°C et 80 MPa [21]. Les cavités sont situées le long des anciens joints de grains austénitiques et des joints de blocs d'après [21].

1.3 Conclusions et démarche de thèse

L'examen de la littérature a montré que les aciers martensitiques à 9-12%Cr soumis au fluage sont affectés par trois principaux mécanismes de ruine : la striction, la cavitation intergranulaire et l'adoucissement du matériau. Cela nous conduit à la démarche de thèse suivante.

La striction pourrait être le mécanisme principal menant à la ruine de l'acier Grade 91 jusqu'à des durées de vie de 160×10^3 h à 500°C et de 94×10^3h à 600°C. La simulation de la striction tenant compte de l'adoucissement du matériau en cours du fluage grâce à une modélisation analytique ainsi que des observations expérimentales seront présentées dans la partie II. Des lois de prédiction de durée de vie obtenues à partir de cette simulation seront appliquées aussi aux autres aciers martensitiques.

Des cavités de fluage intergranulaires ont été observées après les deux essais de fluage de durée de vie de 160×10^3 h à 500°C et de 94×10^3h à 600°C. Ces cavités seront étudiées dans la partie III. Les cavités de fluages seront modélisées grâce à des modèles classiques de germination et de croissance de cavités induites par la diffusion des lacunes le long des anciens joints de grains austénitiques et des joints de blocs. Des observations en microscopie électronique à balayage (FEG-SEM) à la fin des essais de fluage serviront comme des ingrédients à ces modèles. Elles permettront également des comparaisons entre les distributions de taille de cavités prédites et celles mesurées. Les durées de vie prédites grâce à ces modèles de cavitation pour les essais de fluage étudiés seront comparées avec les résultats expérimentaux. A ce stade, les joints sont supposés soumis à des contraintes constantes dans le temps et égales à la contrainte macroscopique.

L'effet de l'hétérogénéité de la microstructure sur les concentrations de contrainte et la nucléation des cavités sera prise en compte par des calculs par éléments finis des champs de contrainte autour des points triples présentées dans la partie IV. L'hypothèse de quasi-2D déformation plane sera utilisée permettant des temps de calculs plus courts et de raffiner considérablement les maillages. Les microstructures utilisées sont construites grâce à un modèle simple de point triple ainsi que des mesures EBSD. Une loi élasto-viscoplastique cristalline nécessitant seulement trois paramètres sera utilisée. Ces paramètres seront identifiés par des simulations des courbes de fluage sur de grands agrégats polycristallins comparées à des courbes expérimentales.

Des conclusions et perspectives seront présentés dans la partie V. Des lois de prédiction des durées de vie comprises dans le domaine des données expérimentales seront montrées. Des extrapolations des durées de vie hors du domaine exploré en laboratoire seront également présentées.

Chapitre 2

Propriétés de l'acier martensitique revenu Grade 91

2.1 Evolution historique des aciers martensitiques revenus au chrome

La famille des aciers au chrome a connu sa première application dans les centrales thermiques dans les années 1930 avec la nuance $2\frac{1}{4}$Cr-1Mo (P/T22) utilisée comme un matériau de cuve et de tubes du générateur de vapeur [23]. Le développement des aciers à 9-12% de Cr a commencé en 1912 en Allemagne avec les nuances 12%Cr et 2-5%Cr conçues pour une bonne résistance à la corrosion [24]. Puis, ils ont évolué décennie après décennie au sein de différentes industries mondiales, comme indiqué sur la Figure 2.1. La nuance 9Cr-1Mo (T9) a été élaborée et introduite dans l'industrie vers l'année 1936 [25,26]. Néanmoins, les aciers à 9-12% chrome avec ajout de Mo et V ont été utilisés comme matériaux de centrales thermiques seulement à partir du milieu du 20$^{\text{e}}$ siècle [27]. Le développement des familles à 9-12%Cr a été particulièrement dynamique à la fin des années 1970 [27]. Durant cette décennie, l'acier 9Cr-1Mo a été modifié par ajout optimisé de V et Nb à Combution Engineering and Oak Ridge National Laboratories aux Etats-Unis, ce qui conduit à la création du Grade 91 (9Cr-1MoVNb) [27]. Ceci a été ensuite approuvé par le code ASME en 1983 [28]. Le développement de cet acier a continué à l'Université de Tokyo et Nippon Steel Corporation [29]. Ce travail a conduit au milieu de la décennie 1980 à un nouvel alliage pour la forge de turbines nommé NF616 [29], qui a été approuvé par le code ASME en 1994 sous le nom Grade 92 [30,31].

Notre étude concerne plus spécifiquement l'acier Grade 91. Cet acier a déjà été utilisé dans les circuits de vapeur des centrales nucléaires [32], comme à Lippendorf (267 bar, 550-580°C), Boxberg (267 bar, 555-578°C), et Nordjylland (290 bar, 590°C). Dans le cadre des réacteurs de la génération IV, il est un candidat pour certains composants du circuit secondaire et les tubes des générateurs de vapeur du prototype SFR (Sodium-cooled Fast reactor) [1].

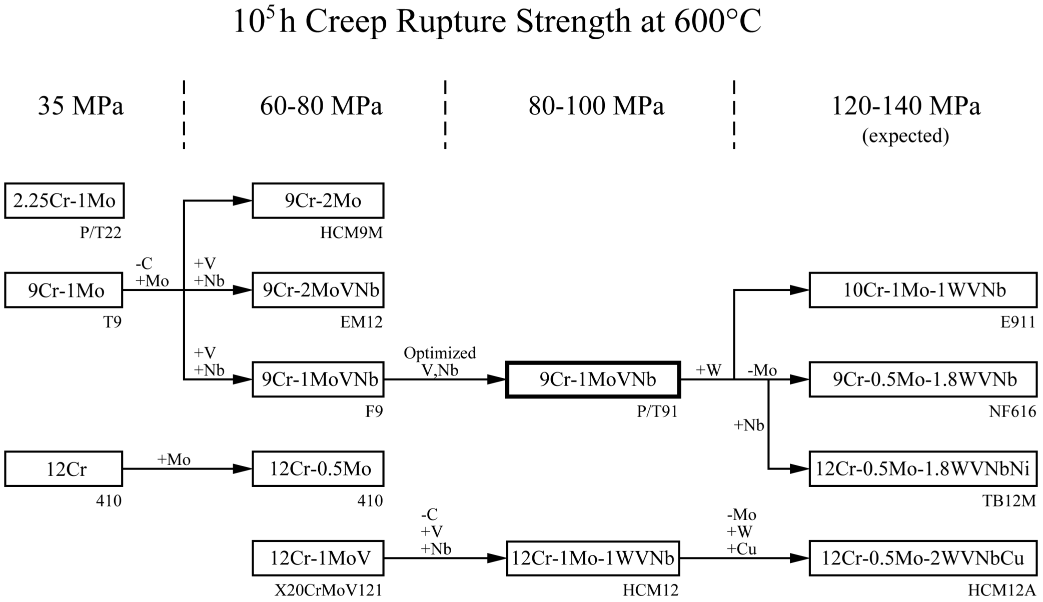
10⁵h Creep Rupture Strength at 600°C
35 MPa
60-80 MPa
80-100 MPa
120-140 MPa
(expected)
2.25Cr-1Mo
P/T22
9Cr-1Mo
T9
-C
+Mo
+V
+Nb
9Cr-2Mo
HCM9M
9Cr-2MoVNb
EM12
+V
+Nb
9Cr-1MoVNb
F9
Optimized
V,Nb
9Cr-1MoVNb
P/T91
+W
-Mo
+Nb
10Cr-1Mo-1WVNb
E911
9Cr-0.5Mo-1.8WVNb
NF616
12Cr-0.5Mo-1.8WVNbNi
TB12M
12Cr
410
+Mo
12Cr-0.5Mo
410
12Cr-1MoV
X20CrMoV121
-C
+V
+Nb
12Cr-1Mo-1WVNb
HCM12
-Mo
+W
+Cu
12Cr-0.5Mo-2WVNbCu
HCM12A

Figure 2.1 – Evolution de la composition chimique des aciers à 9-12%Cr [27, 29].

2.2 Composition chimique

Deux tôles d'acier Grade 91 étudiées ont été fabriquées à Creusot-Marrel et Usinor. La Table 2.1 montre les compositions chimiques exprimées en pourcentage massique des deux tôles [33, 34] ainsi que de l'acier Grade 91 selon ASTM Standard A387 - Grade 91 [35]. Les pourcentages massiques des éléments constituant les deux tôles sont compris dans les limites données par la spécification ASTM. Il est aussi défini dans le code français RCC-MRx [36].

Le rôle des différents éléments chimiques utilisés dans les alliages métalliques a été étudié par Masuyama et al. [37]. L'élément Cr permet une bonne résistance à la corrosion et de bonnes propriétés mécaniques [37]. Les éléments Nb et V permettent la formation des précipités Nb(CN) et VN qui aident à stabiliser les joints de grains austénitiques lors la normalisation [38]. En plus, d'autres précipités Nb(CN) et VN se forment lors du revenu et renforcent le matériau. L'élément Mo est un élément de durcissement de la solution solide [37]. Les éléments de P et S peuvent ségréger aux joints de grains et les fragiliser [4, 38]. Leur quantité doit être donc strictement contrôlée. L'élément Ni peut précipiter sous forme fragile riche en Fe, ainsi sa quantité doit être également contrôlée [4].

2.3 Elaboration

Les tôles d'acier Grade 91 Creusot-Marrel et Usinor ont été élaborées au four électrique à l'arc, puis affinées en poche (vacuum arc degassing), et enfin coulées en coulée continue. Elles ont été laminées respectivement en épaisseur de 300mm et 30mm. Ces tôles ont ensuite subi trois stades de traitement thermique : la normalisation, la trempe, et le revenu. Les caractéristiques de ces trois stades sont reportées dans la Table 2.2.

Table 2.1 – Composition chimique exprimée en pourcentage massique de l'acier Grade 91 selon ASTM Standard A387 - Gr 91 [35](minimum/maximum), et des deux tôles en acier Grade 91 étudiées et fabriquées à Creusot-Marrel (CM) [33] et Usinor [34].

	C	Si	Mn	P	S	Cr	Ni	Mo	V	Nb	N
ASTM	0.08 0.12	0.2 0.5	0.3 0.6	$\leq$0.02	$\leq$0.01	8.0 9.5	$\leq$0.4	0.85 1.05	0.18 0.25	0.06 0.1	0.03 0.07
CM	0.106	0.47	0.38	0.009	0.003	9.0	0.12	1.01	0.21	0.07	0.053
Usinor	0.088	0.324	0.363	0.017	0.001	8.91	0.149	0.917	0.198	0.08	0.041

Table 2.2 – Traitements thermiques des deux tôles de Grade 91 fabriquées à Creusot-Marrel [33] et Usinor [34].

Tôle	Coulée	Traitement thermique		
	Epaisseur	Normalisation	Trempe	Revenu
Creusot-Marrel	300mm	1070°C/7h	à eau	760°C/8h
Usinor	30mm	1050°C/30min	à air	780°C/1h

Normalisation Les aciers à 9%Cr et à faible contenu en C et N sont sous forme austénitique à la température de normalisation comprise entre 850 et 1200°C [38]. Orr et al. [39] constatent que la taille des grains austénitiques croît légèrement durant une normalisation à 1050 voire 1100°C et de durée jusqu'à 24 h. Elle commence à croître significativement seulement à partir de la température de normalisation de 1125°C [39]. Les nitrites VN se dissolvent entièrement à 1100°C [40,41]. Mais, les carbures Nb(CN) ne se dissolvent pas aux températures de normalisation habituelles [38,40,41] (i.e. entre 850 et 1200°C). Cependant, ces carbo-nitrures limitent les mouvements des joints de grains et évitent la croissance excessive de taille de grains austénitiques [38].

Trempe Après la trempe, la microstructure des aciers à 9-12%Cr contient des lattes de martensite et une densité de dislocations élevée [38]. Les lattes de martensite sont riches en Fe-C et ont une structure atomique de type quadratique, Fe-α', qui contient des atomes C en position interstitielle en plus par rapport à Fe-α.

Revenu Un adoucissement rapide du matériau lors du revenu est constaté d'après la chute de dureté (Fig. 2.2). La densité de dislocations diminue. La martensite se transforment en ferrite grâce à la précipitation de carbures. Les lattes s'élargissent et les sous-grains se forment. Les précipités de type $M_{23}C_6$ et MX sont formés [38].

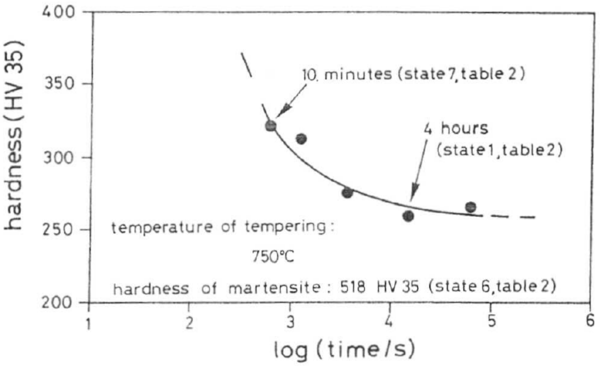

Figure 2.2 – Evolution de la dureté d'un acier à 12%Cr le long du revenu [42].

2.4 Microstructure à l'état de réception

2.4.1 Tailles caractéristiques

La microstructure de l'acier Grade 91 après les trois stades de traitement thermique est montrée sur les Figures 2.3. Sa microstructure est complexe et divisée en plusieurs échelles comme schématisé sur la Figure 2.4 d'après [43]. L'échelle la plus grande est celle des anciens grains austénitiques formés durant la normalisation. Pour l'acier Grade 91, leur taille moyenne est comprise entre 50 et 70 µm [33]. Chaque ancien grain austénitique est divisé en plusieurs paquets de bloc. Les blocs ont une taille moyenne de 2 µm [24] et possèdent entre 5 et 10 lattes alignés et faiblement désorientées entre elles [44–46]. Chaque latte est divisée en sous-grains. Les sous-grains ont une structure atomique de type cubique centré (bcc). Ils représentent l'échelle la plus petite. Pour l'acier Grade 91, leur taille moyenne est comprise entre 0.3 et 0.5 µm [16, 17, 47].

Table 2.3 – Tailles moyennes des anciens grains austénitiques (d_g), des blocs (d_{bl}) et des sous-grains (d_{sg}) pour l'acier Grade 91, obtenus grâce à des traitements thermiques de type de ceux décrits dans la Table 2.2.

Nuance	d_g (µm)	d_{bl} (µm)	d_{sg} (µm)
Grade 91	50-70 [33]	2 [24]	0.3-0.5 [16–18, 47]

2.4.2 Relations entre orientations cristallographiques

Les orientations cristallographiques des blocs appartenant à un même ancien grain austénitique (à l'état de réception) sont liées à celle du grain austénitique (durant la normalisation) par les relations de Kurdjumov-Sachs [48] (Eq. 2.1) ou de Nishiyama-Wasserman [49] (Eq. 2.2) (voire d'un mixte entre ces deux relations). A partir d'un grain austénitique lors de la normalisation, la relation de Kurdjumov-Sachs prédit 24 variants pour les blocs (à l'état de réception) alors que celles de Nishiyama-Wasserman prédit seulement 12 variants.

$$(111)_\gamma \, // \, (011)_\alpha \quad [110]_\gamma \, // \, [1\bar{1}1]_\alpha \tag{2.1}$$

$$(111)_\gamma \, // \, (011)_\alpha \quad [1\bar{2}1]_\gamma \, // \, [1\bar{1}1]_\alpha \tag{2.2}$$

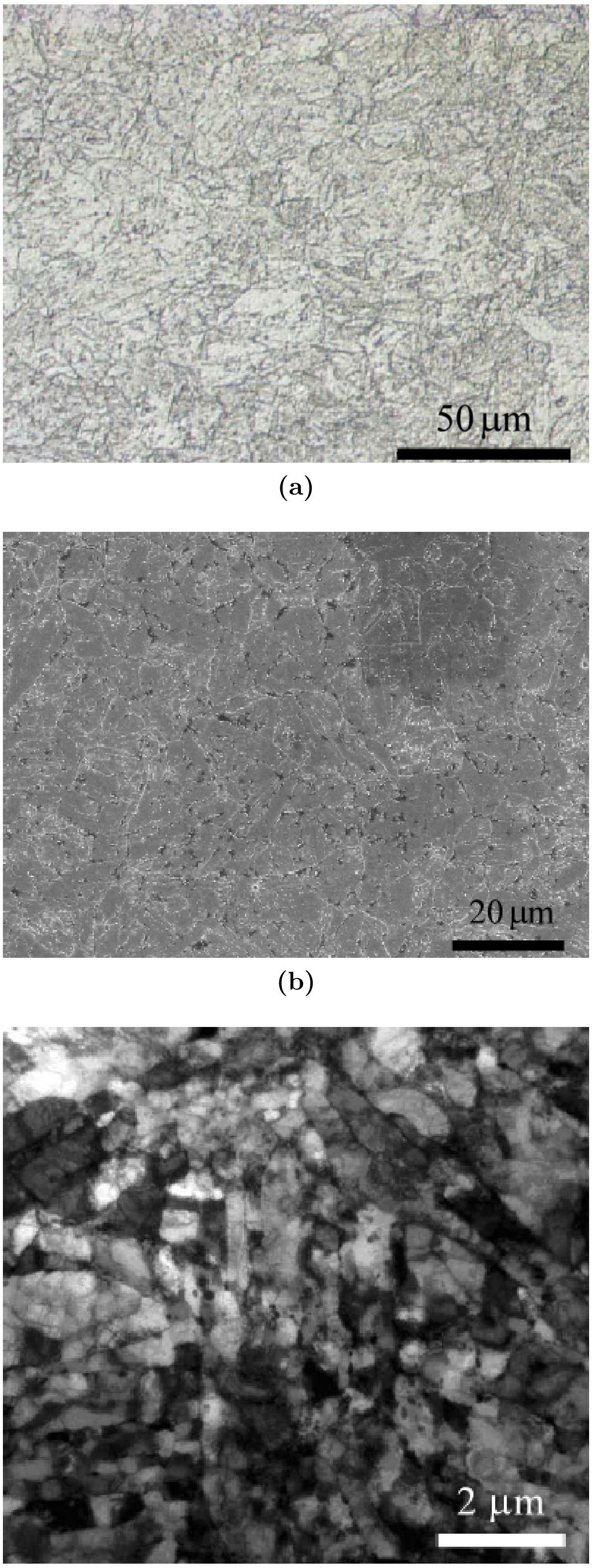

(a)

(b)

(c)

Figure 2.3 – Microstructure de l'acier Grade 91 à l'état de réception observée en (a) microscopie optique, (b) microscopie électronique à balayage (MEB ou SEM) et (c) microscopie électronique à transmission (MET ou TEM) [24].

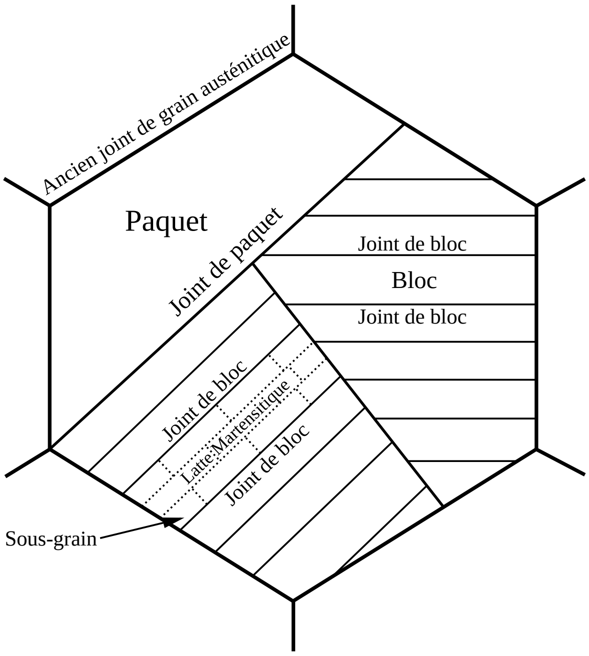

Figure 2.4 – Schéma de la microstructure de l'acier Grade 91 à l'état de réception [43].

Les désorientations entre des blocs appartenant à des anciens grains austénitiques différentes sont aléatoires [50]. Un paquet est constituée de blocs de lattes parallèles allongées le long du même plan $\{111\}_\gamma // \{011\}_\alpha$. Ces blocs de lattes peuvent avoir une parmi les 6 orientations qui correspondent au nombre de possibilités d'associer l'une ou l'autre des deux directions $[1\bar{1}1]_\alpha$ et $[11\bar{1}]_\alpha$ du plan $(011)_\alpha$ aux trois directions parents $[0\bar{1}1]_\gamma$, $[1\bar{1}0]_\gamma$ et $[10\bar{1}]_\gamma$ du plan $(111)_\gamma$. Dans un même paquet, deux lattes voisines peuvent, soit avoir la même orientation, soit former l'un des 15 couples possibles entre les 6 variants existants différents. Chaque bloc de lattes est donc désorienté par rapport aux autres, soit de manière aléatoire (deux blocs appartenant à des paquets différents), soit de l'un des dix angles prévus par la relation de Kurdjumov-Sachs, ou d'un des 5 prévus par celle de Nishiyama-Wassermann [51].

Un bloc peut se distinguer des autres par une désorientation de plus de 10.5° [52]. Les désorientations des lattes et des sous-grains appartenant à un même bloc sont inférieures à celle-ci [52]. Les sous-joints peuvent être confondus avec les parois constitués d'une ou plusieurs familles de dislocations [45, 46]

2.4.3 Dislocations

Les aciers à 9-12%Cr contiennent une densité de dislocations élevée après la trempe [38]. Ces aciers s'adoucissent au fur et à mesure du temps de revenu qui est caractérisé par une baisse de la dureté à l'échelle macroscopique, ainsi que par une diminution des densités totales de dislocations [42]. Pour les aciers à 9-12%Cr, les densités de dislocations après le revenu sont comprises entre $5 - 10 \times 10^{14} \mathrm{m}^{-2}$ [18, 53, 54] et reportées dans Table 2.4.

La Figure 2.5 montre des sous-grains et des dislocations dans l'acier Grade 91 à l'état de réception [24]. Pour l'acier Grade 91 (tôle Creusot-Marrel) ayant subi les traitements thermiques spécifiés dans la Table 2.2 (voir aussi la Table 2.5), la densité de dislocations

Table 2.4 – Densité totale de dislocations pour les aciers à 9-12%Cr.

Nuance	Normalisation et Revenu	Densité (m^{-2})
Grade 91 [18]	N. 1050°C/1h R. 750°C/1h	7.5×10^{14}
Grade 92 [18]	N. 1070°C/2h R. 775°C/2h	7.5×10^{14}
X20CrMoV-12-1 [54]	N. 1050°C/1h R. 750°C/1h	5.3×10^{14}

Table 2.5 – Densité de dislocations mobiles pour les aciers à 9-12%Cr.

Nuance	Normalisation et Revenu	Densité (m^{-2})
Grade 91 [53]	N. 1070°C/7h R. 760°C/8h	1.6×10^{14}
X20CrMoV-12-1 [42]	N. 1050°C/1h R. 750°C/90min	0.6×10^{14}
X20CrMoV-12-1 [54]	N. 1050°C/1h R. 750°C/1h	1×10^{14}

mobiles est de $1.6 \times 10^{14} m^{-2}$ à l'état de réception d'après les mesures en microscopie électronique à transmission (MET ou TEM) [53].

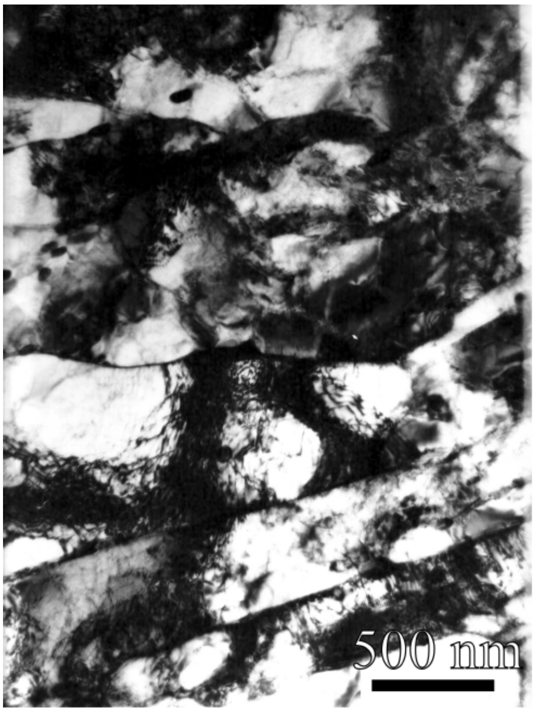

Figure 2.5 – Observations des sous-grains et des dislocations dans l'acier Grade 91 à l'état de réception [24]. La distribution spatiale des dislocations est hétérogène.

La distribution spatiale des dislocations est hétérogène comme le montre la Figure 2.5. Les dislocations sont constituées de celles situées aux joints de sous-grains et celles localisées à l'intérieur des sous-grains (dislocations mobiles) [54]. Pour l'acier à 12%Cr dont les traitements sont indiqués dans les Tables 2.4 et 2.5, les dislocations mobiles constituent 20% de la population totale [54].

2.4.4 Précipités

Table 2.6 – Tailles des précipités $M_{23}C_6$ et MX présents dans les aciers à 9-12%Cr.

Nuance	$M_{23}C_6$ (nm)	MX (nm)
Grade 91 [55]	$\overline{d}_{M23C6} = 137$	-
Grade 91 [16]	$\overline{d}_{M23C6} = 79$	-
Grade 91 [56]	$d_{M23C6} < 150$ (sous-joints) $d_{M23C6} > 350$ (joints γ)	$d_{MX} = 17 - 60$
Grade 92 [47]	$\overline{d}_{M23C6} = 90$	$\overline{d}_{MX} = 20$
X20CrMoV-12-1 [42]	$\overline{d}_{M23C6} = 137$	-
X20CrMoV-12-1 [57]	$d_{M23C6} = 80 - 150$ (sous-joints) $d_{M23C6} = 130 - 310$ (joints γ)	- -

A l'état de réception, l'acier Grade 91 contient deux grands types de précipités : $M_{23}C_6$ et MX [16,55,56]. Les analyses à l'EDS menées par Gieseke et al. [56] sur l'acier Grade 91 ont montré que le nombre de précipités de type $M_{23}C_6$ constituent entre 85 et 90% de la population totale des précipités. Les précipités de type $M_{23}C_6$ sont situés généralement aux joints (de grains austénitiques, de paquets, de blocs et de lattes) [56,57]. Les précipités de type MX sont répartis de manière uniforme dans la microstructure [52,58].

Les tailles des précipités pour les aciers à 9-12%Cr sont reportées dans la Table 2.6. Elles peuvent varier en fonction des nuances d'aciers ainsi que des traitements thermiques appliqués par les auteurs [16,42,47,55–57]. Pour l'acier Grade 91, les tailles moyennes des précipités de type $M_{23}C_6$ et de type MX sont respectivement de l'ordre de 100 nm et 20 nm [16,55,56].

2.5 Traction simple

Le module d'Young de l'acier Grade 91 a été mesuré à des températures différentes et son évolution est donnée par le code RCC-MRx [36]. La Figure 2.6 montre que le module d'Young du matériau diminue en fonction de la température. Un changement de pente sur ce graphe est observé à la température 500°C. Cela pourrait être dû en partie à la déformation anélastique provoquée par la flexion élastique des sous-joints due aux sous-grains [59].

La limite d'élasticité conventionnelle de l'acier Grade 91 (pour une déformation viscoplastique de 0.2%) varie en fonction de la vitesse de déformation comme indiqué sur la Figure 2.7. Les essais de traction sur l'acier Grade 91 menés par Gaffard [4] à 625°C montrent que la limite d'élasticité conventionnelle obtenue au test sous la vitesse de $10^{-5}s^{-1}$ est deux fois plus petite que celle obtenue sous la vitesse de $10^{-2}s^{-1}$. Cela est également vrai pour la résistance maximale de traction [4]. Cet effet est dû à la baisse de la contrainte visqueuse d'après la théorie de l'activation thermique. Il pourrait être également dû à l'adoucissement du matériau qui augmente quand la vitesse de déformation diminue [13]. La limite d'élasticité baisse de 15% alors que la résistance maximale diminue de 35%, quand la température croît de 450 à 625°C sous la même vitesse déformation de $10^{-3}s^{-1}$

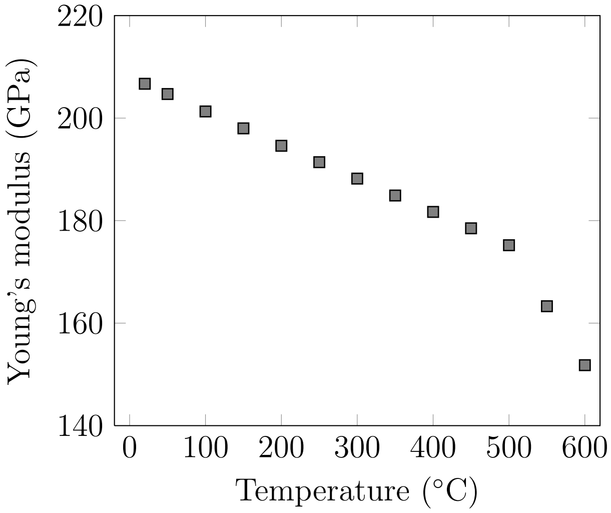

Figure 2.6 – Module d'Young de l'acier Grade 91 [36]

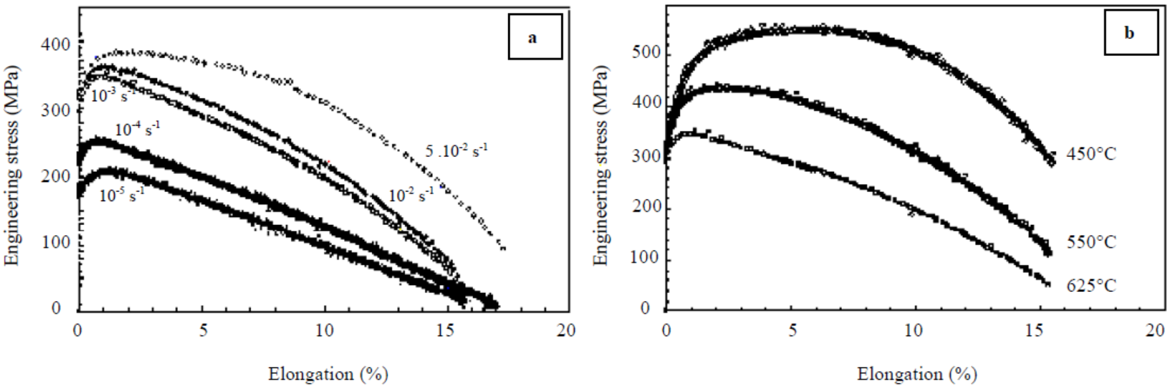

Figure 2.7 – Essais de traction sur l'acier Grade 91 (a) à 625°C à des vitesses de déformation comprises entre 10^{-5} et $5 \times 10^{-2}\text{s}^{-1}$ et (b) à trois températures, à la même vitesse de 10^{-3}s^{-1} [4].

(Fig. 2.7). Ceci pourrait être dû à l'adoucissement du matériau qui croît aussi en fonction de la température.

Les essais de traction monotone indiqués ci-dessus ont duré jusqu'à seulement 5 h. Notre étude menée sur des essais de fluage de durées de vie comprises entre une dizaine d'heures et plusieurs centaines de milliers d'heures est maintenant présentée.

Part II

Necking

Résumé

Les stades tertiaires de nombreux essais de fluage de durée de vie jusqu'à 160 kh à 500°C et 94 kh à 600°C sont modélisés et observés expérimentalement. Après avoir atteint le minimum, la vitesse de déformation croît le long de la déformation. Cela est dû à l'adoucissement du matériau induit par l'évolution microstructurale. Un essai interrompu à plusieurs reprises montre que la striction conduit à une forte réduction d'aire en zone de striction seulement durant les deniers 10% de la durée de vie. Le modèle de Hoff basé sur la réduction homogène de la section prédit correctement seulement les durées de vie à haute contrainte. Le modèle de striction de Hart utilisant la loi de Norton sans adoucissement du matériau permet des prédictions de durée de vie jusqu'à 60 kh à 500°C. Le modèle de striction prenant en compte l'adoucissement du matériau permet de prédire les durées de vie différentes des résultats expérimentaux des essais de fluage étudiés de moins de 50%, ce qui correspond à la dispersion expérimentale. L'évolution de la section en zone de striction prédite est en accord avec un essai interrompu. Deux lois de borne sont déduites du modèle de striction tenant compte de l'adoucissement du matériau. Les durées d'un grand nombre d'aciers martensitiques de durée de vie jusqu'à 200 kh à 500-700°C sont comprises entre les deux lois de borne. A ce stade, les cavités ne sont pas prises en compte dans la modélisation.

Mots clés : fluage, acier Grade 91, stade tertiaire, adoucissement du matériau, striction, durée de vie.

Chapter 3

Modelling and experimental study of the tertiary creep stage of grade 91 steel

(Published in Int. J. Fracture [60])

3.1 Introduction

It is widely considered that modified 9Cr-1Mo (Grade 91) tempered martensitic steel is a suitable candidate material for structural components subjected to high temperature creep, such as coolant pipes of the future Generation IV nuclear reactors. Its mechanical properties are reported by [61]. In the asreceived condition, the grade 91 steel has a complex microstructure [43] made of former austenitic grains (diameter between 10 and 60 µm) [17, 62]. Each austenitic grain is divided into martensite packets, further divided into martensite blocks. Each block is made of 5 to 10 martensitic laths. Finally, each martensitic lath is divided into sub-grains having a size between 0.3 and 0.5 µm [17, 47]. Secondary phases of $M_{23}C_6$ type (M means Fe or Cr) are found next to or at grain boundaries and correspond to about 90% of the total particle distribution [63]. The rest of the particles are of the MX type (M means V or Nb and X means C or N) and are distributed homogeneously in the whole microstructure (within laths and at grain boundaries) [58]. The size of $M_{23}C_6$ particles is about 250 nm and that of MX particles, 40 nm [63]. Dislocations are observed aligned in lattice and pinned at secondary phases and boundaries [54]. Their density is about 1.6 10^{14}m^{-2} for Grade 91 after annealing at 1070°C for 7 h then tempering at 760°C for 8 h [64].

The Hoff model predicts that the creep lifetimes are inversely proportional to the minimum strain rate estimated using the Norton power-law [65]. This model allows fair prediction only for short lifetimes for softening materials such as Grade 91 steel [7]. In the present case, the predictions are accurate for lifetimes up to 60 10^3h at 500°C [7], 10^3h at 650°C [8], and 400 h at 700°C [8]. Beyond these limits, the model overestimates the actual lifetimes due to the drop in slope of the experimental engineering stress vs. the creep lifetime curve. This drop is due to creep softening effect and/or to damage development in the material, which increases with increasing creep lifetime [14, 66]. Monkman and

Grant [5] suggested that the time to failure is inversely proportional to a power function of the minimum creep rate. Experimental creep data of Grade 91 steel approximately obey that relationship (within an error of 50%) for lifetimes up to 160 10^3h and at temperatures between 500 and 625°C [7]. However, this method requires numerous experimental results for the adjustment of the Monkman-Grant parameters for a given material. The lifetime model developed by Hart [67] is based on necking, which was first studied by Considere [12] and more recently by Dumoulin et al. [68]. The Hart model is used for viscoplastic materials obeying the Norton power-law equation. Its failure criterion is based on the reduction in cross-section at fracture. Extensive necking controls the fracture of Grade 91 creep specimens only for short-term creep does. Long-term creep specimens fracture after the coalescence of diffusional creep cavities. These ones nucleated and grew at austenitic grain and packet/block boundaries [21].

For a softening material such as Grade 91 steel, creep softening should also be introduced. In fact, the hardness of Grade 91 steel usually drops during creep and the final drop is maximal at high temperatures and during long-term tests [14]. The creep behaviour of X20CrMoV12-1 steel at 600°C in compression (prescribed axial compressive true stress) and in tension (prescribed axial engineering stress with possibility of necking) were compared by Straub et al. [69]. Their results showed similar true strain rate vs. true strain curves up to a half of the fracture strain under creep tension [69]. The same conclusion holds for the strain acceleration and creep strain rate evolution. In compression, necking and creep cavitation were not expected to occur. Therefore, the acceleration of the strain rate was attributed to the material creep softening of the material itself.

The softening of Grade 91 steel comes from its microstructure evolution during creep. In fact, the higher the temperature, the stronger the sub-grain growth [16]. Similarly, the longer the test duration, the stronger the sub-grain growth [16,70]. The overall dislocation density drops by a factor 3 during a creep time of 125 h (strain of 8%) at 650°C for a 12%Cr tempered martensitic steel [54]. Dislocation annihilation leads to the disappearing of some of the sub-grain boundaries and, consequently, to sub-grain growth. $M_{23}C_6$ carbides grow and their number progressively decreases with increasing creep time [20, 70]. The final size of $M_{23}C_6$ particles increases with increasing creep lifetime [16]. The growth of the $M_{23}C_6$ carbides causes a decrease in their pinning effect on dislocations leading to lath boundary recovery [16]. Laves phases, Fe_2Mo, nucleate and grow significantly during the creep deformation of the Grade 91 steel, e.g. their mean radius reaches about 500 nm after a creep duration of 50 10^3h at 600°C [20]. The precipitation of Laves phases leads in particular to a decrease in solid solution strengthening induced by molybdenum [71].

This paper presents experimental results from a database of 17 creep tests carried out on Grade 91 steel at CEA/SRMA as well as simple analytical simulation of the tertiary creep stage at temperatures between 500 and 600°C. The results of creep tests (Section 3.2) are used in order to identify the parameters of both the Norton power-law and an additional softening term. The evolution of cross-section during an additional creep test interrupted several times at 500°C under 350 MPa is also presented. Analytical modelling of the tertiary creep stage (Section 3.3) takes both mechanical and metallurgical effects into account, namely, the development of necking (due to some surface defect of the specimen, using the Hart model) and the metallurgical softening of the material during creep (using the law mentioned above). The evolution of the specimen cross-section predicted with this model is compared with measurements carried out during the interrupted creep test. Creep lifetimes predicted by lower and upper bounds are then deduced from the necking model including the material softening. These bounds are compared with the experimental creep results of a large number of tempered martensitic steels at temperatures between 500 and 700°C.

3.2 Materials and experiments

3.2.1 Materials

Two materials of Grade 91 type were used for the creep tests. Material 1 was taken from a 300 mm thick plate produced by Creusot-Marrel and Material 2 was taken from a 30 mm thick plate fabricated by Usinor. The chemical compositions and heat treatments are given in Table 3.1 and Table 3.2, respectively. The first material was tested at 500 and 600°C, and the second one at 550°C.

Table 3.1: Chemical composition of both materials under study expressed in wt.%.

Element	Material 1	Material 2
C	0.106	0.088
S	0.003	0.001
P	0.009	0.017
Si	0.47	0.324
Mn	0.38	0.363
Ni	0.12	0.149
Cr	9.0	8.91
Mo	1.01	0.917
V	0.21	0.198
Nb	0.07	0.08
N	0.053	0.041

Table 3.2: Heat treatments of both materials under study.

Materials	Initial state	Austenisation	Cooling	Temper
Material 1	Hot forged and rolled	1070°C / 7 h	water	760°C / 8 h
Material 2	Hot forged and rolled	1050°C / 30 min	air	780°C / 1 h

3.2.2 Mechanical testing

All creep tests were carried out at a constant temperature and a constant load using specimens of 85 mm in total length, 40 mm in gauge length and 5 mm in gauge diameter. The summary of creep tests is reported in Table 3.3. One multiple-loading-unloading creep test was performed at 500˚C and 350 MPa. This test includes three interruptions at three different engineering strain levels: 1.68%, 6.8%, and 10.0% (Table 3.4). The diameter profile of the gauge length along the loading axis was measured at room temperature using a Laser Scan Micrometer before the beginning of the test and after each unloading step; then, the creep specimen was again mounted on the creep machine to continue the test until the next interruption.

Table 3.3: Database of creep tests carried out at CEA/SRMA on the Grade 91 steel. T: temperature, σ^{eng}: engineering stress, t_f: lifetime.

T (˚C)	σ^{eng} (MPa)	t_f (h)
500	370	14.8
500	350	38.0
500	270	10396
500	250	59347
500	230	160
500	210	in progress
550	275	64
550	230	1230
550	215	3236
550	200	10796
550	185	in progress
600	160	543
600	140	2,103
600	125	5,022
600	110	14,946
600	90	93,749

Table 3.4: Creep test carried out at 500˚C and 350MPa on Grade 91 steel at CEA/SRMA, interrupted at three engineering strain levels (ε^{eng}) before fracture.

Interrupted points	ε^{eng}(%)	Time (h)
1	1.68	14
2	6.8	39
3	10	43
rupture (last recorded value)	13.25	46.4

3.2.3 Measurements and observations of fractured specimens

The reduction of area at fracture was measured on SEM pictures as the mean value between both specimen halves. FEG-SEM (Field Emission Gun Scanning Electron Microscopy) observations were carried out at CEA/SRMA to characterize long-term damage for two creep tests, one with a time to failure of 160×10^3h (500°C) and another with a lifetime of 94×10^3h (600°C). FEG-SEM observations were carried out on the longitudinal cross-sections of one-half of the fractured specimen. The observed area were located far from the necking area, as shown in Fig. 3.1. The samples were polished with a colloidal silica solution finish.

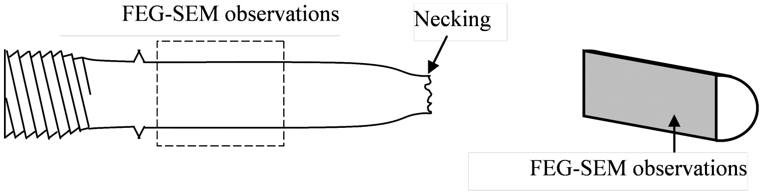

Figure 3.1: Schematic diagram showing the sectioning procedure and zones for FEG-SEM observations.

3.2.4 Analysis of the creep curves

Creep curves are usually divided into three main stages: primary, secondary, and tertiary stage [3]. The secondary stage covers the time interval during which the creep rate varies negligibly or is almost constant. The slope of the straight line in the time-strain plot gives the minimum strain rate. The true strain or logarithmic strain (finite deformation) is expressed as a function of the engineering strain, ε^{eng} (infinitesimal deformation) [3]. The experimental scatter in strain leads to discontinuity of the strain rate derivative at a given time. To solve this problem, the engineering strain rate at a given time, t_i, is taken as the mean value of the left and the right slopes.

3.2.5 Results and discussion

Fig. 3.2 shows the ratios between the time duration of the tertiary stage and the total creep lifetime for various materials and various temperatures. For a given material and temperature, these ratios seem to decrease with increasing lifetime. For Grade 91 steel at temperatures between 500 and 625°C, the tertiary stage extends over 1/3 (long-term tests) to 2/3 (short-term tests) of the lifetime. The time fraction of the tertiary creep stage for Grade 91 steel is similar to that of A5052-0 aluminium alloy, 316 and 316L(N) austenitic stainless steel, and IN100 nickel-based alloy. This large time fraction could be attributed to at least one of the following phenomena: the decrease of the specimen cross section with or without localised necking, metallurgically-induced softening, and the growth of creep cavities.

Figures 3.3, 3.4 and 3.5 show the evolution of the true strain rate during creep tests. These curves allow determination of the minimum true strain rates. The Norton power-law Eq. (3.1) is then adjusted for each temperature using the minimum true strain rates and the engineering stress (Fig. 3.6). The temperature-dependent Norton parameters (n, C) are given in Table 3.5.

$$\dot{\varepsilon}_{min} = C(T)(\sigma^{eng})^{n(T)} \tag{3.1}$$

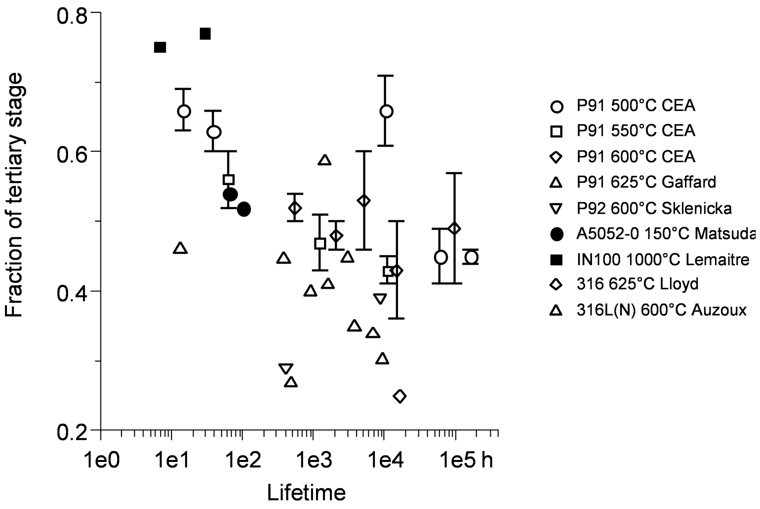

Figure 3.2: Ratio of the time spent in tertiary creep stage to total creep lifetime for Grade 91 steel at 500-600°C (CEA/SRMA) and at 625°C [72], Grade 92 steel at 600°C [73], A5052-0 aluminium alloy at 150°C [74], IN100 nickel-based alloy at 1000°C [3], 316 austenitic stainless steel at 625°C [75], and 316L(N) austenitic stainless steel at 600°C [76].

The Norton exponent decreases with increasing temperature. The values found here are in agreement with those given by [73] ($n = 12$ at 600°C), [77] ($n = 17$ at 550°C and $n = 13$ at 600°C) and finally [78] ($n = 16$ at 550°C and $n = 12$ at 600°C).

Table 3.5: Norton law parameters.

Temperature (°C)	n	$C(\mathrm{MPa}^{-n}\mathrm{h}^{-1})$
500	20.35	1.56×10^{-55}
550	16.76	6.97×10^{-45}
600	9.94	8.42×10^{-27}

The minimum true strain rate is reached at a strain, ε_{min}, ranging between 0.6 and 2.5% for temperatures between 500 and 600°C (Figs. 3.3, 3.4 and 3.5). This means that the minimum engineering and true strain rates differ by less that a few %. Each minimum true strain rate differs relatively by less than a few % from the corresponding “stationary”engineering strain rate, evaluated with the straight line method. For each creep test, the evolution of the logarithm of the true creep strain rate (h^{-1}) with respect to the true strain is plotted in Figs. 3.3, 3.4 and 3.5. Each evolution is linear after the minimum creep strain is reached and before the final acceleration. After reaching the minimum, the true strain rate seems to be an exponential function of the strain until 50% of the fracture strain i.e. the very end of the test. These observations are in agreement with the conclusions of Straub et al. [69] and Abe [79]. For each creep test, the “softening”slope, k, is defined as the slope of the linear part of each curve plotted in Figs. 3.3, 3.4 and 3.5: $k = \frac{\partial \log(\dot{\varepsilon})}{\partial \varepsilon}$. The “softening”slope globally increases with increasing lifetime, i.e. decreasing minimum strain rate (Fig. 3.7).

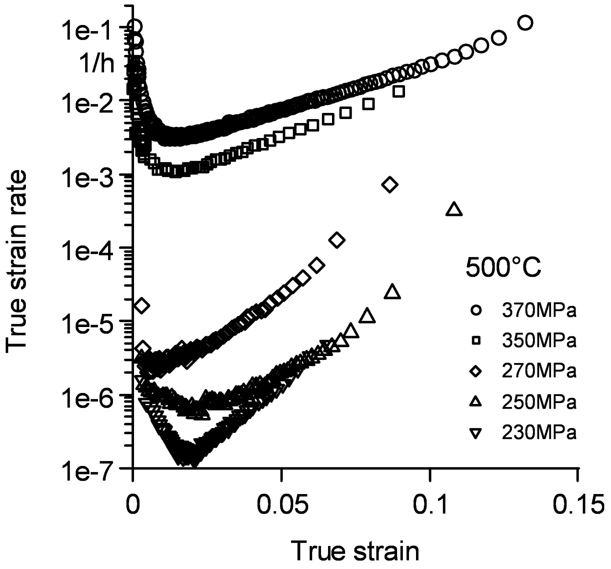

Figure 3.3: True strain rate evaluated using numerical derivation from creep curves (engineering strain vs. time) at 500°C.

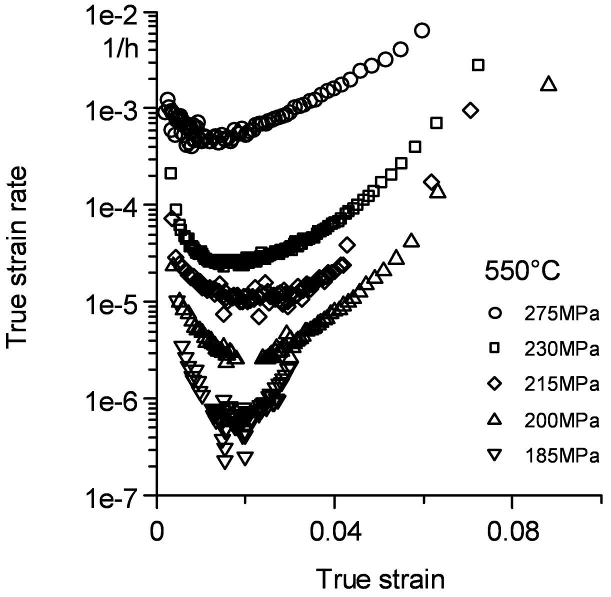

Figure 3.4: True strain rate evaluated using numerical derivation from creep curves (engineering strain vs. time) at 550°C.

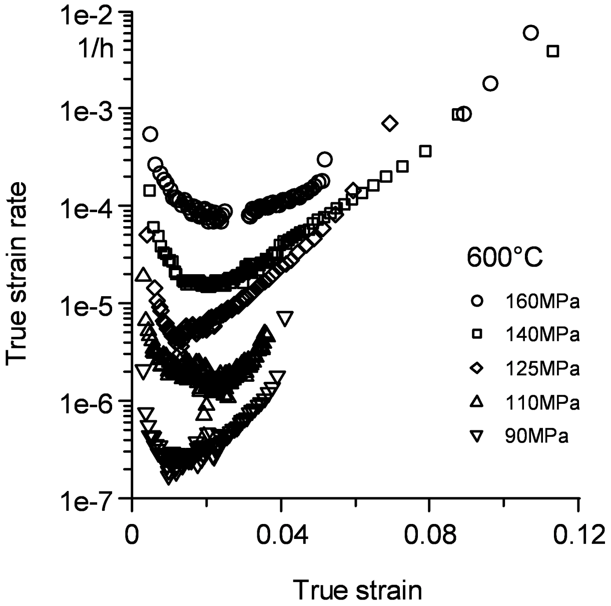

Figure 3.5: True strain rate evaluated using numerical derivation from creep curves (engineering strain vs. time) at 600°C.

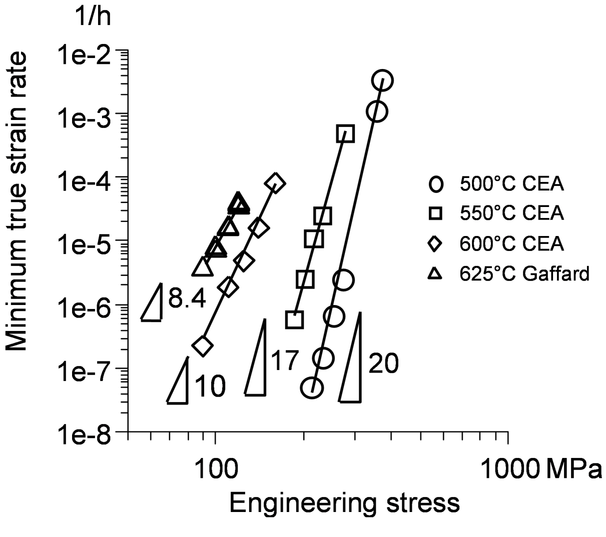

Figure 3.6: Norton power-law fit at 500-600°C (CEA/SRMA) and at 625°C [72].

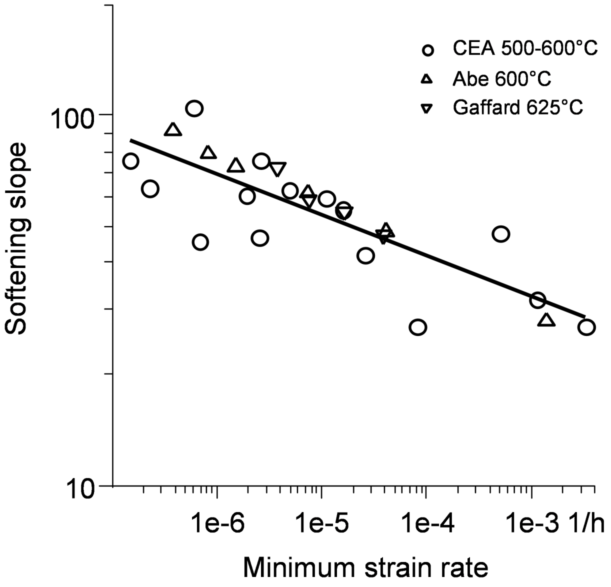

Figure 3.7: Softening slope versus minimum creep rate for Grade 91 steel, according to the date given by CEA/SRMA and [8, 72].

Fig. 3.7 shows that the softening slope can be represented with a power-law function of the minimum creep rate. The results of the present study were used together with literature results at 600°C [8] and at 625°C [72] to adjust the power-law parameters between 500 and 625°C:

$$k = A(\dot{\varepsilon}_{min})^{\alpha} \tag{3.2}$$

with $\alpha = 0.1098$, $A = 15.27$ and the creep strain rate is divided by h^{-1} in the power term.

The measured reduction of area at fracture varies between 20% and 80% (Fig. 3.8). Senior et al. [80] showed that cavities are nucleated and grow up to a size of 40 nm when the true strain of a tensile specimen at room temperature reaches 25%. This true strain corresponds to a reduction of 20% in cross-section. It shows that the critical reduction factor ranges between 20% and 100%. For long-term tests, e.g. 160×10^3h at 500°C and 94×10^3h at 600°C, the reduction of area is lower than that measured after short-term tests. At the end of these long-term creep tests, creep cavities up to 1 µm in size at 500°C and up to 5 µm at 600°C are observed far form the necking area (Fig. 3.9).

Experimental results on the additional test including interruptions and observations are illustrated in Figs. 3.10, 3.11 and 3.12. Before the creep test, the surface roughness leads to a maximum variation of 20 µm in diameter along the gauge length (Fig. 3.12). Observation with naked eye is not enough to see any change in cross-section between the initial state and the second interruption (6.8% of strain), (Fig. 3.11). Laser scan micrometer measurements reveal a reduction of 2% and 9% in cross-section respectively at the first and second interruption (Fig. 3.12). Necking appears visibly only at the third interruption (Fig. 3.11) for which the average longitudinal engineering strain reaches 10% and the reduction in cross-section reaches 16%. The specimen fractured after an engineering strain of 13.3% is reached (last record). The reduction in necking cross-section is 82%. These results imply that for the testing conditions used here, the reduction in cross-section is slow during a large time fraction of the tertiary stage. And it accelerates

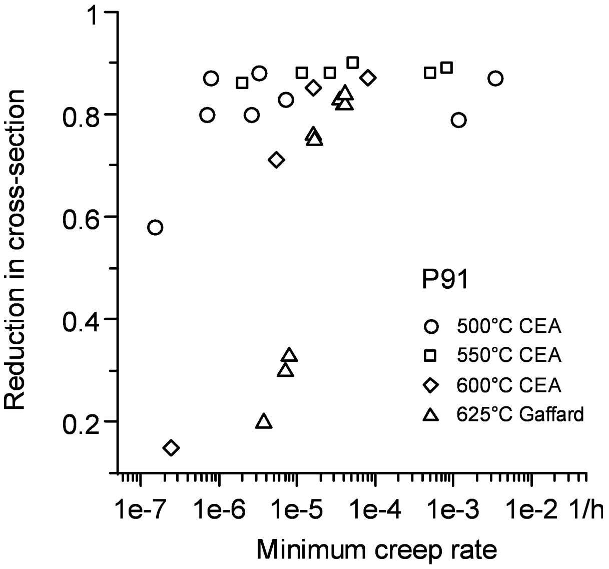

Figure 3.8: Reduction of area measured after fracture as a function of minimum creep rate [7, 72].

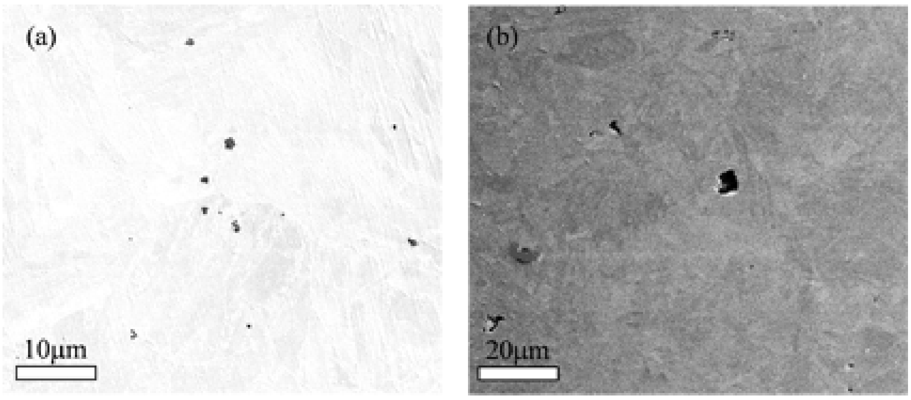

Figure 3.9: FEG-SEM observations of long-term creep damage on longitudinal cross-sections far from the necking area for creep tests on Grade 91 steel at (a) 500°C for 160×10^3 h and (b) 600°C for 94×10^3 h.

very quickly during the last 10% of the lifetime.

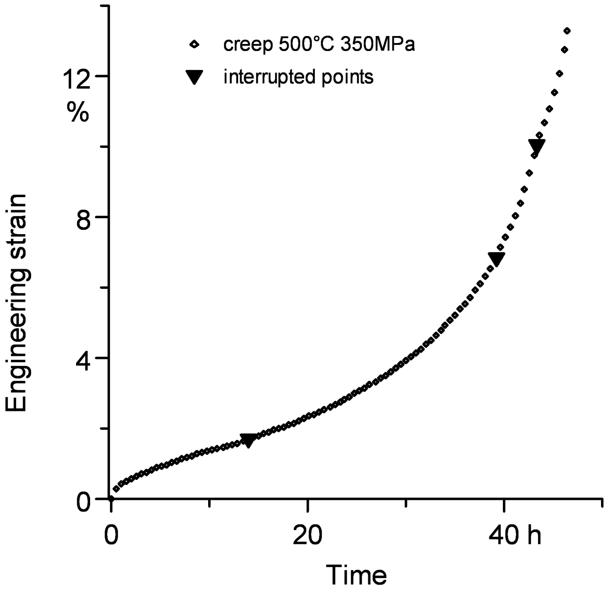

Figure 3.10: Multiple loading-unloading creep test at 350 MPa and 500°C on Grade 91 steel. Unloading and further loading parts of the curve are not indicated.

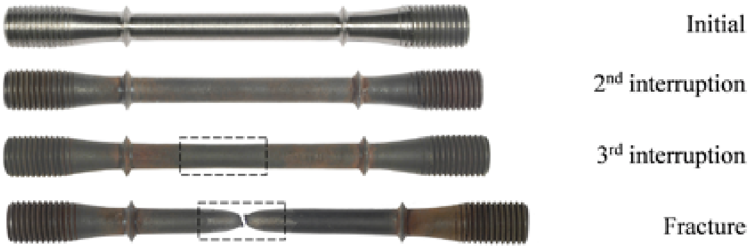

Figure 3.11: Evolution of necking during creep at 350 MPa and 500°C.

3.3 Modelling of the tertiary creep stage

3.3.1 Viscoplastic flow law

a. Norton power-law expressed with the true strain rate and the true stress

The mechanical behaviour during the secondary stage is usually modelled using the Norton power-law given by Eq. (3.1). For a given creep test, we use this law in order to simulate creep deformation starting from its minimum creep rate. At the minimum creep rate and assuming homogeneous deformation (see Fig. 3.12), the axial true stress σ is expressed as a function of the engineering stress σ^{eng}. A material law in true stress should be used provided the axial strain is higher than a few % which is the case in the acceleration stage, after the minimum creep strain rate is reached.

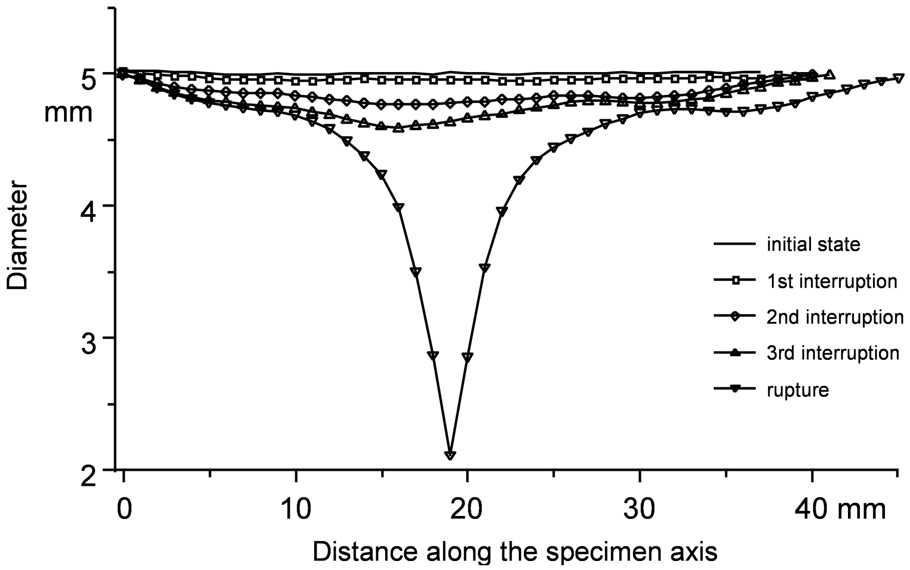

Figure 3.12: Diameter profile of the P91 creep specimen during creep test at 350 MPa and 500°C.

This stress modification leads to a modification of the constant C of Eq. (3.1). The Norton law in true stress starting at the true strain ε_{min} can thus be expressed using a modified constant: $C^m = C\exp(-n\varepsilon_{min})$.

b. Viscoplastic flow law including the creep-softening of the material

This phenomenological viscoplastic flow law consists in combining the acceleration of the creep strain rate during the tertiary stage with the Norton power-law:

$$\dot{\varepsilon}_{min} = C(\sigma^{eng})^n \exp\left[k(\varepsilon - \varepsilon_{min})\right] \tag{3.3}$$

The exponential term represents the creep softening behaviour in the tertiary stage starting at the true strain ε_{min} at which the minimum true strain rate is reached. Then, Eq. (3.3) leads to the law written in terms of true stress:

$$\dot{\varepsilon}_{min} = C\sigma^n \exp(h\varepsilon - k\varepsilon_{min}) \tag{3.4}$$

with $h = k - N$.

For the sake of simplicity, a unique set of parameters (k,ε_{min}) was adjusted for each temperature, which gives fair agreement between simulated and experimental curves of all creep tests at a given temperature. The set of (k,ε_{min})was found to be (0.02, 35) at 500°C and 550°C, and (0.018, 35) at 600°C.

3.3.2 First approach: homogeneous deformation (no localised necking)

As a first approach, we assume that the specimen cross-section reduces homogeneously along the tensile axis during the whole creep test. This approach is similar to the Hoff analysis [65] which allows the prediction of the specimen deformation from the secondary stage until fracture. The analysis is based on the volume conservation which allows the computation of the cross-section and true stress evolution with respect to the strain.

a. Model including the Norton law for true strain and stress

The Norton power-law in true stress leads to the following differential equation:

$$\exp(-n\varepsilon)\dot{\varepsilon} = C^m \left(\sigma^{eng}\right)^n \tag{3.5}$$

For a given engineering stress, this equation can be solved by integration between the time t_{min} and a given time t, corresponding to the strain ε_{min} and a given strain ε. From this, the true strain can be derived:

$$\varepsilon(t) = \varepsilon_{min} - \frac{1}{n} \ln\left[1 + n\dot{\varepsilon}_{min}^{Norton}(t_{min} - t)\right] \tag{3.6}$$

Then, the engineering strain can be deduced as well as the cross-section evolution with time:

$$S(t) = S_{min}\left[1 + n\dot{\varepsilon}_{min}^{Norton}(t_{min} - t)\right]^{1/n} \tag{3.7}$$

with S_{min} the cross-section at the time t_{min}.

This model requires the knowledge of the Norton parameters, (n, C), and time and strain for which the the minimum creep rate is reached, t_{min} and ε_{min}.

b. Model including the creep softening of the material

The integration of Eq. (3.5) between t_{min} and t (corresponding strains: ε_{min} and ε) leads to an expression of the true strain at a given time:

$$\varepsilon(t) = \varepsilon_{min} - \frac{1}{k} \ln\left[1 + k\dot{\varepsilon}_{min}^{Norton}(t_{min} - t)\right] \tag{3.8}$$

Then, the engineering strain and the cross-section are obtained from this equation respectively as:

$$\varepsilon^{eng}(t) = (1 + \varepsilon_{min}^{eng})\left[1 + k\dot{\varepsilon}_{min}^{Norton}(t_{min} - t)\right]^{-1/k} - 1 \tag{3.9}$$

$$S(t) = S_{min}\left[1 + k\dot{\varepsilon}_{min}^{Norton}(t_{min} - t)\right]^{1/k} \tag{3.10}$$

This approach requires the knowledge of the Norton parameters (N and C), the time and strain (t_{min} and ε_{min}), and the softening slope (k). The parameter t_{min} is an experimental value measured from the experimental creep curves when the true strain reaches ε_{min}.

c. Comparison between model predictions and experimental creep curves

The creep curves predicted by the homogeneous deformation model using either the Norton law without softening or taking into account additional softening are shown in Figs 3.13, 3.14 and 3.15. For the first model, the value of parameter C was fitted from the minimum stain rate vs. stress data. At 500°C, the use of the Norton law expressed with the true stress allows fair calculations of the creep curves up to 80% of the lifetime for lifetimes shorter than 60×10^{3}h but up to only 60% for the longest creep test (160×10^{3}h).

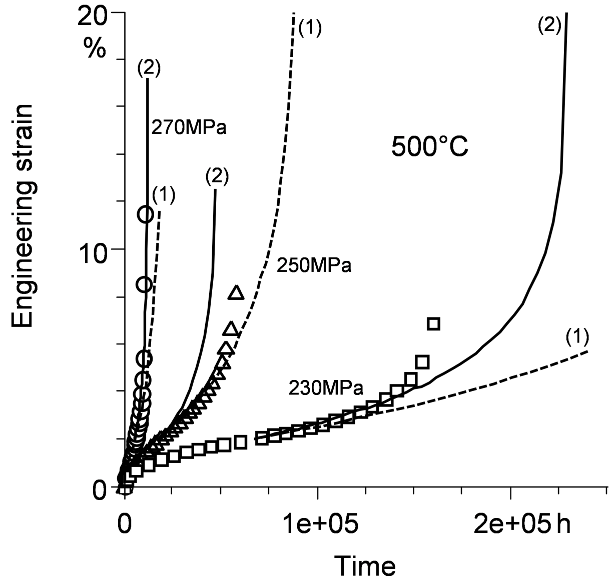

Figure 3.13: Experimental and predicted engineering strain evolution with the homogeneous deformation approach and either (1) the Norton power-law or (2) the modified power-law including the material softening effect, for creep tests at 500˚C.

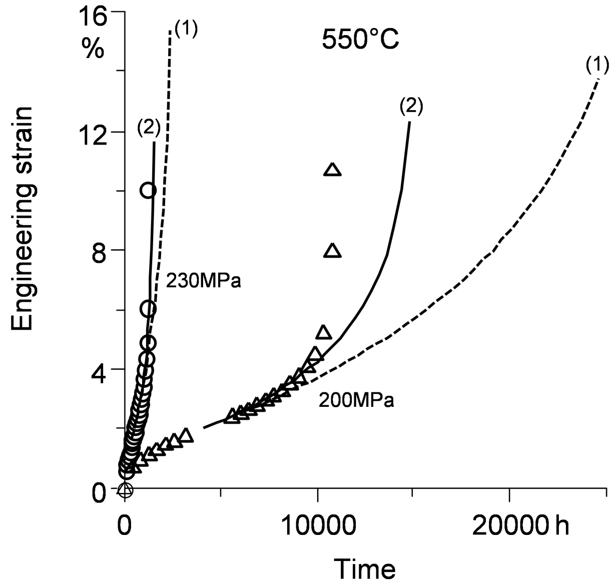

Figure 3.14: Experimental and predicted engineering strain evolution with the homogeneous deformation approach and either (1) the Norton power-law or (2) the modified power-law including the material softening effect, for creep tests at 550˚C.

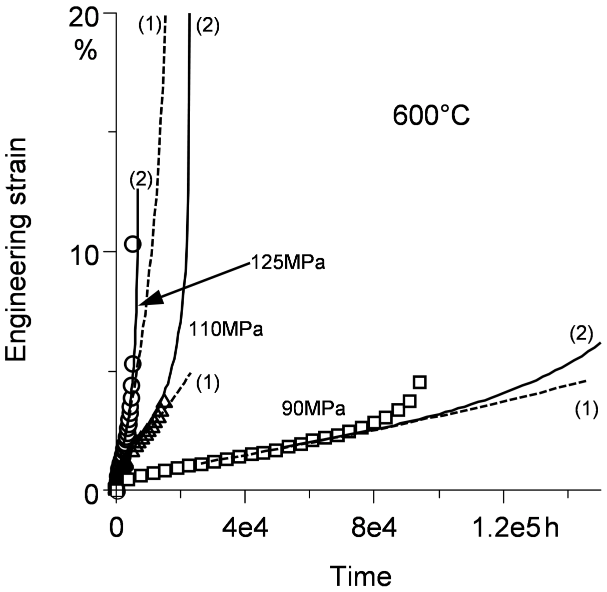

Figure 3.15: Experimental and predicted engineering strain evolution with the homogeneous deformation approach and either (1) the Norton power-law or (2) the modified power-law including the material softening effect, for creep tests at 600°C.

The model allows fair computations of the creep curves until 60% of the lifetime for all creep tests at 550°C and 600°C. Therefore, the model underestimates the creep strain during the end of the tertiary stage.

As expected, the homogeneous deformation model using the viscoplastic flow law including the material softening effect leads to improved calculations of the creep curves. The difference between the creep rates at the starting points is due to the use of the minimum creep rates predicted by the Norton law $\dot{\varepsilon}_{min}^{Norton}$ which are different from the actual experimental minimum creep rates, partly because of experimental scatter. For the longest tests, this model allows correct evaluations up to 80% of the lifetimes at 500°C and up to 90% at 550°C. This suggests that necking controls deformation only during the very final part of the creep tests. For the longest test at 600°C, the calculated curve is correct up to only 60% of lifetime. This is due to the fact that the softening slope used (35) is about twice smaller than its experimental value for this test (64). For all the other creep tests at 600°C, calculations from the model including the softening effect are still better than the first ones neglecting softening. However, the second model still leads to an underestimation of the strain just before failure. That is why necking is now considered.

3.3.3 Instability and necking evolution

a. Prediction of the onset of necking

At any given time, a small portion of the gauge length is assumed to have a cross-section differing by a small amount, δS, from the rest of the gauge part, which is supposed to have a homogeneous cross-section, S. According to the definition of Hart [67], deformation is unstable if this difference in cross-section increases with time. This criterion is defined

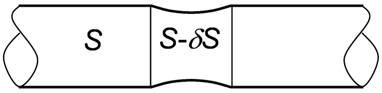

Figure 3.16: Specimen at onset of necking.

as:

$$\delta\dot{S}/\delta S > 0 \tag{3.11}$$

The difference δS is assumed to be produced during a small amount of time δt and could be replaced by $\dot{S}\delta t$. Then, Eq. (3.12) is deduced from Eq.(3.11).

$$\ddot{S} < 0 \tag{3.12}$$

Using the volume conservation assumption and Eq. (3.12) leads to the instability criterion expressed as:

$$\frac{\ddot{\varepsilon}^{eng}}{\dot{\varepsilon}^{eng}} - 2\frac{\dot{\varepsilon}^{eng}}{1+\varepsilon^{eng}} > 0 \tag{3.13}$$

The creep curve is concave before and convex after the minimum creep rate. The Hart criterion predicts thus that the instability can takes place only in the convex part of creep curves, corresponding to the creep rate acceleration domain.

In order to use the Hart instability criterion, Eq. (3.13), calculations of the first and second derivatives with respect to time are required. The experimental scatter of engineering strains causes derivative discontinuities. This was solved by using a polynomial regression. The engineering strain vs. time curves were fitted using a 6th order polynomial function of time. The number of required digits of the polynomial coefficients is a parameter of the regression. When this number is higher than three, there is no significant effect on the prediction of the necking onset. There is a relative difference less than 5% between the minimum creep rate estimated with the 6th order polynomial and the one determined with the straight line method (Section 3.2.5). Using a 4th and 5th order polynomial function leads to a relative change of the prediction lower than 10%. In the following, the 6th order polynomial regression is used.

Necking predictions are reported in Table 3.6 for the all the creep tests. The predictions using the Hart criterion show that strain instability is reached at a time very close to tmin. This criterion predicts early strain instability while from experiments, extensive necking significantly develops only just before fracture (Figs. 3.10, 3.11 and 3.12).

b. Cross-section evolution after the onset of necking

After the onset of necking, the necking part of the specimen shows a curved shape indicated by the dotted line in Fig. 3.17. Following the laser scan micrometer measurements, the radius of curvature of the necking part after fracture is only 1.2-3.4 times larger than the diameter of the necking cross-section radius. Preliminary calculations assuming perfect plasticity behaviour and using the wellknown Bridgman model [81] show that axial stress varies across the necking section by less than 10%. That is why we assume in the following that the axial stress is uniform in the necking section.

The specimen is divided into three homogeneous parts. The first and third ones have the same uniform section: S (homogeneous parts). The second one is the necking part

Table 3.6: Predictions of the onset of necking.

T(°C)	t_f (h)	End stage I		End stage II		Min. creep rate		Predic. necking	
		t (h)	ε (%)	t (h)	ε (%)	t (h)	ε (%)	t (h)	ε (%)
500	15	1.3	0.93	5	2.2	3	1.51	3.1	1.54
500	38	6	1.12	14	2.03	9	1.45	10	1.56
500	10400	385	0.42	3500	1.24	1219	0.625	1267	0.64
500	59350	1500	1.73	32500	2.96	19334	2.04	19418	2.04
500	160000	35000	1.86	88000	0.83	66961	2.02	66961	2.02
550	64	7	0.67	28	1.76	20	1.37	20	1.37
550	1230	170	1.06	650	2.35	372	1.61	402	1.69
550	10800	2800	1.7	6200	2.6	5615	2.43	5615	2.43
600	543	100	1.79	260	3.11	175	2.41	180	2.44
600	2103	400	1.53	1100	2.69	672	1.98	694	2.02
600	5022	700	1.4	2350	1.86	1507	1.4	1507	1.4
600	14950	6000	1.9	8500	2.28	7194	2.07	7226	2.07
600	93750	11000	0.77	47500	1.68	26126	1.14	26319	1.14

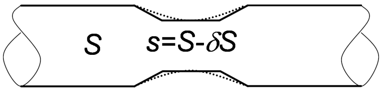

Figure 3.17: Longitudinal section of the specimen after the onset of necking.

and is located between the first and third ones. Its cross-section is assumed to be uniform as well: $s = S - \delta S < S$. The three parts are loaded in series, neglecting the effect of stress triaxiality and stress heterogeneity in the necking part induced by the notch effect.

The two creep strain rate equations mentioned above are used here to predict the cross-section evolution. The first one is the usual Norton power-law. The expression of the homogeneous section S following time, t, starting at the necking onset time, $t_{necking}$, can be written as:

$$S(t) = S_{necking}\left[1 + n\dot{\varepsilon}_{min}^{Norton}(t_{min} - t)\right]^{1/n} \tag{3.14}$$

with $S_{necking} = S_{init}/(1 + \varepsilon_{necking}^{eng})$

The load P is equal in all cross-sections along the gauge length:

$$P = \sigma^{hom} S = \sigma^{necking} s \tag{3.15}$$

The true stress in each cross-section is expressed as a function of the true strain rate using the Norton power-law. Then, the true strain rate is expressed as a function of both the cross-section rate and the cross-section using a volume conservation assumption. Hence, a differential equation linking the homogeneous and necking cross-sections is obtained:

$$s^{n-1} ds = S^{n-1} dS \tag{3.16}$$

Integration of Eq. (3.16) between the onset of necking and a given time t leads to a relationship between the homogeneous and the necking cross-section:

$$s^n - {s_{necking}}^n = S^n - {S_{necking}}^n \tag{3.17}$$

After time integration, if we consider that deformation develops in a ductile way and slowly, the cross-section difference between the homogeneous parts and necking part is thus small ($\delta S << S$). Using the Taylor first order approximation, we deduce the relationship given by Hart [67]:

$$\delta S = \delta S_{necking} \left(\frac{S_{necking}}{S} \right)^{n-1} \tag{3.18}$$

The second model uses the viscoplastic flow law described by Eq. (3.3). This one takes material softening into account. Predictions based on the Hart instability criterion show that necking starts only slightly later than tmin. Therefore, for the sake of simplicity, necking is supposed to start at time t_{min}. The strain reached when the minimum creep strain rate is measured, ε_{min}, is determined from fitting the softening law (Section 3.3.1.b.) and t_{min} is the experimental time corresponding to strain ε_{min}. The cross-section of the homogeneous parts is given by Eq. (3.10). Using the procedure described previously, a relationship between the homogeneous and the necking cross-sections is derived as follows:

$$s^k - {s_{min}}^k = S^k - {S_{min}}^k \tag{3.19}$$

For both necking models, the difference in cross-section $\delta S_{necking}$ between the homogeneous and necking part at the predicted onset of necking is calculated using:

$$\delta S_{necking} \approx \delta D_{necking} \sqrt{\pi S_{necking}} \tag{3.20}$$

with $S_{necking} = S_{init}/(1 + \varepsilon^{eng}_{necking})$ for the first model, or $S_{init} \exp(-\varepsilon_{min})$ for the second model.

$\delta D_{necking}$ is supposed to be equal to the initial variation in diameter along the specimen ($\approx \delta D$), which ranges between 0 and 20 µm following the laser scan micrometer measurements (Section 3.2). To evaluate the sensitivity of the predictions to δD, parametric calculations were carried out by setting this parameter to 1 µm, 10 µm, 20 µm, 50 µm, and 100 µm.

The criterion for final fracture is based on a critical reduction of minimum cross section. From creep results at temperatures between 500 and 625°C (Section 3.2) its value stands within $20 - 80\%$. Therefore, two extreme values of the reduction of the minimum cross-section were chosen: $f_{cinf} = 20\%$ and $f_{csup} = 80\%$. The influence of the choice of the critical reduction value will be discussed in the following.

3.4 Results and discussion

3.4.1 Lifetime predictions using necking modelling

Fig. 3.18 shows the predicted lifetimes for the various values of the initial variation in diameter using the necking model with either the Norton power-law and the modified flow law taking into account the softening effect. For both models, the lifetime predictions become stable with a relative variation lower than 10% when δD varies between 1 and 20 µm. These values correspond to the machining-induced roughness of the present specimens.

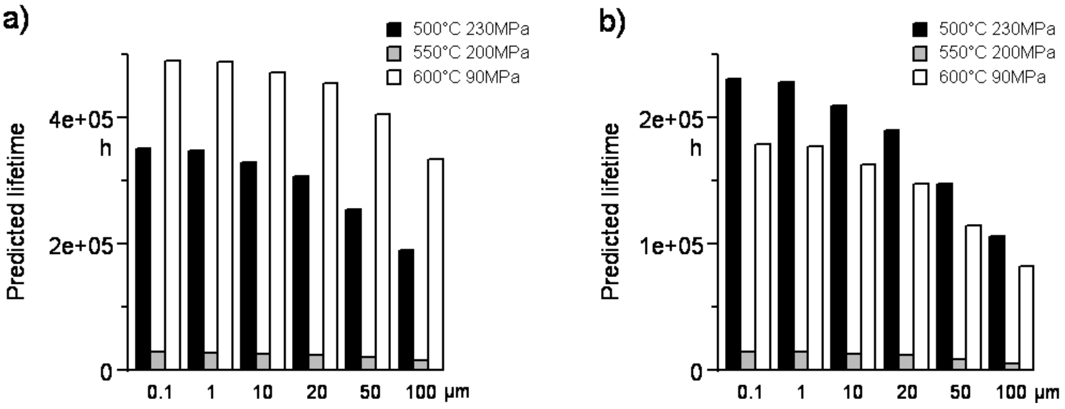

Figure 3.18: Lifetime predicted by the necking model using (a) the Norton power-law and integration formulation and (b) the modified power-law including the softening effect for various values of the initial diameter variation, δD.

The cross-section evolution of long-term creep specimens tested at 500, 550 and 600°C predicted by the necking models including softening or not are plotted in Fig. 3.19 for $\delta D = 20$ µm. The durations predicted for a reduction of 20% and 80% in cross-section differ relatively by less than 10%. Using the Hart formulation, Eq. (3.18), yields to an overestimation of 10% compared to the time integration formulation given by Eq. (3.17). Since the Taylor first order approximation can only be applied for small values of the cross section variation (δS), we suggest the use of the time integration formulation, which is valid for a larger strain range.

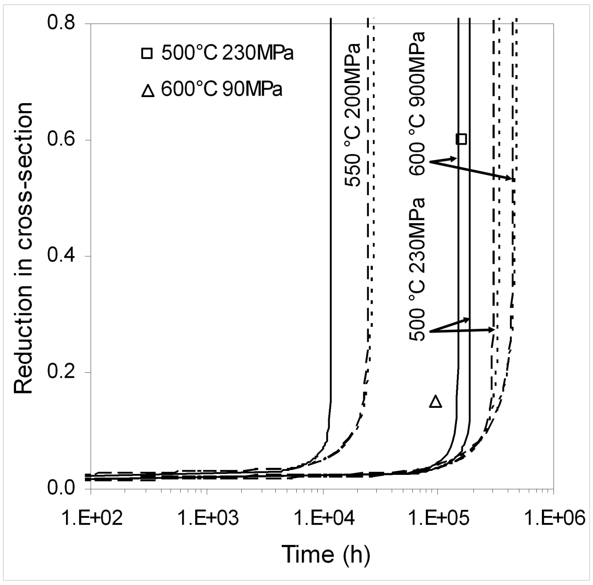

Figure 3.19: Predicted evolutions of the necking section with time. Symbols: experimental fracture surfaces, dotted lines: Norton law and Hart Eq. (3.18), dashed lines: Norton power-law and time integration formulation Eq. (3.17), and solid lines: modified power-law including the softening effect. Initial diameter variation $\delta D = 20$ µm.

The necking model including the creep-softening behaviour gives a better lifetime prediction than the model using only the Norton power-law expressed in true stress. The two models predict that the cross-sections of the creep specimens decrease very slowly with time during the main part of the tertiary stage. The reduction in cross-section significantly accelerates only just before fracture. This evolution is in agreement with observations of the creep specimen during the interrupted creep test (Section 2). Under tensile tests (performed at 650°C and strain rate of 2.5 $10^{-4}s^{-1}$ on Grade P92 steel), Giroux et al. [13] observed a similar slow evolution of the necking cross-section, i.e. the reduction in cross-section accelerates strongly only just before fracture. This is due to the values of the Norton exponent (n) and of the softening slope (k).

Experimental and predicted lifetimes for the various creep tests are shown in Fig. 3.20. The necking model using the Norton power-law expressed in true stress overestimates by 50% the lifetimes shorter than 60×10^3h at 500°C. It overestimates by more than 100% the longest lifetime (160×10^3h) at the same temperature. And it overestimates all lifetimes at higher temperatures. This can be explained by the effect of the material creep-softening, which is not considered in this first model. In fact, as mentioned in the Introduction part of this paper, material softening is more significant for the highest creep temperatures and the longest creep times. The necking model taking into account material softening leads to predicted lifetimes that differ by less than 20% from the experimental data whatever the applied load and temperature. At 600°C, this model overestimates the lifetime of the 94×10^3h long test by 50%, which still remains within the experimental scatter commonly encountered in literature [21]. Therefore, we consider that the necking model including the material creep-softening satisfactorily predicts creep lifetimes.

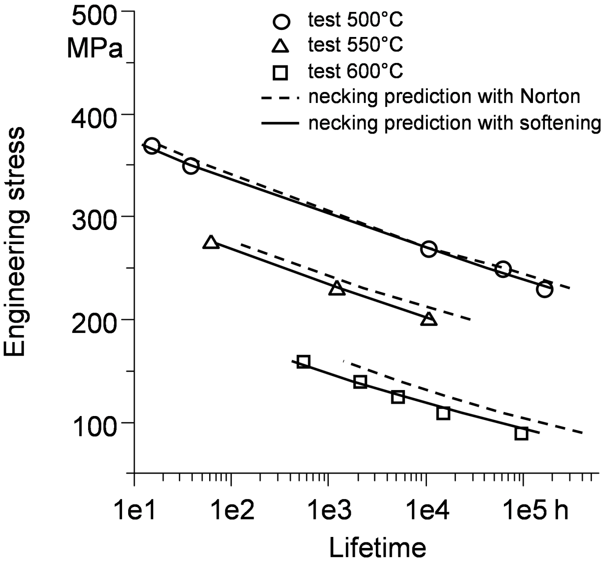

Figure 3.20: Experimental results and lifetimes predicted with the necking model using either the Norton power-law or the modified power-law including the softening effect, for $\delta D = 20$ µm.

The necking model including creep-softening correctly predicts the lifetimes of the creep tests (Fig. 3.21). The necking cross-section predicted by this model first decreases slowly, and then fastly just before fracture, in agreement with the measurements carried out during the interrupted creep test. The model correctly predicts the necking cross-section evolution up to 75% of lifetime. The model underestimates lifetime by 20%. This is consistent with the scatter between the results of tests carried out in similar conditions [21]. When the evolutions with respect to the relative time, t/t_f, are considered, the agreement between the predictions and the measurement values is even better (Fig. 3.21).

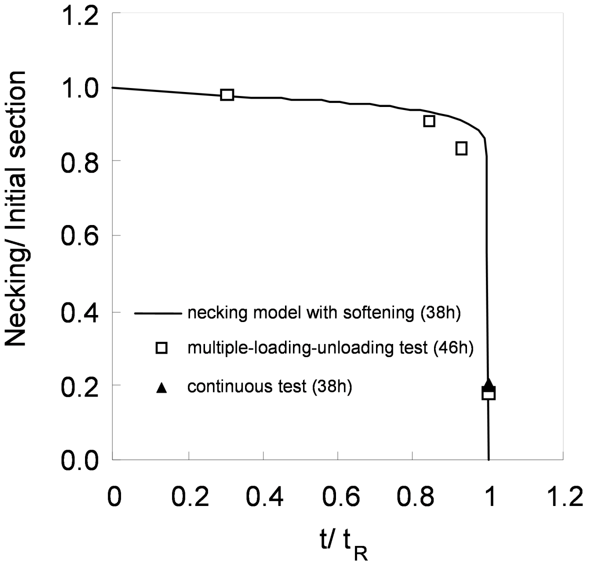

Figure 3.21: Experimental results and evolution of cross-section versus time predicted with the necking model taking into account the creep-induced material softening, for the creep test performed at 500°C and 350 MPa.

3.4.2 Derivation of simple lower and upper bounds

The ratio between the necking section at fracture and the initial cross-section is supposed to be equal to a critical value, f_c:

$$s/S_{init} = f_c \tag{3.21}$$

Then, Eqs. (3.10), (3.19) and (3.21) lead to:

$$t_f - t_{min} = \frac{1}{k\dot{\varepsilon}_{min}} \left\{ (1 - \delta S_{min}/S_{min})^k - \exp\left[k(\varepsilon_{min} + \ln f_c)\right] \right\} \tag{3.22}$$

In Eq. (3.22), the exponential term is small and can be neglected ($< 10^{-2}$ for $k \geq 25$, $f_c \leq 0.8$ and $0.6\% \leq \varepsilon_{min} \leq 3\%$). The time to failure can thus be more simply predicted by Eq. (3.23), where δD_r is the relative variation of the diameter with respect to the initial diameter.

$$t_f - t_{min} = \frac{1}{k\dot{\varepsilon}_{min}} \left[1 - \delta D_r(2 + \varepsilon_{min})\right]^k \tag{3.23}$$

According to creep tests at temperatures between 500 and 625°C, there is a variation range of each of these parameters: $\delta D_r = [10^{-4}, 5.10^3]$, $\varepsilon_{min} = [0.6, 3]\%$ and $t_{min}/t_f = [0.2, 0.5]$. The softening slope, k, is expressed as a function of the minimum true strain rate using

Eq. (3.2). This leads to the expression of the lifetime lower and upper bounds:

$$t_{finf} = \frac{1.25}{A\dot{\varepsilon}_{min}}(0.9899)^{A(\dot{\varepsilon}_{min})^{-\alpha}} \tag{3.24}$$

$$t_{fsup} = \frac{2}{A(\dot{\varepsilon}_{min})^{1-\alpha}} \tag{3.25}$$

For creep tests at temperatures between 500°C and 625°C, the parameters (A,α) are found to be (15.27,0.1098). The upper bound is of the Monkman-Grant type. The lower bound takes the necking effect into account and is not a simple power law.

The lifetimes predicted with Eqs. (3.24) and 3.25 are plotted in Fig. 3.22 for a large number of tempered martensitic steels. The experimental creep data points of the Grade 91 steel are actually bounded by these lower and upper values. The lower bound allows correct predictions for short-term creep but, as expected, leads to an underestimation of lifetimes for long-term creep tests. On the contrary, the upper bound overestimates lifetime for short-term creep, but yields to reasonable predictions for long-term creep.

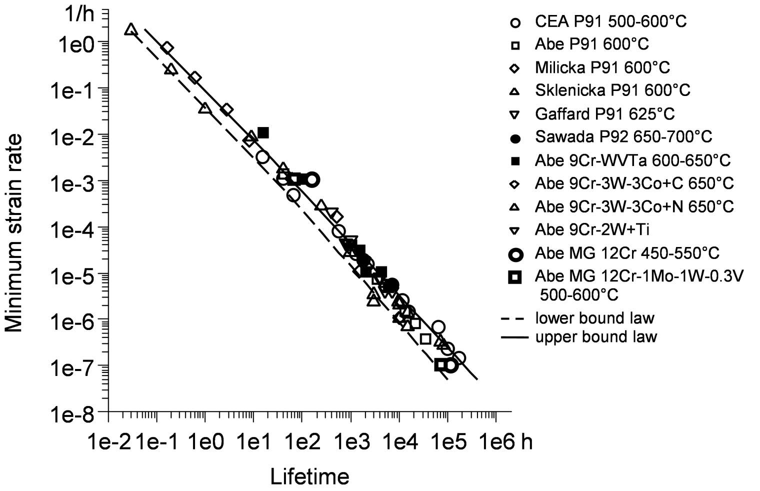

Figure 3.22: Experimental results and lifetimes predicted by the upper and lower bounds for a large number of tempered martensitic materials at temperatures between 500 and 700°C (CEA/SRMA and [4,8,10,59,73,79].

For long-term creep lifetimes ($\approx 2.10^5$h), the predicted lower and upper lifetimes differ by a factor of 4. This is due to the use of the lower and upper limits of δD_r under the exponent k (≈ 90) that leads to a difference by a factor 2.5, and lower and upper bounds of the fraction t_{min}/t_f that causes a difference by a factor 1.6. Therefore, to improve lifetime prediction, the time fraction, t_{min}/t_f, and (if possible) the initial variation of the diameter δD should be more accurately measured.

3.5 Conclusions

The creep deformation and fracture of Grade 91 steel has been studied both experimentally and theoretically, for temperatures ranging from 500°C to 625°C and lifetimes up to 160×10^{3}h. The time fraction spent during the tertiary stage ranges from one to two-thirds and decreases with increasing creep lifetime. Creep-induced microstructure softening leads to an acceleration of strain after the minimum strain rate, whereas necking induces the cross-section to drop quickly only just before fracture (last 10% of the tertiary time stage). The softening slope can be predicted, using a phenomenological law, as an exponential function of the true strain rate.

The Hoff model based on a homogeneous reduction in cross-section including creep-softening of this material still overestimates lifetimes. Taking necking in account, the Hart model using the Norton law expressed in true stress correctly predicts creep lifetimes only up to 60×10^{3}h at 500°C. The necking model including creep softening behaviour (with couples (ε_{min},k)) leads to fair predictions of lifetimes up to 160×10^{3}h at 500°C and 94×10^{3}h at 600°C. The predicted evolution of the necking cross-section is in agreement with measurements carried out during an interrupted creep test. The model is stable with respect to the initial variation in specimen diameter and the failure criterion value.

Lower and upper bound curves describing lifetime vs. minimum creep rate are derived from the model including the matreial softening effect. Experimental lifetimes of a large number of tempered martensitic materials up to 200×10^{3}h at temperatures between 500 and 700°C are bounded by the lower and upper predictions. Above such lifetime duration, the intergranular cavity nucleation and growth might affect the time to fracture.

Acknowledgements

This work is supported by CEA/DEN/DISN/RSTB in collaboration with MINES ParisTech.

Part III

Creep cavitation induced by grain boundary diffusion

Résumé

Des cavités de fluage inter-granulaires sont observées en FEG-SEM après deux essais de fluage long-terme de durées de vie respectivement de 160 kh à 500°C et 94 kh à 600°C. Les porosités mesurées conduisent à une augmentation de la vitesse de déformation prédite par la loi de Norton de 2.5%, utilisant la mécanique de l'endommagement du milieu continu. Le modèle de striction est par conséquence valide jusqu'à ces domaines de durée de vie. Des prédictions valables de l'évolution des cavités permettraient des extrapolations de durées de vie hors du domaine observé expérimentalement.

La croissance et la germination des cavités inter-granulaires sont supposées être associées à la diffusion des lacunes le long des joints de grain et de bloc. La croissance des cavités, supposée soumise à une contrainte normale homogène et égale la contrainte macroscopique, est modélisée en utilisant deux modèles. Le modèle de Raj et Ashby tient compte de la germination instantanée, alors que le modèle de Riedel prend en compte la germination continue simulée par la loi de Dyson. Le premier modèle est plus stable que le deuxième modèle par rapport à ses paramètres, aux coefficients de diffusion, à la vitesse de germination et la fraction d'aire critique des cavités. Les tailles de cavités prédites en fin de fluage sont en accord raisonnable avec les mesures en FEG-SEM. Mais, des valeurs de la vitesse de germination sont utilisées afin d'appliquer ce modèle.

Des cavités sont observées en FEG-SEM majoritairement sur les précipités et les phases de Laves situés le long des joints de grain et de bloc. Ces cavités ont la plus haute probabilité de germination d'après la littérature. La vitesse de germination des cavités de ce type prédite par le modèle de Raj est pratiquement négligeable même en tenant compte de la ségrégation de S et de P aux joints de grain. Des premiers calculs par éléments finis en déformation plane sont menés afin d'estimer le facteur de concentration de contrainte à l'interface entre un précipité élastique isotrope et une matrice simulée par une loi de fluage isotrope. Un facteur de concentration de contrainte de 1.5 estimé ne permet pas de prédire les densités finales de cavités même au même ordre de grandeur que les valeurs mesurées. En effet, le facteur géométrique théorique est de trois ou quatre ordres de grandeur plus grand que la valeur ajustée.

A ce stade, l'influence de l'hétérogénéité géométrique de la microstructure telle que les points triples sur la concentration de contrainte locale n'est pas encore prise en compte.

Mots clés : cavitation intergranulaire, diffusion des lacunes, germination et croissance des cavités, précipités, phase de Laves, germination continue, ségrégation

Introduction

In the last chapter, viscoplastic instability called “necking”was shown to be the main mechanism of failure of Grade 91 steel up to creep lifetimes of 160×10^3 h at 500°C and 94×10^3 h at 600°C. Creep cavities forming along former austenitic grain boundaries (FAGBs) or block boundaries were observed for these creep lifetimes. They probably do not affect the failure mechanism for shorter lifetimes, but they may do for long lifetimes. In order to predict their effect on creep lifetime, we present in this part an experimental and theoretical study of creep cavitation along block/packet boundaries or FAGBs.

The cavitation investigated in this part involves two successive stages that are nucleation and growth of cavities (no coupling with necking). The cavitation mechanisms occurring during these stages can generally be controlled by either vacancy diffusion, or viscoplasticity, or a coupling of both of them. With regards to long-term creep, only diffusion-induced cavitation is studied in this part as justified by computation of the Rice critical length. Diffusion-induced cavitation by mean of experimental observations and modelling will be presented in this part.

Chapter 4 gives a literature review on diffusion cavitation. Section 4.1 focuses on observations of creep cavities in martensitic steels in order to understand the mechanisms of cavitation and to allow us to choose physically-based models. Many models of diffusion cavitation including nucleation and growth will be presented in section 4.2. The choice of the most suitable models will be discussed in section 4.3.

Our works on creep cavitation will be presented in Chapter 5. Section 5.1 presents observations and cavity quantification after failure of four creep tests at 500°C (160 kh and 59 kh) and 600°C (94 kh and 5 kh). Modelling of diffusion cavitation including nucleation and growth will be presented in section 5.2. The predictions are then compared to the previous observations and measured values.

Finally, conclusions will be drawn at the end of this part.

In this part, grain boundaries subjected to damage are supposed to be almost perpendicular to the loading direction and loaded by the macroscopic tensile stress. The effect of microstructure geometry and crystal orientations is neglected at this stage.

Chapter 4

Literature review on creep cavitation induced by grain boundary diffusion

4.1 Observations of creep cavities in martensitic steels

Numerous studies on creep cavitation have been carried out in various metals such as bainitic steel [82], ferritic steels (1Cr-$\frac{1}{2}$Mo, 2$\frac{1}{4}$Cr-1Mo) [83–85], austenitic stainless steels [76,86], copper [87,88], and nimonic alloy [89,90]. The cavitation behaviour depends on grade of metals. The cavitation observations described in this section involve particularly martensitic steels. These include Grade 91 steel and also 12%Cr-Mo-V steel since its microstructure is rather similar to the first one.

Table 4.1: Observations of cavity nucleation after [21,80,82].

Steel alloy	9%Cr steel [80]	12%Cr steel [21]	bainitic steel [82]
- Temperature (°C)	25°C - tensile	650°C - creep	700°C - tensile
- Strain rate (h^{-1})	54	1.1×10^{-5}	3×10^{-4}, 0.3
- Elongation at failure	78%	13%	$\leq$ 5%
- Observation instrument	TEM	SEM	-
- Elongation at the first detection of cavities	28%	<1%	0.05%
- Lowest diameter	20 nm	400 nm	-

Diffusion (or creep) cavities should be distinguished from ductile cavities. The nucleation of cavities in three alloys is reported in Table 4.1. Diffusion creep cavities with nucleation size of 400 nm located along former austenitic grain boundaries (FAGBs) or block boundaries were observed in 12%Cr steel at 650°C after a creep elongation of 1% [21], where the minimum creep strain rate was reached. Their nucleation may be mainly controlled by vacancy diffusion along FAGBs or block boundaries. Indeed, ductile cavities with nucleation size of 20 nm have only been observed at an elongation of 28% in 9%Cr steel at room temperature [80]. Nucleation of ductile cavities occurs when plastic strain is high enough to lead to fracture at carbide-matrix interfaces [80]. Nucleation of cavities along FAGBs has also been observed earlier at an elongation of 0.05% in bainitic steel [82].

The study of Eggeler et al. [21] on creep of 12%-Cr-Mo-V steel shows that cavity nucleation seems to be continuous. The cavity density on polished cross-sections, N_m, was measured and plotted in Fig. 4.1a. The cavity density along block boundary facets, N_a, was then deduced taking the probability of intersecting cavities on block boundary facets into account as in the following equation [91]:

$$N_a = \frac{d_g}{\pi d_H} N_m \tag{4.1}$$

where d_g is the mean linear intersected block size, and d_H the harmonic mean of intersected cavity diameters.

The accumulation of cavity densities N_m and N_a seems to be linear between strain interval of 1 and 12% (Fig. 4.1a). The linear accumulation of N_a has been suggested by Dyson [91] for other metallic materials such as $2\frac{1}{4}$Cr-1Mo steel, 347 steel, Nimonic 80A and Iron base. In exception, the nucleation behaviour is unclear yet before an elongation of 1%. The growth in diameter of the largest (5%) cavities in 12%-Cr-Mo-V steel seems to follow a logarithmic or power function of elongation (Fig. 4.1b). At an elongation of 1%, their mean equivalent-circular diameter reaches 1.5 µm. It then increases by two times larger after an elongation of 5 to 12%.

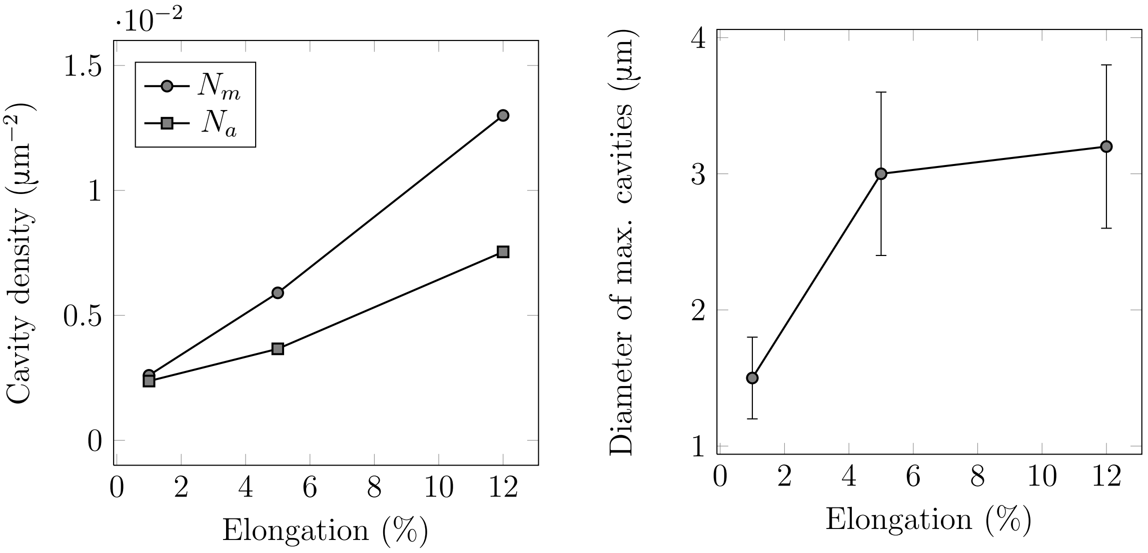

(a) The cavity density in grain boundary facets, N_a, is computed from N_m taking into account a block size of 2 µm (d_g), average block size in Grade 91 steel measured in [24].

(b) Average diameter of the largest 5% cavities.

Figure 4.1: Nucleation and growth of cavities in 12%Cr steel during a creep test carried out at 650°C and 80 MPa from [21].

Creep cavities were observed by Eggeler et al. [21] at block boundaries, FAGBs and at triple junctions between FAGBs (Fig. 4.2). These observations revealed that the creep cavities located at triple junctions of FAGBs and along FAGBs were the largest ones. After an creep elongation of 5%, the average diameter of cavities reach 1.6 μm for the ones located at triple junctions of FAGBs, 1.3 μm for the ones along FAGBs and 1.2 μm for the ones at block boundaries. A high resolution observation allowed the authors to detect a cavity located at a carbide-matrix interface, having a size of 0.5 μm. No mass spectrometry analysis on this carbide was made by the authors, but its characteristics in size and shape match the $M_{23}C_6$ carbide ones [21](Fig. 4.3). No further statistics on this type of cavity nucleation site were studied by the authors.

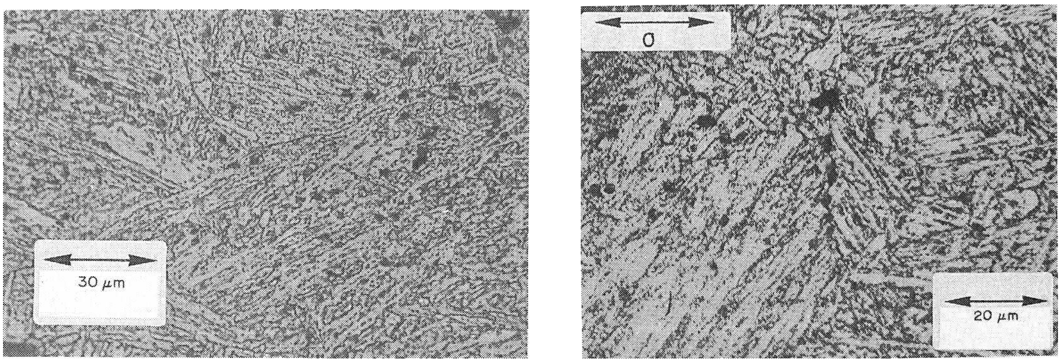

(a) Cavities located along and within FAGBs.

(b) Cavities lining up along FAGB segments perpendicular to the loading axis.

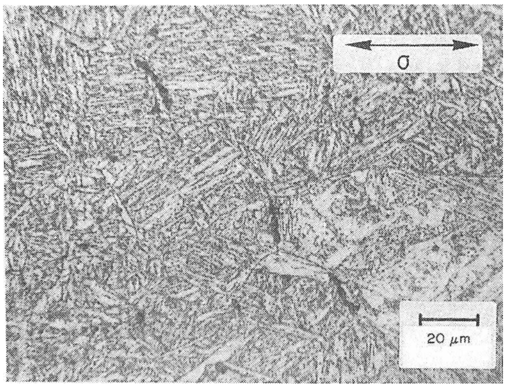

(c) Microcracks forming on FAGB segments mostly perpendicular to the loading axis.

Figure 4.2: Optical micrographs of cavitated 12%Cr-Mo-V steel after a 5% creep elongation at 650°C under 80 MPa after [21].

The cavities located at FAGBs grow fastest and have more important role in failure process if the corresponding FAGB segment are nearly perpendicular to the loading axis [21]. Figure 4.2b shows that cavities line up along FAGBs perpendicular to the loading axis. The average size of cavities located along FAGBs forming with the loading axis angles close to 90° is 1.4 times larger than the ones located along FAGBs for which angles are lower than 30° [21]. Besides, cavity spacing along FAGBs forming with the loading axis angles between 60 and 90° is 3 times lower than FAGBs for which angles are lower than 20° [21]. After a creep elongation of 5%, microcracks formed along FAGB segments closely perpendicular to the loading axis were observed (Fig. 4.2c). Eggeler et al. [21] suggested that these microcracks could result from a coalescence of cavities lining up

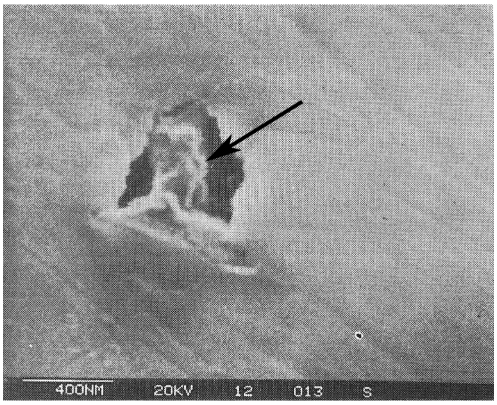

Figure 4.3: SEM micrograph of a typical cavity after a creep elongation of 5% at 650°C under an applied stress of 80 MPa [21].

along FAGBs as observed in Fig. 4.2b.

The observations by Eggeler et al. [21] on the microstructure of 12%Cr steel also revealed that the spacial distribution of cavities were heterogeneous. Figure 4.2a and 4.2b show that there exist different fields where the cavity density is low and high. Figure 4.2c also shows that microcracked FAGB facets are isolated one from another.

Investigations of creep cavities in Grade 91 steel subjected to creep at 625°C have been performed by Gaffard [4] and reported for three creep tests. These creep tests have respectively lifetimes of 3800 h (100 MPa), 1750 h (110 MPa) and 870 h (125 MPa). FEG-SEM observations of cavities were carried out in fields of the creep specimens located far away from the fracture regions. Cavities with a spacial distribution almost uniform were observed [4]. The average size of cavities seems to be weakly stress-dependent since it varies between 2 and 2.5 µm within the stress range studied by the author. More creep tests using a wider stress range could be necessary to obtain significant conclusions.

The observations of Gaffard [4] seem to show a dependence of creep damage with respect to creep stress, but the results are statically not representative enough to conclude. For creep stress varying from 100 to 120 MPa, the final cavity density decreases by 2 times and respectively the area fraction of cavities decreases by 3 times (from 0.3% to 0.1%) [4], see Fig. 4.4.

The observations by Gaffard [4] of cavitation in cross-sections located near the fracture surface allow understanding failure mechanisms in this zone subjected to large viscoplastic strain. First of all, fracture occurs along FAGB or block boundary segments perpendicular to the loading axis (Fig. 4.5), after a lifetime of 7000 h at 625°C. This is in agreement with the observations related in [21] (Figs. 4.2b and 4.2c). In the fracture zone, cavities could be of ductile type [80]. Indeed, the local elongation in the fracture zone is high and equal to 25%, whereas the elongation is not higher than 5% in the homogeneous part. Cavities are located close to Laves phases and $M_{23}C_6$ carbides (Fig. 4.6a and 4.6b), which is in agreement with the observations of Senior et al. [80] who have suggested that ductile cavities were formed by decohesion of the particle-matrix interface. A ductile cavity could also form by ductile fracture at a triple junction as shown in Fig. 4.6c.

The critical area fraction to final failure is not higher than 10% [4, 92]. Area fraction of cavities in regions near the fracture surfaces of specimens has been measured in [4] and shown in Fig. 4.4b. The measured area fraction of cavities ranges between 2 and

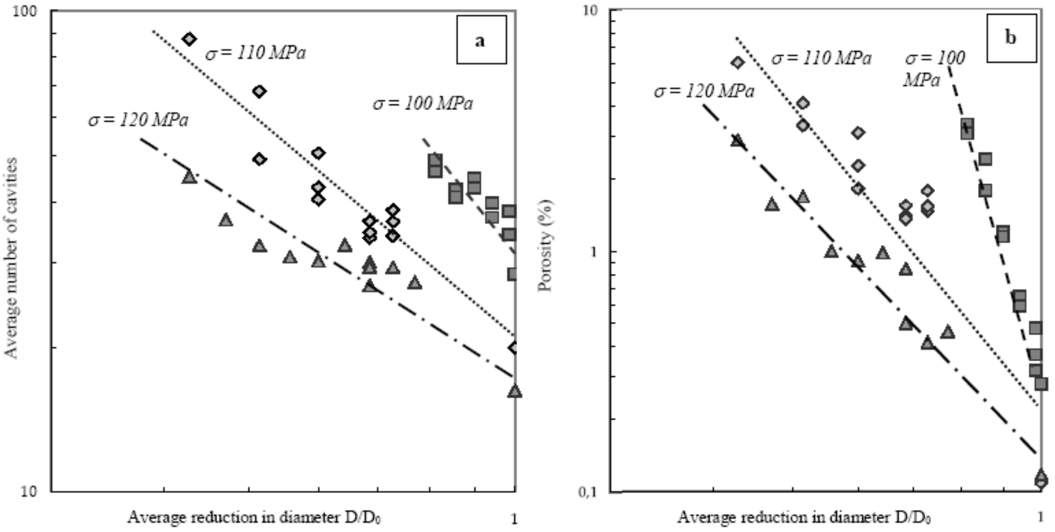

Figure 4.4: (a) Cavity number over cross-section fields of 214×286 µm^2 and (b) area fraction of cavities measured in [4]. $D/D_0 = 1$ for cross-sections located in the homogeneous parts of creep specimens and $D/D_0 < 1$ for cross-sections located in the necking region.

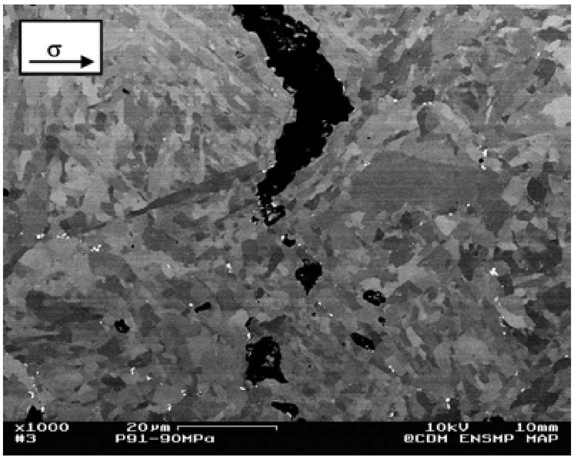

Figure 4.5: Microcracks following FAGB or block boundary segments perpendicular to the loading axis, observed in a cross-section near the fracture surface, after a creep lifetime of 7000 h at 625°C [4].

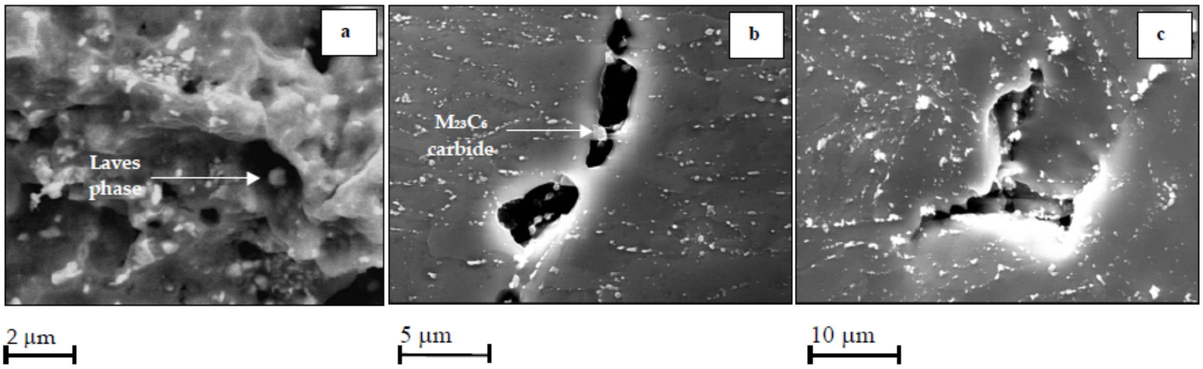

Figure 4.6: Ductile cavities lying on (a) a Lave phase, (b) on M_23C_6 carbides, and forming at a triple point, observed in a cross-section near the fracture surface after a creep lifetime of 7000 h at 625°C [4].

6%. These ratios are much lower than the critical porosity assumed when using classical models [93] (50%). Therefore, overestimations of lifetimes may be expected from these predictions.

The aim of the present study is to build a model to predict cavity development before the onset of localised necking. To this aim, only long-term creep specimens (i.e. in which creep cavities are present outside the necking region) will be considered and the applied loading will be assumed to be uniaxial unless otherwise stated.

4.2 Modelling of creep cavitation induced by grain boundary diffusion

4.2.1 Creep cavity nucleation

The study of nucleation has been influenced for almost 80 years by the famous theories developed by Volmer and Weber [94], Becker and Döring [95], Frenkel [96], and Zeldovich [97]. These theories essentially addressed nucleation of liquid droplets in supersaturated vapour. Additional development was later made in order to apply them to heterogeneous nucleation of precipitates in solids [98].

Only in the 70s, these theories were used to study the cavity nucleation in metallic solids subjected to creep at high temperature. Ones among the first authors were Raj and Ashby [93, 99]. These authors studied nucleation of cavities along grain boundary facets perpendicular to the loading axis. Indeed, they assumed that all perpendicular grain boundary facets contained cavities and that cavitation was controlled by diffusion processes.

a. Void geometry

Voids formed along grain boundaries can display different shapes depending on whether they nucleate at two-grain junctions, three-grain junctions, four-grain junctions (Fig. 4.7a), or at the interface with inclusions present at grain boundaries [93], see Fig. 4.7b. All voids were however assumed in [93] to be spherical segments. Indeed, surface diffusion was supposed to be fast and isotropic so that the curvature was assumed to be maintained uniform as the void grows [93]. The angles formed between the void and the interfaces which contain it must be such as to satisfy equilibrium between surface tension forces [93].

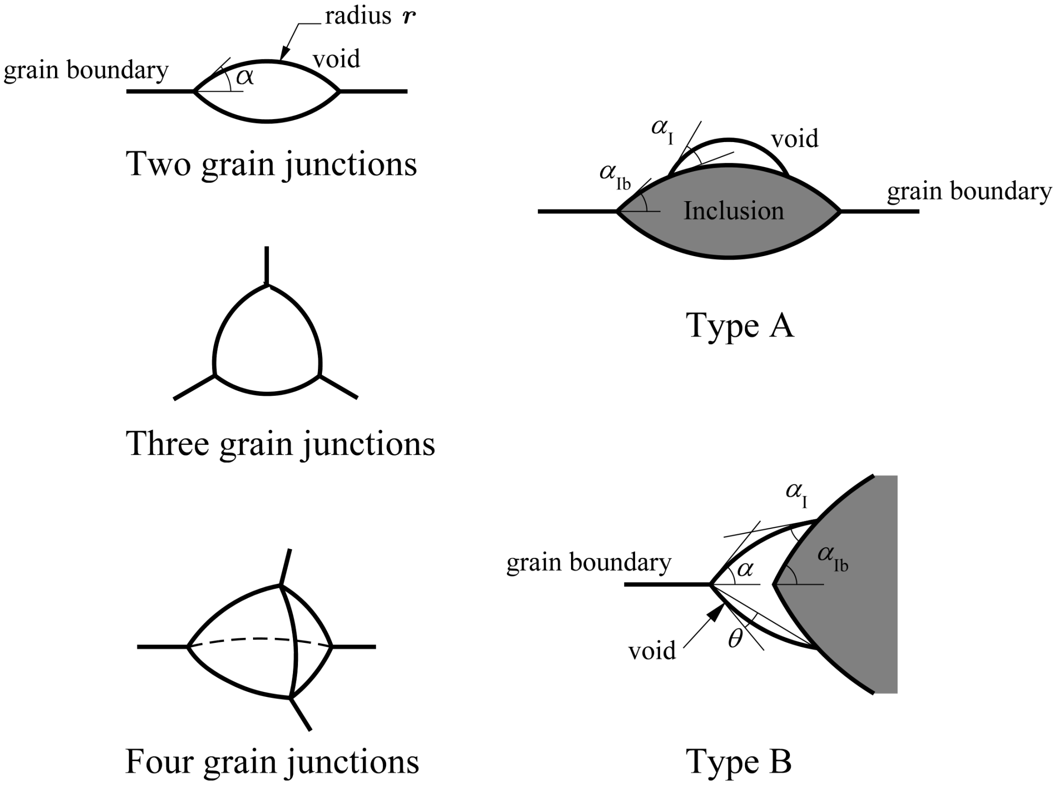
radius *r*
grain boundary
void
α
Two grain junctions
α_{I}
void
α_{Ib}
Inclusion
grain boundary
Type A
Three grain junctions
α_{I}
grain boundary
α
α_{Ib}
void
θ
Four grain junctions
Type B

(a) (b)

Figure 4.7: Voids formed either (a) at grain boundary junctions or (b) at inclusions located at grain boundaries. Replotted after [93].

Figure 4.7a shows the void shapes at two-grain junctions, three-grain junctions and four-grain junctions. The geometry of these voids is described by their curvature radius, r, and the angle, α, formed at the junction of the void and the grain boundary. This angle is dictated by equilibrium between the grain boundary surface energy, γ_b, and the matrix free surface energy at the cavity tip, γ_s, both being assumed to be isotropic [93]:

$$\cos\alpha = \frac{\gamma_b}{2\gamma_s} \tag{4.2}$$

Three geometric properties of the void including its volume, V, its free surface area, S, and the grain boundary area that it replaces, S_b, are expressed as functions of r and α [93]:

$$V = r^3 F_v(\alpha) \tag{4.3a}$$
$$S = r^2 F_s(\alpha) \tag{4.3b}$$
$$S_b = r^2 F_b(\alpha) \tag{4.3c}$$

Geometric functions F_v, F_s and F_b depend on the void type and are taken from [100]. For a cavity at grain boundary facets (top of Fig. 4.7a), these functions are given by:

$$F_v(\alpha) = \frac{2\pi}{3}(2 - 3\cos\alpha + \cos^3\alpha) \tag{4.4a}$$

$$F_s(\alpha) = 4\pi(1 - \cos\alpha) \tag{4.4b}$$

$$F_b(\alpha) = \pi \sin^2\alpha \tag{4.4c}$$

whereas, the geometric functions for three-grain and four-grain junctions are more complicated and given in [93].

Figure 4.7b shows two types of void which can be formed at inclusions. One lies completely at the inclusion-matrix interface (Type A), and the other one extends into the grain boundary (Type B). Two new angles, α_I and α_{Ib}, are needed to describe their geometry (Fig. 4.7b). They satisfy the following equilibrium relationships between surface energies [93]:

$$\cos\alpha_I = \frac{\gamma_{Ib} - \gamma_I}{\gamma_s} \tag{4.5}$$

$$\cos\alpha_{Ib} = \frac{\gamma_b}{2\gamma_{Ib}} \tag{4.6}$$

where γ_I is the inclusion free surface energy and γ_{Ib} is the inclusion-matrix interface energy.

For the sake of simplicity, the void is assumed to be small compared to the inclusion. The geometric functions of type A void are given as a good approximation by Eqs. (4.3) and the following angle functions [93]:

$$F_v = \frac{\pi}{3}(2 - 3\cos\alpha_I + \cos^3\alpha_I) \tag{4.7a}$$

$$F_s = 2\pi(1 - \cos\alpha_I) \tag{4.7b}$$

$$F_b = \pi \sin^2\alpha_I \tag{4.7c}$$

One should notice that the void grows with increasing time. At any given time, its size becomes high enough with respect to the inclusion size so that the approximation above becomes inexact. Then, the angle functions should be recomputed.

Estimation of the geometric properties of type-B void is more complicated. An accurate estimation of these functions is given in [93], whereas an approximation of its volume (to within a factor of two) is made as the following [93]:

$$V = r^3\frac{4\pi}{3}\left(2 - 3\cos\theta + \cos^3\theta\right) \tag{4.8}$$

where $\theta = \frac{1}{2}(\alpha + \alpha_I - \alpha_{Ib})$ as shown in Fig. 4.7b.

b. Thermodynamic barrier and critical nucleus size

A given grain boundary located within a matrix is assumed to be subjected to an uniaxial normal stress, σ_n, (at fixed temperature) as shown in Fig. 4.8. The system constituted of the grain boundary and the matrix changes from a reference state (1) to another state (2). In state (2), an embryo is supposed to have formed and the whole system is assumed to have grown by an amount equal to the embryo volume. The normal stress is supposed to be the same for both states. This change in the considered system leads to a change in Gibbs free energy, ΔG, contributed by (1) the work done by the system on its surrounding, (2) change in the interface area, and (3) change in the stored elastic energy in the system [93, 99]. Term (3) is of order $\sigma_n^2/2E$ ($E \gg \sigma_n$) which is negligible in comparison with term (1) (of same order as σ_n) [93]. Therefore, ΔG is given by the following [93, 99]:

$$\Delta G = -\sigma_n V + \gamma^{free} S^{free} - \gamma^{interface} S^{interface} \tag{4.9}$$

Term $\gamma^{free} S^{free}$ represents the free energy due to the creation of the cavity free surface by considering that a void forms at grain boundary junctions (Fig. 4.7a), but it may also represents the one due to the creation of the inclusion free surface for a type-A or type-B void (Fig 4.7b. Term $-\gamma^{interface} S^{interface}$ represents either the energy loss by opening of the grain boundary surface for a void formed at grain boundary junctions (Fig. 4.7a), or by opening of the matrix-inclusion interface for a type-A void, or by both of them for a type-B void. The normal stress acting on the surrounding matrix, σ_n, is assumed to be uniform for the representative volume (Fig. 4.8). It should not be confused with the normal stress acting on grain boundaries. For sake of simplicity, σ_n is approximated to the normal macroscopic stress, Σ_n, which is not always true with regards to stress heterogeneity within the microstructure and particularly in the vicinity of high-angle boundaries.

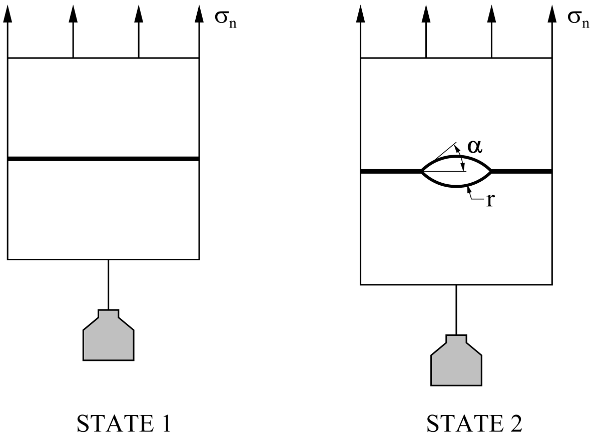

Figure 4.8: Reference (1) and new (2) states of the system as a result of the introduction of a grain boundary cavity [99].

The thermodynamic barrier to the nucleation of cavities can be calculated by considering the maximum value of ΔG [93]. Figure 4.9 shows the evolution of ΔG with increasing nucleus size. The thermodynamic barrier, ΔG_c, is reached when the nucleus size attains the critical size with radius of curvature r_c that can be obtained by setting the derivative of ΔG with respect to r, from Eq. (4.9), to zero. For a particular case where the cavity has an equilibrium and spherical-cap shape and forms at two-grain junctions

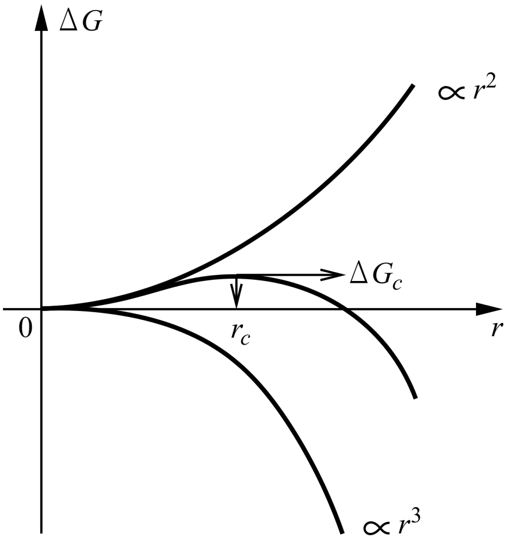

Figure 4.9: Contribution of the volume energy term and surface energy term to the total change in free energy with increasing radius of the cavity [99].

(top of Fig. 4.7a), radius of curvature r_c of the critical cavity and thermodynamic barrier ΔG_c are given by [93]:

$$r_c = \frac{2\gamma_s}{\sigma_n} \tag{4.10}$$

$$\Delta G_c = \frac{\sigma_n}{2} r_c^3 F_v(\alpha) \tag{4.11}$$

where $F_v(\alpha)$ is given in Eq. (4.4).

Note that r_c only depends on σ_n and on free surface energy γ_s (for type-B void, it is an approximation), whereas $F_v(\alpha)$ can yield very different values for different nucleation sites. For example, for the same value of r_c, $F_v(\alpha)$ can vary considerably depending on whether the cavity forms in the matrix, in a single grain boundary, at the interface of a second phase particle with the matrix, or at a triple junction formed by a second phase particle present in the grain boundary as shown in Fig. 4.10 [99]. In the last case, the critical volume is the smallest, therefore, the cavity has the lowest activation barrier and the highest nucleation probability [99].

c. Nucleation rate

In reality, cavities do not nucleate instantaneously but one after another. Continuous nucleation has been suggested by Dyson [91] in various metal alloys ($2\frac{1}{4}$Cr-1Mo steel, 347 austenitic stainless steel and Nimonic), and especially by Eggeler et al. [21] in 12%Cr steel. Continuous nucleation of cavities at grain boundary facets has been modelled by Raj and Ashby [93] using the theories originally developed for nucleation of liquid droplets from supersaturated vapour [94–97]. In the present case, cavities nucleate under an additional loading condition such as creep stress (σ_n) which leads to an increase in nucleation probability.

Since each embryo must overcome the activation barrier, ΔG_c, to become a critical nucleus, the nucleation probability may be given according to the Boltzmann theory

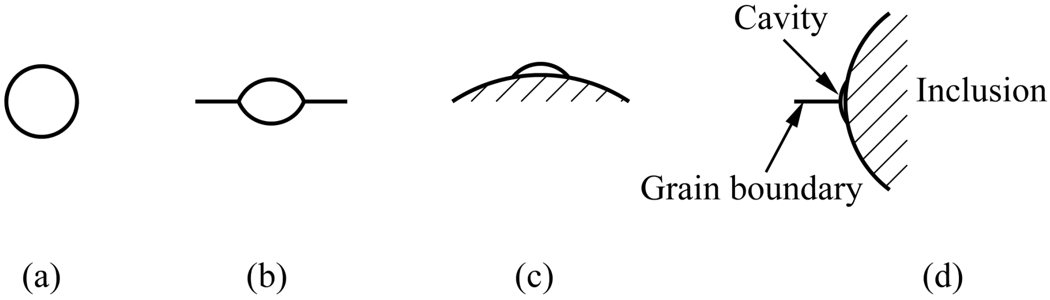

Figure 4.10: The volume of the critical cavity for a fixed value of r_c for (a) homogeneous and (b-d) three types of heterogeneous nucleation. The one with the smallest volume will have the highest nucleation probability. Replotted after [99].

after Becker [95]: $\exp(\Delta G_c/k_bT)$. The density of potential nucleation sites within grain boundaries, N_a, is assumed to be limited with a maximum value of N_a^{max} [93]. Therefore, the number of critical nuclei per unit area of grain boundary is given by [93]:

$$N_a^c = N_a^{max} \exp(\Delta G_c/k_bT) \tag{4.12}$$

where k_b is the Boltzmann constant.

The number of supercritical nuclei formed per unit period of time is N_a^c times the time-dependent probability, p_t, of adding one vacancy to the critical nucleus of size r_c. Probability p_t can be derived from the jumping frequency of a vacancy, which is related to the boundary self diffusion, and from the probability of finding a vacancy at the perimeter of the nucleus of the critical size which depends on the applied stress [93]:

$$p_t = \frac{4\pi\gamma_s D_b\delta}{\Omega^{4/3}\sigma_n} \exp(\sigma_n\Omega/k_bT) \tag{4.13}$$

where $D_b\delta$ is the self-diffusion coefficient in grain boundaries times the grain boundary thickness and Ω the atomic volume.

Combining Eqs. (4.11), (4.12) and (4.13) leads to the nucleation rate of cavities at the steady state (assuming a constant applied stress) given by :

$$\dot{N}_a = \frac{4\pi\gamma_s D_b\delta}{\Omega^{4/3}\sigma_n} N_a^{max} \exp\left(-\frac{4\gamma_s^3 F_v}{\sigma_n^2 k_bT}\right) \exp\left(\frac{\sigma_n\Omega}{k_bT}\right) \tag{4.14}$$

At low stress and high temperature, it is usually assumed that $\sigma_n\Omega/k_bT \ll 1$ [93]. Therefore, the last exponential term will be neglected.

Figure 4.11 shows the nucleation rate of cavities in pure copper as predicted using Eq. (4.14), plotted versus stress normalised by Young's modulus of copper (127 GPa), with $N_a^{max} = 10^{17}\mathrm{m}^{-2}$ [99]. Threshold stress refers to the stress required for the nucleation rate equal to 1 $\mathrm{m}^{-2}\mathrm{s}^{-1}$, assumed by Raj to be the minimum observable. At 650˚C (i.e, 923 K), for $F_v = 10^{-2}$ the threshold stress is 20 times higher than the one for $F_v = 10^{-5}$ [99]. For given values of F_v and temperature, the nucleation rate varies significantly with stress. For example, at 650˚C and $F_v = 10^{-5}$, a change in stress lower than 10% leads to a huge change (10^{10} times) in nucleation rate [99].

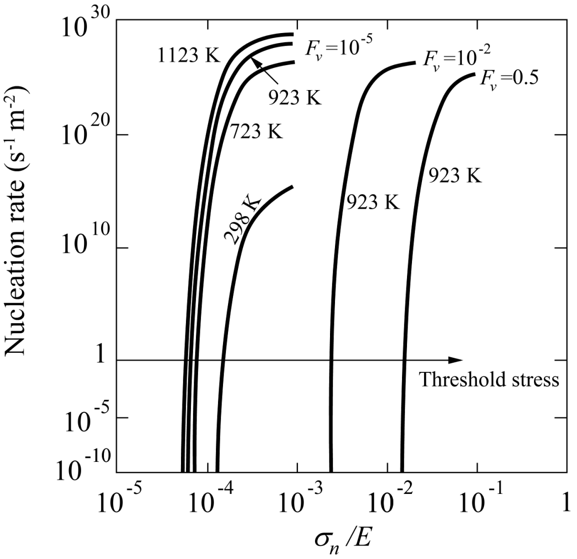

Figure 4.11: Nucleation rate normalised by N_a^{max} as a function of tensile stress in pure copper. The threshold stress refers to the stress for which the normalised nucleation rate is equal to 1 $s^{-1}m^{-2}$. Replotted after [99].

d. Incubation time

The nucleation rate given in Eq. (4.14) is only valid after a steady state has been reached. In fact, there exists a "transient"or "incubation"period required to establish the steady-state nucleation rate (assuming constant applied stress) [99]. The incubation period required to reach the steady state arises from the fact that a finite time is needed to form an embryo containing a critical number of vacancies [99]. Therefore, the incubation time depends on the size of the critical nucleus, the diffusivity and the average vacancy concentration [99].

The transient problem has been studied for nucleation of liquid droplets in pure vapour by Zeldovich [97], Turnbull [98, 101], Kantrowitz [102] and Probstein [103]. A rigorous calculation of incubation time has been carried out by Turnbull [101] for embryos containing only few molecules. The rate equation for the change in the concentration of embryos of sizes ranging from single molecules up to the critical nucleus size was generated and numerically solved. In solid state transformations, critical cluster sizes are of the order of 1000 atoms so that numerical computations take long times. Analytically, the incubation time can be approximately calculated. Using certain simplifying assumptions, Zeldovich [97] and Kantrowitz [102] approximated the incubation time and the dependence of the nucleation rate upon time in an order of:

$$\tau_i = \frac{n_c^2}{q_s k'} \tag{4.15}$$

$$\dot{N}_a^{\tau} = \dot{N}_a \exp(-\tau_i/t) \tag{4.16}$$

where n_c is the number of vacancies in the critical nucleus, q_s the number of vacancy sites at the surface of the critical nucleus, k' the jumping frequency of vacancies into the nucleus across its surface, and $\dot{N}_a$ the nucleation rate at steady state. q_s is estimated by taking the thermodynamic equilibrium concentration in the bulk into account. Jumping frequency k' is assumed to be the migration frequency of vacancies and to be the same as in the matrix (or grain boundary). Since the embryo can form by both the sum of the volume and boundary diffusion processes at the same time, the incubation time from Eq. (4.15) can be expressed as following [99]:

$$\tau_i^{(1)} = \left(\frac{r_c^3 F_v}{\Omega}\right)^2 \frac{6\Omega^{4/3}}{\pi r_c^2 \left[D_v + (\pi\delta/r_c)D_b\right]} \tag{4.17}$$

where D_v is the self-diffusion coefficient in the bulk.

Note that τ_i is a characteristic time called “incubation time”, i.e. the time required for a steady-state nucleation rate to be established. It should not be confused with the “nucleation time”which is the time required for one cavity to form.

Raj [99] has estimated lower bounds of the nucleation time. The minimum diffusion distance of the vacancies was estimated as a function of the vacancy number in the critical nucleus, the thermodynamic equilibrium concentration of vacancies and the grain boundary thickness [99]. Raj [99] suggested that the minimum nucleation time was the required time for a vacancy to diffuse over a diffusion minimum distance. The lower bounds of the nucleation time are given respectively for either boundary or volume diffusion controls by the following relationships [99]:

$$\tau_i^{(2)} = \frac{r_c^3 F_v}{4 D_b \delta} \tag{4.18}$$

$$\tau_i^{(3)} = \frac{\left(r_c^3 F_v\right)^{2/3}}{6 D_v \exp(Q_f/3R_g T)} \tag{4.19}$$

where Q_f is the formation energy of a vacancy in the bulk and R_g is the gas constant.

Figure 4.12 shows a comparison between incubation times measured by Fleck et al. [104] in a commercial copper, and incubation times predicted using Eq. (4.17) as well as using the lower bound given in Eq. (4.18) both taking grain boundary diffusion into account. Based on creep tests carried out for 15 h at 923 K (650°C), cavities were not observed for stress less than 8 MPa, i.e. the threshold stress. Therefore, this threshold stress where the steady state nucleation rate is 1 $\mathrm{m}^{-2}\mathrm{s}^{-1}$ [99], leads to a value of 1.1×10^{-5} for F_v from Fig. 4.11. Then, the critical nucleus size was predicted by Raj [99] to be 5 nm. Predictions of incubation time with the identified value of F_v were compared with the earliest times where cavity nucleation had been observed during creep tests under an applied stress of 11 MPa, at 923 K (650°C) and 1023 K (750°C). The nucleation times predicted by Raj [99] using Eq. (4.18) are lower than the ones predicted using Eq. (4.17) by one order of magnitude. Both of them are much lower than the observed incubation times. This underestimation could be due to the critical nucleus size that is very small to be detected and that the underestimation in time could be a required time for growth of cavities from this size to the observable size.

4.2.2 Creep cavity growth driven by vacancy diffusion

Cavity growth along grain boundaries at high temperature has been suggested to be induced by vacancy diffusion [93, 105–107]. Many models of cavity growth by vacancy

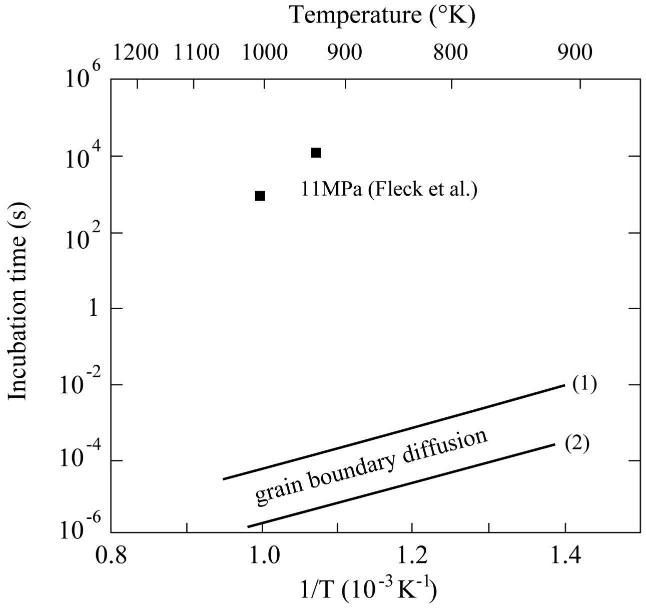

Figure 4.12: Experimental nucleation times in a commercial copper alloy [104] compared with (1) the predicted incubation time given in Eq. (4.17) and (2) the lower bound of the nucleation time given in Eq. (4.18) [99], taking into account the grain boundary diffusion and the coefficient of pure copper.

diffusion have been proposed through many decades. Hull and Rimmer [105] were among the first authors who have proposed a mechanism by which diffusion leads to growth of an isolated cavity in a metal under an external applied stress. The model further have influenced for decades the study of cavity growth in polycrystals through many developments by many other authors such as Raj and Ashby [93], Rice [106], Riedel [107], and Chen and Argon [108], with increasing complexity in representing cavity growth processes. These authors modelled cavities located along grain boundaries subjected to a normal stress approximated to the uniaxial macroscopic stress.

In this family of cavity growth models, creep cavities were assumed to be located along simple grain boundaries. These models do not address cavitation at triple junctions where the maximum size of cavities is experimentally observed [21]. The driving force to cavity growth was assumed to be the normal stress acting on grain boundaries, and not the hydrostatic stress. This normal stress was approximated to the macroscopic stress. Stress heterogeneity due to complicated grain shapes or viscoplastic incompatibilities between neighbouring grains was not taken into account by these models. The models also ignored the stress heterogeneity at triple points and carbide-matrix interfaces for cavities formed at these sites.

a. Applicability domain of diffusion cavity growth models

The applicability domain of the diffusion cavity growth models can be assessed using a length parameter, L_R, given in Eq. (4.20) usually called “Rice length”and introduced in [109]. In fact, Needleman and Rice [110] carried out comparisons between the cavity growth rates induced by either diffusion or viscoplasticity. The first one was estimated using the Riedel cavity growth model [107]. The second one was predicted by considering an ellipsoidal cavity in a linear viscous material under uniaxial tension. The solution was obtained by an elasticity-like approach [111], replacing the Poisson ratio by 1/2 (in non-porous matrix) and remote strain E_n by remote strain rate $\dot{E}_n$ [110]. The ratio of the cavity growth rate by diffusion to the one by viscoplasticity was obtained approximately as $(r_b/L_R)^3$ [110].

$$L_R = \left(\frac{D_b \delta \Omega \Sigma_n}{k_b T} \frac{1}{\dot{E}_n} \right)^{\frac{1}{3}} \tag{4.20}$$

Needleman and Rice [110] suggested that cavity growth is controlled by diffusion alone if $r_b/L_R < 0.2$ (with neglected viscoplasticity effect). The diffusion and viscoplasticity processes combine to produce growth in excess if $0.2 < r_b/L_R < 20$ (very much in excess if $1 < r_b/L_R < 5$), rather than either mechanism acting in isolation [110]. The viscoplasticity process is the dominant mechanism if $r_b/L_R > 20$ [110].

b. Growth of isolated cavities - Hull and Rimmer's theory [105]

Hull and Rimmer [105] modelled homogeneous cavitation assuming that all polycrystal facets perpendicular to the loading axis were affected by cavity development. All cavities were assumed to be spherical and periodically located with the same spacing, $2L$, along each perpendicular facet. The normal stress acting on each perpendicular facet was supposed to be uniform and equal to the uniaxial macroscopic stress, Σ_n. Growth of each cavity was due to diffusion of vacancies within distance $2L$ along the grain boundary. The total number of vacancies was supposed to be unlimited so that the diffusion process is unrestricted for the considered creep time. The diffusion of vacancies on the cavity surface was supposed to be quick enough so that the cavity curvature is maintained with time.

The diffusion flux of vacancies is determined by the chemical potential gradient, $\overline{\nabla}\mu^{ch}$, along the grain boundary plane, as given by Herring [112]:

$$\overline{\mathbf{J}}_b = -\frac{D_b}{\Omega k_b T} \overline{\nabla} \mu^{ch} \tag{4.21}$$

Under the above hypothesis, a grain boundary containing a vacancy leads to a chemical potential given as a function of the remote normal stress, Σ_n, acting on the grain boundary by: $\mu^{ch} = -\Sigma_n \Omega$. This assumption is based on the normal stress and not the hydrostatic pressure. This potential corresponds to the work done by the external stress (Σ_n) to form a vacancy volume (Ω) at the grain boundary by leading to a matrix growth by a similar volume (with no elastic remote strain). Along the cavity free surface, the chemical potential is defined as a function of the free surface energy, γ_s, as following: $\mu^{ch} = -2\gamma_s \Omega / r$.

By using a one-step gradient of chemical potential between the cavity surface and the grain boundary, Hull and Rimmer [105] obtained the flux of vacancy diffusion along the grain boundary approximately as following:

$$J_b = \frac{D_b}{k_b T L} \left(\Sigma_n - \frac{2\gamma_s}{r} \right) \tag{4.22}$$

Vacancies diffuse from the grain boundary of thickness δ across surface area $2\pi r\delta$ of the cavity. The number of vacancies entering the cavity per unit time is equal to $2\pi r\delta J_b$. Therefore, the growth rate of cavity volume is approximated as:

$$\dot{V} = \frac{2\pi\Omega D_b\delta}{k_bT}(\Sigma_n - \frac{2\gamma_s}{r})\frac{r}{L} \tag{4.23}$$

Finally, by considering a spherical shape and neglecting $2\gamma_s/r$ with respect to Σ_n (only true when $r \gg r_c = 2\gamma_s/\Sigma_n$), Hull and Rimmer obtained the size growth rate as following:

$$\dot{r} = \frac{D_b\delta\Sigma_n\Omega}{k_bT}\frac{1}{2Lr} \tag{4.24}$$

c. Raj and Ashby's model [93]

An additional hypothesis was assumed by Raj and Ashby [93]. They supposed that a steady state (time-independent) was established so that all parts of the grain boundary must release or gain the same amount of matter [93]:

$$\overline{\nabla} \cdot \overline{\mathbf{J}}_b = \beta_j \tag{4.25}$$

where β_j is a constant and is equal to the number of atoms removed per unit volume of the boundary per unit time. Combining Eqs. (4.21) and (4.25) leads to the following differential equation:

$$\overline{\nabla}^2(\mu^{ch}) = -\frac{\beta_j k_b T\Omega}{D_b} \tag{4.26}$$

This equation was solved by Raj and Ashby in cylindrical coordinates (radial axis: R, revolution axis: vertical passing by the cavity center). The cavity was assumed to keep a

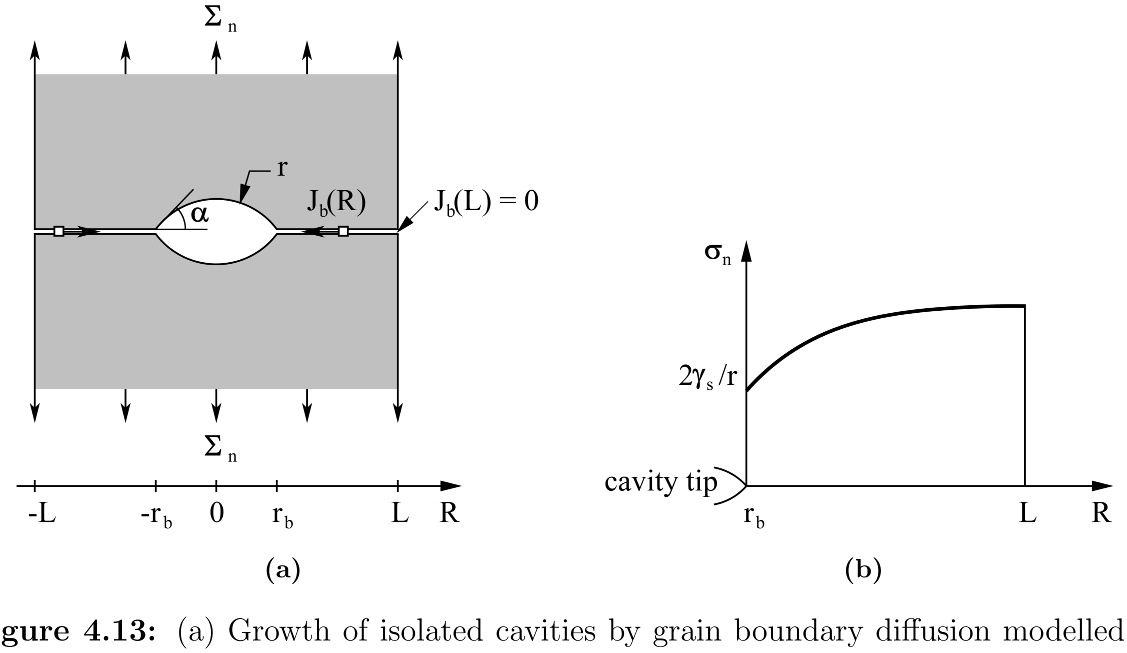

(a) (b)

Figure 4.13: (a) Growth of isolated cavities by grain boundary diffusion modelled by Raj and Ashby [93], (b) resolved normal stress along grain boundary [93].

shape of spherical segment (Fig. 4.7a) with its geometric functions defined by Eqs. (4.4). The resolution used the boundary conditions given by the following [93]:

$$\begin{cases} \mu^{ch} & = & -\dfrac{2\gamma_s\Omega}{r} & \text{for } R = r_b \\ \mu^{ch} & = & -\sigma_n\Omega & \text{for } r_b < R \leq L \\ \dfrac{\partial\mu^{ch}}{\partial R} & = & 0 & \text{for } R = L \end{cases} \tag{4.27}$$

The solution of the differential equation with respect to R is given by [93]:

$$\mu^{ch}(R) = -\frac{\beta_j k_b T\Omega}{4D_b}(R^2 - r_b^2) - \frac{\beta_j k_b T\Omega L^2}{2D_b}\ln\frac{r_b}{R} - \frac{2\gamma_s\Omega}{r} \tag{4.28}$$

The stress profile can then be obtained by using Eq. (4.27). The condition of mechanical equilibrium requires that:

$$\pi L^2\Sigma_n = \int_{r_b}^{L} \sigma_n(R)2\pi R\mathrm{d}R \tag{4.29}$$

Substituting Eqs. 4.28 and 4.29 leads to the final expression of β_j. Since the growth rate of the void is proportional to the amount of atoms added in the grain boundary per unit time, Raj and Ashby [93] found:

$$\dot{V} = -\beta_j\delta\pi L^2\Omega\left(1 - \frac{r_b^2}{L^2}\right) \tag{4.30}$$

By combining Eqs. 4.4 and 4.30, the cavity growth rate can be obtained as following:

$$\dot{r}_b = \frac{2\Omega D_B\delta}{h(\alpha)k_bT}\left(\frac{1}{r_b^2}\right)(1-\omega)\frac{\Sigma_n - \sigma_0(1-\omega)}{q(\omega)} \tag{4.31}$$

where $h(\alpha) = (1-\cos\alpha)/\sin^3\alpha - \dfrac{1}{2}\cot\alpha$, $\omega = r_b^2/L^2$, $\sigma_0 = 2\gamma_s/r$ (sintering stress), and $q(\omega) = 2\ln 1/\omega - (1-\omega)(3-\omega)$.

The Raj and Ashby model assumes that the diffusion flux of vacancies is induced by the normal stress acting on grain boundaries, and not by the hydrostatic pressure. A penny-shaped cavity with radius of curvature r at its tip and size $2r_b$, subjected to a normal stress filed of Σ_n results in a stress concentration factor (in elastic regime) $1 + 2\sqrt{r_b/r} \to \infty$ when $r \to 0$ [113]. In consequent, $\sigma_n(R = r_b) \to \infty$. This problem may be resolved by viscoplastic creep flow.

d. Constraints on diffusive growth of cavities

The previous authors [93, 105] supposed that cavities are uniformly distributed overall transverse facets of polycrystals (Fig. 4.14a). For such uniform cavitation, assuming isolated cavity growth under an average normal stress equal to macroscopic stress Σ_n could be valid.

However, cavitated grain boundary facets might be relatively isolated one from another (Fig. 7.14c). This holds for creep cavitation in Cr-Mo-V bainitic steel at 196˚C [83] and in 12%Cr steel at 650˚C [21]. In this case, cavities were suggested by Dyson [115]

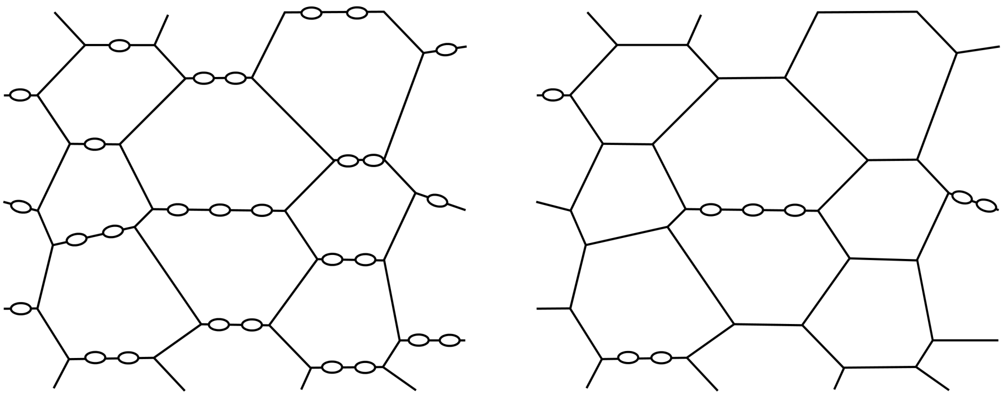

(a) (b)

Figure 4.14: Schemata representing (a) uniform and (b) heterogeneous cavitation at (especially) grain boundaries under vertical loading replotted after [114]. The latter one leads to constrained cavity growth.

to be subjected to constrained diffusion growth. At low creep strain rate, the cavitated facets tend to deform faster that the surrounding matrix [106]. In order to ensure a compatibility of remote strain, the cavitated facets shed load to the surrounding matrix [106]. Therefore, diffusion-controlled cavity growth is constrained and the cavitated facets are subjected to a normal stress relatively reduced with respect to Σ_n. This local stress reduction induces a reduction in cavity growth by grain boundary diffusion.

The constraints on diffusive cavity growth originally suggested by Dyson [115] were then modelled by Rice [106]. The cavity growth rate was suggested to be reduced to:

$$\dot{r}_b = \frac{2\Omega D_B \delta}{h(\alpha) k_b T} \left(\frac{1}{r_b^2} \right) \frac{\Sigma_n - \sigma_0(1-\omega)}{[8L_R^3/\alpha' L^2 d_g] + [q(\omega)]} \tag{4.32}$$

where L_R is the Rice transition length (paragraph a. of section 4.2.2), d_g the grain diameter, and $\alpha' = 2/\pi$ for for linear viscous material. For viscoplastic materials obeying the Norton flow rule with exponent n, Riedel [107] suggested that $\alpha' = 4/[\pi^2(1+3/n)^{\frac{1}{2}}]$.

e. Cavity growth coupled with continuous nucleation

During creep, cavities do not nucleate at the same time but continuously one after another. In fact, cavities nucleate earlier on sites having smaller activation barrier. These sites can be for example triple junctions of polycrystals, where local stress is high compared to another. Following numerous measurements, Dyson [91] suggested that cavities nucleate with approximately constant rates during the creep tests, $\dot{N}_0$.

Cavity growth by vacancy diffusion along grain boundary with continuous nucleation has been modelled by Riedel [107]. The distribution of cavities in size (r_b) and time (t) is represented by a function $N_{rb}(r_b, t)$. This function is defined such that the number per unit area of grain boundary of cavities with sizes ranging between $[r_b, r_b + \mathrm{d}r_b]$ is $N_{rb}(r_b, t)\mathrm{d}r_b$. By analogy with the diffusion problem, the mass-balance equation is given by [107]:

$$\dot{N}_{rb} + \frac{\partial J_n}{\partial r_b} = 0 \tag{4.33}$$

where $J_n(r_b, t)$ is the flux in size space. Cavities can only pass from one size class r_b to the next one $r_b + \mathrm{d}r_b$ only by growth. If an individual cavity of size r_b has growth rate $\dot{r}_b$, the flux in size space is $J_n(r_b, t) = N_{rb}(r_b, t)\dot{r}_b$. The meaning of $J_n(0, t)$ is that J_n for a small value of r_b set to zero corresponds to nucleation rate $\dot{N}(t)$ of cavities, which is the boundary condition for differential equation (4.33). In order to simplify the resolution of differential equation (4.33), Riedel [107] suggested to represent $\dot{r}_b$ and $\dot{N}$ by particular analytical formulas. Thus, the boundary conditions for differential equation (4.33) are given by:

$$N_{rb}(r_b = 0, t)\dot{r}_b = \dot{N}(t) \tag{4.34}$$

$$\dot{r}_b(r_b, t) = A_1 (r_b)^{-\xi} t^{-\eta} \tag{4.35}$$

$$\dot{N}(t) = A_2 t^{\zeta} \tag{4.36}$$

where A_1, A_2, η, ξ and ζ are parameters which should be calculated later. Riedel [107] suggested that a solution in form $N_{rb}(r_b, t) = t^P f(\frac{r_b}{t^Q})$ may exist. Resolving differential equation (4.33) by taking the boundary conditions given in Eqs. (4.34), (4.35) and (4.36) into account, the solution was finally obtained as [107]:

$$N_{rb}(r_b, t) = \left| \begin{array}{ll} \frac{A_2}{A_1}(r_b)^{\xi} t^{\eta+\zeta} \left[1 - \frac{1-\eta}{(1+\xi)A_1}(r_b)^{\xi+1} t^{\eta-1}\right]^{(\eta+\zeta)(1-\eta)} & \text{if } \eta < 1 \\ \frac{A_2}{A_1}(r_b)^{\xi} t^{\eta+\zeta} \exp\left[-\frac{1+\zeta}{(1+\xi)A_1}(r_b)^{\xi+1}\right] & \text{if } \eta = 1 \end{array} \right. \tag{4.37}$$

Since the final fracture criterion is assumed to be based on the critical average area fraction of cavities along grain boundaries, $\overline{\omega}_f$, estimating damage evolution $\overline{\omega}(t)$ is required. It can be calculated by integrating the areas occupied by the individual cavities of area $\pi(r_b)^2$ times their area density $N_{rb}\mathrm{d}r_b$, therefore given by:

$$\overline{\omega}(t) = I_1(\eta, \xi, \zeta) A_2 {A_1}^{2/(1+\xi)} t^{\eta+\zeta+(1-\eta)(\xi+3)/(\xi+1)} \tag{4.38}$$

where the factor $I_1(\eta, \xi, \zeta) = \pi(1+\xi)^{(\xi+3)/(\xi+1)} \int_0^u x^{\xi+2} \left[1 - (1-\eta)x^{\xi+1}\right]^{(\eta+\zeta)/(1-\eta)} \mathrm{d}x$, with $u = \infty$ if $\eta > 1$ and $u = (1-\eta)^{-1/(\xi+1)}$ if $\eta < 1$. Note that $I_1(\eta, \xi, \zeta)$ is a numerical value independent of model parameters A_1 and A_2 and also of time t. Then, for $\eta < 1$, the average radius of cavities is deduced from Eq. (4.37) and given by the following:

$$\overline{r}_b(t) = \frac{\int_0^{r_{bmax}} r_b N_{rb} \mathrm{d}r_b}{\int_0^{r_{bmax}} N_{rb} \mathrm{d}r_b} = (1+\zeta) I_2 {A_1}^{1/(1+\xi)} t^{(1-\eta)/(1+\xi)} \tag{4.39}$$

where the factor $I_2 = (1+\xi)^{(\xi+2)/(\xi+1)} \int_0^u x^{\xi+1} \left[1 - (1-\eta)x^{\xi+1}\right]^{(\eta+\zeta)/(1-\eta)} \mathrm{d}x$, $u = (1-\eta)^{-1/(\xi+1)}$, and maximum cavity size r_{bmax} giving $N_{rb} = 0$.

The Dyson nucleation equation, $\dot{N}(t) = \dot{N}_0$, can be introduced into Eq. (4.36). Unfortunately, the unconstrained diffusion growth rate deduced from Eq. (4.32) is not compatible with the power-law form defined by Eq. (4.35). To solve this problem, Riedel [107] neglected the sintering stress, $\sigma_0 = \frac{2\gamma_s}{r}$, and proposed a lower bound of $q(\omega) = 1$. The author then deduced $\eta = 0$, ξ=2, and $\zeta = 0$. Therefore, the lower bound of fracture time for unconstrained growth and continuous nucleation is given by [107]:

$$t_f = 0.33 \left(\frac{h(\alpha) k_b T}{\Omega D_b \delta \Sigma_n}\right)^{2/5} \left(\frac{\overline{\omega}_f}{\dot{N}_0}\right)^{3/5} \tag{4.40}$$

Two new bounds of $q(\omega)$ are used. The upper bound is $0.65\omega^{-0.209}$ (true for ω up to 0.2) leading to $\eta = -0.209$, $\xi = 1.582$, $\zeta = 0$). The upper bound is $0.75\omega^{-0.5}$ leading to $\eta = -0.5$, $\xi = 1$, $\zeta = 0$). Two bounds of t_f can be then deduced as following:

$$0.301 \left(\frac{h(\alpha)k_bT}{\Omega D_b\delta\Sigma_n}\right)^{2/5} \frac{(\overline{\omega}_f)^{0.5164}}{(\dot{N}_0)^{2/5}} \leq t_f \leq 0.354 \left(\frac{h(\alpha)k_bT}{\Omega D_b\delta\Sigma_n}\right)^{2/5} \frac{(\overline{\omega}_f)^{2/5}}{(\dot{N}_0)^{2/5}} \tag{4.41}$$

Then, the bounds of average radius are respectively given by the following:

$$1.97 \left(\frac{\Omega D_b\delta\Sigma_n}{h(\alpha)k_bT}\right)^{0.5} (\dot{N}_0)^{0.25}t^{0.75} \leq \overline{r}_b(t) \leq 1.74 \left(\frac{\Omega D_b\delta\Sigma_n}{h(\alpha)k_bT}\right)^{0.3873} (\dot{N}_0)^{0.0809}t^{0.4682} \tag{4.42}$$

In constraint limit, $q(\omega)$ in Eq. (4.32) was neglected by Riedel [107]. The sintering stress, $\sigma_0 = \frac{2\gamma_s}{r}$, was again neglected [107]. The growth rate $\dot{r}_b$ deduced from Eq. (4.32) is compatible with the analytical formula given in Eq. (4.35). The exponents in Eqs. (4.34), (4.35) and (4.36) were deduced by Riedel as $\eta = 1$, $\xi = 2$ and $\zeta = 0$. Therefore, lifetime for continuous and constrained cavity growth is predicted as following [107]:

$$t_f = 0.78 \left(\frac{1+\frac{3}{n}}{\dot{N}_0}\right)^{1/3} \left(\frac{h(\alpha)}{d_g\dot{E}_n}\right)^{2/3} \overline{\omega}_f \tag{4.43}$$

f. Experimental validation of the models for cavity growth

Figure 4.15 illustrates a comparison between predicted growth rates using Eq. (4.32) [107] and experimental results of Needham [30] for two ferritic steels at 550°C. The growth rates predicted using the constrained cavity growth model are in fair agreement with the measured rates. The growth rates predicted using the unconstrained cavity growth model are much faster [107]. Riedel [107] concluded that the constrained cavity growth model describes cavity growth rates fairly well for these experiments.

Figure 4.16 illustrates the effects of continuous nucleation as distinct from instantaneous one. The curves for instantaneous nucleation were calculated assuming that all cavities which were present at the end of the test had been nucleated instantaneously at the beginning of the test [107]. The figure shows that the effect of continuous nucleation on lifetime is substantial if the cavities grow by unconstrained diffusion, whereas the effect is weaker for constrained cavity growth. Lifetimes predicted using the constrained cavity growth model [107] are in good agreement with experimental data given in [116] for $2\frac{1}{4}$Cr-1Mo steel at 565°C.

These results show that for both 1Cr-$\frac{1}{2}$Mo and $2\frac{1}{4}$Cr-1Mo ferritic steels, the constrained cavity growth model is the most satisfactory one. It should be mentioned that for both steels, cavitated facets were observed to be isolated one from another as suggested by Dyson [115].

g. Coupled viscoplasticity and diffusion-driven cavity growth models

Another cavity growth mechanism which has been studied by many authors is a coupling between diffusion growth and viscoplasticity growth. This coupling corresponds to: $0.2 <$

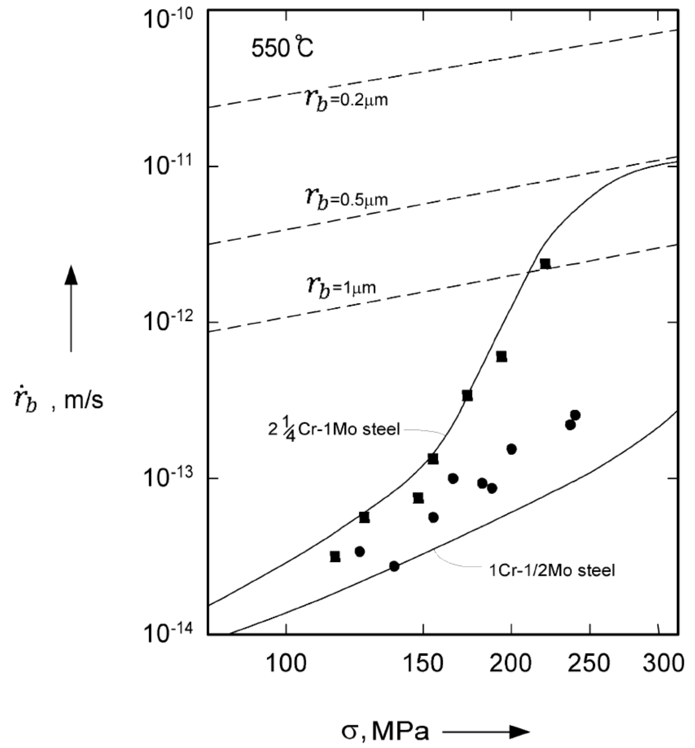

Figure 4.15: Cavity growth rates predicted using an unconstrained cavity growth model (dashed lines) and a constrained cavity growth model [107](solid lines), compared with experimental measurements in bainitic steels [84]. Redrawn in [114].

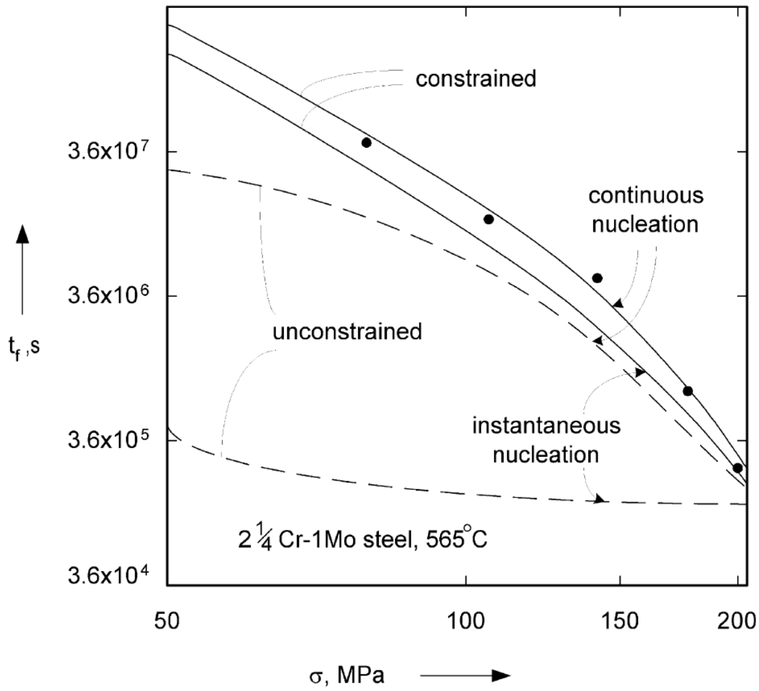

Figure 4.16: Predicted fracture lifetime taking into account unconstrained cavity growth (dashed lines) and constrained cavity growth (solid lines) with either continuous or instantaneous nucleation [107]. The predictions are compared with the measured lifetimes of $2\frac{1}{4}$Cr-1Mo steel in over-heated condition [116]. Redrawn in [114].

$r_b/L_R < 20$ (paragraph a.). A model coupling both mechanisms was first proposed by Needleman and Rice [110] and then improved by Chen and Argon [108]. Van Der Giessen et al. [117] proposed a coupling model by taking the effect of high triaxialities into account. Gaffard et al. [72] used a viscoplastic potential of Leblond-Perrin-Suquet type to describe the creep cavitation in Grade 91 steel.

However, for the creep tests at 500°C under 230 MPa and 250 MPa, and at 600°C under 90 MPa and 125 MPa, diffusion alone is assumed to be the dominant mechanism of cavity growth following predictions of Rice length that will be shown in section 5.2.2.

4.3 Discussion and choice of models

Models of diffusion cavity growth presented in section 4.2.2 will be used to simulate cavitation along packet/block boundaries or FAGBs [4,21] in Grade 91 steel under study. These models assume generally that the normal stress acting on grain boundaries is equal to the macroscopic uniaxial stress. Hull and Rimmer [105] used a rough approximation of the flux gradient of diffusion leading to an underestimation of the cavity growth rate. Raj and Ashby resolved this diffusion problem more accurately by using integration of diffusion flux gradient along the grain boundary. However, the Raj and Ashby model considers instantaneous nucleation of cavities. Continuous nucleation suggested by Dyson [91], also observed in 12%Cr steel [21], was included in the Riedel model.

As observed by Gaffard in a Grade 91 steel (see also section 5.1), cavities seem to be isolated one from another on each grain boundary. Therefore, the constrained cavity growth model does not present yet strong interest for the applications under study.

Critical minimum strain rates below which the constrained growth effect become critical and to be taken into account could be computed using the constrained growth model [118]. The distance between cavities is taken as 40 µm which is the average size of former austenitic grains. For the creep test at 500°C and 230 MPa, the estimated critical minimum strain rate is 10 times lower than the experimental one. For the creep test at 600°C and 90 MPa, the estimated critical minimum strain rate is equal to the experimental one. Therefore, for creep tests at 600°C under lower stress, contrained growth mechanism may be required to take into account.

For the creep tests under study, considering only diffusion cavity growth is sufficient. The Raj and Ashby model and the Riedel model will be used and their results will be compared with the experimental observations based on our creep tests.

The Raj nucleation model presents a great interest to be used with the Riedel model of diffusion cavity growth and continuous nucleation. After Raj, cavities could nucleate at grain boundaries without or with carbides. In the last case, cavity nucleation was suggested by Raj to have the highest probability. The Raj nucleation model will be used for both nucleation sites, and the predictions will be compared with our experimental observations in Grade 91 steel.

One should mention that all these analytical models do not consider stress heterogeneity that could occurs at triple junctions, grain boundaries and carbide-matrix interfaces. This could affect the diffusion cavity growth and nucleation rates. The stress heterogeneity could only be studied using the finite element method or other sophisticated numerical approaches.

Chapter 5

Observations and modelling of long-term creep cavitation in Grade 91 steel

5.1 Creep cavity observations in Grade 91 steel

This section presents observations of creep cavities at the end of four long-term creep tests on Grade 91 steel at 500˚C and 600˚C reported in Table 5.1. Numerous observations for two creep specimens, one tested at 500˚C under 230 MPa and another at 600˚C under 90 MPa, had already been carried out by Haney and Bonnaillie [7]. Additional observations were carried out on these specimens as well as on two others, one loaded at 500˚C under 250 MPa and another at 600˚C under 125 MPa, to get more extensive experimental database for both temperatures (500 and 600˚C).

Table 5.1: Characteristics of the creep tests considered for studying creep cavitation in Grade 91 steel.

T (˚C)	Engineering stress (MPa)	Lifetime (h)	Reduction in cross-section at fracture [7]
500˚C	230	160×10^3	0.60
500˚C	250	59×10^3	0.80
600˚C	90	94×10^3	0.15
600˚C	125	5×10^3	0.70

5.1.1 Preparation of creep samples

All samples were taken from homogeneous zones of the creep specimens, i.e. located far away from the necking zones. The cross-section was taken parallel to the loading axis and at the middle of the cylindrical creep specimens. Polishing of all observed cross-sections was finished with a colloidal silica solution (OPS).

5.1.2 Procedure used for quantitative measurements of cavitation

Micrographs for creep tests carried out at 500˚C under 230 MPa (Fig. 5.1) and at 600˚C under 90 MPa (Fig. 5.2) were provided from previous FEG-SEM observations made by Bonnaillie and Haney [7]. The parameters of the creep cavity observations used by these authors are reported in Table 5.2. The resolution of the provided micrographs only allows detection of cavities with a minimum size. This minimum size is 0.2 µm (an area of 4 pixels) for the specimen loaded at 500˚C under 230 MPa and respectively 0.5 µm (an area of 4 pixels) for the other one.

For the sample loaded at 500˚C under 250 MPa (59 kh), the FEG-SEM magnification as used for the observations of the one loaded at 500˚C under 230 MPa was kept. The corresponding micrographs are presented in Fig. 5.4. Exceptionally, for the specimen loaded at 600˚C and 250 MPa, the magnification of 500 (i.e. as used for the one loaded at 600˚C under 90 MPa) did not allow us to distinguish between cavities and pixel noises. Instead, a magnification of 1000 was chosen and allowed detecting cavities with a minimum size of 150 nm. For a fair quantification of cavities, the minimum size was kept the same for each temperature, i.e. 0.2 µm at 500˚C and 0.5 µm at 600˚C.

Cavity statistics by mean of Image Processing were carried out for both specimens, one loaded at 500˚C under 230 MPa (over a field of 9.38×10^5µm^2) and another one at 600˚C under 90 MPa (over a field of 1.32×10^6µm^2). The procedure of image analysis starts by transforming greyscale images into binary images where cavities are represented by white-pixel areas and the rest by black pixels. Then, all white-pixel objects are subjected to morphological dilation and erosion. The final transformed images are compared with the original images. The pixel numbers of white objects provide a measure of the cavity areas, whereas their equivalent diameters are estimated by considering circular shapes. Image processing respects the conditions that only cavities with diameter not lower than the minimum detectable size (0.2 µm for creep at 500˚C under 230 MPa, and 0.5 µm for the other one) are taken into account. Indeed, lower-size cavities could be confused with pixel noises. The observation parameters and numbers of observed cavities are reported in Table 5.2.

However, fully automated image processing could not be applied to the creep samples loaded at 500˚C under 250 MPa and at 600˚C under 125 MPa because of the very small size of cavities. Since the grey level of cavities is easily confused with the surrounding pixels, the transformation from greyscale to binary images causes a pixel lost in cavity areas. Therefore, detection of cavities was carried out manually on FEG-SEM micrographs taken over a field of 9.83×10^3µm^2 for the sample loaded at 500˚C and 250 MPa and respectively of 1.97×10^4µm^2 for the one loaded at 600˚C and 125 MPa. The observation parameters and numbers of cavities are reported in Table 5.2 as well.

Cavity observations with higher resolution are carried out for the creep samples loaded at 500˚C under 250 MPa and respectively at 600˚C under 125 MPa in order to measure the sizes of smallest cavities. A magnification of 10000 allowed us to detect smallest cavities in both samples and their sizes are reported in Table 5.3. This high resolution will allow comparisons with the nucleation sizes of cavitation presented in section 5.1.4.

Table 5.2: Statistics parameters of the quantitative study of creep cavities in Grade 91 steel.

Creep characteristics			Observation parameters				
T (°C)	σ^{eng} (MPa)	Lifetime (h)	Magnification	d_{min} (µm)	Field area (µm^2)	Average number of γ-grains	Number of detected cavities
500	230	$160{\times}10^3$	1000	0.2	9.38×10^5	375	1505
500	250	$59{\times}10^3$	1000	0.2	9.83×10^3	4	10
600	90	$94{\times}10^3$	500	0.5	1.32×10^6	528	291
600	125	$5{\times}10^3$	1000	0.5	1.97×10^4	8	4

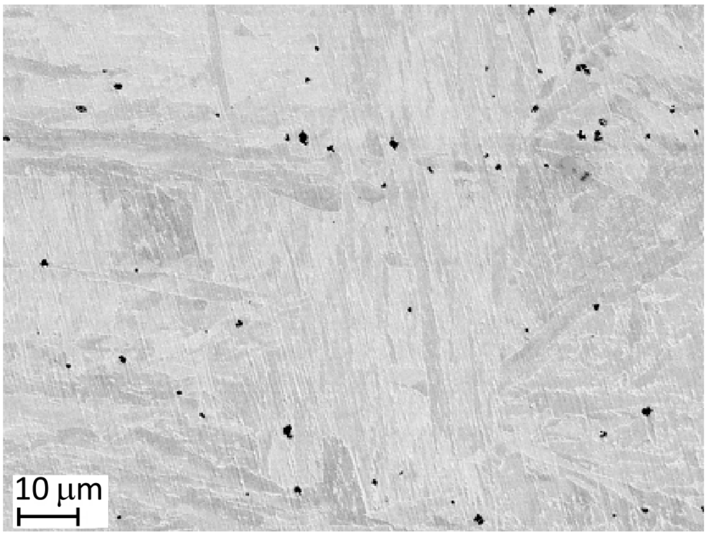

Figure 5.1: Creep cavities in Grade 91 steel subjected to creep at 500˚C under 230 MPa, after a lifetime of 160×10^{3}h. FEG-SEM observations by Bonnaillie and Haney [7] using a magnification of 1000.

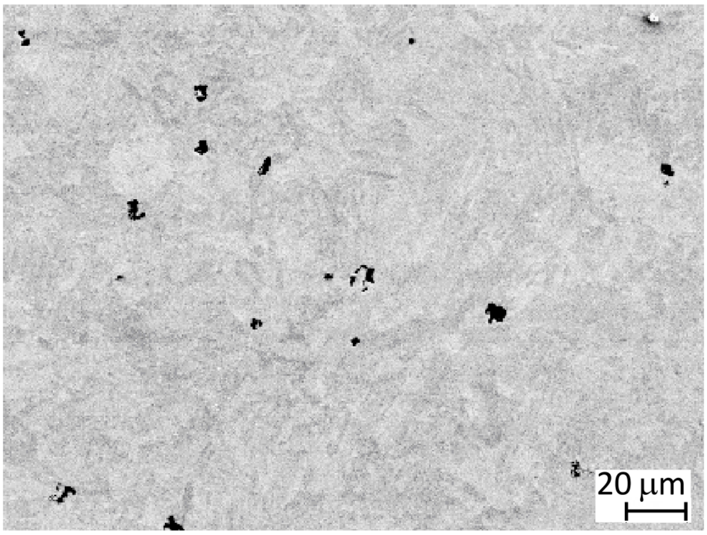

Figure 5.2: Creep cavities in Grade 91 steel subjected to creep at 600˚C under 90 MPa, after a lifetime of 94×10^{3}h. FEG-SEM observations by Bonnaillie and Haney [7] using a magnification of 500.

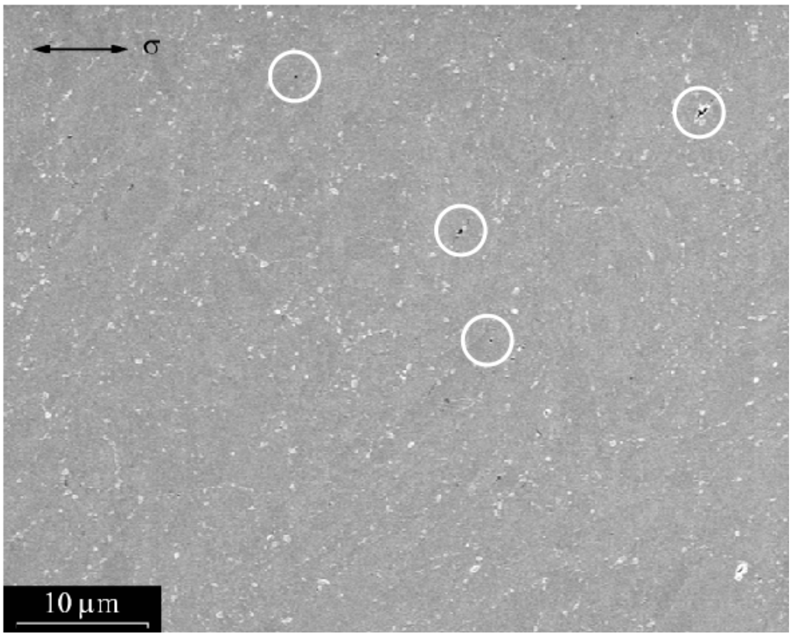

Figure 5.3: Creep cavities in grade 91 steel subjected to creep at 500˚C under 250 MPa, after a lifetime of 59 × 10^3h. FEG-SEM observations using a magnification of 1000 at Ecole des MINES with A.-F. Gourgues-Lorenzon and A. Laurent.

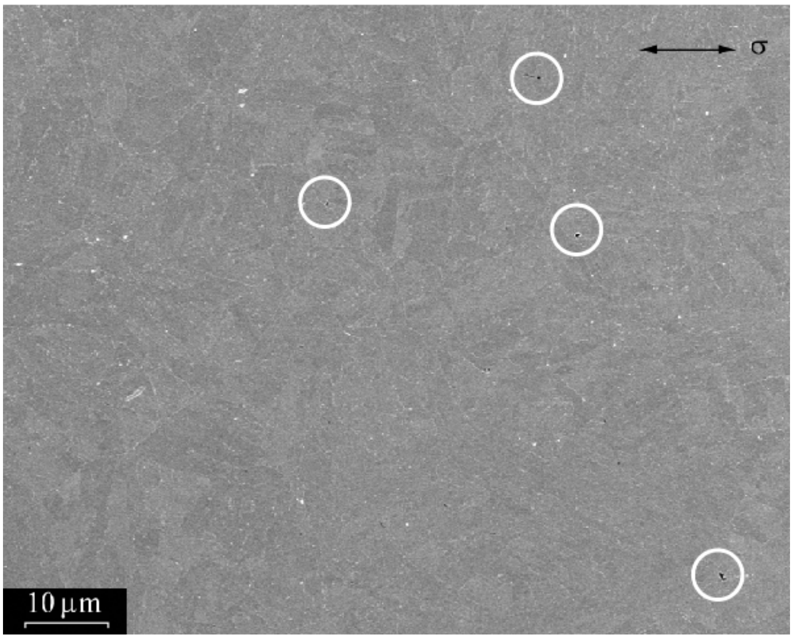

Figure 5.4: Creep cavities in Grade 91 steel subjected to creep at 600˚C under 125 MPa, after a lifetime of 5×10^3h. FEG-SEM observations using a magnification of 1000 at Ecole des MINES with A.-F. Gourgues-Lorenzon and A. Laurent.

Table 5.3: Smallest sizes of creep cavities in Grade 91 steel.

Creep characteristics		Observation parameters		Smallest	Density
T (˚C)	σ^{eng} (MPa)	Magnification	Field area (µm^2)	size (µm)	(µm^{-2})
500	230	5000	1070	0.05	6×10^{-2}
500	250	10000	772	0.05	1.9×10^{-2}
600	90	500	$1.32{\times}10^6$	< 0.5	-
600	125	10000	1867	0.08	8×10^{-4}

5.1.3 Cavity characteristics with regards to creep lifetime

The results of cavity quantification are reported in Table 5.4. At 500˚C, creep cavities were observed after a creep lifetime of $59{\times}10^3$ h, but their sizes are low (up to 1 µm). At 600˚C after a creep lifetime of $5{\times}10^3$ h, creep cavities with sizes up to 0.9 µm were observed. At 625˚C after a creep lifetime of 870 h, Gaffard observed creep cavities with an average size of 2 µm in Grade 91 steel. At 650˚C in martensitic 12%Cr steel, creep cavities with sizes up to 3.8 µm were observed after a creep lifetime of only 280 h [21]. These results seem to show that with increasing temperature cavitation tends to occur earlier.

Area fraction of cavities for various lifetimes and temperatures are reported in Table 5.4. At a constant temperature, the amount of cavity damage increases with increasing lifetime. At 500˚C, the measured area fraction of cavities is of $6.86{\times}10^{-4}$ for a lifetime of $160{\times}10^3$ h, and is lower by an order of magnitude for a lifetime of $59{\times}10^3$ h. At 600˚C, the area fraction of cavities is of $2.5{\times}10^{-3}$ for a lifetime of $94{\times}10^3$ h, and is 30 times lower for a lifetime of $5{\times}10^3$ h. At 625˚C, the area fraction of cavities increases from $1{\times}10^{-3}$ to $3{\times}10^{-3}$ when lifetime increases from 870 h to 3800 h [4].

Table 5.4: Summary on the quantification of creep cavities after observations at 500˚C (CEA data), 600˚C (CEA data) and 625˚C [4]. N_m is the 2D number density of cavities measured from polished cross-section, $\overline{d}$ is the average 2D cavity diameter by considering circular areas. The used observation parameters are given in Table 5.2.

Creep characteristics				
T (˚C)	σ^{eng} (MPa)	t_f (kh)	N_m (µm^{-2})	Area fraction of cavities
500˚C	230	160	1.6×10^{-3}	6.9×10^{-4}
500˚C	250	59	1.02×10^{-3}	5.2×10^{-5}
600˚C	90	94	2.2×10^{-4}	2.5×10^{-3}
600˚C	125	5	2×10^{-4}	8.3×10^{-5}
625˚C [4]	100	3.8	5.5×10^{-4}	3×10^{-3}

The cavity densities in polished cross-sections, N_m, for different values of the applied stress and temperatures are reported in Table 5.4. N_m should be distinguished from the cavity density along FAGB or block boundary facets, N_a, given in Eq. (4.1) [91]. Results for the creep tests at 500˚C seem to show a decrease in number density of cavities with increasing stress. However, the cavity density varies by lower than 60% which is close to the experimental uncertainty due to possible sampling effects. The creep tests carried out at 600˚C also show no stress dependence. The study of Gaffard [4] on Grade 91 steel shows a decrease of cavity density with a factor 3 between stresses of 100 and 120 MPa, but only these specimens were used. A large range of applied stress may be required to clarify a dependence of the cavity density with respect to stress. The limit resolution of FEG-SEM usually constraints a minimum size of detectable cavities and leads to an underestimation of numbers of cavities having lower sizes.

Size distributions of cavities after the creep tests at 500˚C under 230 MPa and at 600˚C under 90 MPa are plotted in Figs. 5.5 and 5.6. For the first creep test, the most probable cavities have (equivalent circular) diameters lower than 1 µm, whereas the largest cavities (3.5 µm) have a relative probability of about 0.1%. The cumulative probability seems to be linear following the cavity size, except for sizes larger than 1 µm. For the second creep test, the most observed cavities have diameters lower than 5.5 µm, whereas the largest cavities (8.5µm) have a relative probability of only 0.34%. The probability distribution is more flatter than the one at 500˚C. The cumulative probability seems to be linear following the cavity size, except once for sizes larger than 5.5 µm. Therefore, distribution queues with the highest cavity sizes are observed in both long-term specimens.

Mean cavity sizes were computed using the probability distributions plotted in Figs. 5.5a and 5.6a. Mean distances between cavities were computed by considering uniform square distributions. The results are reported in Table 5.5.

Table 5.5: Characteristic size and average distance between cavities in the considered Grade 91 steel using the observation parameters in Table 5.2. d_{min} is the lower cut-off value of the size distribution.

T (˚C)	σ^{eng} (MPa)	t_R (h)	d_{min} (µm)	d_{max} (µm)	$\overline{d}$ (µm)	$1/\sqrt{N_m}$ (µm)
500˚C	230	160×10^3	0.2	3.5	0.67	25
500˚C	250	59×10^3	0.2	1	-	31
600˚C	90	94×10^3	0.5	8.5	3.3	67
600˚C	125	5×10^3	0.5	0.9	-	71
625˚C	100	7×10^3	-	-	2.5	43

5.1.4 Location of creep cavities

The observations show that there are three types of cavity nucleation sites: FAGBs/packet/block boundaries, triple junctions and interfaces between intergranular particles and the matrix.

At 500 and 600˚C, creep cavities are usually located along FAGBs/packet/block boundaries (Figs. 5.1, 5.2 and 5.8a). A cavity formed at a triple junction of block boundaries was observed after a creep lifetime of 5×10^3 h at 600˚C (Fig. 5.9a), which is the largest detected cavity of that specimen. An analysis using SEM-EBSD carried out by Barcelo and Fournier [119] on a cavity (Fig. 5.7) shows that it is located at a triple junction of block boundaries.

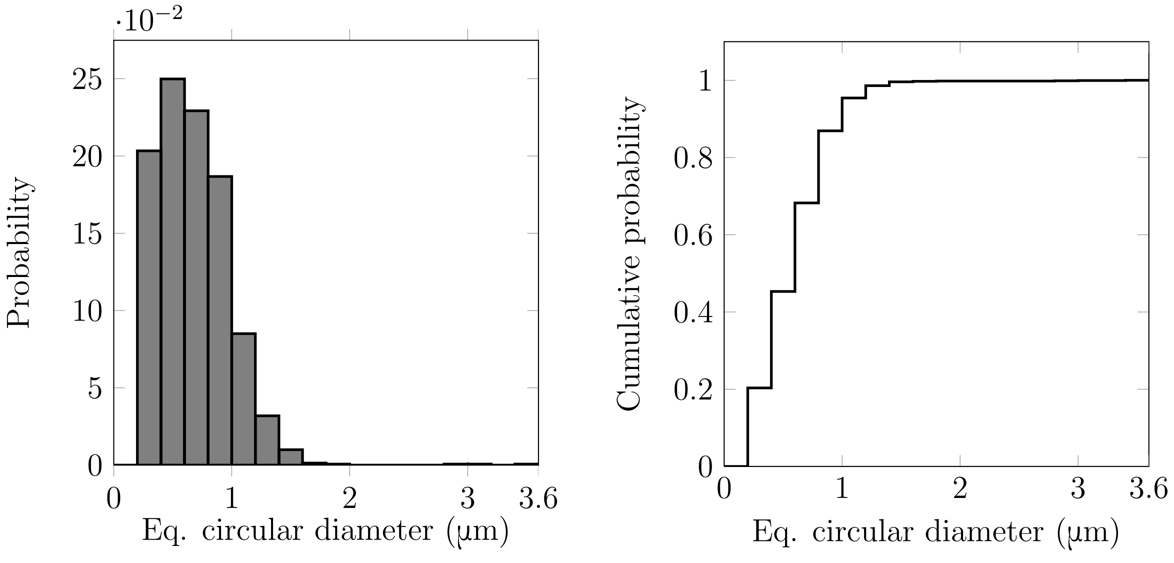

(a) **(b)**

Figure 5.5: Sizes distribution of creep cavities (equivalent circular diameter) in Grade 91 steel represented by (a) probability and (b) cumulative probability after a creep lifetime of 160 × 10^3 h at 500˚C (230 MPa). Magnification: 1000, minimum size of detectable cavities: 0.2 µm.

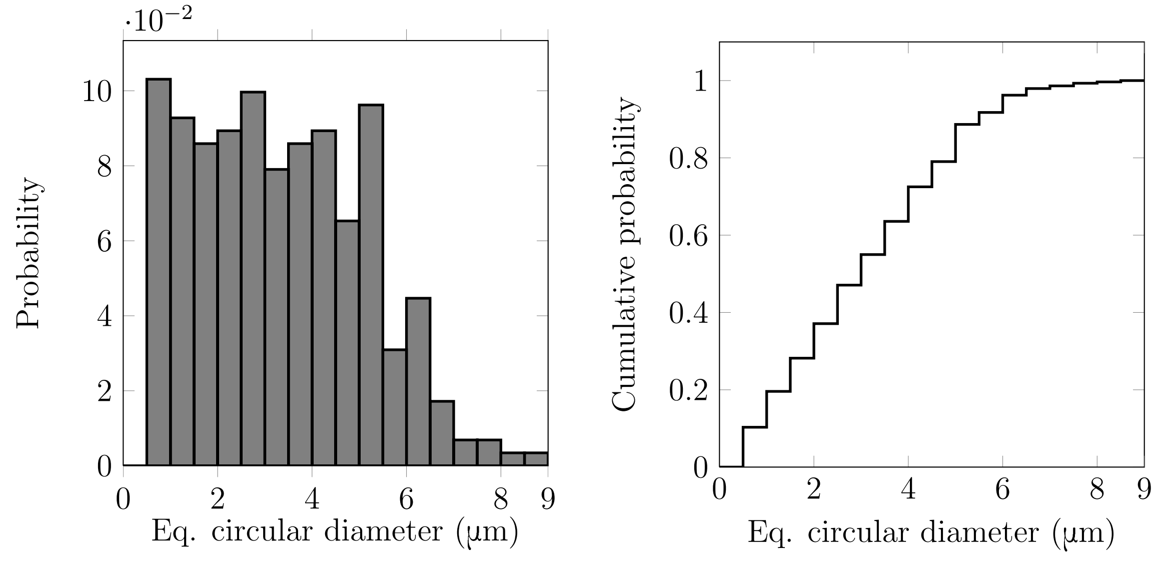

(a) **(b)**

Figure 5.6: Size distribution of creep cavities (equivalent circular diameter) in Grade 91 steel represented by (a) probability and (b) cumulative probability after a creep lifetime of 94 × 10^3 h at 600˚C (90 MPa). Magnification: 500, minimum size of detectable cavities: 0.5 µm.

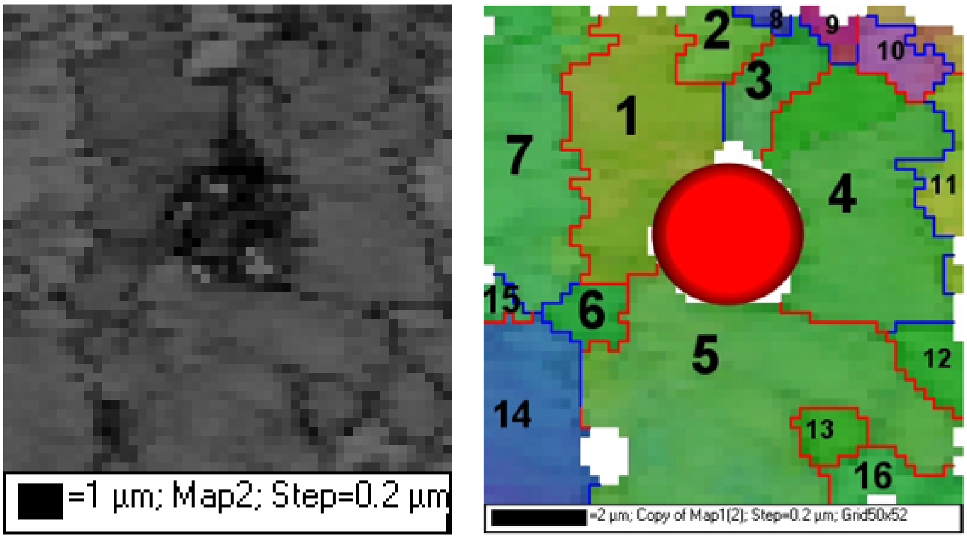

(a) **(b)**

Figure 5.7: A cavity located at a triple junction of block boundaries of Grade 91 steel subjected to the creep test at 600°C and 90 MPa (94 kh), identified using (a) SEM observations and (b) SEM EBSD analysis [119].

FEG-SEM observations of creep cavities were carried out with higher spacial resolution for the creep specimens loaded at 500°C under 250 MPa (59 kh) and 600°C under 125 MPa (5 kh). For the first one, cavities located at matrix-$M_{23}C_6$ interfaces (Figs. 5.8b, 5.8c and 5.8d) constitute the majority of the cavity population following observations on numerous micrographs. After Raj and Ashby (Fig. 4.7b), these cavities are described by type-A (Fig. 5.8b), type-B (Fig. 5.8c), and another one similar to type-B but the cavity is located between two neighbouring carbides (Fig. 5.8d). The particles may have been fractured as well. For this test, the type-B cavities are the majority. For the second creep test, no cavities were detected at matrix-$M_{23}C_6$ interfaces, but one is observed at a Laves phase-matrix interface. The cavity size is about 80 nm and the size of the Laves phase is of 250 nm (Fig. 5.9b). This measured diameter is in agreement with the measured value given by Hald [20] after an ageing time of 5000 h at 600°C (300 nm). However, cavitation close to Laves phases constitutes a rare case at 600°C.

FEG-SEM observations using a magnification of 5000 were also carried out for detecting cavities in the creep specimen loaded during 160 kh at 500°C under 230 MPa. Cavities having sizes of about 40 nm were observed, whereas the ones whose sizes range between 100 and 500 nm were not detected. The majority of the cavities are located at Laves phase interfaces, with 2/3 of them are of type B. They were sometimes detected at grain/block boundaries parallel to the loading axis.

5.1.5 Conclusions

Following the literature [4,21], only cavitation along FAGBs/packet/bolck boundaries almost perpendicular to the loading direction, where the final cavity size is the maximum, will be focused. Only cavities located at the middle of FAGBs/packet/bolck boundaries will be first assumed. Cavitation at triple junctions will be studied later taking into

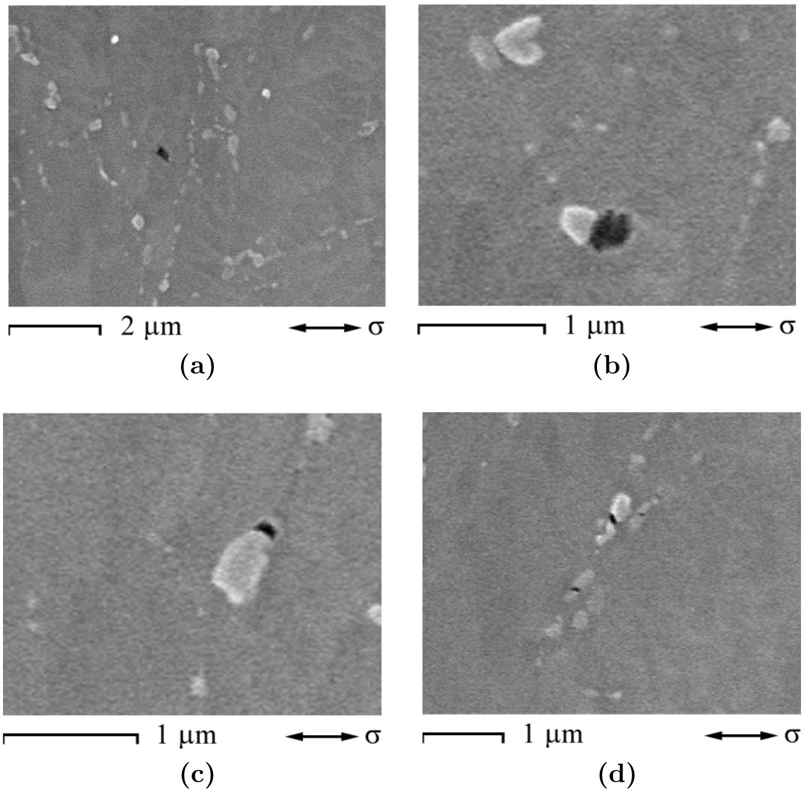

Figure 5.8: cavities located (a) at a packet or block boundary (size of 290 nm), (b) at a carbide-matrix interface - type A (size of 320 nm), (c) at the triple junction of a carbide and a boundary of the matrix - type B (size of 160 nm) and (d) at a matrix boundary between two carbides (size of 90 nm). Creep lifetime: 59 × 10^3h, temperature: 500°C, applied stress: 250 MPa.

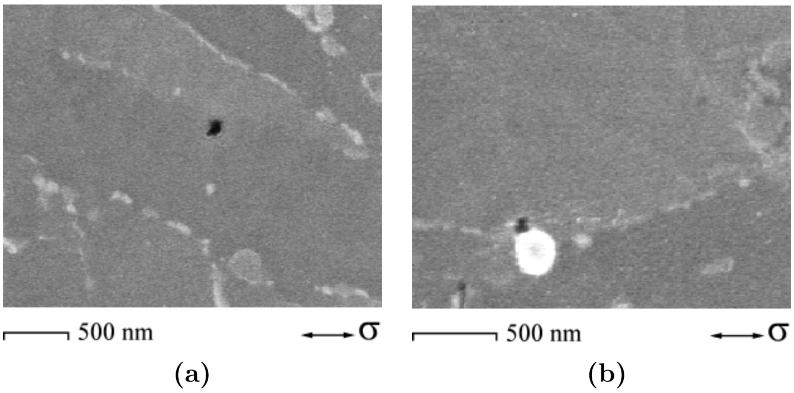

Figure 5.9: Cavities located at (a) a triple junction of block boundaries (a size of 120 nm) and (b) at Laves phase-matrix interface (size of 80 nm). Creep lifetime: 5 × 10^3h, temperature: 600°C, applied stress: 125 MPa.

account stress concentrations computed using the finite element method in the viscoplasticity framework.

After our observations together with the literature [4,21], an amount of cavities seem to have approximately spherical shapes (Figs. 5.2 and 5.1) and the others have complex shapes. For the modelling of cavity growth, all cavities are assumed to have spherical shapes. They are assumed to be located at FAGBs/packet/block boundaries perpendicular to the loading axis without particles. The measured cavity density and the average deduced distance between cavities will be used as parameters of this modelling. The predicted cavity sizes will be compared with the measured ones.

For the modelling of cavity nucleation, nucleation sites at FAGBs/packet/block boundaries without particles will be first considered. The results will be then compared with the modelling of cavity nucleation at particle-matrix interfaces.

5.2 Modelling of cavitation along matrix boundaries

In this section, cavitation along FAGBs/packet/block boundaries almost perpendicular to the loading axis is modelled using analytical approaches previously discussed. The stress heterogeneity induced by the various crystallographic orientations of the matrix crystals is not considered. The local normal stress acting on considered boundary is assumed to be equal to the macroscopic uniaxial stress.

5.2.1 Diffusion data of tempered martensitic chromium steels

Self-diffusion coefficients along FAGBs, D_b, and in the bulk, D_v, have been measured by Huntz and co-workers [120–122] for tempered martensitic steels with chromium content ranging from 6.8% to 9.1% in weight. Ahrrenius parameters for self-diffusion coefficients are reported in Table 5.6. These parameters values are given for temperature ranges with lower bounds close a temperature under study, 600˚C, and higher than another one (500˚C) by an amount between 100 and 150˚C. An extrapolation out of the temperature range of measurements could lead to an error in value of self-diffusion coefficients. Its effect on the modelling of cavitation will be checked.

Table 5.6: Ahrrenius parameters for self-diffusion coefficients along grain boundaries and in the bulk for tempered martensitic steels [120–122].

Diffusive atom	Cr (wt.%)	$D_{b0}\delta$ ($\mathrm{m^3s^{-1}}$)	Q_b ($\mathrm{kJ.mol^{-1}}$)	D_{v0} ($\mathrm{m^2s^{-1}}$)	Q_v ($\mathrm{kJ.mol^{-1}}$)	T range (˚C)
Fe	6.8	8.2×10^{-10}	234.3	3.56×10^{-1}	309.6	$650 - 800$
	7.8	8.41×10^{-12}	205.9	2.48×10^{-3}	267.6	$659 - 771$
	8.9	8.65×10^{-2}	402.4	1.11×10^{-1}	305.4	$652 - 808$
	9.1	1.01×10^{-8}	254	1.88	326.4	$652 - 808$
Cr	9.1	8.36×10^{-8}	271	8.49×10^{1}	355.6	$623 - 827$

Figures 5.10a and 5.10b show the evolution of both $D_b\delta$ and D_b with respect to the chromium content. For 9.1%Cr steel, the two points on the vertical line represent the

diffusion coefficients of either Fe or Cr atoms in Fe-9.1%Cr. The self-diffusion coefficients of both atoms differ by a factor lower than 2. The values of $D_b\delta$ measured in 9.1%Cr steel differ from the ones measured in 6.8%Cr and 7.8%Cr steels by a factor lower than 3. Exceptionally, the values of $D_b\delta$ in 8.9%Cr steel are lower than the ones measured in 9.1%Cr steel by a factor about 1000 at 500°C and respectively by a factor about 30 at 650°C. However, the values of D_v measured in both steels are not significantly different. Since, only 8.9%Cr steel which does not exhibit a clear martensitic microstructure [122], presents a fairly different diffusion behaviour along boundaries with regards to the other chromium steels, only the values of $D_b\delta$ measured for diffusion of Fe atom in 9.1%Cr steel will be used.

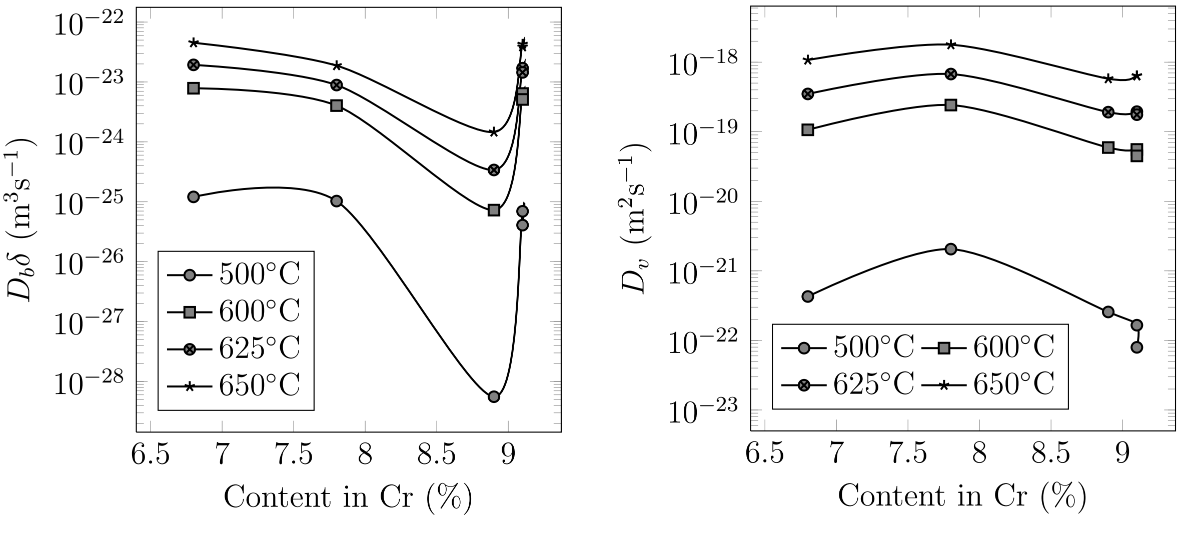

(a) **(b)**

Figure 5.10: Diffusion coefficients in function of contents in Cr for (a) grain boundary diffusion and (b) volume diffusion given from [120–122].

5.2.2 Dominant mechanism predicted with Rice length

Figure 5.11 shows comparisons between the diameter deduced from the Rice length (Eq. (4.20)), $2L_R$, and the measured cavity diameter after creep lifetimes. For the creep test at 500°C under 230 MPa (160 kh), the ratio of the measured maximum size (3.5 µm) to the Rice diameter is 0.24. This value is close to the lower of the range (ratio between 0.2 and 20) where the cavity growth is influenced by both mechanisms of self-diffusion and viscoplasticity. The viscoplasticity effect is assumed to be still low at this ratio (i.e. 0.2). Besides, the relative probability of the cavity size to be 3.5 µm is very low ($\approx$ 0.07%, see Fig. 5.5), whereas most of the cavities have a diameter lower than 2 µm leading to a ratio lower than 0.2. Therefore, the dominant mechanism of cavity growth is considered to be self-diffusion alone for this creep test. For three creep tests, one at 500°C under 250 MPa (59 kh) and two others at 600°C under 90 MPa (94 kh) and 125 MPa (5 kh), the ratio of the maximum measured diameter to the Rice diameter are lower than 0.2.

Finally for all creep tests considered here, based on Rice predictions [110] the dominant mechanism of cavity growth is assumed to be diffusion.

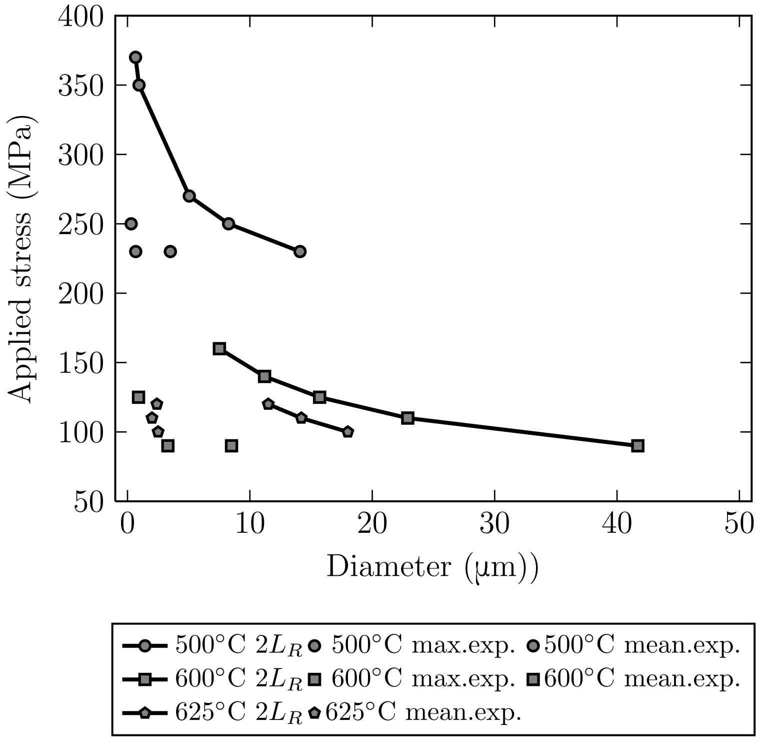

Figure 5.11: Comparison between cavity diameter predicted using the Rice length ($2L_R$) and the measured maximum and average diameters of cavities.

5.2.3 Diffusion growth of cavities

a. Parameter values for the modelling

The observations carried out for the creep specimens in the present study show that cavitated facets are uniformly distributed within the microstructure. Thus, constraints on diffusion cavity growth are not taken into account in the modelling.

Two models are used to predict diffusion cavity growth. The first one was proposed by Raj and Ashby by assuming instantaneous nucleation, see Eq. (4.31). This model requires the knowledge of an influential parameter, $2L$, which is the average distance between cavities along boundaries. This parameter is taken as the average distance between cavities on observed cross-sections reported in Table 5.4. The second model proposed by Riedel assuming continuous nucleation along the creep tests are represented by two Riedel bounds given in Eq. (4.41). This model requires the knowledge of the parameter of the Dyson nucleation law, $\dot{N}_0$ (see paragraph d of section 4.2.2), which is supposed to be equal to N_m/t_f. Measured values of N_m for the creep tests under study are given in Table 5.4. Here, we use an approximation that $N_a \approx N_m$ since this leads to a low difference in L.

The failure criterion is supposed to be based on the critical area fraction of cavities (or critical amount of damage), $\overline{\omega}_f$. After the measurements of the area fraction of cavities in zones close to fracture surfaces of Grade 91 creep specimens loaded at 625°C [4], $\overline{\omega}_f = 0.1$. Similar values were also used by Koplik and Needleman [92] as critical amount of damage above which their model expected a very quick viscoplasticity growth of damage up to failure.

b. Prediction of time to failure by diffusion cavity growth

Predicted times to failure at 500°C and 600°C are plotted in Figs. 5.12 and 5.13. Parameters L and $\dot{N}_0$ were taken from the measurements for the creep tests at 500°C under 230 MPa (160 kh) and 600°C under 90 MPa (94 kh), see Table 5.5. These values were also used for the prediction at lower and higher stress. Lifetimes predicted using the Raj and Ashby model as well as by the Riedel bounds are longer than the experimental lifetimes. The lifetimes predicted using the first model are longer than the ones predicted using the Riedel upper bound by less than 30%. The lifetimes predicted using the Riedel lower and upper bounds differ by less than 50%. The predictions using the Riedel bounds are proportional to $(\sigma^{eng})^x$ with $x = -0.4$. This can be deduced from Eq. (4.41) considering a constant value of $\dot{N}_0$ at each temperature.

c. Prediction of the time evolution of the average cavity diameter

The evolution of the average cavity diameter during the creep tests at 500°C under 230 MPa and at 600°C under 90 MPa were predicted using the Raj and Ashby model as well as using the Riedel bounds. The results are illustrated in Figs. 5.14a and 5.14b.

The cavity diameter predicted at times equal to the experimental lifetimes using the Raj and Ashby model is in good agreement with the maximum measured diameter. But, it is 4 times larger than the measured mean diameter for the creep test at 500°C under 230 MPa, and respectively 3 times larger for the one at 600°C under 90 MPa. The model seems to correctly predict first cavities to have nucleated.

The cavity diameter predicted using the Riedel upper bound is about 2 times larger than the prediction using the Riedel lower bound. The Riedel upper bound approximately correctly predicts the maximum cavity size, whereas the lower bound approximately correctly predicts the mean cavity size. The cavity diameter predicted using the Riedel upper bound are slightly higher (by 10% after 160 kh at 500°C, and 15% after 94 kh at 600°C) than the one predicted using the Raj and Ashby model. Indeed, the Riedel upper bound considers a lower bound of size growth rate in order to simplify the resolution of the differential equations (see section 4.2.2). This lower bound is higher than the size growth rate given by the Raj and Ashby model.

d. Size distribution of cavities predicted using the Riedel bounds

The size distribution of cavities predicted using the Riedel bounds are compared with the ones given from the experimental measurements (Fig. 5.15). The predicted cumulative probabilities were assumed to be power functions of cavity size in order to be able to solve analytically the coupled problem. Following the predicted distributions, the predicted cavity sizes are globally larger than the measured ones with a factor of 2 or 3. This is probably due to the overestimation of the boundary normal stress by the tensile stress. The agreement between the predictions and the measurements is better for the creep test at 600°C under 90 MPa than for the one at 500°C under 230 MPa.

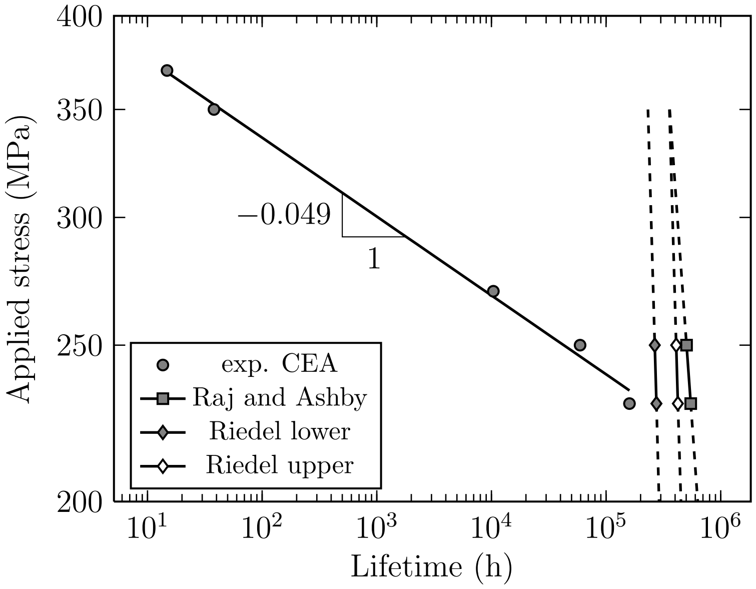

Figure 5.12: Comparison between experimental lifetime at 500°C (CEA) and times to failure predicted using the Raj and Ashby model and using the Riedel bounds. The values of L and $\dot{N}_0$ were evaluated from the observations of the specimen loaded at 500°C and 230 MPa (the values are slightly different at 500°C and 250 MPa).

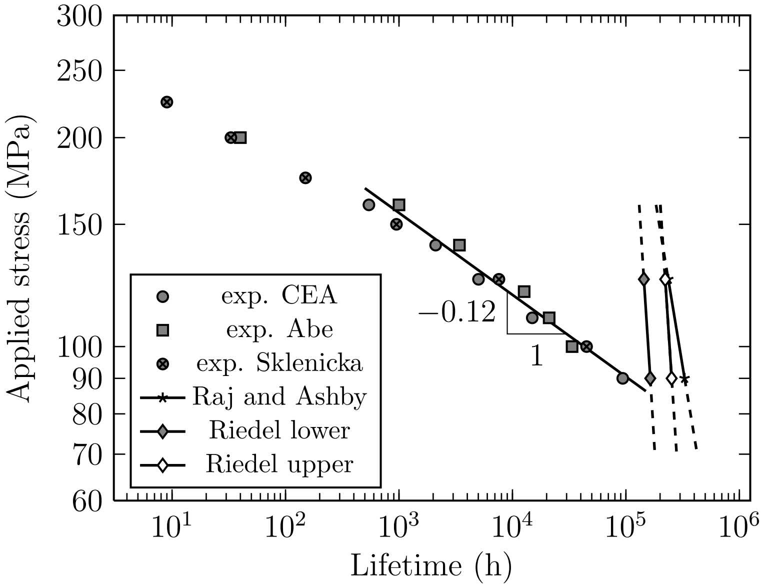

Figure 5.13: Comparison between experimental lifetime at 600°C, after creep experiments at CEA and ones reported in [4, 8, 73], and times to failure predicted using the Raj and Ashby model and using the Riedel bounds. The values of L and $\dot{N}_0$ were evaluated from the observations of the specimen loaded at 600°C and 90 MPa (the values are slightly different at 600°C and 125 MPa).

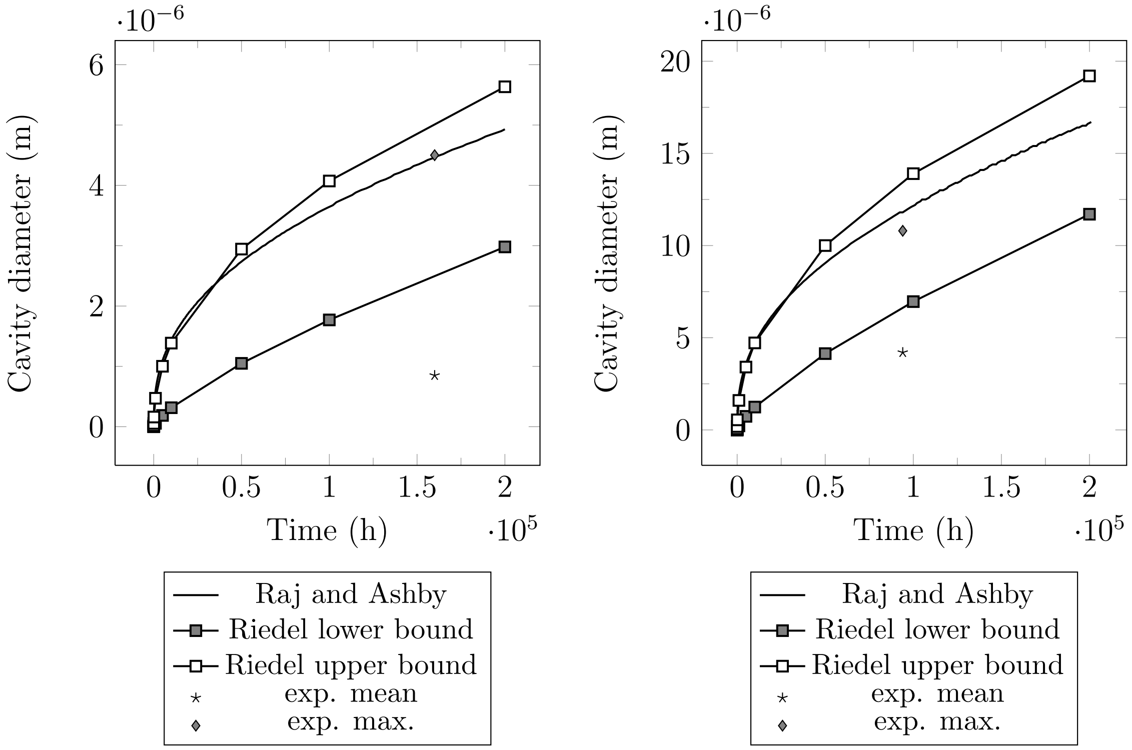

(a) **(b)**

Figure 5.14: Comparisons between the measured maximum and average values of diameter and the diameter predicted using the Raj and Ashby model and using the Riedel bounds. (a) 230 MPa at 500˚C and (b) 90 MPa at 600˚C. Corrected experimental values to take into account 3D shape of cavities (measured 2D size times a factor $4/\pi$).

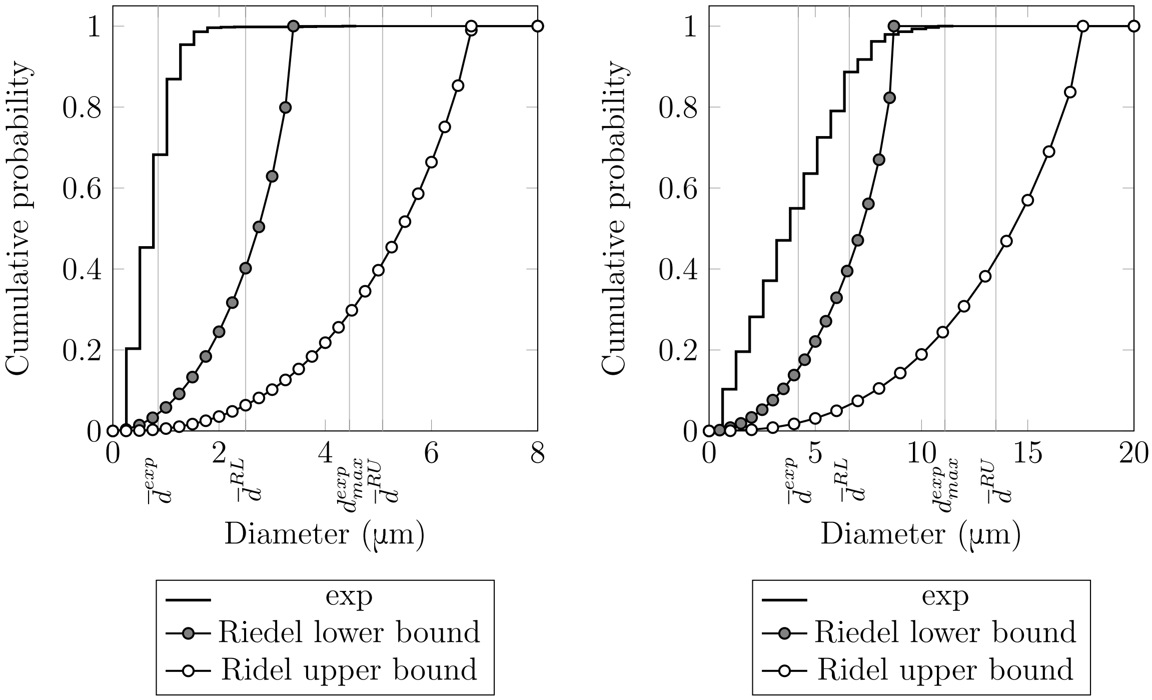

(a) **(b)**

Figure 5.15: Comparisons between the experimental size distributions and the ones predicted using the Riedel bounds for the creep tests at (a) 230 MPa at 500°C and (b) 90 MPa at 600°C. Mean experimental diameter: $\overline{d}^{exp}$, maximum experimental diameter: d^{exp}_{max}, mean diameter predicted using respectively the Riedel lower and upper bounds: $\overline{d}^{RL}$, $\overline{d}^{RU}$.

5.2.4 Sensitivity of model predictions of cavity growth to the values of model parameters

Predictions of cavity growth could be sensitive to the values of parameters $D_b\delta$, $\overline{\omega}_f$, L, and $\dot{N}_0$. The self-diffusion coefficient in grain boundaries, $D_b\delta$, generally varies following different authors. Scatter of diffusion coefficients measured in [120–122] could lead to a value of $D_b\delta$ 5 times lower or greater. If nucleation of cavities along FAGBs is considered, distance $2L$ between cavities could vary between 10 and 60 µm (range of former austenitic grain size). The critical area faction of cavities, $\overline{\omega}_f$, could vary and be lower than 10% [4,89] or possibly higher. To study its effect on predictions of cavity growth, $\overline{\omega}_f$ is assumed to range within 0.1 ± 0.05. Uncertainty of cavity quantification is assumed to cause a variation in $\dot{N}_0$ by a factor 1/2 or 2.

The sensitivity of the two cavity growth models, Raj and Ashby model and Riedel bounds, to the individual values of their parameters is studied in relationship with the predictions for the creep tests at 500°C under 230 MPa and at 600°C under 90 MPa (Table 5.7).

For the Raj and Ashby model, if $\overline{\omega}_f$ varies by −50% or +50%, the predicted lifetime becomes respectively 2 times shorter or 1.5 longer than in the reference case. If the value of $D_b\delta$ changes by a factor 5 or 1/5, the predicted lifetime increases or decreases by a factor 5. Then, the predicted cavity diameter is respectively 1.4 times smaller or 2 times larger than in the reference case. At 500°C under 230 MPa, for $2L = 10$ µm (to be compared with the measured value, 25 µm) the predicted lifetime becomes 15 times shorter. Instead, the predicted lifetime only increases by 40% for $2L = 60$ µm. At 600°C under 90 MPa, for $2L = 10$ µm (to be compared with the measured value, 67 µm) t_f becomes 280 times shorter, and instead reduces by 30% for $2L = 60$ µm. The Raj and Ashby model seems to be less sensitive to the increasing value of L than to the decreasing one.

For the Riedel bounds, the variations in predicted lifetime and in cavity size due to the variation in parameters can be estimated directly from Eqs. (4.41) and (4.42). If the value of $\overline{\omega}_f$ varies by −50% or +50%, lifetimes predicted using the Riedel bounds reduce by 30% or increase by 20%. If the value of $D_b\delta$ is 5 times lower or greater, the predicted lifetime becomes approximately 2 times longer or shorter respectively. The predicted cavity diameter becomes respectively 2 times smaller or larger. If the value of $\dot{N}_0$ is 2 times lower or greater, the predicted lifetime respectively increases or reduces by 30%. The change in cavity diameter predicted using the Riedel lower bound is of −20% or +20%, and respectively of −5% or +5% for the upper bound.

In conclusion, the Riedel bounds are less sensitive to the values of parameters $D_b\delta$, $\overline{\omega}_f$ and L with regards to the Raj and Ashby model. The Riedel bounds represent therefore advantages with respect to robustness. As in addition their physical basis are stronger than the ones of the Raj and Ashby theory, they should be preferred.

The Riedel model requires the knowledge of cavity nucleation rate that is at present determined from the experimental measurements. In the following section, this one is predicted using the Raj nucleation model.

Table 5.7: Sensitivity of predictions of lifetime and cavity size to the values of model parameters. Reference values: $\overline{\omega}_f = 0.1$, $2L = 25$ µm at 500°C and 67 µm at 600°C, $\dot{N}_0 = 2.8$ m^{-2}s^{-1} at 500°C and 0.65 m^{-2}s^{-1} at 600°C , $D_b\delta$ determined from Table 5.6 (for diffusion of Fe in 9.1%Cr steel). The studied creep tests: (1) at 500°C under 230 MPa and (2) at 600°C under 90 MPa. (3): Riedel lower bound, (4) Riedel upper bound.

		Raj and Ashby		Riedel bounds	
		Lifetime	Cavity size	Lifetime	Cavity size
$D_b\delta$	1/5 times	1/5 times	1/1.4 times	2 times	1/2 times
	5 times	5 times	2 times	1/2 times	2 times
$\overline{\omega}_f$	−0.05	1/2 times	unchanged	−30%	unchanged
	+0.05	1.5 times	unchanged	+20%	unchanged
L	10 µm	$\frac{1}{15}$ $^{(1)}$, $\frac{1}{280}$ times$^{(2)}$	-		
	60 µm	+40%$^{(1)}$, −30%$^{(2)}$	−20%$^{(1)}$, +3%$^{(2)}$		
$\dot{N}_0$	1/2 times			+30%	−20%$^{(3)}$, −5%$^{(4)}$
	2 times			−30%	+20%$^{(3)}$, +5%$^{(4)}$

5.2.5 Nucleation of cavities

First, spherical cavities are assumed to nucleate along boundaries perpendicular to the loading axis. Incubation times predicted using the Raj model after Eq. 4.17 are presented in Figs. 5.16a and 5.16b. At 500°C under 230 and 250 MPa, the predicted incubation times are respectively equal to 2% and 4% of the corresponding experimental lifetimes. These incubation times correspond to creep stage I. For two shorter creep tests carried out under applied stress of 350 and 370 MPa, the predicted incubation times are longer than the corresponding experimental lifetimes. For the creep tests at 600°C under 90 and 110 MPa, the predicted incubation times belong to creep stage I. For creep tests at 600°C under 125 and 160 MPa, the predicted incubation lifetimes correspond to the beginning of creep stage II. These predicted times are in agreement with the observations of cavities in all the considered specimens.

The nucleation rate is predicted using Eq. (4.14) with $F_v = \frac{4\pi}{3}$ for spherical cavities for creep tests at 500°C under 230 MPa and at 600°C under 90 MPa. The results show that using such high theoretical value of F_v leads to a predicted nucleation rate practically equal to zero for both creep tests.

Cavities of type B (Fig. 4.7b) suggested by Raj [99] to have the highest nucleation probability are now considered. They are assumed to have nucleated at $M_{23}C_6$ interfaces following the observations on the specimen loaded at 500°C under 250 MPa. The effect of segregation of S and P leads to a reduction in γ_s to 1.42 Jm^{-2} [118]. The free surface energy of $M_{23}C_6$ is given in [123] as $\gamma_I = 1.1$ Jm^{-2}. The grain boundary energy is $\gamma_b = 1.7$ Jm^{-2} for general boundaries [124] and the precipitate-matrix interface energy value, γ_{Ib}, ranges between 0.5 and 1 Jm^{-2} for incoherent interfaces of precipitates [124]. Angles α and α_I (Fig. 4.7b) could be deduced from these energy values, whereas angle α_{Ib} is assumed to be equal to 90° following numerous observations. Using Eqs. (4.2), (4.5), (4.6)

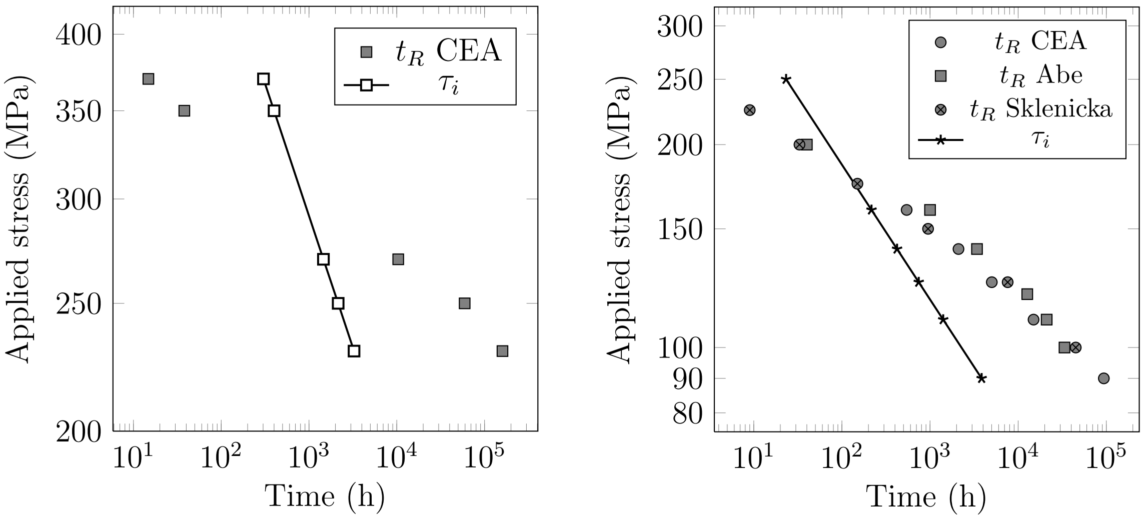

(a) 500°C **(b)** 600°C, t_R given from CEA tests and in [6, 73]

Figure 5.16: Incubation times predicted using the Raj model given by Eq. (4.17), for spherical shapes with $F_v = \frac{4\pi}{3}$.

and (4.8), the value of F_v is minimized to be 0.18. By using this value, the predicted nucleation rates are still negligible.

The geometry factor, F_v, is adjusted to predict the final densities of cavities in agreement with the measured ones. Cavities of type B nucleated at $M_{23}C_6$ interfaces located along boundaries are assumed. The maximum density of nucleation sites, N_a^{max}, is evaluated by assuming that the average distance between $M_{23}C_6$ carbides is equal to the average block size (2 µm [24]). This leads to a value of N_a^{max} equal to 0.25 µm^{-2}. The adjusted values of F_v are reported in Table 5.8.

Table 5.8: Comparison between cavity densities measured after creep tests and predictions using Eq. (4.14) and the adjusted values of the geometry factor F_v.

T (°C)	Stress (MPa)	Lifetime (h)	N_a^{exp} (µm^{-2})	F_v	N_a^{Raj} (µm^{-2})
500°C	230 MPa	160×10^3	1.53×10^{-3}	4.1×10^{-4}	2.09×10^{-3}
600°C	90 MPa	90×10^3	4.24×10^{-5}	8.7×10^{-5}	2.78×10^{-5}

These adjusted values of F_v are now used to predict the incubation time using Eq. 4.17. For the creep tests at 500°C under 230 MPa and 600°C under 90 MPa, the predicted incubation time is lower than one second. The steady-state nucleation regime is thus predicted to be quickly reached. However, the corresponding predicted nucleation rates are respectively 1.3×10^{-8}µm^{-2}h^{-1} and 3×10^{-10}µm^{-2}h^{-1}. At this incubation time, the predicted cavity density is very low and cause a difficulty for detection of cavities.

The obtained values of F_v were adjusted by assuming that σ_n at the precipitate-matrix interface is equal to the uniaxial macroscopic stress, σ^{eng}. At this location, stress concentrations could occur and that may lead to lower adjusted values of F_v.

5.2.6 Effect of stress concentrations at precipitate-matrix interfaces on the adjusted value of F_v

A 2D plane strain finite element model was used to compute stress concentrations at the interface of a precipitate with the matrix. The linear isotropic elasticity flow rule was used to model the mechanical behaviour of the precipitate and respectively an isotropic viscoplasticity flow rule defined in RCC-MRx code [36] for modelling the creep flow of the matrix. The parameters of this one were readjusted to represent correctly the uniaxial $\varepsilon^{eng}(t)$ curves of creep tests under study (section 8.1.2). The size of the matrix is 10 times larger than the precipitate diameter.

The distribution of computed axial stress is plotted in Fig. 5.17. These normal stress fields at the interface of the precipitate with the matrix increase by 50% with respect to the applied macroscopic stress, σ^{eng}. Two values of Young's modulus were used, but both corresponding results differ slightly (Table 5.9).

The computed value of stress concentrations, 1.5, is now used to readjust the values of F_v for the creep tests in the present study. The readjusted values of F_v are 2.25 times lower than the previous ones adjusted considering the macroscopic uniaxial stress (Table 5.8). However, these values are still higher than the theoretical value by 3 to 4 orders of magnitude.

Table 5.9: Computed normal stress at the precipitate-matrix interface with respect to the applied engineering stress. $\sigma^{eng} = 90$ MPa, temperature: 600°C, creep time: 94×10^3h.

Young modulus (GPa)		
Inclusion	Matrix	Normal stress
151	151	$\Sigma_n + 50\%$
200	151	$\Sigma_n + 52\%$

5.3 Discussion

Diffusion-induced creep cavities were observed in Grade 91 steel at least after a lifetime of 59×10^3 h at 500°C and respectively 5×10^3 h at 600°C. The values of area fraction of cavities for these lifetimes are much lower than the ones measured for lifetimes of 160×10^3 h at 500°C and 94×10^3 h at 600°C, for which the area porosities are respectively 6.9×10^{-4} and 2.5×10^{-3}. These values of area porosity lead to an increase in creep strain rate of less than 2.5%, assuming a stress exponent of 20.35 at 500°C and 9.9 at 600°C and using continuous damage mechanics (see chapter 3). Therefore, necking kinetics is almost unaffected.

For applying the cavity growth models, cavities were assumed to have spherical shapes and to be located along boundaries perpendicular to the loading axis. Numerous nucleation cases were observed at $M_{23}C_6$ carbides (one case in 12%Cr steel [21]) as well as at Laves phases. The assumption of the spherical shape is valid as soon as the cavity size reaches the typical size of carbides (100 nm). The stress heterogeneity due to spherical carbides may lead to an excess of 50% over the local normal stress with respect to the

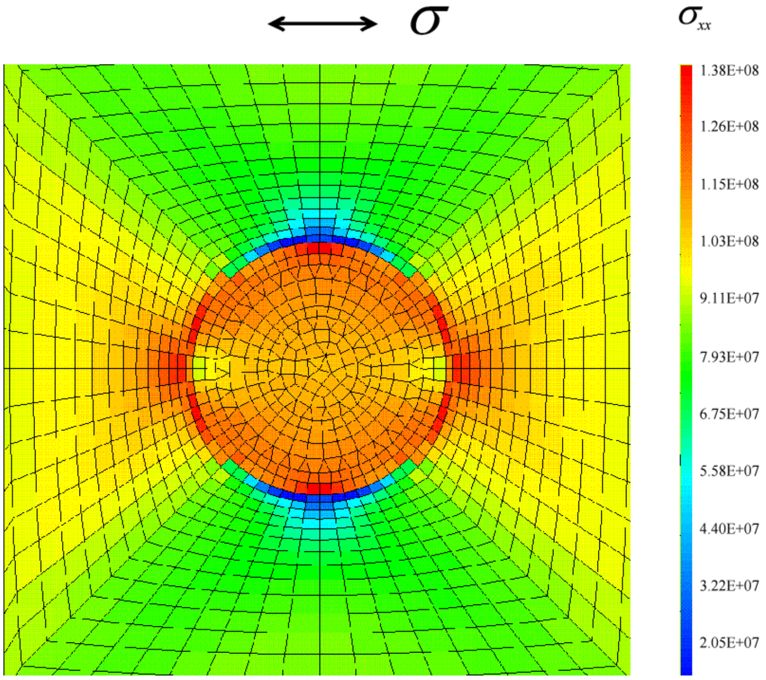

Figure 5.17: Axial stress distribution given in Pa. Horizontal loading axis. Stress: 90 MPa, temperature: 600°C, creep time: 94×10^3h.

macroscopic stress (Fig. 5.17). This leads to a reduction of 30% in lifetime predicted using the Raj and Ashby model, and only of 15% in lifetime predicted using the Riedel bounds. It can be noticed that the Riedel bounds are less sensitive to the parameters ($D_b\delta$, $\overline{\omega}_f$, L) than the Raj and Ashby model (see section 5.17).

Cavities located at boundaries but far from carbides have a low nucleation probability which yields a negligible density according to the Raj model. Similarly, the use of literature data [118] leads to similar conclusions for nucleation close to precipitates. Type-B cavities located at carbide-matrix interfaces, with adjusted geometry parameter $F_v = 4.1 \times 10^{-4}$ at 500°C and $F_v = 8.7 \times 10^{-5}$ at 600°C, could be nucleated at a rate leading to final densities in agreement with the measured ones (based on creep tests at 500°C under 230 MPa and at 600°C under 90 MPa). However, the local stress heterogeneity that could occur within the microstructure such at triple junctions of FAGBs and at carbide-matrix interface is not taken in account. Indeed, an excess of 50% over the normal stress due heterogeneity, for the creep tests at 500°C under 230 MPa and at 600°C under 90 MPa, could lead to predicted nucleation rate of 4×10^9 and 5×10^{11} times higher using the Raj formula and the adjusted values of F_v. In the other words, readjusted values of F_v are lower.

The use of a stress concentration factor of 1.5 obtained using the finite element computations previously described leads to an increase in the predictions of Rice length of only 15%. Therefore, the assumption of diffusion-induced cavity growth is still valid.

Conclusions

Creep cavities were observed at least after lifetimes of 59×10^3 h at 500°C and 5×10^3 h at 600°C, but the measured area fraction of cavity is very low. After lifetimes of 160×10^3 h at 500°C and 94×10^3 h at 600°C, the area fraction of cavities is higher but leads to an increase of less than 2.5% (for $n = 10$) in creep strain rate using the continuum damage approach. Therefore, necking is still the dominant mechanism in such loading conditions.

Times to failure predicted using the Raj and Ashby model as well as using the Riedel bounds (not coupled from any effects induced by necking) are longer than experimental lifetimes up to 160×10^3 h at 500°C and 94×10^3 h at 600°C. Indeed, in these lifetime ranges, failure was observed to be induced mainly by necking. The Raj and Ashby model allows fair predictions of the maximum diameter of cavities, whereas the average diameter predicted using the Riedel bounds ranges between the mean measured size and the maximum measured size of cavities. The Riedel bounds are more stable than the Raj and Ashby model with respect to the values of model parameters (within the range studied here).

Following the Raj nucleation theory, the nucleation probability is higher for cavities located at intergranular carbide-matrix interfaces with regards to cavities simply located at boundaries. However, the cavity density could be correctly predicted only using adjusted values of the cavity geometry parameter, $F_v = 4.1 \times 10^{-4}$ at 500°C and 8.7×10^{-5} at 600°C.

Stress heterogeneity could affect strongly cavity nucleation. Using the adjusted values of F_v, nucleation rate becomes strongly dependant on stress which is in contrast with the observations carried out by Dyson and McLean [89].

Following the 2D plane strain finite element model, the local stress at precipitate-matrix interfaces could reach 1.5 times the macroscopic uniaxial stress. This leads to a decrease in adjusted value of F_v by 2.25 times. However, the readjusted values of F_v are still higher than the theoretical value by 3 or 4 orders of magnitude.

Another stress heterogeneity is due the forms neighbouring blocks or grains and their different crystal orientations which induce strain incompatibilities and local stress concentrations at the boundaries. In the next part, stress heterogeneity at triple junctions of block boundaries or FAGBs will be studied in details using finite element simulation taking into account crystal viscoplasticity.

Part IV

Contribution of Finite Elements Analysis

Résumé

Une singularité logarithmique de contrainte au point triple en thermoélasticité est obtenue d'après la littérature. Des calculs par éléments finis en élasto-viscoplasticité cristalline de la concentration de contrainte locale près des points triples sont menés afin de prédire son influence sur la germination des cavités pour deux essais de fluage de durées de vie de 160 kh à 500°C et 94 kh à 600°C. Les paramètres d'une loi viscoplastique cristalline utilisée sont ajustés en utilisant des simulations des courbes de fluage de larges agrégats poly-cristallins le plus possible en accord avec les courbes expérimentales. La distribution des contraintes moyennes par bloc, contraire à celle des déformations moyennes par bloc, est stable par rapport au raffinement du maillage, au nombre de blocs et aux valeurs des paramètres choisies. Des calculs en déformation plane en utilisant des microstructures construites par un modèle simple de point triple ainsi que construites par des mesures à l'EBSD. Le modèle de point triple tenant compte des orientations aléatoires des blocs permettent de représenter approximativement de manière correcte les contraintes normales aux joints de blocs près des points triples construits par des mesures à l'EBSD. Un facteur de concentration de contrainte près des points triples maximum de 2 est estimée en utilisant le modèle de point triple tenant compte des orientations aléatoires. Tenant compte de l'hétérogénéité géométrique des points triples et le facteur géométrique théorique des cavités, les densités de cavités finales prédites par le modèle de germination de Raj ne sont même pas au même ordre de grandeur que les mesures en FEG-SEM. En utilisant le facteur géométrique théorique des cavités, un facteur de concentration de 20 voire 50 est requis pour des prédictions valables par le modèle de Raj.

Mots clés : point triple, concentration de contrainte locale, singularité de contrainte, viscoplasticité cristalline, dislocation, activation thermique, géométrie des blocs, orientation cristallographique.

Introduction

In the previous part, the normal stress acting on grain boundaries was assumed to be the driving force of cavitation. The normal stress was supposed to be equal to the macroscopic stress, which is only an approximation. In reality, mechanical fields are heterogeneous at block, packet or former austenitic grain boundaries and triple junctions, including normal stress. This is due to the difference in crystal orientation and grain geometries which induces strain incompatibility [125, 126]. A study of the normal stress field at block/packet/former austenitic grain boundaries and triple junctions has been performed by finite element analysis in the crystal elasto-viscoplasticity framework. Our aim is to predict stress fields and distributions at triple junctions as well as their effect on cavity nucleation. This study is applied to two long-term creep tests with lifetimes of 160×10^3h at 500°C and 90×10^3h at 600°C as described previously.

Chapter 6 is a literature survey on finite element simulation of polycrystalline aggregate deformation in the crystal elasto-viscoplasticity framework. The chapter describes studies of stress heterogeneity in polycrystalline aggregates and the choice of crystalline viscoplasticity constitutive equations for our study.

Chapter 7 presents the adjustment of the crystal viscoplasticity parameters based on the prediction of the macroscopic uniaxial creep strain curves. Creep curves of large polycrystalline aggregates made of cubic blocks having random crystal orientations are computed. The stress and strain sensitivity with respect to mesh refinement, the number of blocks and the values of constitutive parameters are also discussed. These parameters are needed for computing the stress fields around triple junctions and block boundaries.

Chapter 8 focuses on the normal stress at block boundaries obtained by finite element computations assuming a quasi plane strain hypothesis. Firstly, a basic microstructure containing a triple junction whose neighbouring blocks have random crystal orientations is used. Then, computations are carried out on actual microstructures meshed from EBSD maps. The stress concentration effect on the prediction of cavity nucleation is then discussed.

Finally, conclusions on the stress concentration effect on cavity nucleation is given at the end of this part.

Chapter 6

Literature review on polycrystal models

6.1 Stress and strain concentrations at polycrystalline grain boundaries

Nucleation of cavities has been observed by Caré and Zaoui [127] at polycrystalline triple points of a Zr alloy subjected to tensile test at room temperature (Fig. 6.1). These authors used an analytical model to compute stress singularity at triple points. They assumed uniform free strain in each grain. The internal stress field was calculated according to an elastic accommodation assumption; it is derived by superposition of the stress field contributions associated with each uniform grain boundary. They showed that the model predicts a logarithmic stress singularity close to triple points. Thermoelastic stress singularities close to free surface at the boundary between two anisotropic elastic materials emerging at the free surface and having different elasticity constants were also computed in [128]. The results showed that stress singularities were obtained as an inverse power law function of the distance to the boundary between both materials [128].

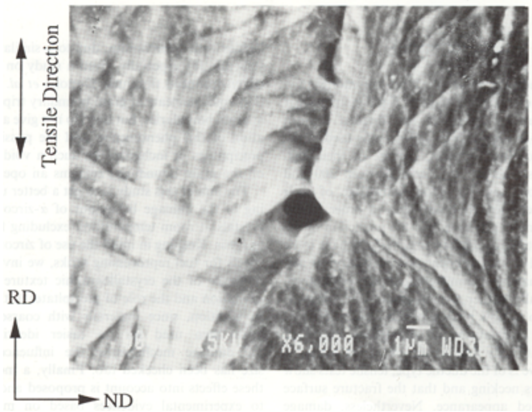

Figure 6.1: Cavity located at a polycrystalline triple point of a Zr alloy observed by Caré and Zaoui [127] at a tensile strain of 24% and room temperature. Many slip bands are observed and the strain field is heterogeneous around the triple point [127].

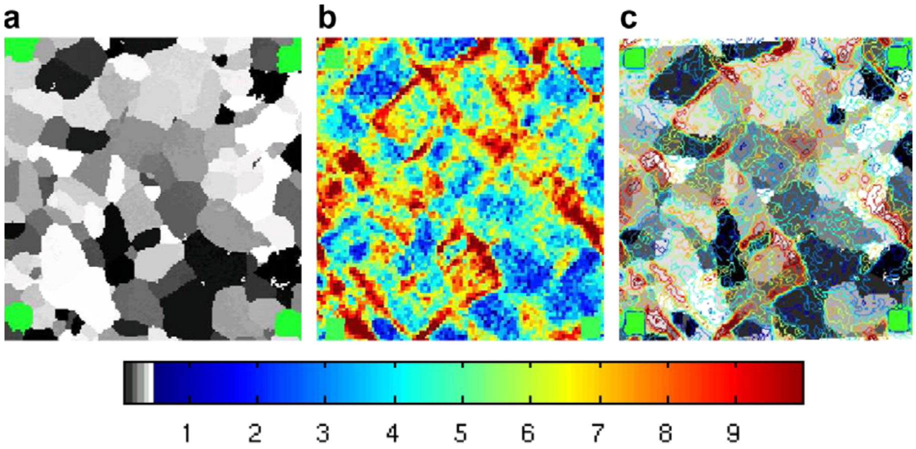

Figure 6.2: (a) Microstructure of zirconium built using EBSD measurements (the Schmidt factor is high in white grains and low in black grains) [129]. (b) Axial strain fields measured using microextensometry at a macroscopic strain of 2.5% at room temperature [129]. (c) Superposition of both experimental results [129]. The loading direction is horizontal.

However, the uniform plastic strain distribution in each grain supposed by [127] is not in agreement with SEM observations of the heterogeneity of plastic strain fields in each grain around triple points (Fig. 6.1). Localised strain at grain boundaries of zirconium polycrystals has also been observed and measured by Héripré et al. [129] using microextensometry as shown in Fig. 6.2. Computations based on uniform plastic strain in each grain lead to stress overestimations even at the macroscopic scale [130]. Santacreu [131] has carried out finite element modelling to compute stress fields at the interface of two materials. The first one is an isotropic elastic material and the second one is an isotropic elastoplastic material. His computations based on either plane strain, plane stress or axisymmetric hypothesis resulted in stress lower than the values predicted by the analytical models proposed in [132, 133] which suggested that the stress singularity increases linearly with increasing plastic strain.

Normal stress fields at grain boundaries of a Zr alloy have been computed by Diard et al. [125, 126] using finite element modelling of Voronoï polycrystalline aggregates (Figs. 6.3a and 6.4a). These aggregates were subjected to tensile tests. The first one was carried out at a strain rate of $10^{-5}\mathrm{s}^{-1}$ at room temperature [125] and the second one at a strain rate of $2 \times 10^{-4}\mathrm{s}^{-1}$ at 350°C [126]. The mechanical behaviour of Zr crystals was modelled by crystal elastoviscoplasticity constitutive equations. Hardening was taken into account and the viscoplastic slip rate was expressed by a power law dependence upon the viscoplastic potential [125,126]. Normal stress fields averaged along grain boundaries for both tensile tests were computed and are plotted in Figs. 6.3b and 6.4b. For the room temperature test, the average normal stress to grain boundaries perpendicular to the loading direction varies by ±50% with respect to the macroscopic tensile stress. For the second test, only the standard deviation was evaluated and equal to 10% of the macroscopic stress (for grain boundaries perpendicular to the loading direction). The standard deviation is generally lower than the real amplitude. Thus, for the second test, the amplitude of variation of the average normal stress may be not strongly different from the one computed for the first test. A rather large stress amplitude was found.

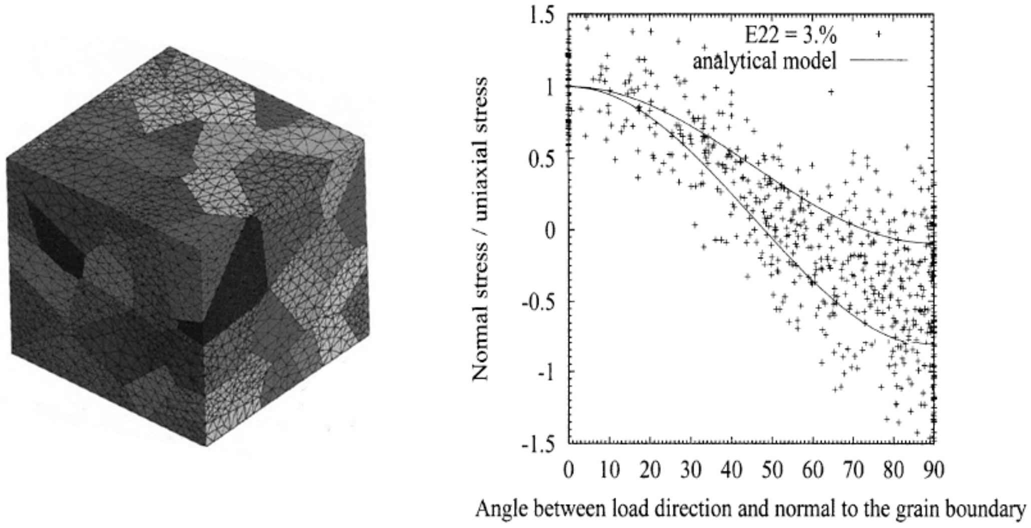

(a) (b)

Figure 6.3: (a) Voronoï polycrystalline aggregate containing 100 grains meshed by tetrahedral finite elements [125]. (b) Normal stress averaged along different grain boundaries in a Zr alloy subjected to a tensile test at a strain rate of 10^{-5}s^{-1} at room temperature, compared with an analytical model assuming uniform stress field in the whole polycrystal (upper curve) [125].

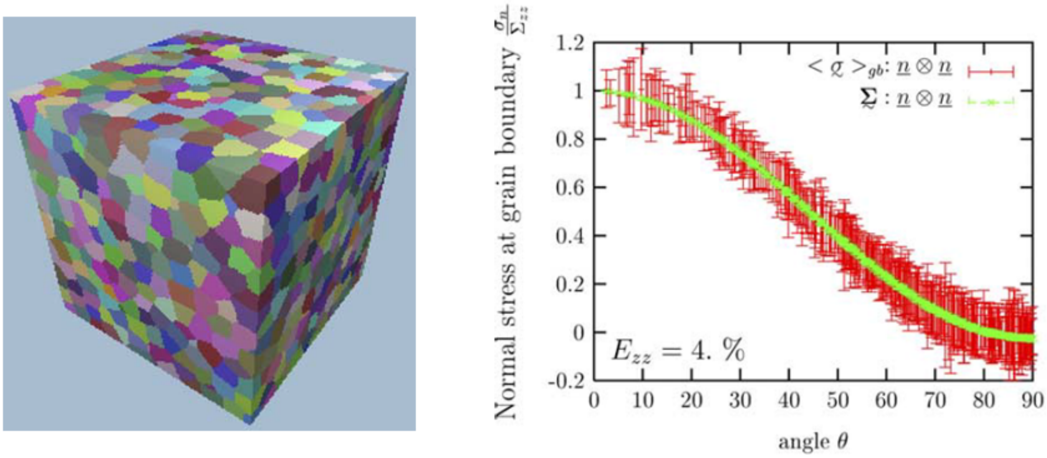

(a) (b)

Figure 6.4: (a) Voronoï polycrystalline aggregate containing 2197 grains meshed by cubic elements. (b) Normal stress averaged along different grain boundaries and standard deviations, in a Zr alloy subjected to a tensile test at strain rate of $2 \times 10^{-4}\text{s}^{-1}$ at 350°C [126].

The results on normal stress heterogeneity in polycrystalline aggregate given by Diard et al. [125,126] only concern monotonic tensile tests. Our study involves creep tests having lifetimes of 160×10^3h at 500°C and 94×10^3h at 600°C. These may yield a different ratio of the grain boundary normal stress to the macroscopic stress due to stress redistribution during creep. Diard et al. [125, 126] computed the normal stress averaged along grain boundaries. However, normal stress fields close to triple points could be even higher following [127, 129]. This problem will be studied using triple junction models and the finite element method in chapter 8.

6.2 Crystal elasto-viscoplasticity constitutive equations

6.2.1 Basic kinematics in the finite strain framework

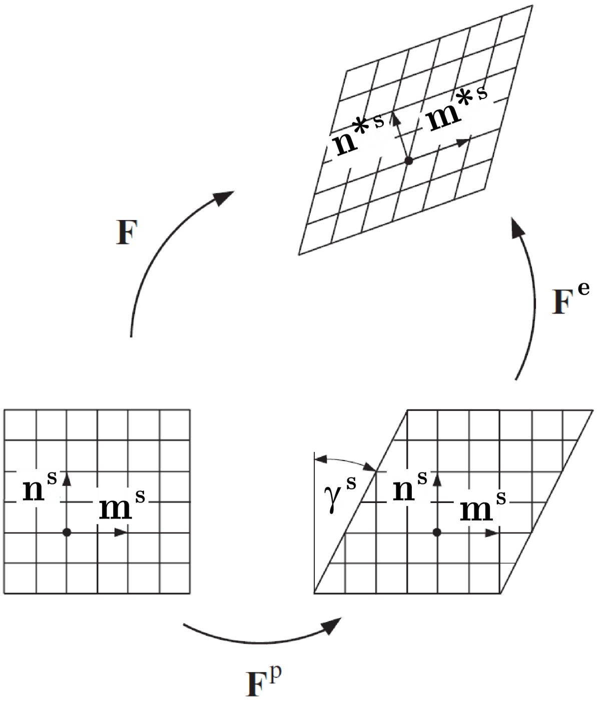

Figure 6.5: Kinematic model of elastoplastic transformation at the single crystal scale after [134].

In crystalline solids, a finite transformation is assumed to occur in two steps [134] (Fig. 6.5). In the first step, starting from the reference state (left side), the material flows by crystallographic slip, which gives the viscoplastic sliding gradient tensor $\dot{\underset{\sim}{\mathbf{F}}}^p$ (right bottom, intermediate configuration). Following this step, the material is deformed elastically from the intermediate configuration to the current configuration (top right). Thus, the transformation gradient is decomposed as:

$$\underset{\sim}{\mathbf{F}} = \underset{\sim}{\mathbf{F}}^e \cdot \underset{\sim}{\mathbf{F}}^p \tag{6.1}$$

The velocity gradient tensor due to the elasticity contribution, $\underset{\sim}{\mathbf{L}}^e$, the tensor of slip induced viscoplastic velocity gradient, $\underset{\sim}{\mathbf{L}}^{*p}$, and the total velocity gradient tensor, $\underset{\sim}{\mathbf{L}}$, are given by the following [134]:

$$\underset{\sim}{\mathbf{L}}^e = \dot{\underset{\sim}{\mathbf{F}}}^e \cdot \underset{\sim}{\mathbf{F}}^{e-1} \tag{6.2}$$

$$\underset{\sim}{\mathbf{L}}^{*p} = \underset{\sim}{\mathbf{F}}^e \cdot \dot{\underset{\sim}{\mathbf{F}}}^p \cdot \underset{\sim}{\mathbf{F}}^{p-1} \cdot \underset{\sim}{\mathbf{F}}^{e-1} \tag{6.3}$$

$$\underset{\sim}{\mathbf{L}} = \underset{\sim}{\mathbf{L}}^e + \underset{\sim}{\mathbf{L}}^{*p} \tag{6.4}$$

The Green-Lagrange strain tensor due to the elasticity contribution, $\underset{\sim}{\mathbf{E}}^e$, is given by Eq. (6.5) after [134]. The anisotropic elasticity constitutive equation is given by Eq. (6.6) [135], in which $\breve{\underset{\sim}{\boldsymbol{\sigma}}}$ is the Trusdell derivative of Cauchy stress tensor $\underset{\sim}{\boldsymbol{\sigma}}$, $\underset{\sim}{\mathbf{D}}^e$ is the symmetric part of $\underset{\sim}{\mathbf{L}}^e$ and $\underset{\approx}{\mathcal{C}}$ is the fourth-order tensor of elastic moduli. For bcc crystals, tensor $\underset{\approx}{\mathcal{C}}$ has three independent components: C_{11}, C_{12}, C_{44} due to the cubic symmetry.

$$\underset{\sim}{\mathbf{E}}^e = \frac{1}{2}\left(\underset{\sim}{\mathbf{F}}^{e\mathrm{T}} \cdot \underset{\sim}{\mathbf{F}}^e - \underset{\sim}{\mathbf{I}}\right) \tag{6.5}$$

$$\breve{\underset{\sim}{\boldsymbol{\sigma}}} = \underset{\approx}{\mathcal{C}} : \underset{\sim}{\mathbf{D}}^e \tag{6.6}$$

$$\breve{\underset{\sim}{\boldsymbol{\sigma}}} = \dot{\underset{\sim}{\boldsymbol{\sigma}}} - \underset{\sim}{\mathbf{L}}^e \cdot \underset{\sim}{\boldsymbol{\sigma}} - \underset{\sim}{\boldsymbol{\sigma}} \cdot \underset{\sim}{\mathbf{L}}^{e\mathrm{T}} + \mathrm{Tr}\left(\underset{\sim}{\mathbf{L}}^e\right)\underset{\sim}{\boldsymbol{\sigma}} \tag{6.7}$$

The velocity gradient tensor due to crystallographic slip is given by Eq. (6.8) after [135]. The resolved shear stress on slip system (s), τ^s, is given by Eq. (6.9) after [135]. For the bcc structure, 24 easy slip systems are considered (Table 6.1) [136, 137].

$$\underset{\sim}{\mathbf{L}}^{*p} = \sum_{i=1}^{24} \dot{\gamma}^s \underline{\mathbf{m}}^{*s} \otimes \underline{\mathbf{n}}^{*s} \tag{6.8}$$

$$\tau^s = \underset{\sim}{\boldsymbol{\sigma}} : \left(\underline{\mathbf{m}}^{*s} \otimes \underline{\mathbf{n}}^{*s}\right) \tag{6.9}$$

Table 6.1: Easy slip systems in the bcc structure [136, 137].

Slip system family	number of slip systems
$\{110\}\ \langle 111\rangle$	12
$\{112\}\ \langle 111\rangle$	12

6.2.2 Viscoplastic slip rate and thermal activation

In addition to Eq. (6.8), a flow rule allowing the computation of the rate-dependent slip is needed. Many crystal viscoplasticity equations have been proposed to describe the viscoplastic slip rate in each slip system. Diard et al. [125, 126] used phenomenological crystalline viscoplasticity flow rules including hardening. They assumed that the viscoplastic slip rate on slip system (s) was expressed as a power function of the resolved shear stress on this system. In the contrary to numerous alloys, softening occurs rather than hardening during creep of tempered martensitic steels [42].

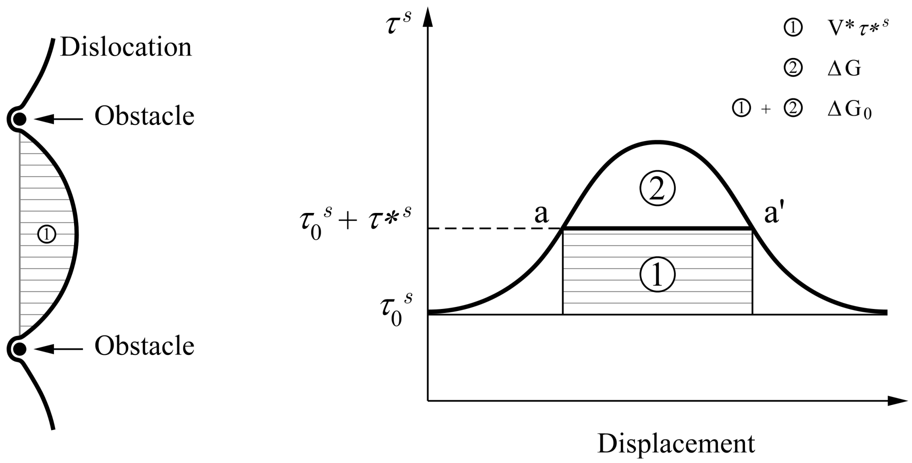

Figure 6.6: Obstacle profile in the framework of thermal activation.

In our study, a flow rule describing viscoplastic slip by dislocation glide will be used. Indeed, the creep tests carried out on the grade 91 steel under study lead to the Norton creep flow rule with stress exponents ranging between 10 and 20. Sklenička et al. [73] have suggested that for this range of stress exponent, the creep flow of grade 91 steel is controlled by dislocation glide rather than dislocation climb.

Dislocations overpass though some short-range obstacles by thermal activation, after Caillard and Martin [137]. The scheme of a dislocation overcoming obstacles on a slip system (s) is represented in Fig. 6.6. The work done by the dislocation over the swept area under an effective or viscous stress τ^{*s} is $V^*\tau^{*s}$. If ΔG_0 is the barrier energy of obstacles, then the necessary Gibbs energy to overcome these obstacles by thermal activation is $\Delta G^s = \Delta G_0 - V^*\tau^{*s}$. This leads to a probability proportional to $\exp\left(\Delta G^s/k_bT\right)$ following the Boltzmann theory. The backward motion of dislocations is neglected, i.e. for monotonic loading conditions (even at this very local scale). The slip rate on slip system (s) is given by [137]:

$$\dot{\gamma}^s = \begin{cases} \dot{\gamma}_0^s \exp\left(-\dfrac{\Delta G_0}{k_bT}\right) \exp\left(\dfrac{V^*\tau^{*s}}{k_bT}\right) \mathrm{sign}\left(\tau^s\right) & \text{if } |\tau^{*s}| > 0 \\ 0 & \text{if } \tau^{*s} = 0 \end{cases} \tag{6.10}$$

where $\dot{\gamma}_0^s = \rho_m^s b^2 \nu_d$, with ρ_m^s the density of mobile dislocations on the slip system (s), b the Burgers vector norm, and ν_d the Debye vibration frequency of atoms. Dislocations could be decomposed in screw and edge segments which are not distinguished in our study even if these overcoming obstacles may differ: cross-slip for screw dislocations, climb for edge dislocations.

The shear stress is decomposed into the viscous stress, τ^{*s}, and the athermal stress due to the obstacles, τ_0^s. The viscous stress is then given by:

$$\tau^{*s} = |\tau^s| - \tau_0^s \tag{6.11}$$

The creep evolution of the stress τ_0^s should be modelled by a creep-induced softening equation representing the softening behaviour of the grade 91 steel due to sub-grain growth and dislocation density decrease along creep time [42]. Up to day, no crystalline constitutive equations are available for simulating the softening behaviour during creep. In order to reduce the number of parameters which allows us to simplify their identification by finite element simulation of polycrystalline large scale aggregates, τ_0^s is assumed to be constant.

The critical shear stress values for slip systems $\{110\}\langle 111\rangle$ and $\{112\}\langle 111\rangle$ in Fe-α after the experimental results reported in [138] are plotted in Fig. 6.7. These results show that the difference between the critical shear values of both slip families is negligible for temperatures higher than 200 K. Therefore, at 773 K (500°C) and 873 K (600°C) which are the temperatures of the creep tests under study, only one constant value of τ_0^s for all 24 slip systems needs to be identified. Henceforth, this parameter is annotated as τ_0.

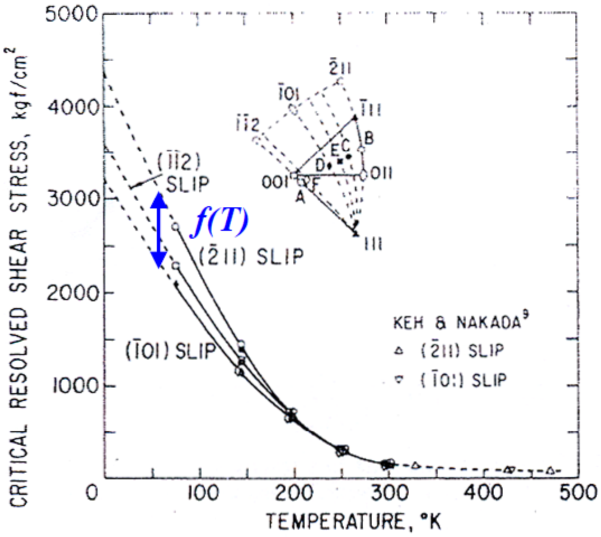

Figure 6.7: Evolution of critical resolved shear on slip systems $\{110\}\langle 111\rangle$ and $\{112\}\langle 111\rangle$ in Fe-α after [138].

6.3 Crystal viscoplasticity parameters

The values of the three independent constants (C_{11}, C_{12}, C_{44}) of cubic tensor $\underset{\approx}{C}$ are given in [139] after measurements by the ultrasonic method and are reported in Table 6.2. The high values of the anisotropic coefficient of cubic elasticity, $a > 3$, show that the ferrite steel is highly anisotropic at high temperature.

Table 6.2: Independent elastic constants of Fe-α single crystals [139].

	C_{11} (GPa)	C_{12} (GPa)	C_{44}(GPa)	$2C_{44}/\left(C_{11}-C_{12}\right)$
500°C	196.8	128	107.2	3.1
600°C	186.7	126.5	105.3	3.5

Rare studies have given the estimations of the values of the crystal viscoplasticity parameters, ΔG_0, τ_0, V^* for tempered martensitic 9%Cr steels. Some authors have provided their values in a range of creep strain rate many orders of magnitude higher than ours ($4.1\times10^{-11}\text{s}^{-1}$ for creep at 500°C and 230 MPa, $6.4\times10^{-11}\text{s}^{-1}$ for creep at 600°C and 90 MPa). Fournier et al. [140] have used an uniaxial model equivalent to Eq. (6.10) and have identified the value of the corresponding $V^* = 230b^3$ based on uniaxial tests of 9%Cr steels at 550°C with strain rates in the order of magnitude of 10^{-5}s^{-1}. This corresponds to a value of $V^* = 460b^3$ at the crystal scale (supposing a Schmid factor of 0.5). This value of V^* was given in a range of strain rate higher than the creep strain rates of both creep tests of grade 91 steel under study by more than 5 orders of magnitude. This could influence deformation mechanisms and thus the value of V^*. The value of the activation energy, ΔG_0, ranges between 2.7 and 4.7 eV after the evaluations in [141] using creep tests of 9%Cr-1%Mo steel at temperatures between 500 and 600°C. These studies provide the orders of magnitude of the crystal viscoplastic parameter values that help their identification in application to our creep tests (500°C under 230 MPa and 600°C under 90MPa).

Many authors [125, 126, 142] have used different meshes of polycrystalline aggregate to identify the crystalline viscoplasticity parameters. Diard et al. [125, 126] used Voronoï polycrystalline aggregates (Figs. 6.3a and 6.4a) whereas Libert [142] used polycrystalline aggregates constituted of regular cubic grains. In fact, Diard et al. [125, 126] were interested in studying the local stress and strain at grain boundaries which are influenced by grain geometry. The polycrystalline aggregates constituted of regular cubic grains proposed in [142] are much more simple to build and could be sufficient for only adjusting the crystalline viscoplasticity parameters by using the average creep response of the aggregates.

Recent Fast Fourier Transform computations (FFT) carried by Lebensohn et al. [143, 144] have focused on the macroscopic effect of the grain shapes. The first FFT computations were carried out in the crystal linear viscosity framework using 2D-plane strain hypothesis and an aggregate constituted of either regular square grains or Voronoï polygons. The second FTT computations were performed in the crystal viscoplasticity framework using a 3D aggregate constituted of either regular cubic grains or Voronoï polyhedral grains. These calculations showed that the grain shapes only affect slightly the predicted macroscopic behaviour. Therefore, polycrystalline aggregates constituted of regular cubic blocks will be used to adjust the crystal viscoplasticity parameters used in Eqs. (6.10) and (6.11).

6.4 Conclusions

Our study concerns creep tests at 500°C under 230 MPa (a lifetime of 160×10^3h) and at 600°C under 90 MPa (a lifetime of 94×10^3h). The crystal elasto-viscoplasticity constitutive equations given by Eqs. (6.10) and (6.11) require the adjustment of only three crystal viscoplasticity parameters: ΔG_0, τ_0, V^*. In order to identify these parameters in chapter 7, finite element simulations of creep deformation of polycrystalline aggregates constituted of regular cubic blocks will be carried out. Different numbers of blocks as well as various numbers of finite elements per block will be chosen, whereas Libert [142] used only 8 FEs per grain. The fitting procedure is based on the simulation of the macroscopic creep strain curves and comparison with our experimental data.

The normal stress fields averaged over a grain boundary in a Zr alloy subjected to monotonic strain rate at room temperature as well as at 350°C differs from the macroscopic tensile stress by ±50% [125, 126]. Not many results concerning the normal stress during very long-term creep tests at high temperature have been reported in the literature. Our study in chapter 8 will focus on the normal stress distribution at block boundaries in grade 91 steel subjected to the both creep tests previously described. In addition, we will focus on the computations of stress fields around triple junctions where the stress and strain heterogeneity should be the highest (Figs. 6.1 and 6.2).

Chapter 7

Finite element modelling of polycrystalline aggregates

7.1 Geometry description and meshing

The polycrystalline aggregates used in this study have cubic shapes meshed into regular cubic blocks (Fig. 7.1). Each cubic polycrystalline aggregate contains the same number of blocks along each edge. Each cubic block is meshed into regular cubic finite elements (CUB8 element, 8 integration points) with the same number of finite elements along each block edge.

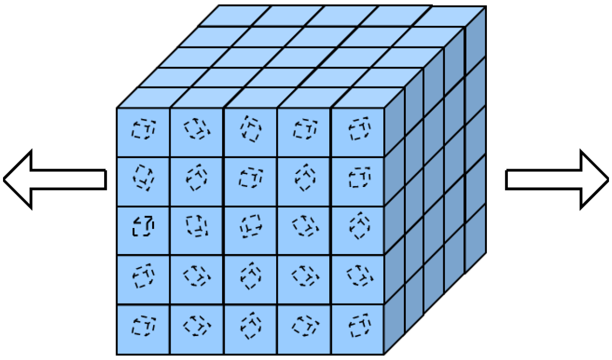

Figure 7.1: Polycrystalline aggregate containing 125 blocks of random orientations. Issued from [145].

The crystal orientations of the blocks of the grade 91 steel with respect to one and another are either random (when they belong to two different former austenitic grains) or related after the relationships of Kurdjumov-Sachs [48] and Nishiyama-Wassermann [49]. However, for the sake of simplicity, we assumed that all blocks of the polycrystalline aggregates have random crystal orientations. Assuming random orientations of the neighbours instead of Kurdjumov-Sachs or Nishiyama-Wassermann orientations should probably not strongly affect macroscopic predictions. At the macroscopic scale, EBSD measurements have shown that the material is almost texture free [119].

7.2 Crystal elasto-viscoplasticity constitutive equations

The anisotropic elasticity equation is described in chapter 6 by Eq. (6.6) as well as the crystal viscoplasticity equations by Eqs. (6.10) and (6.11). The values of the three independent constants of anisotropic elasticity for Fe-α are given in [139] and reported in Table 6.2 for both temperatures under study (500 and 600°C). For the crystal viscoplasticity equations, only three parameters are needed to be adjusted: ΔG_0, τ_0, V^*. The study of Fournier et al. [140] allows us to choose the V^* values of the order of magnitude of $460b^3$ for 9%Cr steels given at 550°C. This value of V^* corresponds to strain rate of the order of magnitude of $10^{-5}\mathrm{s}^{-1}$. The value of the activation energy, ΔG_0, ranges between 2.7 and 4.7 eV (for 9%Cr steels at $500 - 600$°C) after [141].

The UMAT algorithm allowing the time integration of these crystal elastoviscoplasticity laws in the finite strain formulation was implemented in CAST3M by Vincent [146, 147]. The numerical procedures originate from a collaborative work between LPMTM Villetaneuse, CEA Saclay - SRMA and LMS Polytechnique [135]. The procedures were transformed into UMAT procedures and introduced in the CAST3M software for the fcc structure [148] and bbc structure [146, 147] using an explicit algorithm for the time integration.

7.3 Boundary conditions and creep loading

The boundary conditions are set as shown in Fig. 7.2. Some of the displacement components of three vertexes are set to zero to block any degrees of freedom (3 rotations and 3 translations) preventing from any rigid body motion. Engineering stresses are applied to the TOP and BOTTOM surfaces shown in Fig. 7.2, whereas the lateral surfaces are free from any load and deformation constraints.

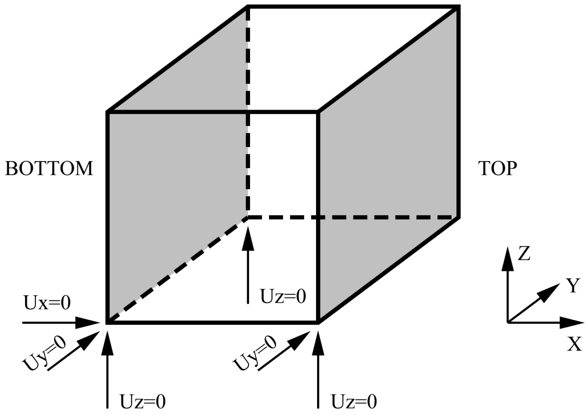

Figure 7.2: Boundary conditions, six degrees of freedom of rigid body motion are blocked.

Two creep tests at 500°C under creep engineering stress $\sigma^{eng} = 230$ MPa and at 600°C under $\sigma^{eng} = 90$ MPa are simulated using the finite element method. The loading stages of both creep tests are applied after the experimental records (Fig. 7.3). These finite element computations are carried out using CAST3M finite element software in the 2009 version.

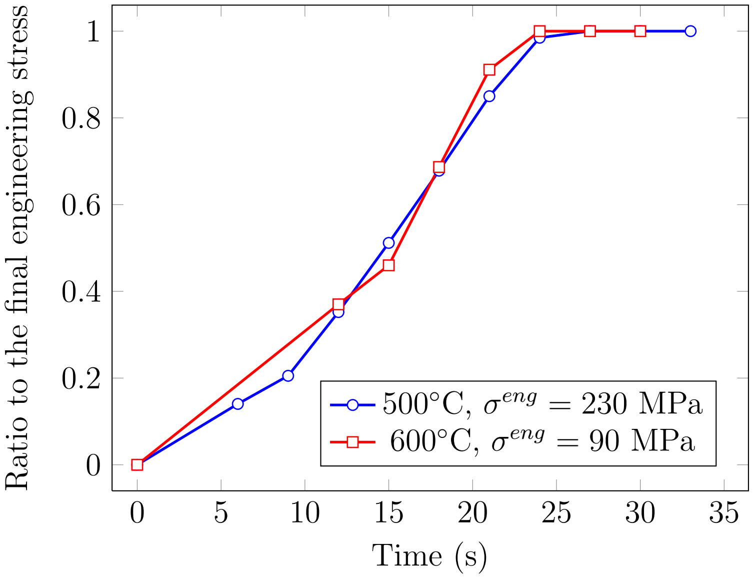

Figure 7.3: Experimental loading stages of the creep tests at 500°C and 600°C before reaching their final creep engineering stress (σ^{eng}) which are respectively 230 MPa and 90 MPa. Similar loading curves are used for applying the boundary conditions during the starting of the finite element computations.

The computations are stopped before failure at times 50×10^3h and 30×10^3h respectively for the creep tests at 500°C under 230 MPa and at 600°C under 90 MPa. In fact, longer computations show that at these times the minimum creep strain rates are mostly reached. Following these times, creep strain rates vary very weakly.

7.4 Adjustment of the crystal viscoplasticity parameters

The adjustment of these crystal viscoplasticity parameters are based on the use of the macroscopic curves displaying engineering strain versus creep time. The macroscopic creep engineering strains are cumulated from the creep beginning (after the loading stage). The crystal viscoplasticity parameters are identified using a step-by-step procedure to predict the creep curves that should be as the most accurate as possible. The adjustment of the viscoplasticity parameters is constrained by the choice of the same value for the activation energy ΔG_0 at both temperatures under study (500°C and 600°C). The activation volumes at both temperatures are imposed to differ by a factor lower than one order of magnitude. The initial value of τ_0 is slightly lower than 0.5 times the macroscopic engineering stress. The values of the crystal viscoplasticity parameters allowing a reasonable agreement between the predicted macroscopic creep curves and the experimental ones are reported in Table 7.1. The selected values of V^* are discussed at the end of this section.

Table 7.1: Parameter values for the crystal viscoplastic constitutive equations.

	ΔG_0 (eV)	τ_0 (MPa)	V^* (b^3)
500°C	3.3	78	350
600°C	3.3	27	400

7.4.1 Effect of mesh refinement

Two numbers of blocks, 3^3 and 5^3, are chosen to study the effect of mesh refinement on the creep strain curve for the creep test at 600°C and 90 MPa. The polycrystalline aggregate containing 3^3 blocks is meshed using four values of the meshing parameter: 2^3 FEs/block, 4^3 FEs/block, 6^3 FEs/block and 8^3 FEs/block. The one containing 5^3 blocks is meshed using three values of the meshing parameter (because of longer computation time): 2^3 FEs/block, 4^3 FEs/block and 6^3 FEs/block. For each one of both polycrystalline aggregates, one set of random crystal orientations is used.

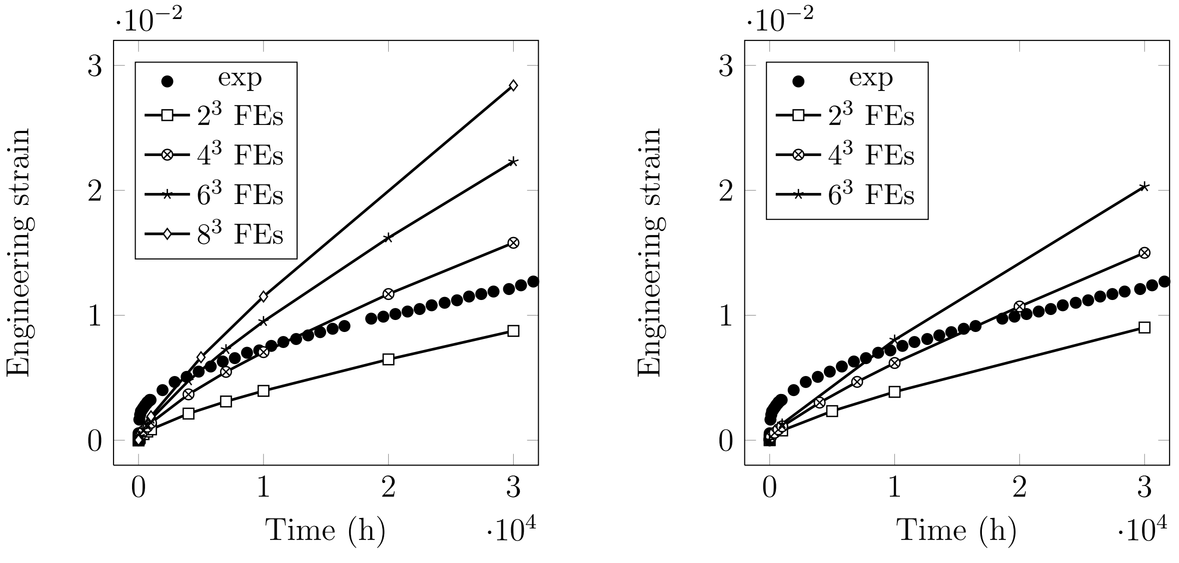

(a) Aggregate of 3^3 blocks **(b)** Aggregate of 5^3 blocks

Figure 7.4: Effect of the number of finite elements per block on the macroscopic engineering strain vs. time curve for the creep test at 600°C and 90 MPa. The material parameters are given in Tables 6.2 and 7.1. For each number of blocks, only one set of random crystal orientations is chosen.

The macroscopic engineering strain vs. time curves predicted using the polycrystalline aggregate containing 3^3 blocks are plotted in Fig. 7.4a. The engineering strain at which the minimum strain rate is reached (30×10^3h, see Fig. 7.4) is evaluated from the use of the different meshing parameters. The results show that an increase in the meshing parameter from 2^3 to 6^3 FEs/block leads to an increase in engineering strain by a factor 2.55. The minimum creep strain rates, $\dot{\varepsilon}^{eng}_{min}$, are evaluated as the average engineering strain rates between creep times of 10×10^3h and 30×10^3h. They are reported in Table

7.2. The results show that the use of 4^3 FEs/block rather than 2^3 FEs/block leads to an increase in value of $\dot{\varepsilon}^{eng}_{min}$ by a factor 1.8. The use of 6^3 FEs/block rather than 4^3 FEs/block yields a further increase by a factor 1.5. Finally, the use of 8^3 FEs/block rather than 6^3 leads to a further increase in value of $\dot{\varepsilon}^{eng}_{min}$ by a factor 1.3.

Table 7.2: Computed minimum creep strain rate depending on the meshing parameters. The material parameters are given in Tables 6.2 and 7.1. One set of random crystal orientations is assigned to each polycrystalline aggregate.

	Predictions (10^{-7}h^{-1})				Experiment (10^{-7}h^{-1})
	Number of Blocks				
FEs/block	3^3	5^3	6^3	7^3	
2^3	2.40	2.58	-	-	2.3
4^3	4.38	4.42	3.93	3.44	2.3
6^3	6.40	6.38	-	-	2.3
8^3	8.45	-	-	-	2.3

The macroscopic engineering strains, ε^{eng}, predicted using the polycrystalline aggregate containing 5^3 blocks are plotted in Fig. 7.4b. The engineering strain at the minimum creep strain rate increases by a factor 2.25 when the meshing parameter increases from 2^3 to 6^3 FEs/block. The minimum strain rates are evaluated and reported in Table 7.2. The results show that the use of 4^3 FEs/block rather than 2^3 FEs/block leads to an increase in value of $\dot{\varepsilon}^{eng}_{min}$ by a factor 1.7. The use of 6^3 FEs/block rather than 4^3 FEs/block leads a further increase by a factor 1.4.

The results presented above seem to show that the macroscopic minimum strain rate, $\dot{\varepsilon}^{eng}_{min}$, is less dependant on mesh refinement as the number of blocks is higher. The value of $\dot{\varepsilon}^{eng}_{min}$ computed using the polycrystalline aggregate containing only 3^3 blocks have been shown to depend strongly on the random crystal orientations. On the contrary, the polycrystalline aggregate containing 5^3 blocks will be shown to yield values of $\dot{\varepsilon}^{eng}_{min}$ depending weakly on the random crystal orientations. The meshing parameter 4^3FEs/block is chosen. Coarser mesh refinement does not allow stable predictions of the minimum strain rate, whereas finer mesh refinement seams to yield a low change in minimum strain rate and longer computation times.

7.4.2 Effect of random crystal orientations

The effect of random crystal orientations is studied for the creep test at 600°C and 90 MPa. Four sets of random crystal orientations are chosen for 5 similar aggregates containing 5^3 blocks. Each block is meshed by 4^3 cubic finite elements. The computed creep engineering strain curves using these four aggregate configurations are plotted in Fig. 7.5. This figure shows that the predicted creep strain rates vary by less than 10%. The prediction is therefore weakly dependent on the set of crystal orientations.

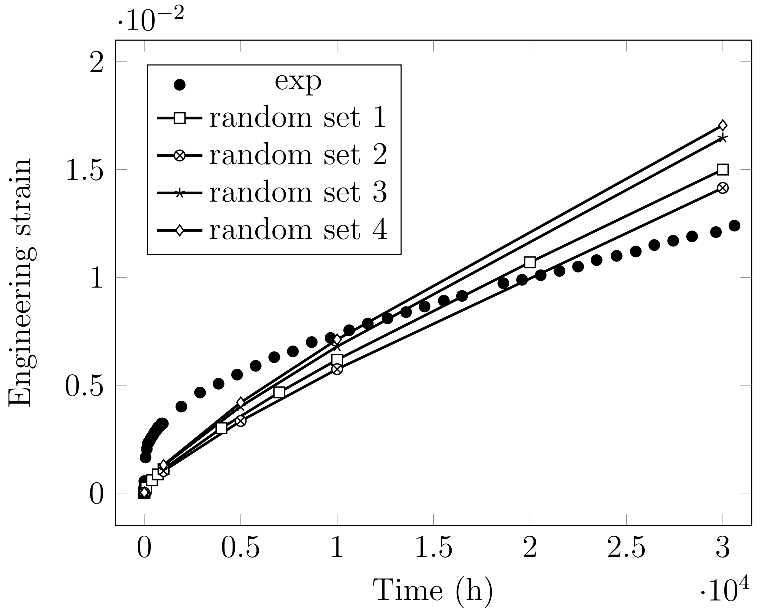

Figure 7.5: Predicted creep engineering strain vs. time curves of the creep test at 600°C and 90 MPa, using one aggregate of 5^3 blocks meshed by 4^3 FEs per block and four independent sets of crystal orientations. The used crystal elastoviscoplasticity parameters are reported in Tables 6.2 and 7.1.

7.4.3 Effect of the number of blocks

In this paragraph, the effect of the polycrystalline aggregate size is studied using four numbers of blocks: 3^3, 5^3, 6^3 and 7^3. The four aggregates are meshed by 4^3 FEs per block. For each of these aggregates, one set of random crystal orientations is used. They are sorted out from the same set of random crystal orientations.

The computed creep engineering strain vs. time curves for the creep test at 600°C and 90 MPa are plotted in Fig. 7.6. The results show that the computed creep engineering strain decreases as the number of blocks increases. Indeed, in the aggregate containing a high number of blocks, the deformation of each block may be constrained by its neighbours. The distribution of the average strain fields within the blocks will be studied in section 7.5.

Minimum engineering strain rates are evaluated from the creep engineering strain curves predicted using the four polycrystalline aggregates. Their values are reported in Table 7.2. The computed minimum strain rate using 7^3 blocks decreases by 20% with respect to the one computed using 5^3 blocks. This difference ranges within the experimental scatter of creep strain rates. Thus, a number of 5^3 blocks is sufficient for the polycrystalline aggregate to be used for adjusting the crystal viscoplastic parameters.

7.4.4 Effect of the V^* parameter

In this paragraph, the effect of the V^* parameter is studied using two values, $350b^3$ and $400b^3$. These values are used for the finite element simulation of the creep test at 500°C and 230 MPa. The used polycrystalline aggregate contains 5^3 blocks and one set of crystal orientations. The aggregate is meshed by 4^3 FEs per block.

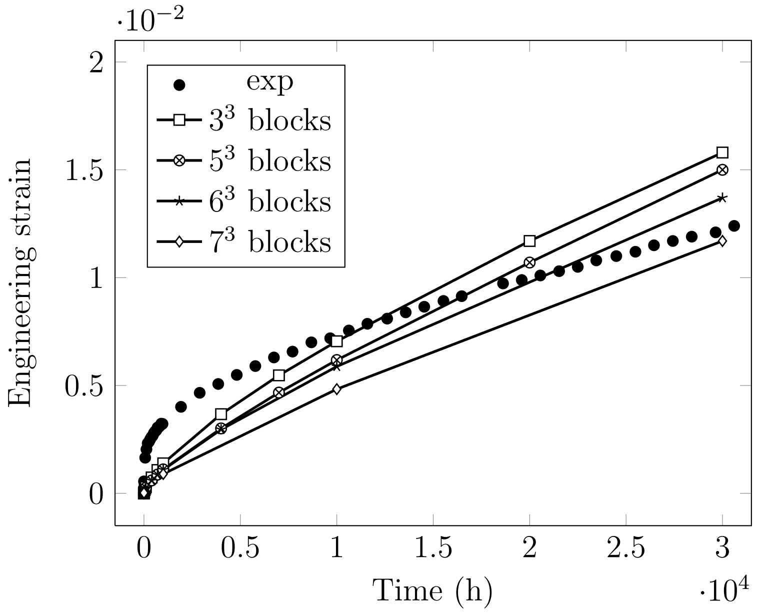

Figure 7.6: Predicted evolution of the macroscopic engineering strain during creep at 600°C under 90 MPa using four numbers of blocks for the polycrystalline aggregate. The aggregate is meshed by 4^3 FEs per block. The used crystalline elastoviscoplasticity parameters are reported in Tables 6.2 and 7.1.

The values of creep engineering strain, ε^{eng}, computed using both values of V^* are plotted in Fig. 7.7. The value of $V^* = 400b^3$ leads to the predictions of ε^{eng} in better agreement with the experimental results than the ones using the value of $V^* = 350b^3$. For the last value of V^*, the predictions of ε^{eng} are 2 times lower than the experimental ones.

The minimum strain rates, $\dot{\varepsilon}^{eng}_{min}$, obtained using both values of V^* are evaluated as the mean strain rates between creep times of 30×10^3h and 50×10^3h. Contrary with the previous observation concerning engineering strain, the computed minimum strain rate using the value of $V^* = 350b^3$ is in better agreement with the experimental results. In this case, the computed value of $\dot{\varepsilon}^{eng}_{min}$ is lower than its experimental value by only 30%. The computed value of $\dot{\varepsilon}^{eng}_{min}$ using the value of $V^* = 400b^3$ is 2 times higher than the experimental value. As no value of V^* gives definitely better prediction of the creep curve, both are kept for the sensitivity study.

For either of both V^* values, $350b^3$ or $400b^3$, the effect of mesh refinement on the polycrystalline aggregate containing 5^3 blocks is studied. Three meshing parameters are used: 2^3/block, 4^3/block and 6^3/block. The computed creep engineering strains using this mesh refinement and both values of V^* are plotted in Figs. 7.8.

Figure 7.8a shows that the use of 2^3 FEs per block is not sufficient to predict either ε^{eng} or $\dot{\varepsilon}^{eng}_{min}$ in agreement with the experimental results. Choosing 6^3 FEs per block, the predicted value of $\dot{\varepsilon}^{eng}_{min}$ is two times higher then the one obtained using 4^3 FEs per block.

Figure 7.8b shows that the computed value of $\dot{\varepsilon}^{eng}_{min}$ is strongly dependent on mesh refinement. The use of 6^3 FEs per block leads to a predicted value of $\dot{\varepsilon}^{eng}_{min}$ 4 times higher than the one obtained using 4^3 FEs per block. In order to get stability with respect to mesh refinement the value of $V^* = 350b^3$ is chosen.

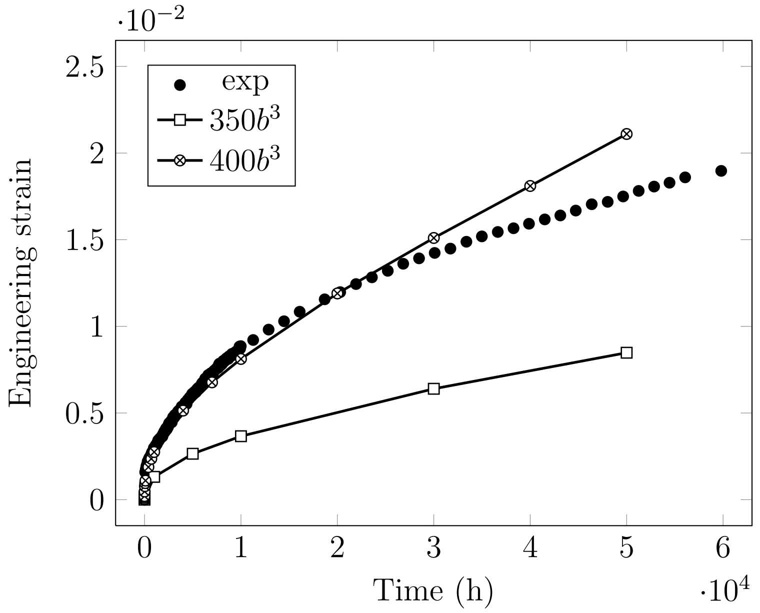

Figure 7.7: Evolution of the macroscopic engineering strain during creep at 500°C under 230 MPa predicted using two values for the parameter V^*. The polycrystalline aggregate contains 5^3 block and is meshed by 4^3 FEs per block. The values of the parameters ΔG_0 and τ_0 at 500°C are reported in Table 7.1.

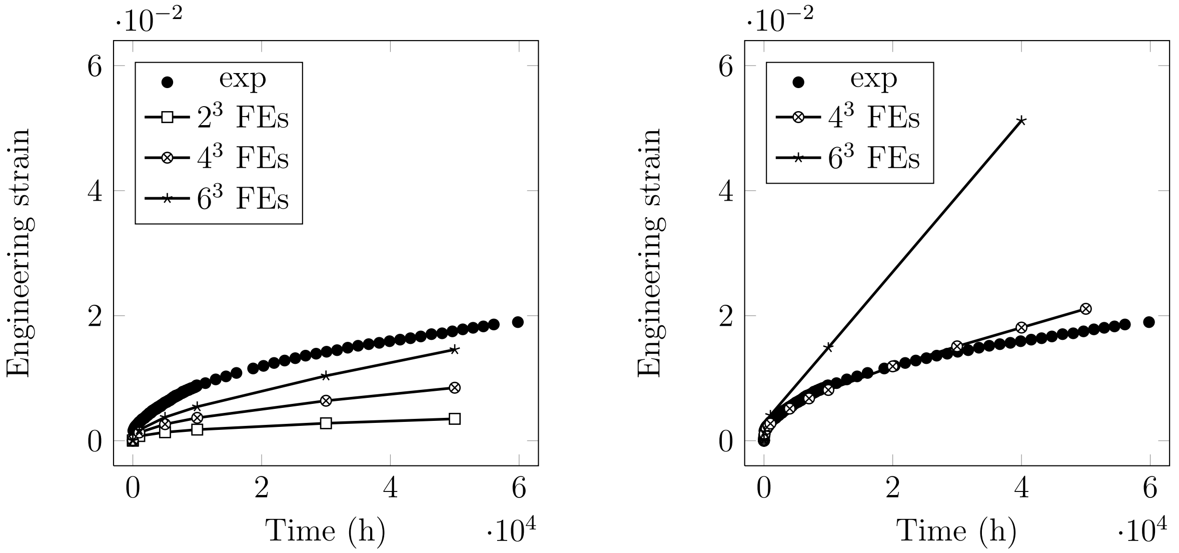

(a) $V^* = 350b^3$ **(b)** $V^* = 400b^3$

Figure 7.8: Sensitivity of predicted engineering strains of creep at 500°C under 230 MPa due to mesh refinement for two V^* values. Polycrystalline aggregates of 5^3 blocks and the same values of the parameters ΔG_0 and τ_0 at 500°C reported in Table 7.1 are used.

7.4.5 Discussion

The previous results show that the predicted macroscopic strain increases with increasing number of finite elements. This effect although tends to decrease when the chosen number of blocks increases (see Figs. 7.4 and 7.6). Consequently, numbers of finite elements per block higher than 4^3 have not been used in the meshing of the polycrystalline aggregate containing high numbers of blocks (6^3 and 7^3). Indeed, the RAM capacity of the machine is very limited (of only 16 Go for CAST3M in the 2009 version) and causes failure of this type of heavy computation. The computation times lasted for: 5 days for the use of 5^3 blocks meshed by 4^3 FEs/block, 9 days for 5^3 blocks (4^3 FEs/block) and between 2 and 3 weeks for 7^3 blocks (4^3 FEs/block).

The use of 5^3 blocks leads to an error in computed minimum strain rate with respect to the one computed using higher number of blocks lower than 20%. This ranges within the scatter of the experimental creep strain rate. The polycrystalline aggregate containing 5^3 blocks meshed by 4^3 FEs/block is therefore preferentially used for identification of the crystal viscoplasticity parameters. The stability of the minimum creep rates discussed above is an additional supporting element for the choice of the parameters in Table 7.1.

The effect of time increment refinement is also checked. Time increment sufficiently small is used allowing stability of the presented results.

7.5 Analysis of the mean block stress and strain distributions

This section focuses on analysis of the predicted distributions of mean block stress and strain fields. Firstly, predicted distributions based on a reference choice will be presented. This reference choice corresponds to the use of the crystal viscoplasticity parameters reported in Table 7.1, a polycrystalline aggregate containing 5^3 blocks and the meshing parameter as 4^3 FEs/block.

The effect of the choice of the number of blocks for the polycrystalline aggregate, of the meshing parameter and the value of one crystal viscoplasticity parameter (V^*) will be discussed later.

As the creep lifetime is closely related to the minimum strain rate, values of stress and strain are evaluated at the time when the minimum strain rate is reached, namely at creep times of 50×10^3h at 500°C and of 30×10^3h at 600°C.

7.5.1 Analysis based on the reference choice of parameters

The distributions of the mean axial stress and strain fields per finite element after a creep time of 30×10^3h at 600°C and 90 MPa are presented in Figs. 7.9a and 7.9b. The isovalue plots show that the σ_{xx} field is almost uniformly distributed through the polycrystalline aggregate, except in some blocks where σ_{xx} reaches a value higher than the applied macroscopic stress by 50%. Contrary to the σ_{xx} field, the ε_{xx} field is strongly heterogeneous though the polycrystalline aggregate (factor 5). In fact, the macroscopic behaviour of the material obeys the Norton creep flow rule with an exponent of $n = 10$ at 600°C. This exponent leads to a scatter in the ε_{xx} field much higher than the one in the σ_{xx} field.

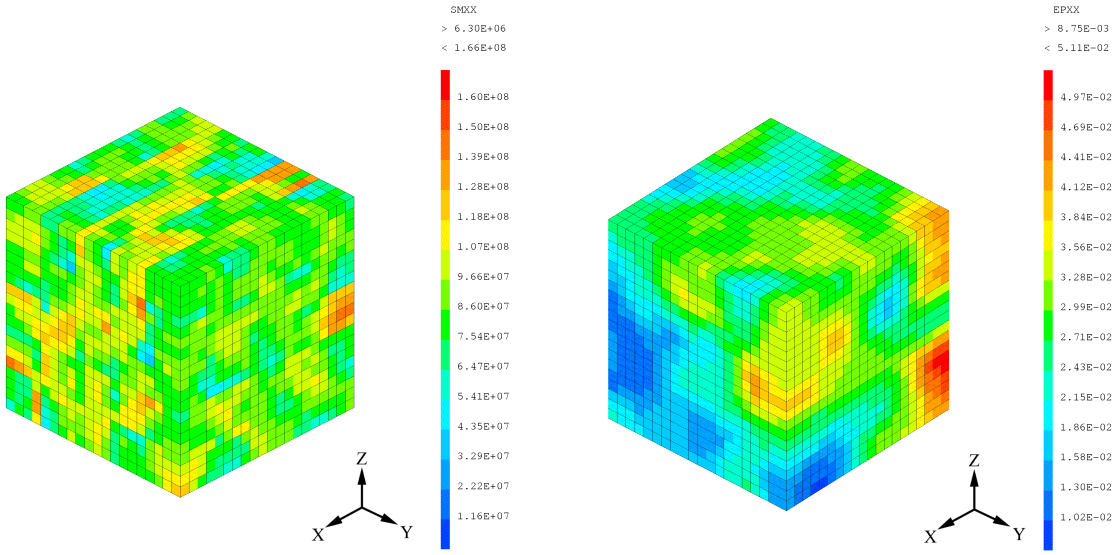

(a) σ_{xx} **(b)** ϵ_{xx}

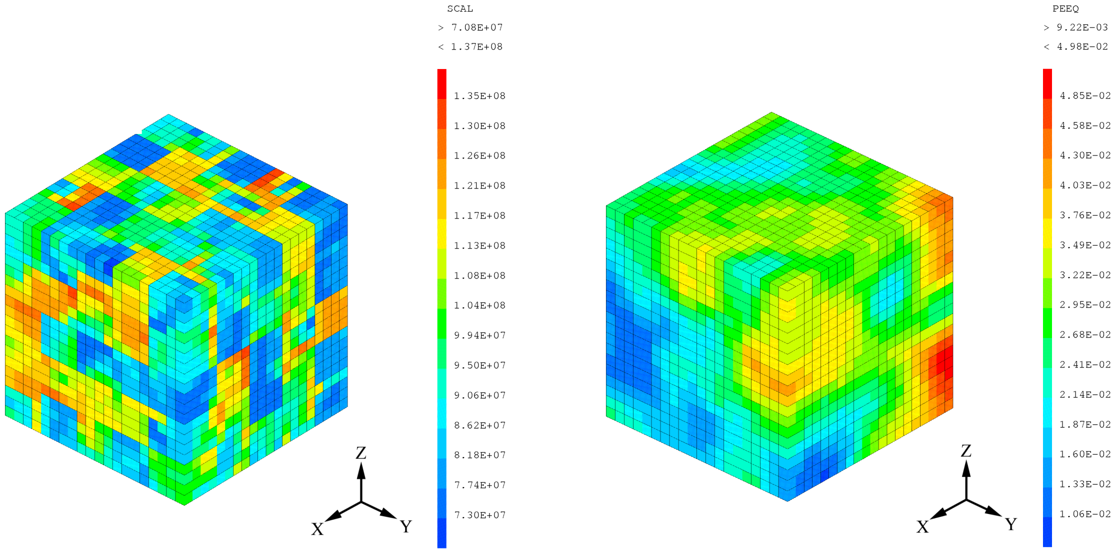

(c) σ_{eq} **(d)** ϵ^{v}_{eq}

Figure 7.9: Distributions of (a) axial stress fields, (b) axial strain fields after a creep time of 30×10^3 h at 600°C and 90 MPa, given at the surface of the polycrystalline aggregate constituted of 5^3 blocks using the following parameter values: $\Delta G_0 = 3.3$ eV, $\tau_0 = 27$ MPa and $V = 400b^3$.

The distributions of the mean Von Mises stress and viscoplastic equivalent strain per finite element are plotted in Figs. 7.9c and 7.9d. The isovalue plots show that the value of σ_{eq} are relatively different from one block to another. Some blocks are subjected to multiaxial loading (compare Figs. 7.9a and 7.9c) and others to uniaxial loading. The distribution of the ε^v_{eq} value is heterogeneous and similar to that of ε_{xx}.

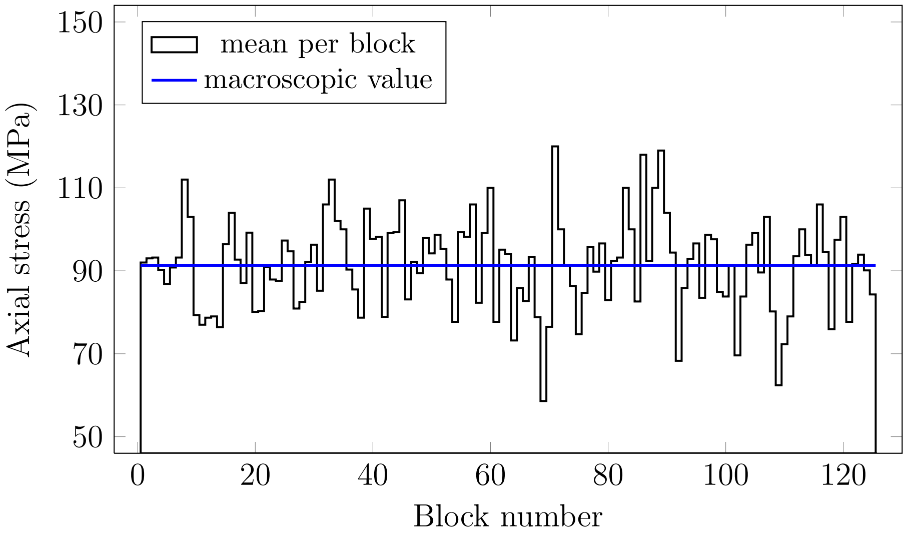

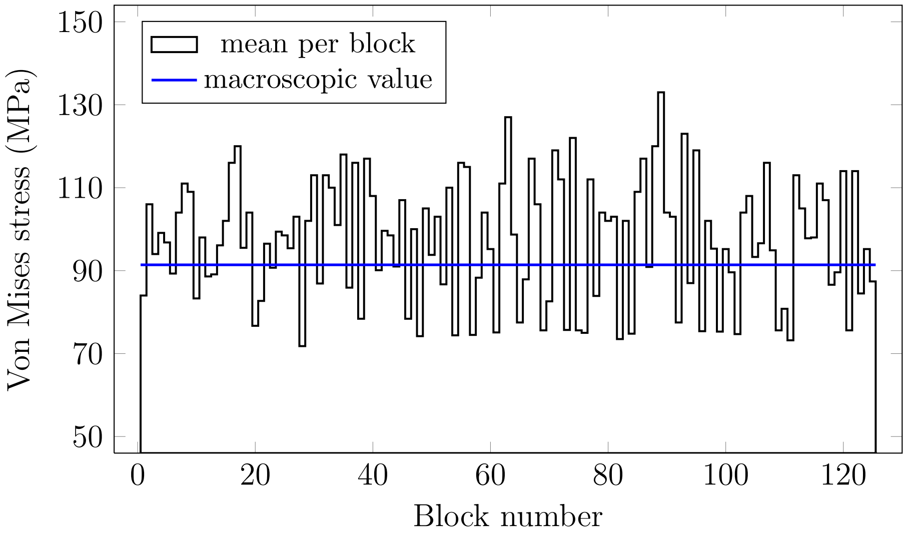

Figure 7.10: Distribution of the mean values per block of $\langle\sigma\rangle^{block}_{xx}$ and $\langle\sigma\rangle^{block}_{eq}$ after 30×10^3 h of creep at 600°C under a creep stress of 90 MPa.

In the following, distributions of the average values per block of axial stress, axial strain, Von Mises stress, viscoplastic equivalent strain and stress triaxiality will be evaluated. The average axial stress and strain fields per block, $\langle\sigma\rangle^{block}_{xx}$ and $\langle\varepsilon\rangle^{block}_{xx}$, are respectively computed using Eqs. (7.1) and (7.2). The average Von Mises stress per block, $\langle\sigma\rangle^{block}_{eq}$, is evaluated using the mean Cauchy stress tensor per block, $\langle\underset{\sim}{\boldsymbol{\sigma}}\rangle^{block}$, given in Eq. (7.1). The average viscoplastic equivalent strain per block, $\langle\varepsilon^v_{eq}\rangle^{block}$, is obtained by integration over the block volume (V_b) of the ε^v_{eq} values given by the CAST3M software at Gauss integration points of finite elements as in Eq. (7.3). The average stress triaxiality

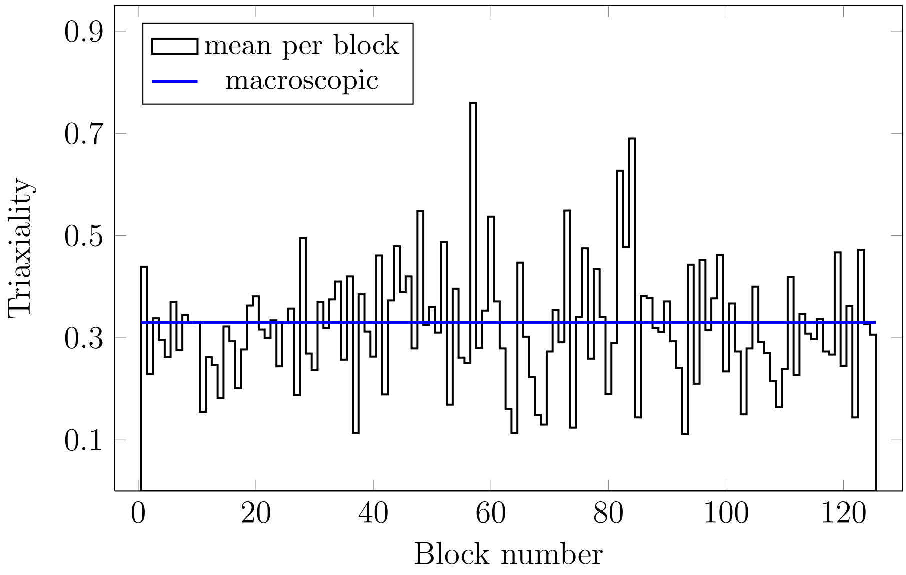

Figure 7.11: Triaxiality of each block in the polycrystalline aggregate of 5^3 blocks for creep at 600˚C and 90 MPa.

per block, $\langle t_\sigma \rangle^{block}$, is defined by Eq. (7.4).

$$\langle \underset{\sim}{\sigma} \rangle^{block} = \frac{1}{V_b} \int\limits_{V_b} \underset{\sim}{\sigma} \,\mathrm{d}V \tag{7.1}$$

$$\langle \underset{\sim}{\varepsilon} \rangle^{block} = \frac{1}{V_b} \int\limits_{V_b} \underset{\sim}{\varepsilon} \,\mathrm{d}V \tag{7.2}$$

$$\langle \varepsilon^v_{eq} \rangle^{block} = \frac{1}{V_b} \int\limits_{V_b} \varepsilon^v_{eq} \,\mathrm{d}V \tag{7.3}$$

$$\langle t_\sigma \rangle^{block} = \frac{1}{3} \frac{\mathrm{Tr}\left(\langle \underset{\sim}{\sigma} \rangle^{block}\right)}{\langle \sigma \rangle^{block}_{eq}} \tag{7.4}$$

Figures 7.10a and 7.10b present respectively average values per block of axial stress, $\langle \sigma \rangle^{block}_{xx}$, and Von Mises stress, $\langle \sigma \rangle^{block}_{eq}$, after a creep time of 30×10^3 at 600˚C and $\sigma^{eng} = 90$ MPa. The value of $\langle \sigma \rangle^{block}_{xx}$ varies by ±30% with respect to the mean macroscopic Cauchy stress, Σ_{xx}, which is only slightly higher than the macroscopic engineering stress, σ^{eng}. The value $\langle \sigma \rangle^{block}_{eq}$ varies by −20%/+40% with respect to the mean macroscopic Von Mises stress Σ_{eq}. This one is equal to Σ_{xx}; in fact, the polycrystalline aggregate is subjected to only uniaxial loading at the macroscopic scale.

Figures 7.10a and 7.10b show that the values of $\langle \sigma \rangle^{block}_{xx}$ and $\langle \sigma \rangle^{block}_{eq}$ evaluated for the same blocks are different. In fact, the computed triaxialities of blocks range between 0.1 and 0.75 (Fig. 7.11). Some blocks are subjected to uniaxial loading ($\langle t_\sigma \rangle^{block} = 0.33$, Fig. 7.11) and others to multiaxial loading ($\langle t_\sigma \rangle^{block} \neq 0.33$). For the triaxiality values $\langle t_\sigma \rangle^{block} > 0.33$ (e.g. in block number 60 $\langle t_\sigma \rangle^{block} = 0.53$, Fig. 7.11), we observed that $\langle \sigma \rangle^{block}_{xx} > \langle \sigma \rangle^{block}_{eq}$ (in block number 60, $\langle \sigma \rangle^{60}_{xx} = 110$ MPa and $\langle \sigma \rangle^{60}_{eq} = 95$ MPa, Figs. 7.10). On the contrary, for the values $\langle t_\sigma \rangle^{block} < 0.33$ we observed in Figs. (7.10) that

$\langle\sigma\rangle_{xx}^{block} < \langle\sigma\rangle_{eq}^{block}$ (e.g. block number 80).

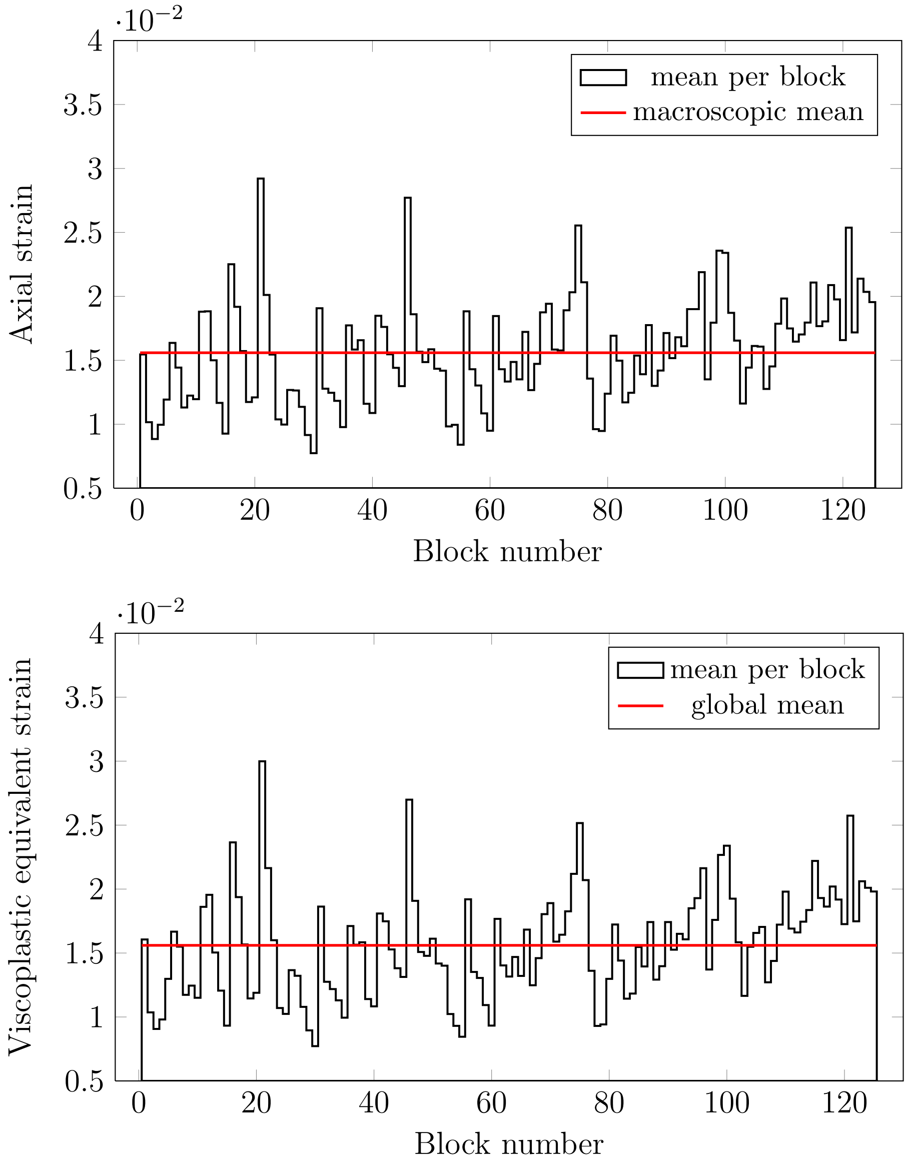

Figure 7.12: Distributions of the mean values of (a) $\langle\varepsilon\rangle_{xx}^{block}$ and (b) $\langle\varepsilon_{eq}^{v}\rangle^{block}$ after 30×10^3 h of creep time at 600°C and 90 MPa. Both distributions seem to be described by a periodicity of 25 blocks, number of blocks comprised in each layer of the aggregate of 5^3 blocks perpendicular to the loading axis.

The distributions of the values of $\langle\varepsilon\rangle_{xx}^{block}$ and $\langle\varepsilon\rangle_{eq}^{block}$ are plotted in Figs. 7.12a and 7.12b. The results show that $\langle\varepsilon\rangle_{xx}^{block}$ and $\langle\varepsilon\rangle_{eq}^{block}$ have the same distribution. All crystals have 24 slip systems. The majority of these slip systems may be activated (the analysis of the number of activated slip systems per block is still in progress) so all the blocks behave similarly to an isotropic matrix. In consequence, the axial strain ($\varepsilon_{xx} \approx \varepsilon_{xx}^{v}$, neglecting ε_{xx}^{e}) could be approximately equal to the viscoplastic equivalent strain, ε_{eq}^{v}. Figures 7.12a and 7.12b also show that the distributions of $\langle\varepsilon\rangle_{xx}^{block}$ and $\langle\varepsilon\rangle_{eq}^{block}$ seem to be described by a periodicity of 25 blocks. This number of blocks constitutes each layer in the aggregate of 5^3 blocks perpendicular to the loading axis.

Figure 7.12a shows that the $\langle\varepsilon\rangle_{xx}^{block}$ fields vary by a factor 2 with respect to the macroscopic axial strain, ε^{eng}. Contrary to the $\langle\varepsilon\rangle_{xx}^{block}$ fields, the $\langle\sigma\rangle_{xx}^{block}$ fields vary only by ±30% with respect to the macroscopic engineering stress, σ^{eng}. This difference previously shown in Figs. 7.9a and 7.9b could be explained by the high nonlinearity of the material described by the Norton flow rule with a stress exponent $n = 10$ at 600˚C.

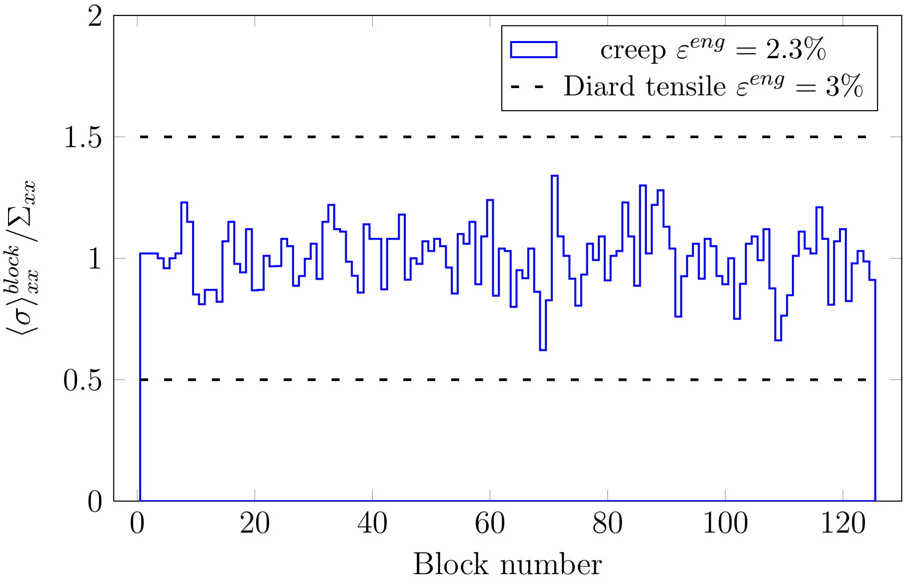

Figure 7.13: Ratios $\langle\sigma\rangle_{xx}^{block}/\Sigma_{xx}$ at an engineering strain of 2.3% (after 50×10^3h) during the creep test at 600˚C and 90 MPa on the grade 91 steel, compared with the bound values computed by Diard et al. [125] at an engineering strain of 3% during a tensile test carried out on a Zr alloy at room temperature and at a strain rate of 1×10^{-5}s^{-1}.

The computation using a polycrystalline aggregate containing 5^3 blocks loaded at 600˚C under 90 MPa has been stopped at an engineering strain of 2.3% and a creep time of 50×10^3h because of the long computation time. Nevertheless, at this time the stress distribution seems to be stabilized with respect to creep time (Fig. 7.14). The computed ratio $\langle\sigma\rangle_{xx}^{block}/\Sigma_{xx}$ at this creep strain is compared with the bounds obtained from the computations carried out by Diard et al. [125] on a polycrystalline aggregate of a Zr alloy subjected to a tensile test at room temperature up to a macroscopic strain of 3% (Fig. 7.13). The variation amplitudes of $\langle\sigma\rangle_{xx}^{block}/\Sigma_{xx}$ computed during the creep test on the grade 91 steel are slightly lower than the ones estimated by Diard et al. [125] for the tensile test on the Zr alloy (Fig. 7.13). This is may be due to the used number of slip systems for the Zr alloy [125] lower than the one used for our computations (24 slip systems for the bcc structure). Besides, the crystal orientations of the Zr alloy aggregate are represented by a texture on the pole figure [125], whereas the ones used for grade 91 steel are random.

7.5.2 Effect of creep time

The evolution of the cumulative distributions of $\langle\sigma\rangle_{xx}^{block}$ and $\langle\varepsilon\rangle_{xx}^{block}$ with creep time are presented in Fig. 7.14. The scatter in distribution of $\langle\sigma\rangle_{xx}^{block}$ increases with increasing creep time. The mean macroscopic stress increases only by 0.2% after a creep time of 50×10^3h, due to a reduction in the aggregate cross-section. The fraction of the blocks subjected to a tensile stress lower than the engineering stress (90 MPa) is 50% at almost the creep beginning. This fraction reduces then to 40% at a creep time of 50×10^3h. The distribution of $\langle\sigma\rangle_{eq}^{block}$ is different from the one of $\langle\sigma\rangle_{xx}^{block}$ (Figs. 7.14), which is due to local stress multiaxiality (see stress triaxiality distributions plotted in Fig. 7.11). The average of all $\langle\sigma\rangle_{eq}^{block}$ values increases with increasing time, but the macroscopic Mises stress is almost constant.

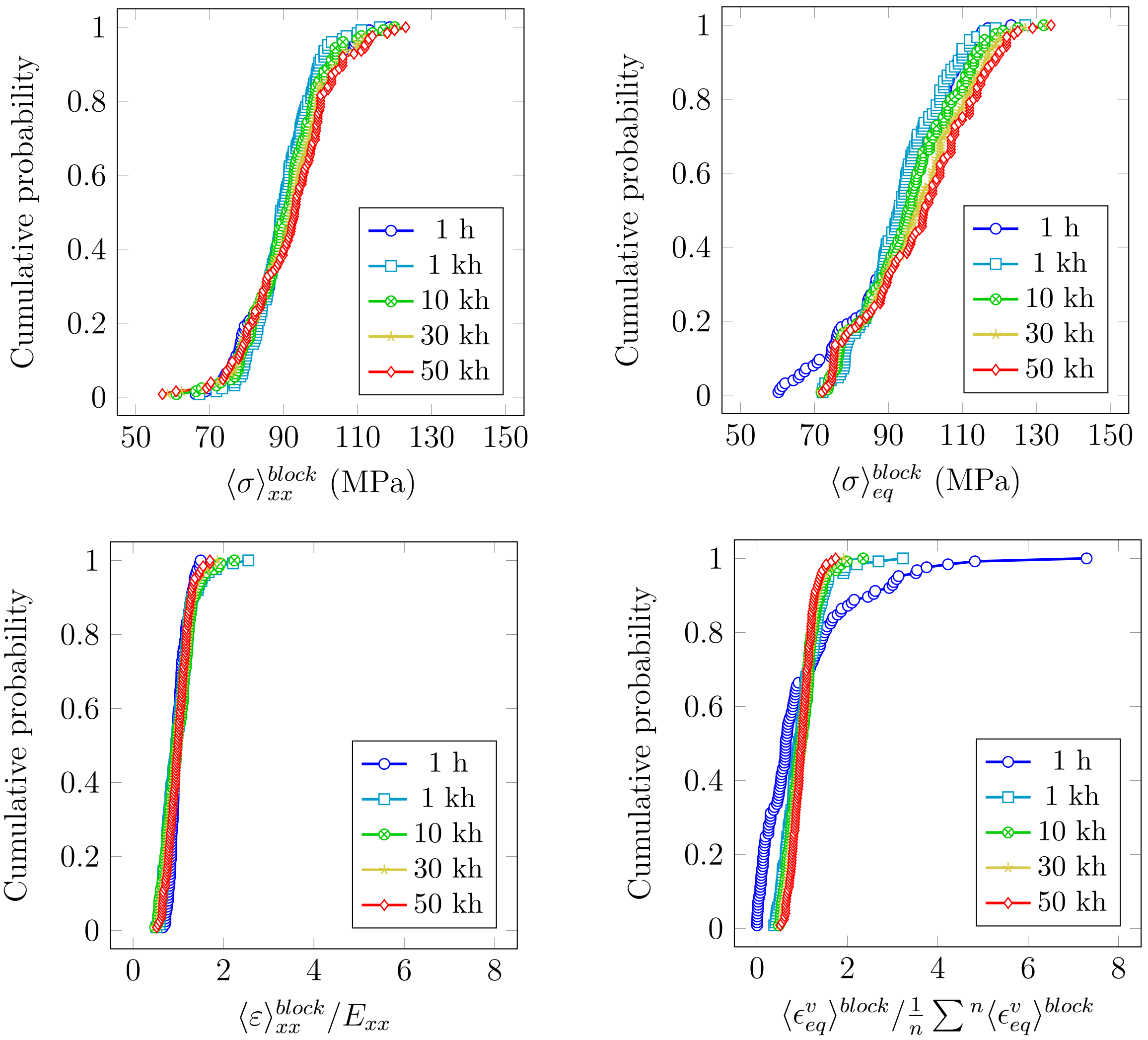

Figure 7.14: Effect of creep time on the cumulative probability distributions of the average mechanical fields per block during the creep test at 600°C and 90 MPa. A polycrystalline aggregate constituted of 5^3 blocks meshed by 4^3FEs/block is used. The crystal viscoplasticity parameter values are given in Table 7.1.

The distributions of $\langle\varepsilon\rangle_{xx}^{block}$ along creep time is plotted in Fig. 7.14. With increasing creep time, this strain tends to be more and more homogeneous through the polycrystalline aggregate. From a creep time of 1000 h, the distribution of $\langle\varepsilon\rangle_{eq}^{block}$ follows the same evolution as the one of $\langle\varepsilon\rangle_{xx}^{block}$ (Fig. 7.12). At the creep beginning, the scatter in $\langle\varepsilon_{eq}^{v}\rangle^{block}$

is high. At this time, only a small number of blocks are viscoplastically deformed. At the same time, the distribution of $\langle\varepsilon\rangle_{xx}^{block}$ is almost homogeneous. This strain contain indeed the elastic contribution not negligible at the creep beginning. As the creep time is longer, this contribution is negligible.

Figure 7.14 show that the viscoplastic equivalent stress tends to be more and more heterogeneous with increasing engineering strain (or increasing creep time). Contrary to the viscoplastic equivalent stress, the viscoplastic equivalent strain tends to be more and more homogeneous. Similar results have been obtained from the simulation of fatigue tests on nickel polycrystalline aggregates in the crystal elastoplasticity framework carried out by Steckmeyer et al. [145]. These results showed that the more the macroscopic plastic strain amplitude is high, the more the distributions of viscoplastic equivalent strain tend to be uniform.

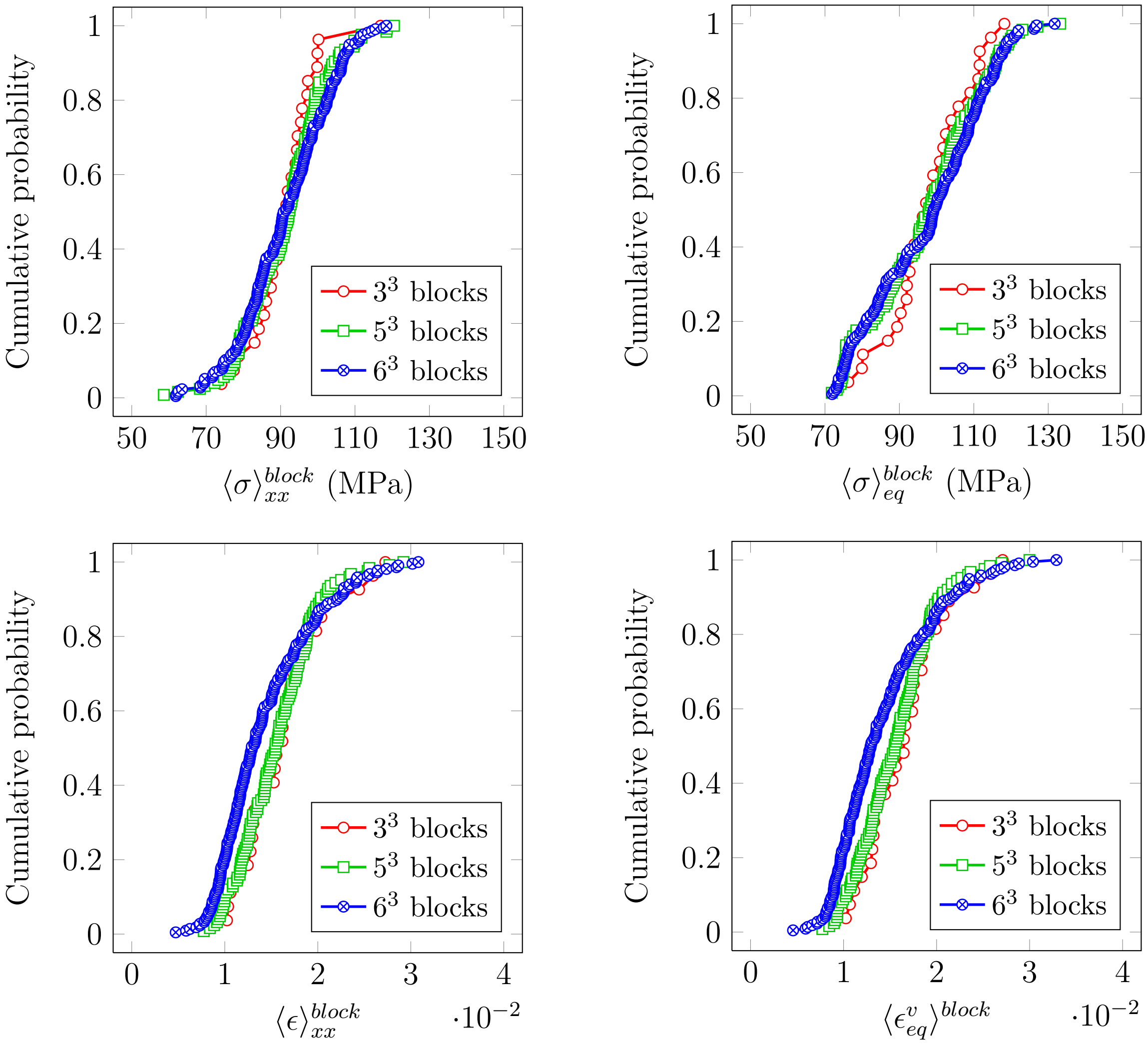

Figure 7.15: Influence of the number of blocks on the distributions of $\langle\sigma\rangle_{xx}^{block}$, $\langle\varepsilon\rangle_{xx}^{block}$, $\langle\epsilon_{eq}^{v}\rangle^{block}$ and $\langle\sigma\rangle_{eq}^{block}$ after 30×10^3h of creep test at 600°C and 90 MPa. All polycrystalline aggregates are meshed by 4^3 FEs/block. the crystal viscoplasticity parameter values reported in Table 7.1 are used.

7.5.3 Effect of the number of blocks

Three polycrystalline aggregates containing respectively 3^3, 5^3 and 6^3 blocks are used to study the distributions of $\langle\sigma\rangle_{xx}^{block}$, $\langle\varepsilon\rangle_{xx}^{block}$, $\langle\sigma\rangle_{eq}^{block}$ and $\langle\varepsilon_{eq}^{v}\rangle^{block}$ during the creep test at 600˚C and 90 MPa. For each polycrystalline aggregate, only one set of random crystal orientations is used. All polycrystalline aggregates are meshed by 4^3 FEs/block, whereas the effect of finer meshing density will be studied in the next section.

Figure 7.15 shows the distributions of the four variables after a creep time of 30×10^3h. By using 5^3 and 6^3 blocks, the corresponding distributions of $\langle\sigma\rangle_{xx}^{block}$ are only slightly different. The same observation is hold for the distributions of $\langle\sigma\rangle_{eq}^{block}$. The distributions of $\langle\varepsilon\rangle_{xx}^{block}$ for the three numbers of blocks converge only for $\langle\varepsilon\rangle_{xx}^{block} \geq 2\%$. For a higher number of blocks, the distribution of $\langle\varepsilon\rangle_{xx}^{block}$ is more scattered and the average value of $\langle\varepsilon\rangle_{xx}$ over the polycrystalline aggregate is lower. The same observation is made concerning the distribution of $\langle\varepsilon_{eq}^{v}\rangle^{block}$. For larger aggregates, blocks may be constrained by their neighbours and their deformation fields are scattered. This effect may allow explaining the decrease in engineering strain curves shown in Fig. 7.6 as well as a tendency of the primary creep stage to last for longer amounts of time for higher numbers of blocks.

7.5.4 Effect of mesh refinement

Two numbers of FEs per block are chosen to study the sensitivity of the stress and strain distributions due to mesh refinement: 4^3 and 6^3. A polycrystalline aggregate of 5^3 blocks and one set of random crystal orientations are used. The polycrystalline aggregate is subjected to uniaxial tensile creep at 600˚C and 90 MPa.

The distributions of $\langle\sigma\rangle_{xx}^{block}$ and $\langle\epsilon\rangle_{xx}^{block}$ after a creep time of 30×10^3h using either the lower or the higher number of finite elements are plotted in Fig. 7.16. Using either of both meshing parameters, the corresponding values of $\langle\sigma\rangle_{xx}^{block}$ only differ by less than 5%. By increasing the meshing parameter from 4^3 to 6^3, the values of $\langle\epsilon\rangle_{xx}^{block}$ increase by up to 60%. This is due to the high non-linearity obeying the Norton flow rule with a stress exponent of $n = 10$ at 600˚C. Thus, the axial stress is significantly less sensitive to the mesh refinement than the axial strain.

7.5.5 Effect of the choice of the V^* values

The identified value of V^* for 500˚C is reported in Table 7.1, i.e. $350b^3$. An additional value of V^* is chosen, $400b^3$, in order to study the stress sensitivity due to the choice of this parameter for the creep test at 500˚C and 230 MPa. The used polycrystalline aggregate contains 5^3 blocks and each block is meshed by 4^3 FEs.

The distributions of $\langle\sigma\rangle_{xx}^{block}$ and $\langle\epsilon\rangle_{xx}^{block}$ after a creep time of 50×10^3h (required time to reach the minimum creep strain rate) are plotted in Fig. 7.17. Using either of both V^* values, the axial stress only differ by less than 5%. But when using the value of $V^* = 400b^3$ rather than $350b^3$, the axial strain increases by a factor ranging between 2 and 2.5. In fact, as shown in section 7.4.4 (see also Fig. 7.7) that using the value $400b^3$ for V^* the predicted macroscopic minimum strain rate is approximately 2 times higher than the one obtained using the other value of V^*.

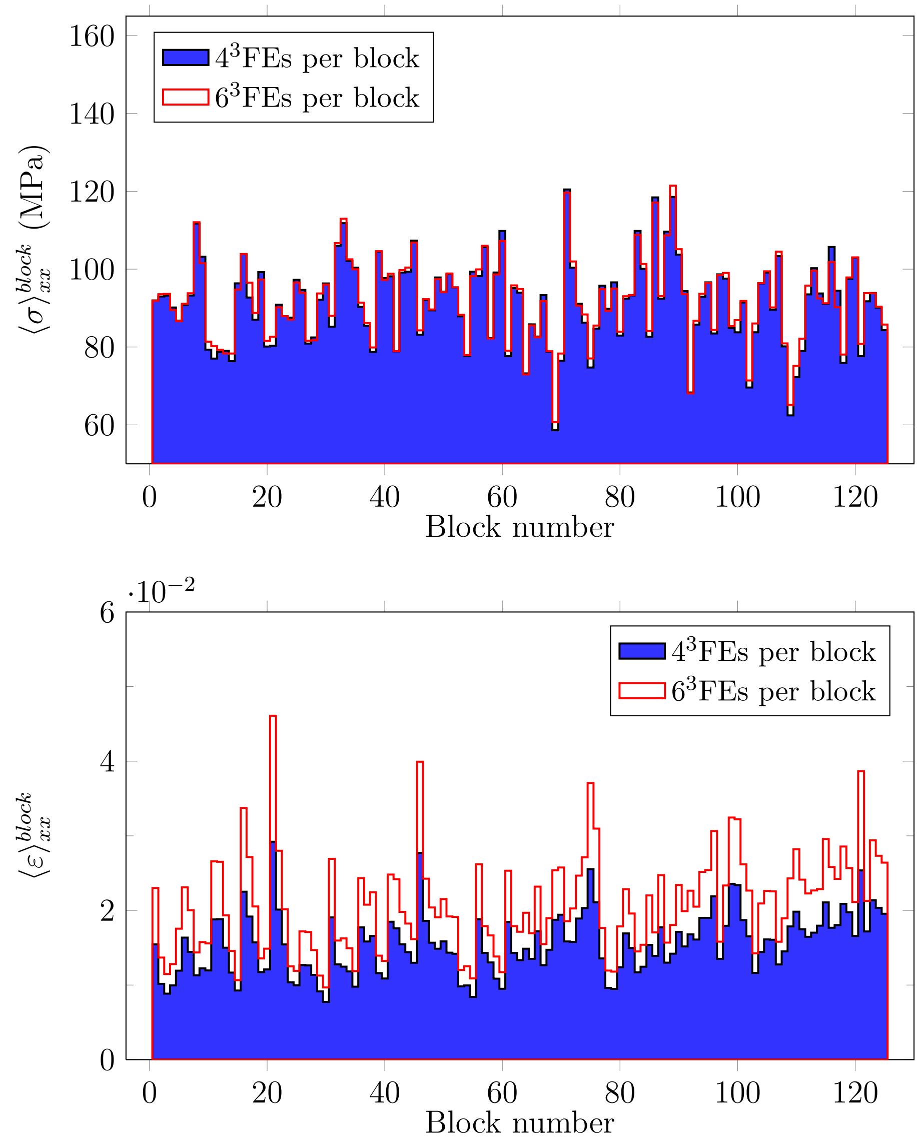

Figure 7.16: Effect of mesh refinement on the distributions of $\langle\sigma\rangle_{xx}^{block}$ and $\langle\epsilon\rangle_{xx}^{block}$ after 30×10^3h of creep test at 600˚C and 90 MPa, using a polycrystalline aggregate of 5^3 blocks and one set of random crystal orientations.

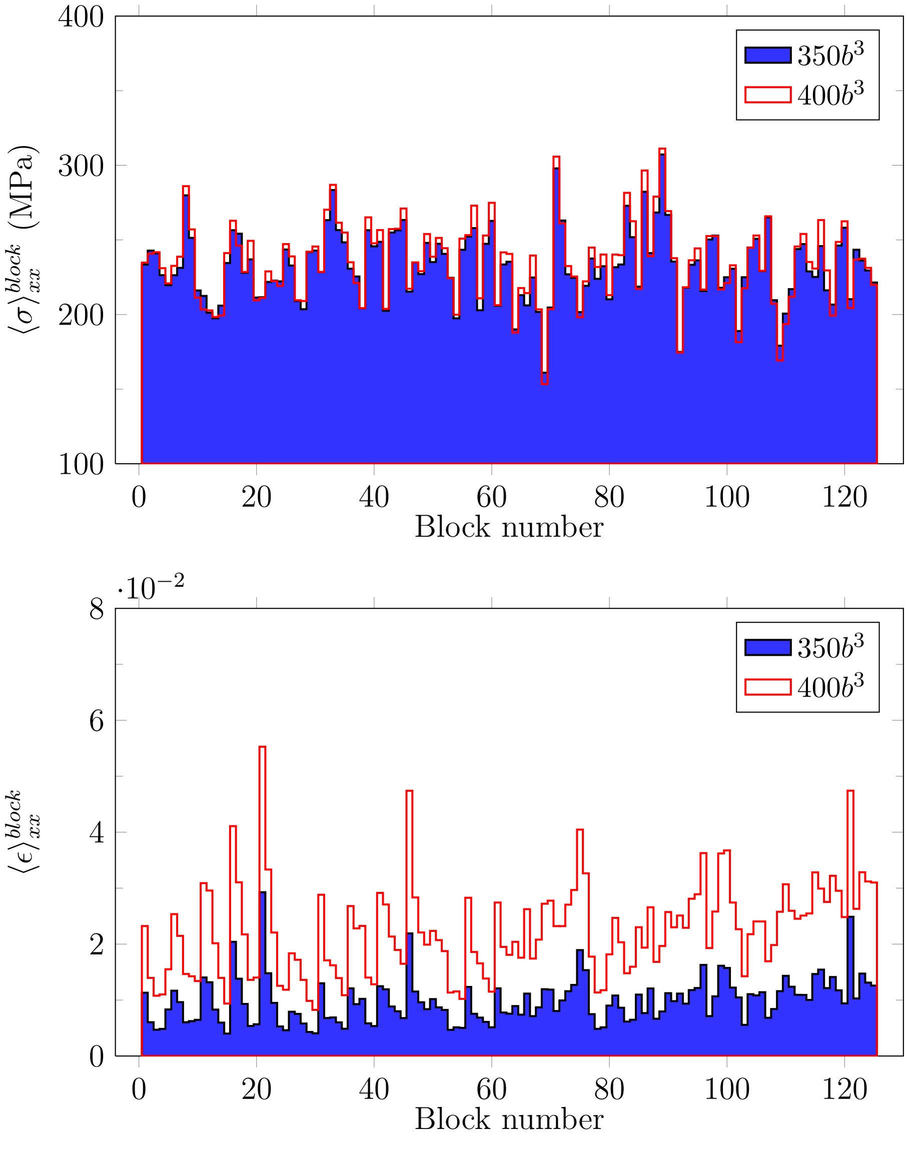

Figure 7.17: Effect of the V^* value choice on the distributions of $\langle\sigma\rangle_{xx}^{grain}$ and $\langle\epsilon\rangle_{xx}^{grain}$ after 50×10^3h of creep test at 500°C and 230 MPa. A polycrystalline aggregate of 5^3 blocks is used and meshed by 4^3 FEs/block.

7.6 Conclusions

Identification of the crystal viscoplasticity constitutive parameters results in a unique value of ΔG as well as values of V^* that differ by about 15% and are lower than the one experimentally determined in [140] by about 25%. Numerous computations have been carried out in order to obtained the parameter values obeying these conditions.

The limited availability of computation facilities did not allow us to carry out heavier calculations using very fine meshing (more than 4^3 FEs per block) of polycrystalline aggregates containing high numbers of blocks (6^3 and 7^3). The computation times corresponding to different aggregate sizes are: 3 days using 2^3 blocks meshed by 4^3 FEs/block, 5 days using 5^3 blocks (4^3 FEs/block), 9 days using 6^3 blocks and between 2 and 3 weeks using 7^3 blocks (4^3 FEs/block). To save computation time, the adjustment of the crystal viscoplasticity constitutive parameters was based on the macroscopic response of the polycrystalline aggregate containing 5^3 blocks meshed using 4^3 FEs per block. The results show that the minimum strain rate could increase by a factor lower than 2 if finer meshing density is used.

The mean block stress analyses show that the distribution of the average stress per block is weekly dependent on the choice of the V^* value as well as on meshing refinement. This is not the case for the distribution of the average strain per block because of the strong non-linearity of the viscoplasticity flow rule (Norton stress exponent $n = 10$ at 600°C, $n = 20$ at 500°C).

The finite element computations show that the average axial stress per block varies by ±40% with respect to the macroscopic axial stress for the creep test at 600°C and 90 MPa when the engineering creep strain reaches 2.3%. The absolute variation amplitude is slightly lower than the one computed by Diard et al. [125] for a tensile test carried out on a Zr alloy at room temperature. Indeed, zirconium microstructures present a crystallographic texture and has a number of slip systems lower than Grade 91 steel.

The viscoplasticity constitutive law identified in this chapter is now used to study the stress and strain concentrations at triple junctions presented in the following chapter. This study is carried out using the plane strain hypothesis and 2-D microstructures built from either a simple triple point model or EBSD maps. A very fine meshing density is applied to zones close to triple junctions.

Chapter 8

Finite element computations of normal stress fields close to polycrystalline triple junctions

8.1 Model of polycrystalline triple junctions

8.1.1 Microstructure geometry and meshing

In this section, we use the crystal viscoplasticity model as calibrated in the previous chapter. Normal stress fields are predicted for block boundaries perpendicular to the loading axis, at which cavities are preferentially observed. The "Triple point model" is constituted of three adjacent blocks surrounded by an isotropic homogeneous matrix (Fig. 8.1). The block boundaries form between them a regular angle of 120°. One of these boundaries, L2, is perpendicular to the loading axis. The matrix represents the average behaviour of all surrounding blocks.

The crystal orientations of the blocks in tempered martensitic ferritic steels with respect to one and another are either random (when they belong to two different former austenitic grains) or follow the relationships of Kurdjumov-Sachs [48] and Nishiyama-Wassermann [49]. In the first case, the crystal misorientations could be high and lead to more important stress concentration at the triple point. Thus, the three blocks belonging to the triple point are assumed to have random crystal orientations.

In order to study cavities located in the bulk material, only quasi 2D plane strain analysis is carried out. This leads to less time consuming computations than full 3D computations and allows using very fine meshing and numerous independent sets of random crystal orientations. Under such circumstance, the 2D microstructure in plane XY shown in Fig. 8.1 is extruded into the 3D dimension along the Z-direction. This model contains only one finite element in the thickness. Zero displacement along the Z-direction is prescribed at the lower and upper 2D surfaces. This approach is similar to 2D plane strain analysis. Quasi 2D plane stress analysis has also been carried out, but this did not lead to large differences in normal stress to block boundaries with respect to quasi-plane strain analysis.

The meshing of the triple point model is shown in Figs. 8.1a and 8.1b. The three crystals are meshed using very fine finite elements, whereas the meshing of the surround-

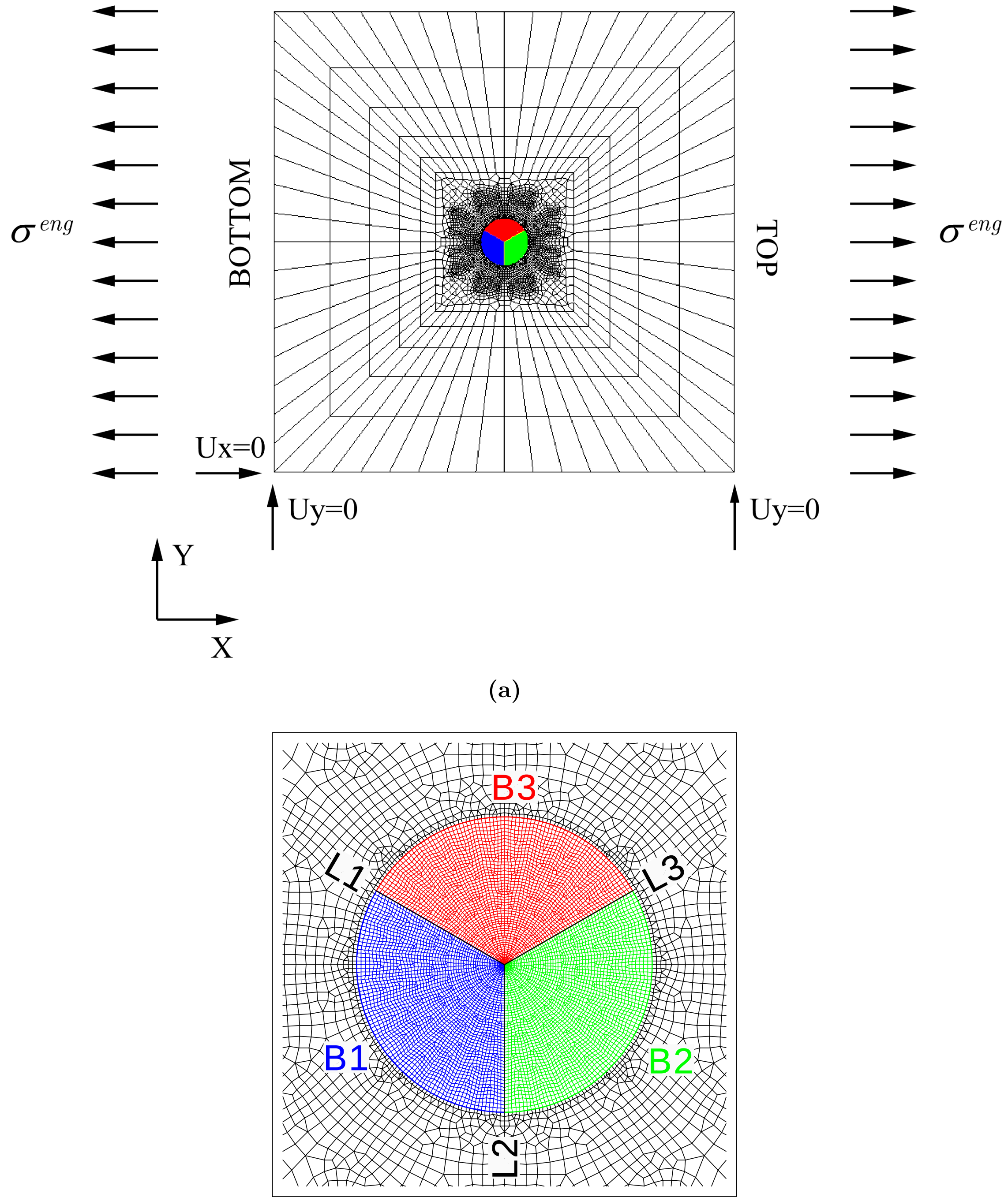
σ^{eng}
BOTTOM
TOP
σ^{eng}
Ux=0
Uy=0
Uy=0
Y
X
B3
L1
L3
B1
B2
L2

(a)

(b)

Figure 8.1: Meshing of the triple point area including one triple point and their boundaries. The thickness of the model is equal to the size of finite elements located at the triple junction (0.4, 0.1 or 0.05 units).

ing matrix is coarser. The finest meshing is assigned to the zone around the triple point using different element sizes in order to check mesh size independence. The thickness along the Z-direction is chosen so that the element aspect ratio ranges between 1/5 and 5.

The crystal elasto-viscoplasticity constitutive equations assigned to the three crystals are described in section 6.2 with parameters given in Tables 6.2 and 7.1. The matrix obeys the isotropic creep flow rule described in the following section.

The applied boundary conditions are shown in Fig. 8.1a. The six degrees of freedom are blocked to prevent any rigid body motion. Engineering stresses are applied to the BOTTOM and TOP edges, whereas the lateral edges are free surfaces.

8.1.2 Isotropic creep flow rule

The uniaxial creep behaviour is modelled in the RCC-MRx code [36] by the following equations:

$$\varepsilon_{xx}^{p(1)} = C_1 \left(\sigma_{xx}\right)^{n_1} t^{p_1} \qquad \text{for } t < t_{fp} \tag{8.1}$$

$$\varepsilon_{xx}^{p(2)} = \varepsilon_{xx}^{p(1)}(t_{fp}) + C_2 \left(\sigma_{xx}\right)^{n_2} \left(t - t_{fp}\right) \qquad \text{for } t \geq t_{fp} \tag{8.2}$$

where $\varepsilon_{xx}^{p(1)}$ and $\varepsilon_{xx}^{p(2)}$ are respectively uniaxial creep (or viscoplastic) strain during creep stage I and creep stage II. The end time of creep stage I is annotated as t_{fp}, which could be determined from Eqs. (8.1) and (8.2). Equation (8.2) is equivalent to the Norton flow rule with constants C_2 and n_2, also annotated as C and n. The values of the constants of these equations are given in the RCC-MRx code [36] for 9%Cr steels (also for 316 austenitic steel), but do not allow modelling creep strain vs. time curves in agreement with the experimental results of the creep tests under study (at 500˚C and 230 MPa, at 600˚C and 90 MPa). Thus, the values of these constants are readjusted using creep data at 500˚C (σ^{eng} ranges between 210 and 270 MPa, see Table 3.3) and at 600˚C (σ^{eng} ranges between 70 and 125 MPa, see Table 3.3). These parameter values are reported in Table 8.1. The identified parameter values are checked to yield predicted creep strain vs. time curves of the two creep tests, one at 500˚C and 230 MPa and another at 600˚C and 90 MPa, using analytical equations (8.1) and (8.2) in agreement with the experimental results till the end of creep stage II.

Table 8.1: Ajusted parameter values for the creep flow rule described by Eqs. (8.1) and (8.2), using creep data at 500˚C for σ^{eng} ranging between 210 and 270 MPa (see Table 3.3) and at 600˚C for σ^{eng} ranging between 70 and 125 MPa (see Table 3.3).

	$t < t_{fp}$			$t \geq t_{fp}$	
T (˚C)	n_1	p_1	C_1 (MPa$^{-n_1}$h$^{-p_1}$)	n_2	C_2 (MPa$^{-n_2}$h^{-1})
500	2.97	0.360	2.81×10^{-11}	20.35	1.56×10^{-55}
600	3.84	0.347	9.83×10^{-12}	9.94	8.27×10^{-27}

The three-dimensional isotropic creep behaviour is then modelled using the Von Mises components of stress and strain tensors for the implementation in CAST3M. In this case, the uniaxial stress and strain components in Eqs. (8.1) and (8.2) are replaced by the Von Mises components. The three-dimensional isotropic creep flow rule with constants given in Table is then used for computation of axial creep strain of a cube subjected to two uniaxial creep tests, one at 500°C under 230 MPa and another 600°C under 90 MPa. The computed creep strain vs. time curves are weakly different from the ones obtained using uniaxial equations (8.1) and (8.2).

8.1.3 Effect of mesh refinement on normal stress fields

The microstructure model does not contain only one triple point which is the junction of the three block boundaries. Indeed, the intersections between these block boundaries and the interfaces between the blocks and the matrix are also kinds of triple points even if the matrix does not behave like a crystal. Since only the first triple point is the aim of our study, only a half of the block boundary length (measured from the center of the three blocks) is taken into account to plot normal stress field along L2.

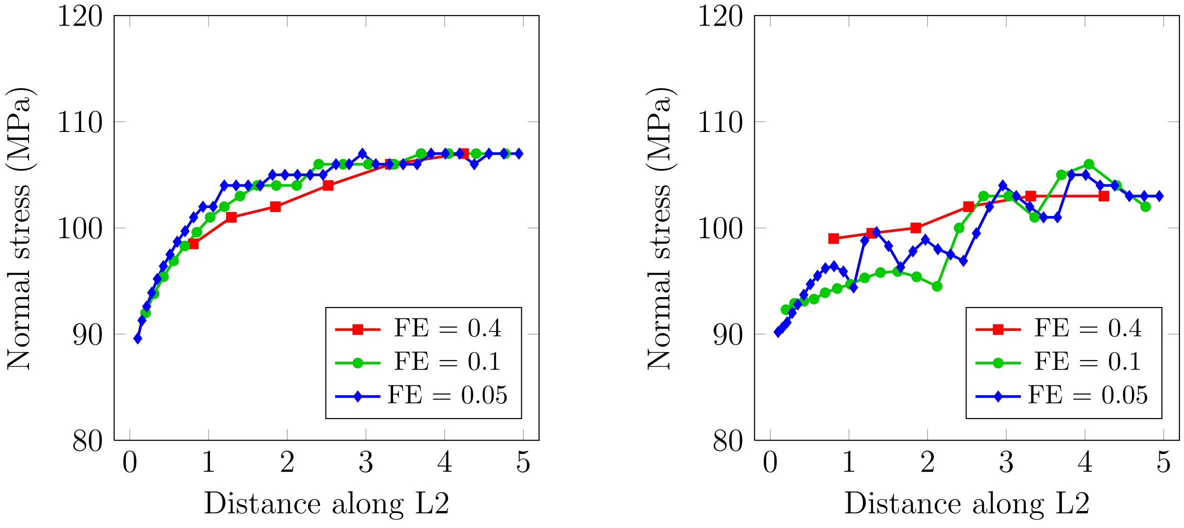

(a) After 1×10^3h **(b)** 30×10^3h

Figure 8.2: Effect of mesh refinement on the normal stress field along block boundary L2 during creep at 600°C and 90 MPa for one set of random crystal orientations. The length of block boundary L2 is 10 length units. The triple point is located at distance 0 and the middle of block boundary L2 at distance of 5 units.

Different element sizes at the triple point are chosen in order to study the effect of mesh refinement on the normal stress along block boundary L2. Figure 8.2 shows that an element size of FE = 0.05 units (1/200 of block size) is considered to be sufficiently fine for mesh refinement independence of the normal stress field along L2. This meshing parameter will be used for the study of the distributions of normal stress fields for the different sets of random crystal orientations presented in the following section.

8.1.4 Effect of the sets of random crystal orientations on normal stress fields

In this section, normal stress fields to block boundary L2 during creep tests at 500°C under 230 MPa and at 600°C under 90 MPa are presented. For each creep test, normal stress fields are obtained from twenty computations. These 20 computations correspond to 20 independent sets of random crystal orientations applied to the three blocks. These crystal orientations are verified to represent no texture from inverse pole figure representations.

The normal stress fields to block boundary L2 at the triple junction, σ_{nn}^{tp}, computed from the 20 sets of crystal orientations are plotted along creep time in Fig. 8.3. Their average values are slightly higher than the macroscopic stress, σ^{eng}, with a relative difference not higher than 10%. During the first creep test, the normal stress field close to the triple junction varies by ±30% at the creep beginning and by -70%/+80% after 50×10^3h. During the second creep test, the normal stress field close to the triple junction varies by -30%/+35% at the creep beginning and by amplitudes of -50%/+70% after 30×10^3h.

The normal stress profiles along block boundary L2 obtained from all the 20 sets of random crystal orientations are presented in the following paragraph.

a. Normal stress profile along block boundary L2

The normal stress profiles for both creep tests computed for the same sets of random crystal orientations are very similar (compare Fig. 8.4 and 8.5). These normal stress profiles are mainly influenced by the block crystal orientations.

Generally, the results do not show high stress singularity at the triple junction, ratio $\sigma_{nn}^{tp}/\sigma^{eng} \leq 1.5$. Exceptionally, the 8th set of random crystal orientations leads to a value of normal stress at the triple junction about 2 times higher than the macroscopic stress, $\sigma_{nn}^{tp}/\sigma^{eng} \approx 2$. This is explained by the following analysis of strain fields in the three blocks.

The strain and stress fields along the loading direction (XX) during the creep test at 600°C under 90MPa computed using the 8th set of random crystal orientations are compared with the ones using the first set. This one leads to normal stress fields along block boundary L2 representing the average value of the all normal normal stress fields obtained from the 20 sets (see Fig. 8.5a for set 1). In this case, the tri-crystal is constituted of one harder block (B3), one moderately hard block (B1) and one softer block (B2) (Fig. 8.6a). As the block B2 is softer than B3, load is transferred to B2 which is subjected to higher stress (Fig. 8.6c). For the 8th set, B1 and B2 are harder whereas B3 is softer (Fig. 8.6b). Additional load (indicated by the arrows) is transferred to the blocks B1 and B2. This is similar to the problem of a V-crack (having the shape of the block B3) subjected to a tensile stress which leads to high stress at the triple point (Fig. 8.6). In this case, the normal stress field close to the triple junction (see set 8 in Fig. 8.5a) is about 2 times higher than the one computed using the first random set (see set 1 in the same figure).

Considering with the explanation above, all cases where the normal stress fields at the triple point are higher than the one using the first set (Figs. 8.4 and 8.5), could correspond to tri-crystals constituted of B1 and B2 that are harder and of B3 that is softer. Among them, the 8th set could represent an extreme case where B3 is the softest and B1 and B2 are the hardest. All cases where the normal stress fields at the triple point are lower than one using the first set (Figs. 8.4 and 8.5) could correspond to tri-crystals

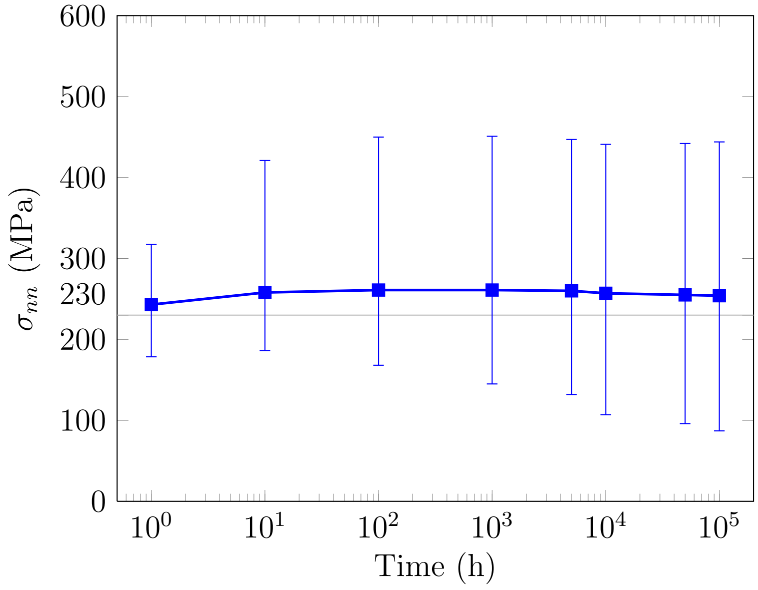

(a) Creep at 500°C under $\sigma^{eng} = 230$ MPa

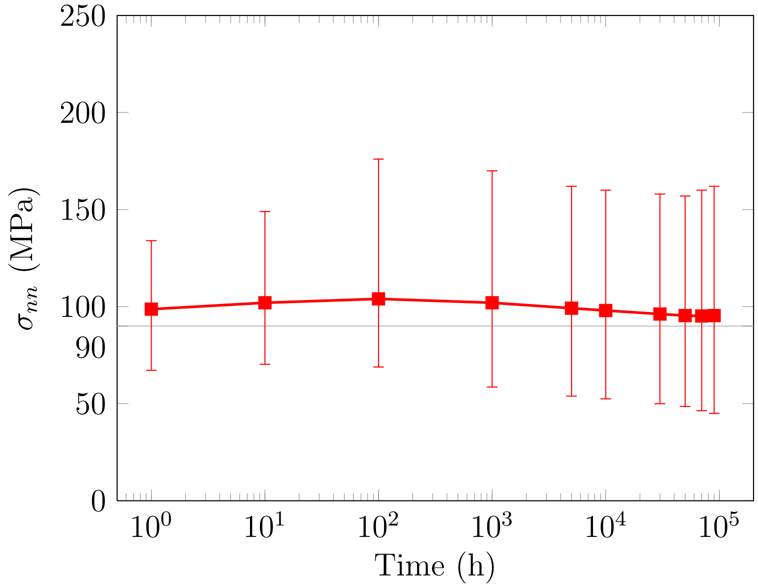

(b) Creep at 600°C under $\sigma^{eng} = 90$ MPa

Figure 8.3: Time evolution of normal stress fields at block boundary L2 close to the triple junction. Average value and amplitudes using 20 sets of random crystal orientations.

constituted of B1 and B2 that are both softer and of B3 that is harder.

The normal stress is maximum either close to the triple point, or close to the middle of L2 (Figs. 8.4 and 8.5) and more rarely somewhere between (see set 2 in the same figures). In the following paragraph, only the first two locations are chosen to study the normal stress statistics. The normal stress averaged on the half-length of L2 is also studied.

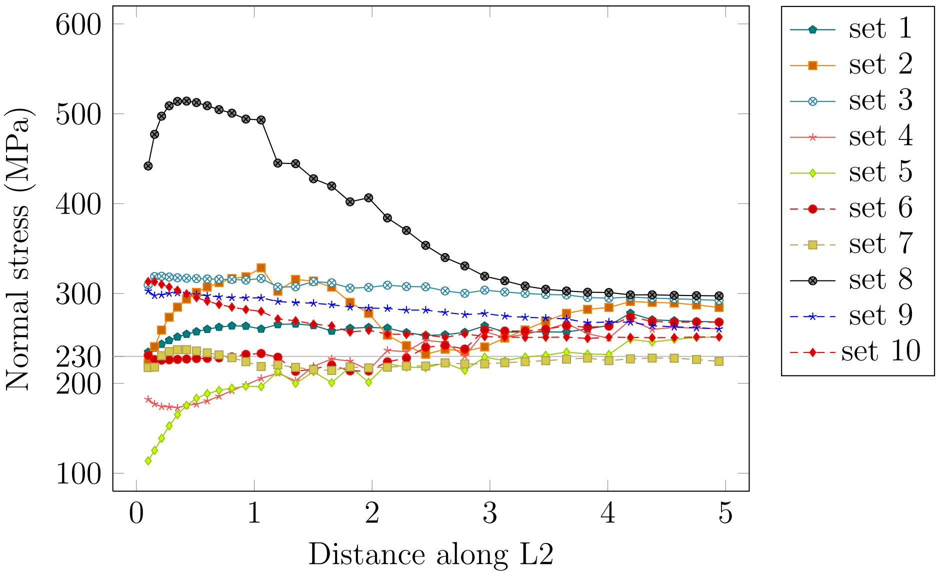

(a) First ten sets of random crystal orientations

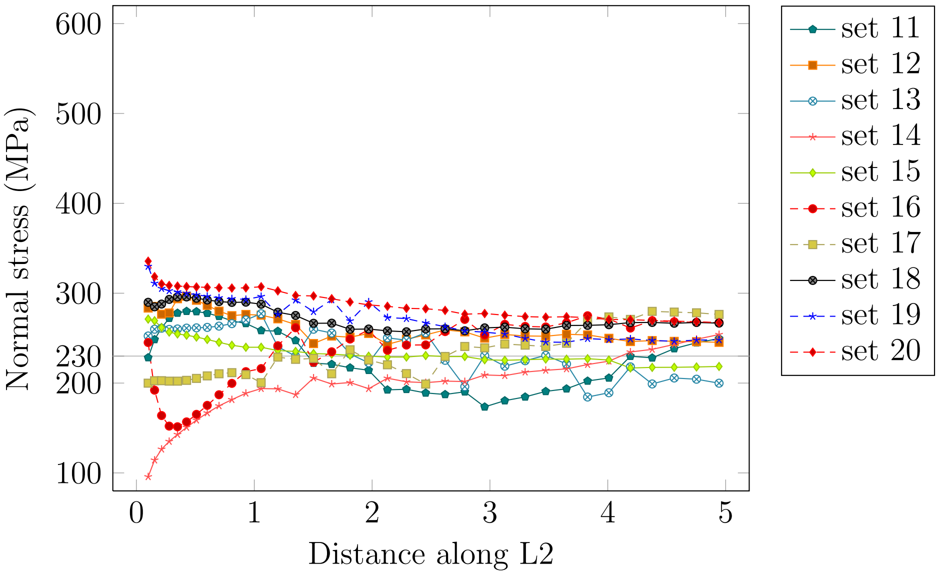

(b) Second ten sets of random crystal orientations

Figure 8.4: Normal stress profiles along a half length of block boundary L2 after 50×10^3h of creep at 500˚C under $\sigma^{eng} = 230$ MPa computed using 20 sets of ransom crystal orientations. The triple junction corresponds to distance 0. The total length of block boundary L2 is 10 units.

b. Time evolution of the normal stress fields

The time evolution of the normal stress fields at block boundary L2 close to the triple junction, σ_{nn}^{tp}, is plotted for the creep test at 500˚C and 230 MPa in Fig. 8.7a. Considering quite all of the 20 random sets of crystal orientations, the maximum time evolution of σ_{nn}^{tp} represents ±35%. This corresponds to the 8th and 14th sets. The maximum time evolution of the normal stress fields at the middle of L2, σ_{nn}^{mid} represents only ±15%. These maximum time evolution represents approximately the same amplitudes for the

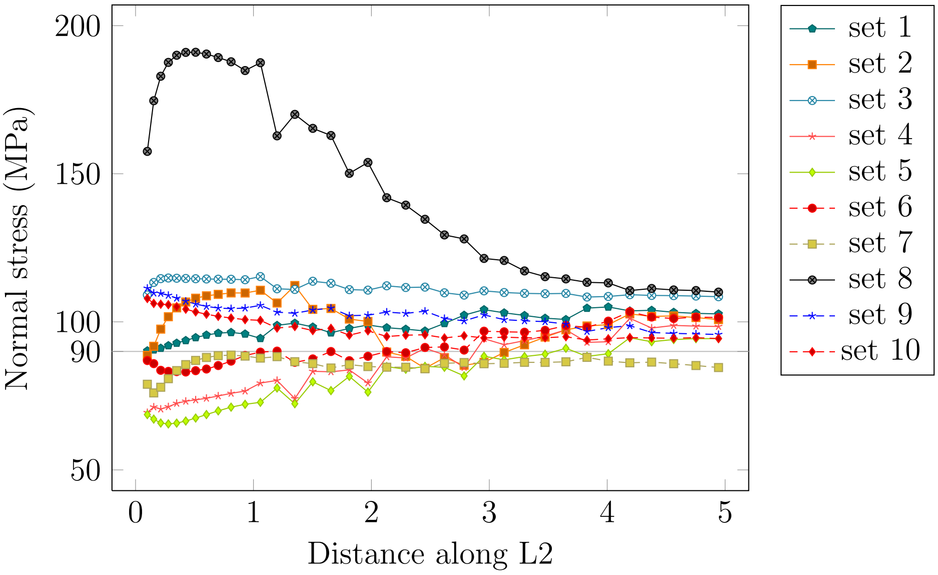

(a) First ten sets of random crystal orientations

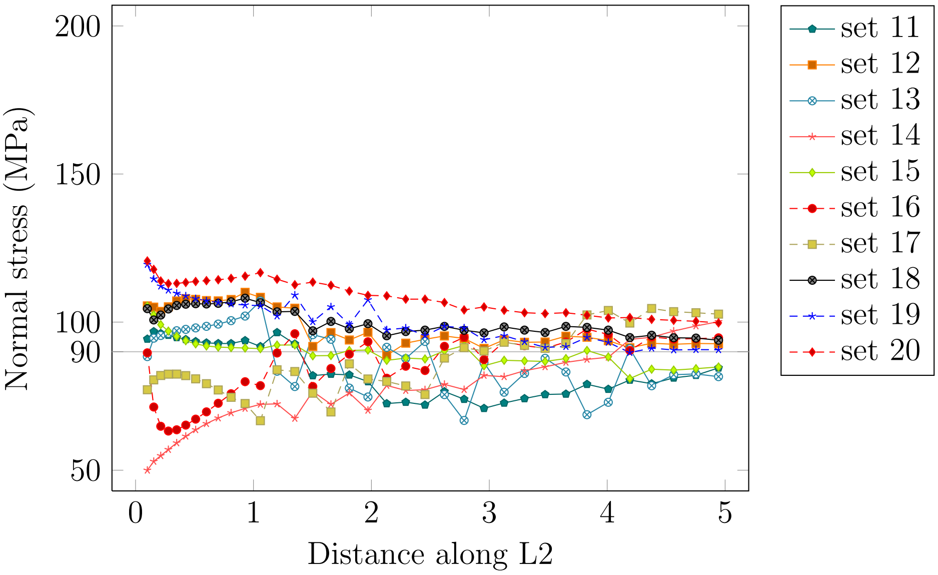

(b) Second ten sets of random crystal orientations

Figure 8.5: Normal stress profiles along a half length of block boundary L2 after 30×10^3h of creep at 600˚C under $\sigma^{eng} = 90$ MPa computed using 20 sets of random crystal orientations. The triple junction corresponds to distance 0. The total length of block boundary L2 is 10 units.

creep test at 600˚C and 90 MPa.

Figure 8.7a shows that all values of normal stress higher than the macroscopic stress ($\sigma^{eng} = 230$ MPa) at the quasi-beginning of creep (10 h) are then still higher during all along creep time. The ones lower than σ^{eng} at the quasi-beginning of creep (10 h) are still lower. This is also confirmed for the creep test at 600˚C and 90 MPa. This phenomenon might be explained by the effect of local block softness described in the previous paragraph.

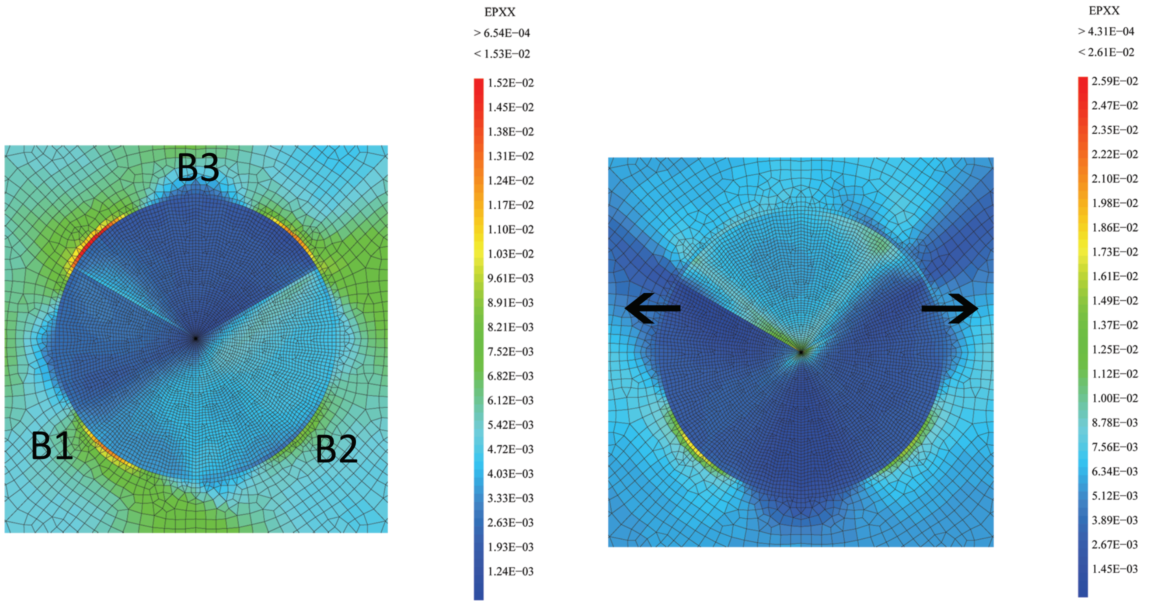

(a) ε_{xx}, 1st set **(b)** ε_{xx}, 8th set

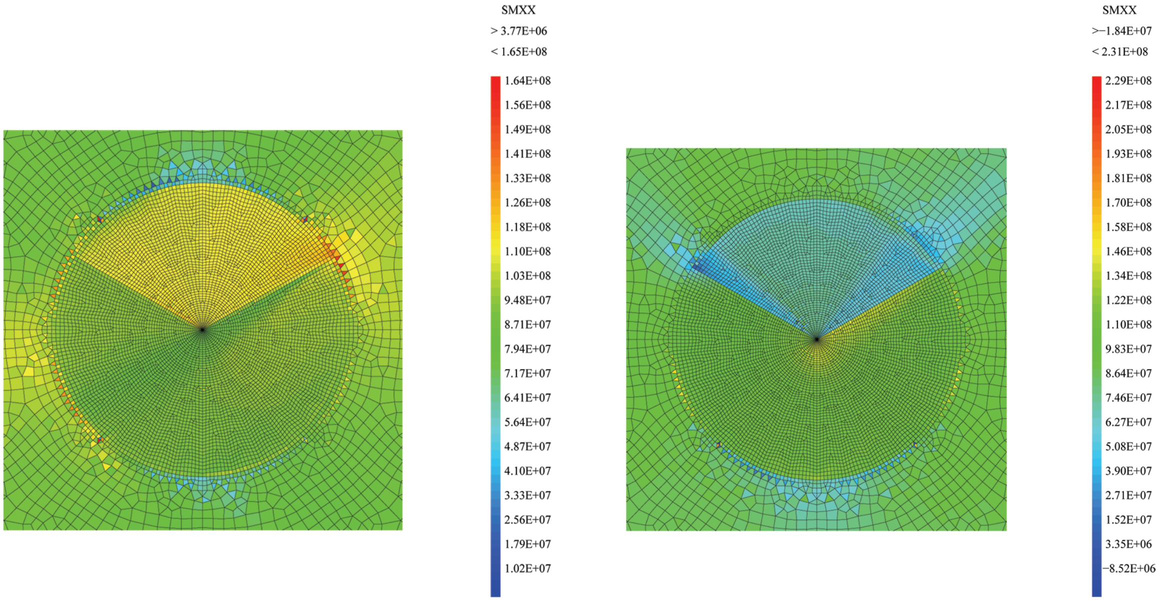

(c) σ_{xx}, 1st set **(d)** σ_{xx}, 8th set

Figure 8.6: Effect of the block softness on the normal stress distribution (in Pa) for two sets of random crystal orientations, after 30×10^3h of creep at 600°C under $\sigma^{eng} = 90$ MPa.

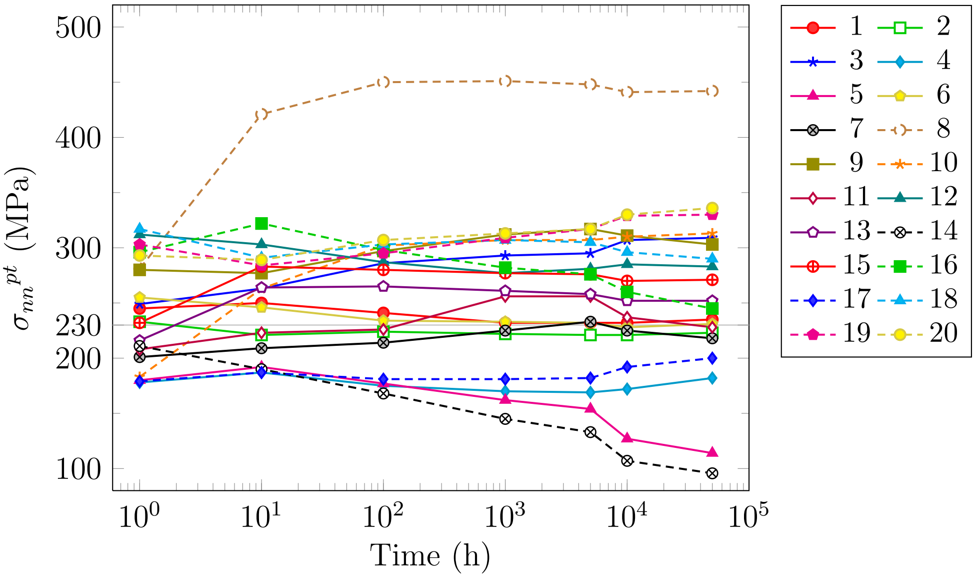

(a) Close to the triple junction

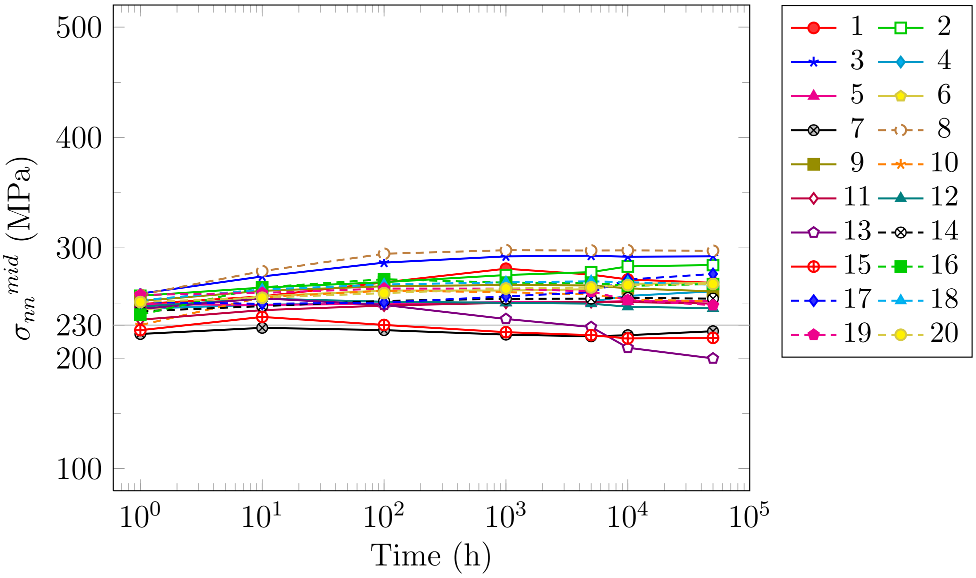

(b) At the middle of block boundary L2

Figure 8.7: Time evolution of the normal stress at block boundary L2 at two locations during creep at 500°C under 230 MPa.

The normal stress averaged along the half length of block boundary L2, $\overline{\sigma}_{nn}$ is evaluated. The average normal stress fields computed using all 20 sets of random crystal orientations are plotted along time of creep at 500°C and 230 MPa (Fig. 8.8). Considering all 20 sets, the maximum increase of the average normal stress represents 20%. This corresponds to the 8th set.

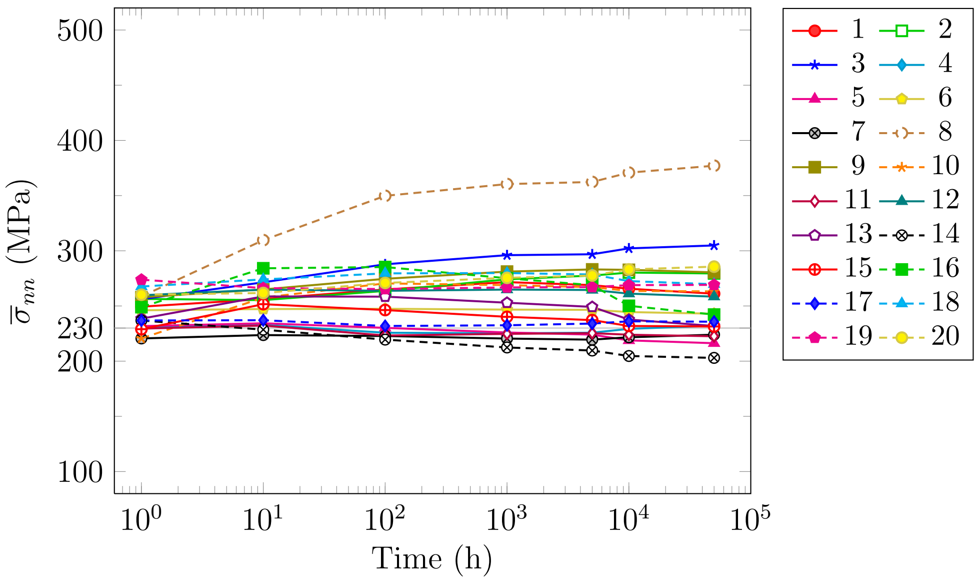

Figure 8.8: Time evolution of the normal stress averaged along the half length of block boundary L2 during creep at 500°C under 230 MPa. Symbols are related to the individual sets of blocks

c. Normal stress fields to L2 with respect to the macroscopic stress

Variation amplitudes of σ_{nn}^{tp}, σ_{nn}^{mid} and $\overline{\sigma}_{nn}$ with respect to the macroscopic stress, σ^{eng}, obtained from 20 computations for each creep test are estimated and reported in Table 8.2.

Normal stress σ_{nn}^{tp} corresponds to the highest amplitudes of variation with respect to the macroscopic stress. For the creep test at 500°C and 230 MPa, these amplitudes represent -20%/+40% at the creep beginning. When the minimum creep strain rate is reached, these amplitudes represent -60%/+40%, with the exception of the 8th microstructure configuration for which the difference from σ^{eng} represents +95%. For creep at 600°C and 90 MPa, the variation amplitudes represents -25%/+50% at the creep beginning. When the minimum creep strain rate is reached, the variation amplitudes represent -45%/+35%, with the exception of the 8th microstructure configuration where the difference from σ^{eng} represents +75%.

Normal stress σ_{nn}^{mid} corresponds to the lowest amplitudes of variations with respect to the macroscopic stress. For both creep tests, the absolute amplitudes of variation represent up to 15% at the creep beginning and up to 30% when the minimum creep strain rate is reached.

For the creep test at 500°C and 230MPa, random crystal orientations lead to values of $\overline{\sigma}_{nn}$ varying with respect to σ^{eng} by -10%/65% at an engineering strain of 2%. Diard et al. [125] have carried out finite element calculations of normal stress fields to grain boundaries in Zr alloy subjected to monotonic tensile test at room temperature. These authors found a ratio ranging between 0.5 and 1.5. The variation amplitudes during creep seem to be sightly higher than the ones computed for tensile test [125].

Table 8.2: Amplitude of variation of the normal stress at block boundary L2 with respect to the macroscopic stress due to random orientations. The minimum creep strain rate corresponds to creep times of 30×10^3h for the first creep test and of 50×10^3 of the second one. Twenty microstructure configurations are considered (Fig. 8.1).

500°C - 230 MPa	Probability	1 h	50 kh ($\varepsilon^{eng} = 2\%$)
Triple junction	19/20	-20% to +40%	-60% to +40%
	1/20 (8th)	+20%	+95%
Middle of L2	20/20	-5% to +15%	-15% to +30%
Mean value along one half of L2	19/20	-5% to +20%	-10% to +35%
	1/20 (8th)	+15%	+65%
600°C - 90 MPa	**Probability**	**1 h**	**30 kh ($\varepsilon^{eng} = 1\%$)**
Triple junction	19/20	-25% to +50%	-45% to +35%
	1/20 (8th)	+25%	+75%
Middle of L2	19/20	0 to +15%	-10% to +25%
Mean value along one half of L2	19/20	0% to +25%	-10% to +25%
	1/20 (8th)	+20%	+55%

8.2 Normal stress fields computed using microstructures based on EBSD measurements

In this section, more realistic microstructures are used to compute normal stress fields at block boundaries. Two microstructures have been identified using EBSD measurements by Barcelo and Fournier [119] after the two creep tests considered above, one at 500°C and 230 MPa (Fig. 8.9a) and another at 600°C and 90 MPa (Fig. 8.10a). These microstructures are located in the middle of the specimen diameter and on a longitudinal section of the specimen far from the fracture surface. Creep cavities are observed on both microstructures. Triple junctions containing some of these cavities are chosen for computation of normal stress fields at block boundaries.

8.2.1 Meshing

Figures 8.9b and 8.10b show the meshing of the modelled blocks based on two EBSD maps. The other surrounding blocks are not taken into account explicitely and are replaced by a homogeneous matrix which represent the average mechanical behaviour of microstructure. For each of both microstructures, two triple junctions (indicated by the red circles in Figs. 8.9b and 8.10b) are chosen for fine regular meshing. This analysis is carried out using the quasi-2D plane strain condition previously described; in fact, these microstructures are located in the bulk of the creep specimen.

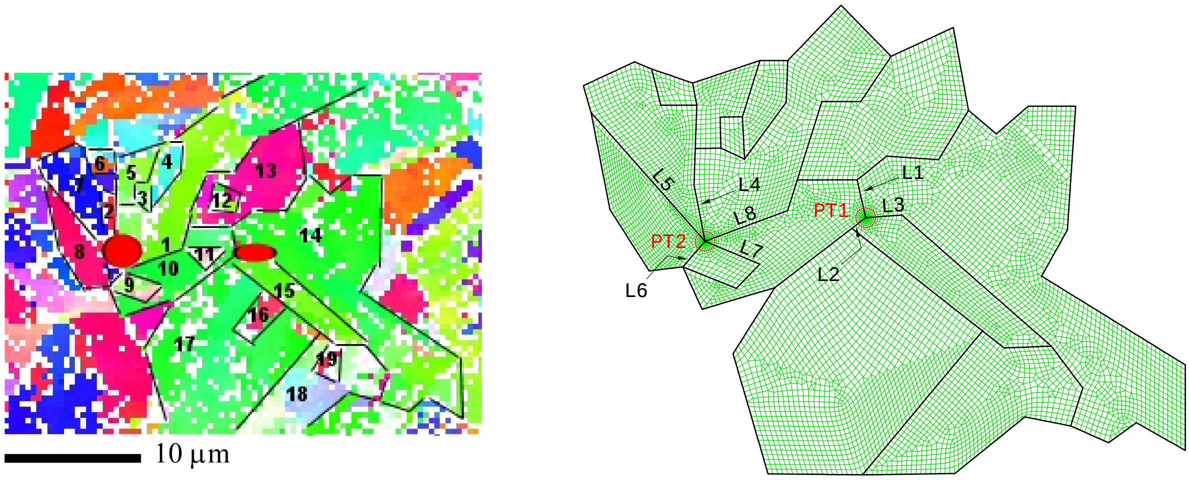
1
2
3
4
5
6
7
8
9
10
11
12
13
14
15
16
17
18
19
10 µm
L1
L2
L3
L4
L5
L6
L7
L8
PT1
PT2

(a) EBSD map of microstructure indexed and given in [119] containing cavities represented by the red oval or round regions.

(b) Microstructure after refilling the cavity areas and meshing. The element size at the two triple junctions, PT1 and PT2, is 0.05 µm.

Figure 8.9: Microstructure of grade 91 steel after the creep test at 500°C under 230MPa before and after meshing. The loading axis is horizontal. The EBSD map contains a high number of non-indexed pixels which could lead to an uncertainty of microstructure filling.

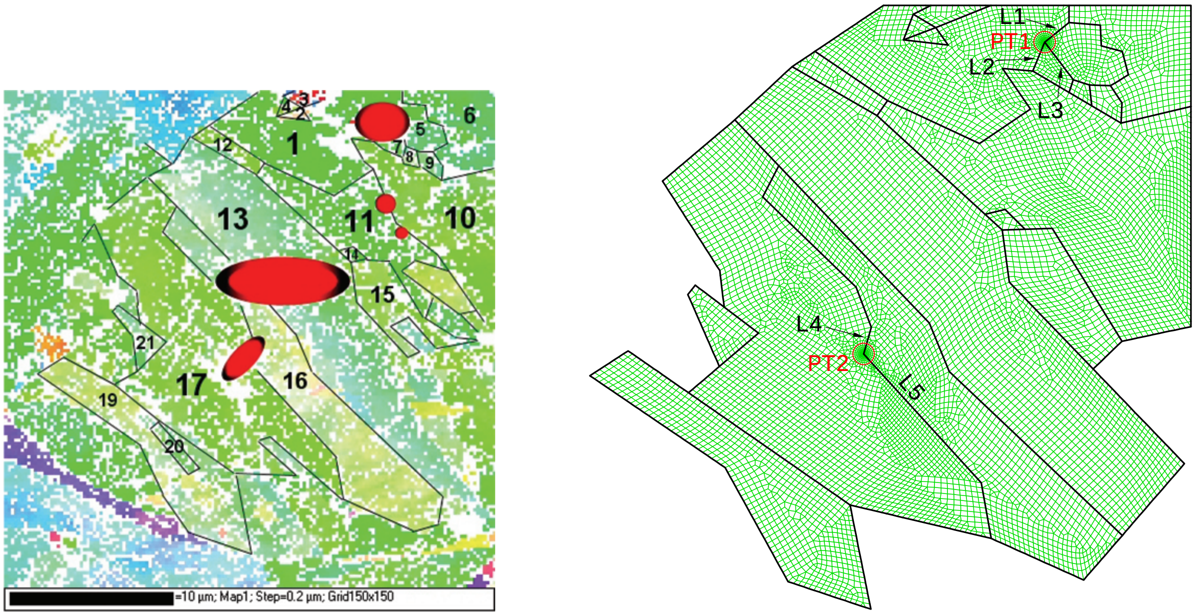
1
2
3
4
5
6
7
8
9
10
11
12
13
14
15
16
17
19
20
21
=10 µm; Map1; Step=0.2 µm; Grid150x150
L1
L2
L3
L4
L5
PT1
PT2

(a) EBSD map of microstructure indexed and given in [119] containing cavities represented by the red oval or round regions

(b) Microstructure after refilling the cavity areas and meshing. The element size at the two triple junctions, PT1 and PT2, is 0.05 µm.

Figure 8.10: Microstructure of grade 91 steel after the creep test at 600°C under 90MPa before and after meshing. The loading axis is vertical. The EBSD map contains a high number of non-indexed pixels which could lead to an uncertainty of microstructure filling.

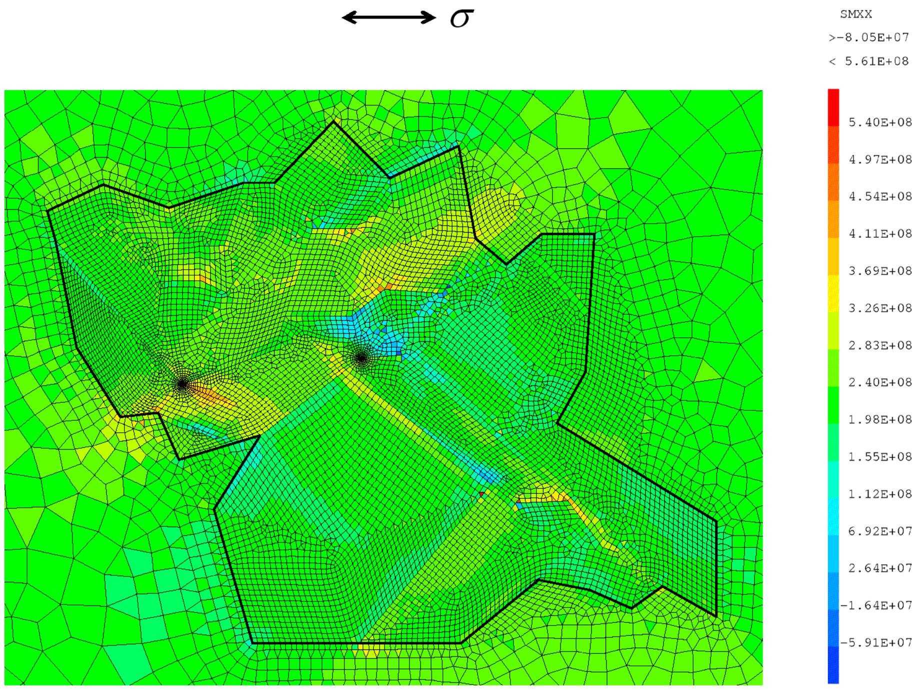

(a) σ_{xx} in Pa

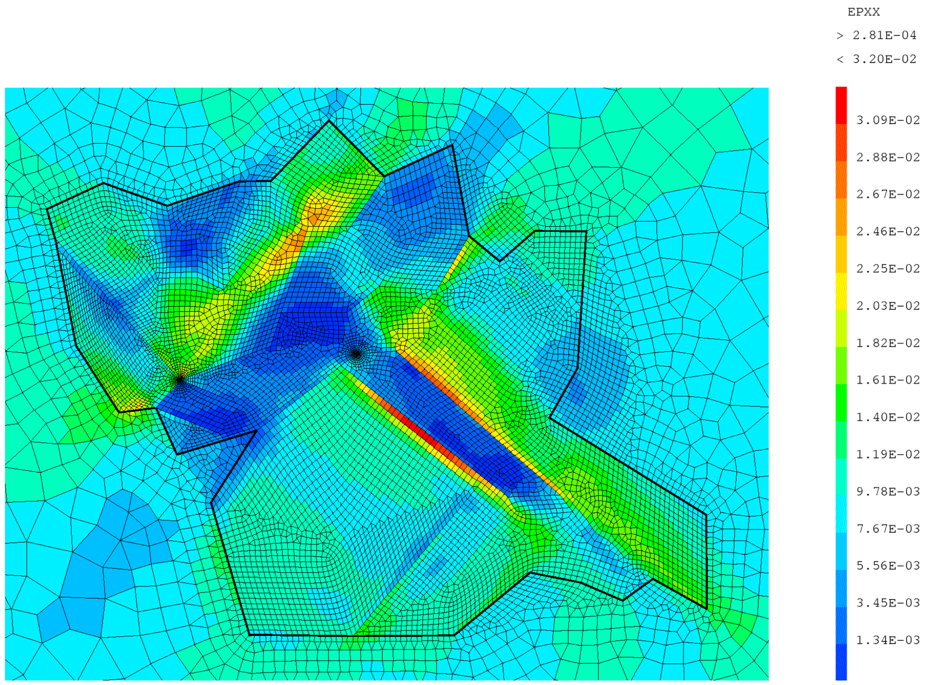

(b) ε_{xx}

Figure 8.11: Distribution of the axial stress and strain fields after 50×10^3h of creep time at 500°C and 230 MPa computed using the microstructure in Fig. 8.9 surrounded by a homogeneous matrix (10 times larger). The loading direction is horizontal.

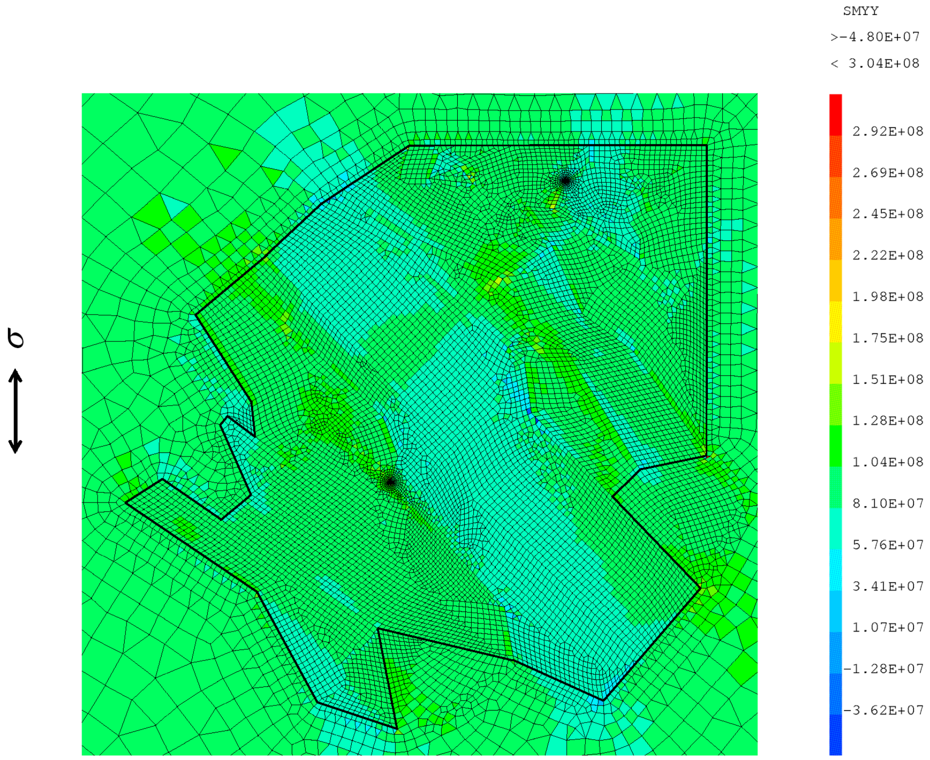

(a) σ_{yy} in Pa

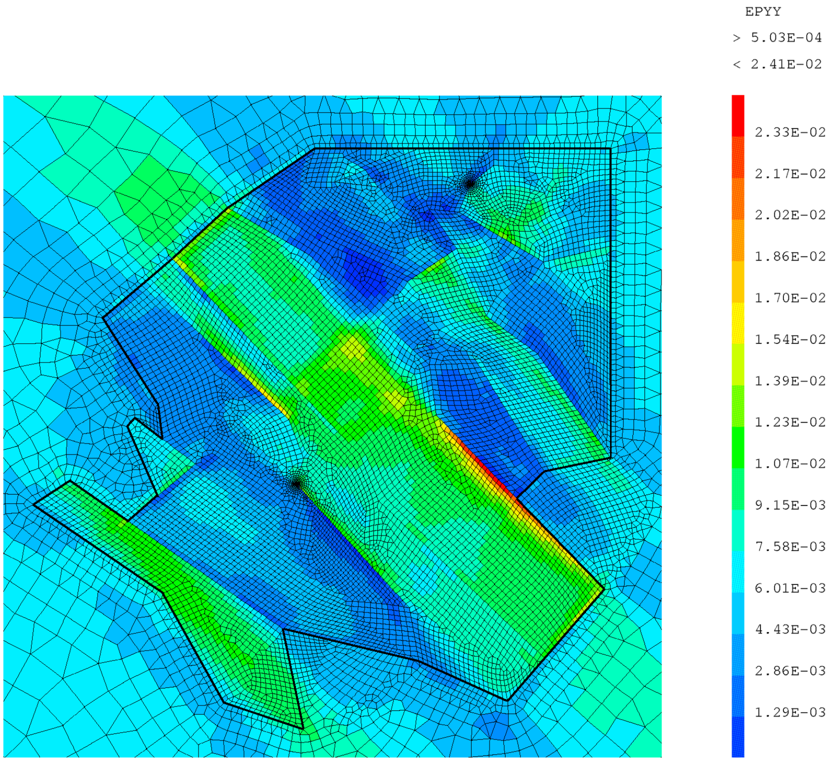

(b) ε_{yy}

Figure 8.12: Distribution of the axial stress and strain fields after 30×10^3h of creep time at 600°C and 90 MPa computed using the microstructure in Fig. 8.10 surrounded by a homogeneous matrix (10 times larger). The loading direction is vertical.

8.2.2 Stress and strain distributions in the microstructures

The distributions of axial stress and strain fields after 50×10^3h of creep time at 500°C and 230 MPa are shown in Figs. 8.11a and 8.11b. The axial stress is almost homogeneous within each block, except along a few block boundaries where overstress is observed. The axial strain is heterogeneous within each block with two parallel boundaries are subjected to high deformation. The regions around triple junctions PT1 and PT2 are subjected to axial stress higher than their surroundings. These are hard blocks subjected to axial strain lower than their surroundings.

The distribution of axial stress and strain fields after 30×10^3h of creep time at 600°C and 90 MPa are shown in Figs. 8.12a and 8.12b. The axial stress is almost homogeneous in each block. The axial strain is still heterogeneous within each block. Axial strain is strongly localised along one block boundary.

For both computations, axial strain is highly localised along some block boundaries. Observations on the EBSD microstructures (Figs. 8.9a and 8.10b) do not show cavities formed along theses block boundaries. Therefore, localised deformation is shown not to be potential mechanism promoting cavitation. On the contrary, high stress is located at both triple points, PT1 and PT2 (Fig. 8.11b), at which cavities are observed experimentally after the end of creep at 500°C and 230 MPa (Fig. 8.9).

In the following paragraph, normal stress fields at block boundaries close to two triple junctions for each microstructure are presented.

8.2.3 Normal stress fields along block boundaries close to triple junctions

The stress profiles along block boundaries at triple junctions PT1 and PT2 (Fig. 8.9b) after 50×10^3h of creep time at 500°C and 230 MPa are plotted in Figs. 8.13a and 8.13b. Block boundary L3 at triple point PT1, which is almost parallel to the loading direction, is subjected to compression. The finite element computations using 3D aggregates performed by Diard et al. [125, 126] have also shown that among the grain boundaries parallel to the loading direction, some are subjected to compression.

Figures 8.13a and 8.13b show that normal stress fields at block boundary L1 close to triple point PT1 and at block boundary L4 close to triple point PT4 reach the maximum values. These block boundaries form with the loading direction angles close to 90°. The first one represents approximately the macroscopic stress. The second one is higher than the macroscopic stress by about 50%. Since the angle formed between L4 and the loading direction is closer to 90° than the one formed between L1 and the loading direction, the normal stress at block boundaries seem to be related to this angle. Numerous computations might be carried out for validation of this conclusion.

The normal stress fields at block boundary L1 close to PT1 and at block boundary L4 close to PT4, respectively 220 and 350 MPa, range within the values computed using the triple point model and 20 sets of random crystal orientations (Fig. 8.4). The EBSD observations carried out by [119] show that creep cavities formed at triple points PT1 and PT2 (Fig. 8.9a).

The stress profiles along block boundaries at triple junctions PT1 and PT2 (see Fig. 8.10b) after 30×10^3h of creep time at 600°C and 90 MPa are plotted in Figs. 8.14a and 8.14b. At both triple junctions, the maximum normal stress to block boundaries is only

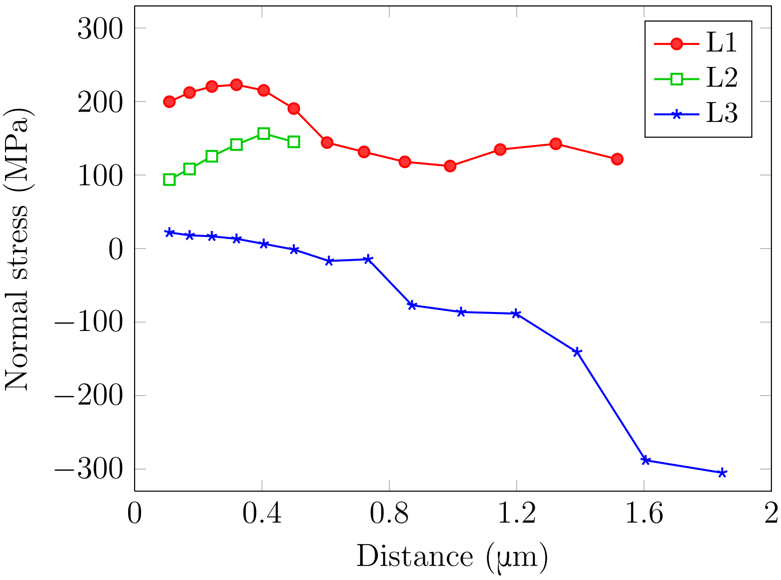

(a) Triple point PT1

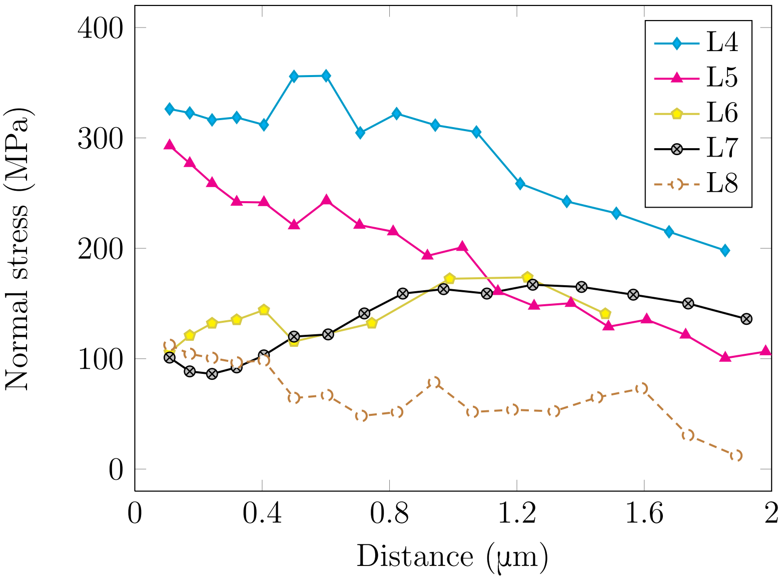

(b) Triple point PT2

Figure 8.13: Normal stress profiles along block boundaries belonging to two triple points (Fig. 8.9b) after 50×10^3h at 500˚C and 230MPa. The triples points correspond to the distance equal to 0.

55% of the macroscopic stress. The assumed block shapes at triple junctions PT1 and PT2 (Fig. 8.10b) might not be as exact as they would be. In fact, the exact informations about the block shapes at the triple junctions were lost because of the cavities and the high number of non-indexed pixels (Fig. 8.10a). For another reason, these triple junctions may contain precipitates that are expected to lead to higher stress concentrations.

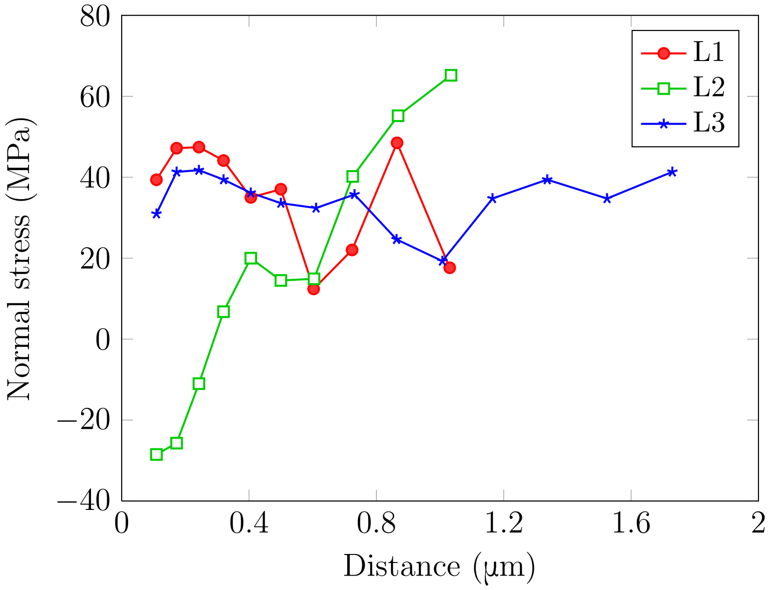

(a) Triple point PT1

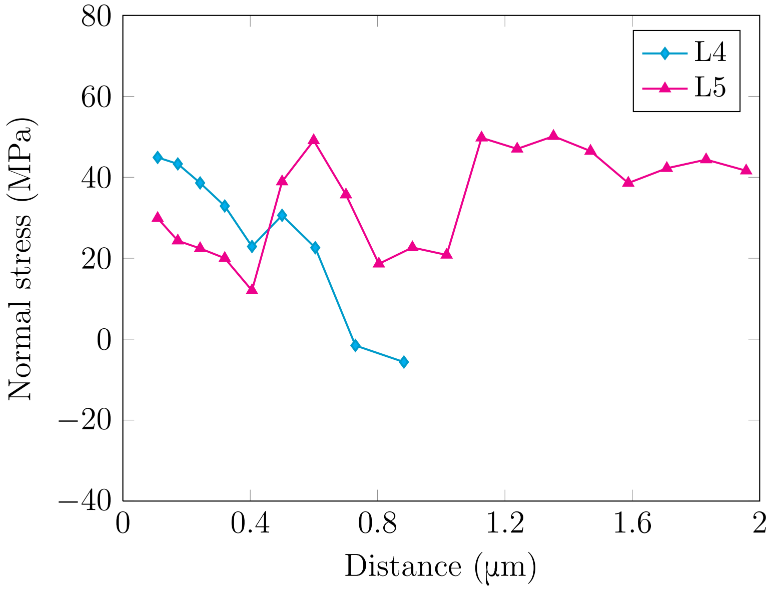

(b) Triple point PT2

Figure 8.14: Normal stress profiles along block boundaries belonging to two triple points (Fig. 8.10b) after 50 × 10^3h at 600˚C and 90MPa. The triples points correspond to the distance equal to 0.

8.3 Discussion about assessment of normal stress fields at block boundaries

The normal stress fields at block boundaries during the creep tests at 500˚C under 230 MPa and at 600˚C under 90 MPa are computed in the quasi 2D plane strain condition. This was chosen to correspond to block boundaries located in the bulk material. Two types of meshed microstructures are used.

The first one is a triple junction model containing one block boundary perpendicular to the loading direction. The distribution of normal stress fields at this block boundary close to the triple junction is computed using 20 sets of random crystal orientations for the three blocks. These finite element computations result in ratios of normal stress close to the triple junction to the macroscopic stress that could reach the maximum value of about 2.

The ones of the second type are 2D microstructures based on EBSD measurements. High mesh refinement is applied to triple junctions where cavities are experimentally observed. At these triple junctions, computed ratios of normal stress at block boundaries to the macroscopic stress could reach 1.5. This ratio ranges within the ones estimated using the triple junction model using using 20 independent sets of random crystal orientations.

In the following, the maximum ratio of normal stress at block boundaries close to triple points to the macroscopic stress is chosen as 2. This evaluation is now used for evaluating the influence of stress heterogeneity on the prediction of cavity nucleation at triple junctions.

8.4 Application to the prediction of cavity nucleation

Nucleation rates of cavities are predicted using the Raj model [93] as in Eq. (4.14). Two types of cavity are taken into account: spherical-cap cavity formed at block boundaries (Fig. 4.7a) and cavity of Type B formed at carbide-matrix interfaces (Fig. 4.7b). Volume factors $F_v = 0.875$ for the first type and $F_v = 0.18$ are evaluated taking into account the effect of P and S segregation at grain boundaries [118] as mentioned in section 5.2.5.

The normal stress estimated using the finite element model can be applied to the study of spherical-cap cavities taking into account the overstress at block boundaries. For the study of type-B cavities, the stress concentration at the junction of the carbide and block boundaries could be different. However, we assume that the same ratio of the normal stress (at block boundaries) to the macroscopic stress could be reached as well. Finite element computations based on a triple point model containing a carbide (isotropic elasticity) at the triple junction is still in progress.

The predictions of nucleation rates taking into account the normal stress concentration close to triple junctions as well as two types of cavity are reported in Table 8.2. The results show that the Raj model still predicts negligible nucleation rates because of the high theoretical values of F_v.

8.5 Conclusions

For the studied long-term creep tests, normal stress at block boundaries close to triple junctions was estimated using crystalline finite element computations. This study does not lead to stress singularity as predicted by the model of Caré and Zaoui [127] taking into account only thermoelastic accommodation. This could be due stress relaxation induced by viscoplastic deformation.

The finite element computations using the triple junction model show that the normal stress is maximum close to triple junctions (Figs. 8.4 and 8.5). During the creep test at 500°C under 230 MPa, the normal stress fields close to triple junctions varies with respect

Table 8.3: Predictions of nucleation rates using the Raj nucleation model and taking into account the maximum tensile stress concentration factor of 2 obtained by the triple point model. $\dot{N}_{a0} = \frac{4\pi\gamma_s D_b\delta}{\Omega^{4/3}\sigma_n} N_a^{max} \exp\left(\frac{\sigma_n\Omega}{k_bT}\right)$, $\frac{\Delta G_c}{k_bT} = \frac{4{\gamma_s}^3 F_v}{{\sigma_n}^2 k_bT}$ and $\dot{N}_a = \dot{N}_{a0}\exp\left(-\frac{\Delta G_c}{k_bT}\right)$ from Eq. (4.14). $\gamma_s = 1.42$ Jm^{-2} [118], $\gamma_b = 1.7$ Jm^{-2} [124], $\gamma_I = 1.1$ Jm^{-2} [123], $\gamma_{Ib} = 1$ Jm^{-2} [124], $Q_b = 254$ kJmol^{-1} [120], $D_{b0}\delta = 1.88$ m^{2}s^{-1} [120], $k_b = 1.3806488 \times 10^{-23}$ JK^{-1} and $\Omega = 1.18 \times 10^{-29}$m^3.

	Cavity at block boundary $F_v = 0.85$			
Creep tests	$\dot{N}_{a0}$ (µm^{-2}s^{-1})	$\Delta G_c/k_bT$	$\dot{N}_a$ (µm^{-2}s^{-1})	$\dot{N}_a^{exp}$ (µm^{-2}s^{-1})
500°C - 230 MPa	4.16×10^{29}	4.31×10^{3}	2.7×10^{-1843}	2.8×10^{-12}
600°C - 90 MPa	7.05×10^{31}	2.49×10^{4}	8.3×10^{-10783}	6.5×10^{-11}
	Cavity at M$_{23}$C$_6$ - type B $F_v = 0.18$			
Creep tests	$\dot{N}_{a0}$ (µm^{-2}s^{-1})	$\Delta G_c/k_bT$	$\dot{N}_a$ (µm^{-2}s^{-1})	$\dot{N}_a^{exp}$ (µm^{-2}s^{-1})
500°C - 230 MPa	4.16×10^{29}	9.13×10^{2}	1.3×10^{-367}	2.8×10^{-12}
600°C - 90 MPa	7.05×10^{31}	5.28×10^{3}	6.0×10^{-2262}	6.5×10^{-11}

to the macroscopic stress with maximum amplitudes of -60%/+100% (at the minimum creep strain rate), due to random orientations. During the creep test at 600°C under 90 MPa, the corresponding maximum amplitudes are -50%/80%.

For both creep tests, the normal stress fields at the middle of block boundaries perpendicular to the loading direction vary with respect to the macroscopic stress with maximum amplitudes of about -10%/+30%, due to random orientations.

The average normal stress along the block boundary perpendicular to the loading direction varies with respect to the macroscopic stress with maximum amplitudes of $-15\%/+70\%$. This variation is slightly higher than the one estimated by Diard et al. [125] which is ±50% during monotonic tensile test carried out on a Zr alloy at room temperature. In fact, the viscoplastic slip law used in our study is an exponential function of stress following the theory of thermal activation. During long creep times, the stress scatter increases and becomes more important at the end.

For the creep test at 500°C under 230 MPa, the normal stress concentration factors close to triple junctions computed based on the EBDS microstructure belong to the range of values computed using the triple junction model with 20 sets of random crystal orientations. For the creep test at 600°C and 90 MPa, the normal stress fields computed based on the EBDS microstructure could not be represented by the triple junction model by using even 20 sets of random orientations. In this case, the presence of creep cavities at triple junctions does not allow determining accurate geometries of block boundaries. Consequently, only a hypothesis on block boundary geometries at the studied triple junctions have been made and may leads to an underestimation of stress concentrations.

The maximum stress concentration factor of 2 is obtained from finite element computations at triple junctions. This stress concentration factor is not sufficient for the prediction of cavity nucleation using the Raj model, even taking into account type-B cavities which are the most critical ones as well as the effect of P and S segregation at grain boundaries.

The stress concentration at the carbide-matrix interface for carbides located at triple points is not yet studied. A stress concentration factor ranging between 20 and 50 is however required for correct predictions of nucleation rates using the Raj model and the theoretical values of F_v. Furthermore, theses high stress concentration factors could strongly influence the Rice length. Then, the competitiveness between both cavitation mechanisms, one controlled by diffusion and another by viscoplasticity, should be discussed.

Part V

Conclusions and recommendations for future works

Chapter 9

Conclusions

Creep of grade 91 steel was investigated at temperatures of 500°C with lifetime up to 160 kh and of 600°C with lifetime up to 94 kh. This study involves three possible causes of creep failure: necking, creep softening of the material and cavitation.

9.1 Necking and Softening

The onset of necking was first predicted using the Hart criterion of viscoplastic instability for the creep tests mentioned above. The computations showed that the onset of necking occurs just after the minimum creep rate is reached. At this time, the measurements during two interrupted creep tests at 500°C, one during 46h and another during 7000 h, revealed that the diameter profile is almost uniform. After this point, a reduction of area in the necking section by 20% occurs and the diameter profile along the necking part is elongated. Therefore, the gauge length was assumed to be divided into three parts, one is located at the necking zone and another ones (equal cross-sections) are located outside this zone. These parts were supposed to have uniform diameter profiles and be loaded in series.

Necking models were studied and applied to a large number of creep tests of Grade 91 steel at 500°C and 600°C. Creep damage was not taken into account in this modelling. The creep softening of the material was introduced into the model as well. A phenomenological model of creep softening was then proposed to account for additional acceleration of creep strain rate occurring just after its minimum (without necking and cavitation effect). The corresponding material parameters were identified based on the creep tests under study. They were first assumed to be stress-independent at a given temperature.

Two additional parameters were needed to apply this model. The first one is the initial difference in area between the necking part and homogeneous parts at the onset of necking. The second one is the final reduction in area in the necking section used as the failure criterion. The stability of the predictions with respect to these parameters was checked.

This necking model leads to predictions of creep lifetimes of Grade 91 steel up to 160 kh at 500°C and 94 kh at 600°C in agreement with the experimental results. The evolution of the necking section predicted using this model is in agreement with the measurements during one interrupted creep test (at 500°C and t_f =46 h), as well as a more recent one (at 500°C and t_f =7000 h). Lifetimes could be correctly predicted by using a final reduction in area in the necking section by 20% as the failure criterion. Indeed, after this value, the reduction of area in the necking section accelerates very quickly to failure (80%). The value of the critical reduction in area is only weekly influential. Senior et al. [80] have shown that nucleation of ductile cavities occurs at a strain of 25% (reduction in area in the necking section by 20%). In consequence, during the creep acceleration period, ductile cavities could contribute to the final failure of the material. Even so, this final acceleration period due to necking represents only 10% of creep lifetime after the measurements carried out during the interrupted creep test at 500°C with a creep time of 46 h, as predicted by the modelling.

The softening increasing with respect to creep lifetime was then taken into account. This softening behaviour were not considered in the previous necking modelling in which the softening constants were unique at each temperature. The variations of the parameter values for this necking model (failure criterion value, difference in area at the onset of necking) were taken into account as in the previous modelling. Two bound laws of creep lifetime were finally obtained. The upper bound is of Monkman-Grant type. Experimental lifetimes of a large number of tempered martensitic-ferritic steels up to 200 kh at temperature between 500 and 700°C range between both bounds.

9.2 Cavitation induced by boundary diffusion

Creep cavities located along former austenitic grain/packet/block boundaries were observed using FEG-SEM after creep lifetimes of 160×10^3h and 59×10^3h at 500°C, as well as of 94×10^3h and 5×10^3h at 600°C. After the longest creep tests at 500°C and at 600°C, the area fractions of porosity are highest. These porosities yield an increase in creep strain rate predicted using the Norton creep law by only 2.5% following continuum damage mechanics. Therefore, the necking predictions previously presented are not affected by the creep cavity damage for the range of creep lifetimes under study. Nevertheless, correct physically-based predictions of the nucleation and growth of cavities during these creep tests may allow extrapolations of creep lifetimes out of the creep data domain (Cocks and Ashby [2]).

The growth of cavities induced by boundary diffusion was shown to be the dominant mechanism using the predictions of Rice length. Observations using FEG-SEM microscopy of cavitated facets distributed almost uniformly allow us to neglect the effect of constrained cavity growth (provided viscoplastic strain is not so low). This one may be relevant for longer lifetimes.

Two models of diffusion cavity growth were used. The first one proposed by Raj and Ashby takes spontaneous nucleation of cavities into account. On the other hand, the second one proposed by Riedel assumes continuous nucleation described by the Dyson experimentally-based law. This one leads to two bounds. The first model was shown to depend strongly on the parameters such as the self-diffusion coefficient and the distance between cavities. Contrary to this model, the Riedel bounds were shown to be stable with respect to the corresponding parameters such as the nucleation rate as well as the boundary diffusion self-coefficient. This model allowed predictions of the average cavity size at the end of both longest creep tests in the same order of magnitude as the measured ones. However, the parameter of the Dyson nucleation law was adjusted using measured final densities of cavities. Therefore, predictions of cavity nucleation rates are necessary.

High resolution observations using FEG-SEM revealed nucleation sites located along grain/block boundaries and at carbide or Laves phase interfaces with the matrix. The Raj model of cavity nucleation was applied. Very low values of geometry factor F_v (in the order of 10^{-4} and 10^{-5}) were required for predicting nucleation rates in agreement with the measured final cavity densities. Adjusted values of F_v of the same order of magnitude had also been used by Raj [99] and Riedel [118]. These values are lower than the theoretical values by 3 to 4 orders of magnitude whatever the nucleation site. Segregation of S and P proposed by Riedel could lead to a reduction in theoretical value of F_v to 0.18. Using this value, the predictions based on the Raj model leads to negligible nucleation rates with respect to the experimentally measured values, as expected by comparison with the adjusted values of F_v.

These very low adjusted values could be due to underestimation of local stress induced by heterogeneity, e.g. carbides, Laves phase or triple junctions. Preliminary finite element computations were carried out to compute stress concentrations at the interface of an isotropic elastic carbide and an isotropic matrix obeying phenomenological creep constitutive equations whose parameters had been adjusted using experimental creep curves. The 2D-plane strain hypothesis was used. A stress concentration factor of 1.5 with respect to the macroscopic stress was computed. This leads to a reduction in theoretical value of F_v to 0.08 and cannot allow predictions of nucleation rates in the same order of magnitude as the measured ones.

Logarithmic stress singularities induced following thermoelastic accommodation at the vicinity of triple junctions have been shown in the literature. Stress concentrations at polycrystalline triple junctions of Grade 91 steel subjected to the two longest creep tests previously described were computed by the finite element method in the crystalline elasto-viscoplasticity framework.

9.3 Finite element computations of stress concentrations at triple junctions and their effect on cavity nucleation

These computations required calibrations of the crystalline viscoplasticity parameters. The calibration procedure was based on simulations of macroscopic creep strain curves of polycrystalline aggregates meshed by finite elements. The obtained values of the parameters allowed the predictions of macroscopic creep strain curves at 500°C under 230 MPa and at 600°C under 90 MPa in satisfactory agreement with the experimental ones. The distribution of stress fields averaged over blocks was shown to be weakly dependent on the number of blocks in the aggregate, mesh refinement, and the choice of the V^* value. In contrary, predicted strain fields are strongly dependent on these parameters because of the high non-linearity (Norton stress exponents of 10 and 20 respectively at 600 and 500°C).

Stress concentrations at block boundaries close to triple junctions were computed using finite element simulations. Microstructures were built using either a simple model of triple junction or EBSD measurements. A quasi 2D-plane strain hypothesis was used leading to lower computation times and allowed us to increase mesh refinement. Finite element computations were carried out in the crystalline elasto-viscoplasticity framework. Stress concentrations were obtained using both microstructure types. The results show that the triple points junctions using EBSD measurements could be represented by the simple model of triple junction for which the crystal orientations of the blocks are randomly determined. These computations do not yield higher stress singularity in the crystal elasto-viscoplasticity framework as in the thermoelastic one.

Finite element computations of stress concentrations at triple junctions yielded normal stress fields at block boundaries perpendicular to the loading direction that could be two times higher than the macroscopic stress. As stated for the vicinity of precipitates/Laves phases, this stress concentration still leads to predictions of cavity nucleation rates not of the same order of magnitude as the experimental ones. Indeed, the required adjusted values of F_v are very low and are of the orders of magnitude of 10^{-5} and 10^{-4}. Even taking into account the stress concentration and the effect of S an P segregation suggested by Riedel, predicted nucleation rates are still not at least of the same order of magnitude as the experimental ones. If the Raj model is valid a high stress concentration factor ranging between 20 and 50 may be required to obtain predicted nucleation rates using the theoretical values of F_v in agreement with the measured ones.

9.4 Criticism of the Raj model

During the nucleation phase, a nucleus was assumed by Raj to keep its equilibrium shape assured by surface tension equilibrium. This may be true in the domain where crystal deformation is purely controlled by diffusion. However, the finite element computations in the crystal elasto-viscoplasticity framework revealed stress and strain heterogeneity at block boundaries as well as close to triple junctions. This heterogeneity also occurs at nucleation sites such as carbide interfaces. This implies that, in the framework of crystal elasto-viscoplasticity, the Raj model may lead to a strong underestimation of nucleation rates.

Raj assumed the thermal equilibrium concentration of vacancies to be reached even at the region close to the cavity surface. This may not be always true.

Cavity nucleation is still an unresolved problem. In order to provide the required nucleation rates, $\dot{N}_0$, to compute Riedel bound laws, the phenomenological model proposed by Dyson is used: $\dot{N}_0 = \alpha_d \ \dot{\varepsilon}_{min}$. The value of the α_d parameter has been suggested by Dyson to vary weekly with stress at a given temperature. This hypothesis seems reasonable with respect to our measured cavity densities. For grade 91 steel, values of α_d were identified based on the cavity density measurements carried out after the creep tests at 500°C under 230 MPa and at 600°C under 90 MPa. These values are respectively $6.78 \times 10^{10}\text{m}^{-2}$ at 500°C and $1.027 \times 10^{10}\text{m}^{-2}$ at 600°C.

9.5 Final predictions of creep lifetimes and extrapolation out of creep data domain

The final predictions and extrapolations of creep lifetimes are deduced from two models interpreting the failure mechanisms studied in this PhD thesis. The first one is the upper bound of the necking model taking into account the material creep softening. The second one is constituted of two bound laws deduced from the Riedel model of diffusion cavity growth taking in account a continuous nucleation law of Dyson type.

The predictions of creep lifetimes using these models are applied to many creep conditions on Grade 91 steel at 500°C and 600°C (Fig. 9.1). The upper bound of the softening-enhanced necking model leads to predictions of creep lifetimes in agreement with the experimental creep data up to 200×10^3h at 500°C and 100×10^3h at 600°C (for lifetimes lower than 100 h, the lower bound should be used). The bound laws based on diffusion-induced cavitation permit extrapolations of creep lifetimes longer than 10^6h at 500°C ($\approx$ 110 years) and 3×10^5h at 600°C ($\approx$ 34 years).

One creep test at 600°C under 70 MPa has reached the end of creep stage II at 150 kh and is now in progress in the tertiary stage (Fig. 9.1). If the strain rate acceleration regime observed under 90 MPa at 600°C (Lim et al. [60], Lim et al. Creep 2012 Kyoto) is taken into account, it represents between 40% and 60% of creep lifetime. The experimental creep lifetime is therefore estimated to be $250 - 375$ kh. The creep lifetime given by the bound laws based on diffusion-induced cavitation is $400 - 700$ kh. This isolated test seems to combine the change in damage regime predicted by Fig. 9.1, of course, this should be confirmed by other test results, particularly after applying similar approaches to tests carried out at higher temperatures.

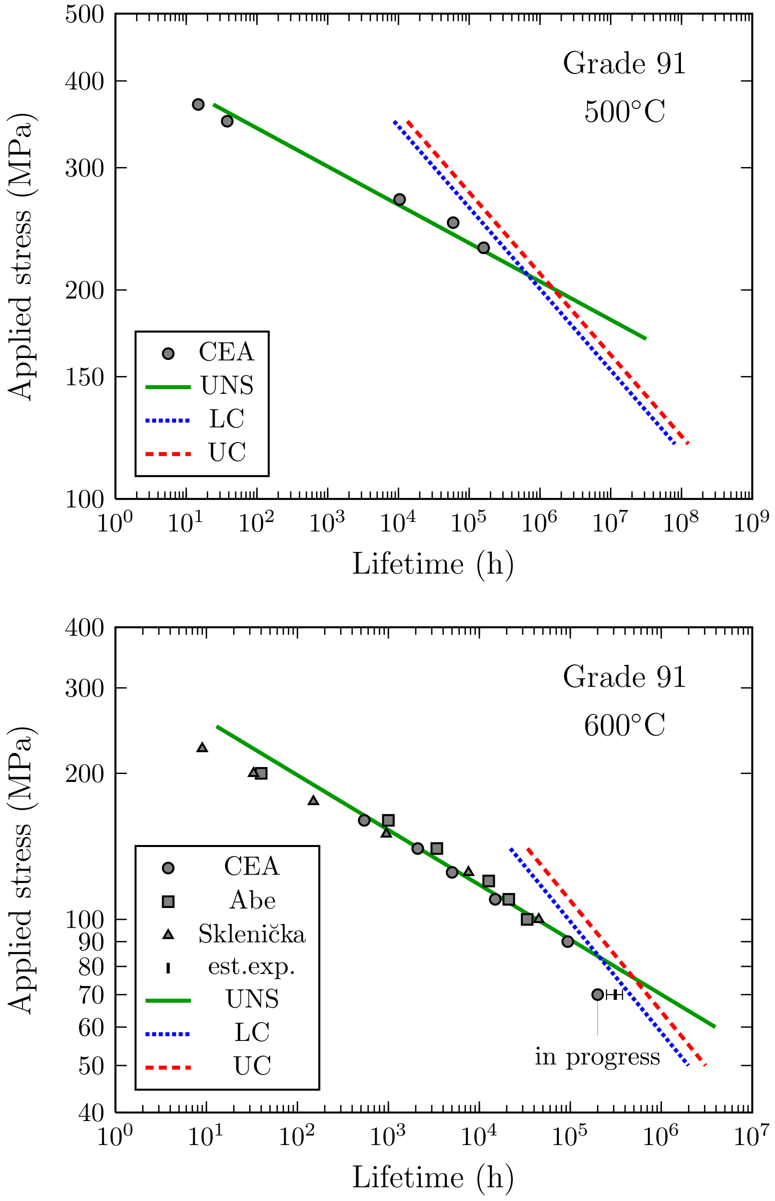

Figure 9.1: Comparisons between experimental creep lifetimes after CEA creep tests and [6,73] and the predictions using either the upper bound of the necking model including material creep softening (UNS), or the Riedel lower bound and Dyson law (LC) or the Riedel upper bound and Dyson law (UC). One creep test at 600˚C has reached the end of the secondary stage 50 kh ago is still in progress at CEA/SRMA. Its estimated experimental lifetime is noted by”est.exp“.

Chapter 10

Recommendations for future works

10.1 Cavity nucleation equation

Nucleation rate estimations are needed for the prediction of cavity diffusion-induced growth modelling based on continuous nucleation. The Dyson phenomenological equation requires the identification of the α_d parameter at various temperatures. Fair values of this parameter require numerous creep tests at different temperatures as well as a large number of measurements of cavity density and sophisticated counting procedures.

A new model of cavity nucleation is required to be established. Raj assumed simple shapes of cavities such as spherical shapes or spherical segments as well as surface tension equilibrium. Computations of the nucleus growth of a cluster from few atoms to thousands or one million atoms (cavity of 25 nm) using nanoscale energy values could be eventually required, based on cluster dynamics. But, these seem to be heavy computations. The use of vacancy equilibrium concentration is questionable as well.

10.2 Mechanisms of cavity nucleation

The modelled cavities whose sizes are larger than 200 nm were assumed to have grown by boundary diffusion. However, much more numerous cavities with sizes from 50 nm to 100 nm were observed. They are located especially at the interfaces of carbides or Laves phases located not only at grain/block boundaries perpendicular to the loading direction but also at the ones parallel to it. Cavity with sizes ranging between 100 and 200 nm are almost absent. Nucleation of some of the small cavities may be not associated to diffusion of vacancies. They may have been nucleated by viscoplasticity like the ones observed by Senior et at. [80] and then subjected to low diffusion growth because of their location. Interrupted creep tests may be useful for concluding about the responsible nucleation mechanism and the respective effect of strain and time.

10.3 Local stress concentration

Once a more suitable nucleation equation will be established, computations of local stress concentrations close to triple junctions and/or particles could be an asset. Indeed, continuous nucleation was confirmed by Dyson based on their measurements of the evolution of cavity densities. Cavities nucleate earlier at some sites and later at other ones. This could be explained by microstructural heterogeneity inducing stress concentrations. Therefore, stress concentrations close to triple junctions and precipitates could be coupled with the use of the nucleation equation. The triple junction model previously presented could be enhanced by taking step by step the following configurations into account:

- Different angles, high or low, formed between block boundaries at the triple junction in order to generalize the results obtained with regular angles of 120°
- The triple junction may contain a carbide or a Laves particle as triple points are generally favourable sites for nucleation of these particles and then of cavities during creep
- Extension of the triple point microstructure from 2D to 3D may be necessary to take the effect of 3D neighbouring blocks into account.

10.4 Effect of material creep softening

The stress concentration of a factor two is obtained considering various triple point configurations without taking creep softening into account, whereas it is usually observed for tempered martensitic-ferritic steels. A stronger scatter in stress concentrations or a higher stress concentration factor could be obtained. This could be studied using a crystal viscoplasticity constitutive behaviour that takes softening during creep time into account. Some of its parameters could be then identified using computations carried out using large polycrystalline aggregates.

References

[1] CEA. Systèmes nucleares du futur génération IV. *Clefs*, (55), 2007.

[2] A.C.F. Cocks and M.F. Ashby. On creep fracture by void growth. *Progress in Materials Science*, 27(3-4):189–244, 1982.

[3] J. Lemaitre and J. L. Chaboche. *Mechanics of solid materials*. Cambridge University Press, Cambridge, New York, 1994. 257 pp.

[4] V. Gaffard. *Experimental study and modelling of high temperature creep flow and damage behaviour of 9Cr1Mo-NbV steel weldments*. PhD thesis, MINES ParisTech, 2004. `http://tel.archives-ouvertes.fr/tel-00162118/fr/`.

[5] F. C Monkman and N. J Grant. An empirical relationship between rupture life and minimum creep rate in creep-rupture tests. In *proc. ASTM*, volume 56, pages 593–605, 1956.

[6] Fujio Abe. Creep life estimation of Gr.91 based on creep strain analysis. *Materials at High Temperatures*, 28(2):75–84, 2011.

[7] Erin M. Haney, F. Dalle, M. Sauzay, L. Vincent, I. Tournié, L. Allais, and B. Fournier. Macroscopic results of long-term creep on a modified 9Cr-1Mo steel (T91). *Materials Science and Engineering: A*, 510-511:99–103, June 2009.

[8] F. Abe, T. Horiuchi, M. Taneike, K. Kimura, S. Muneki, and M Igarahi. Creep strain behavior during microstructure evolution in tempered martensitic advanced 9cr steels. In *Proceedings of the 10th Joint International Conference on Creep and Fracture of Engineering Materials and Structures - Creep resistant metallic materials*, pages 16–25, Czech Republic, 2001. VÍTROVICE-Reseach and Development.

[9] K. Kimura, H. Kushima, and F. Abe. Heterogeneous changes in microstructure and degradation behaviour of 9Cr-1Mo-V-Nb steel during long term creep. *Key Engineering Materials*, (171/174):483–490, 2000.

[10] K. Milicka and F. Dobes. Small punch testing of p91 steel. *International Journal of Pressure Vessels and Piping*, 83(9):625–634, September 2006.

[11] V. Sklenicka, K. Kucharova, A. Dlouhy, and J. Krejci. In Coutsouradis et al., editor, *Materials for Advanced Power Engineering - Part I*, page 435, Liège, 1994. Springer.

[12] M. Considère. *Mémoire sur l'emploi du fer et de l'acier dans les constructions.* Vue Ch. Dunod, Paris, 1885.

[13] P.F. Giroux, F. Dalle, M. Sauzay, J. Malaplate, B. Fournier, and A.F. Gourgues-Lorenzon. Mechanical and microstructural stability of p92 steel under uniaxial tension at high temperature. *Materials Science and Engineering A*, 527(16-17): 3984–3993, June 2010.

[14] F. Masuyama. Hardness model for creep-life assessment of high-strength martensitic steels. *Materials Science and Engineering: A*, 510-511:154–157, June 2009.

[15] F. Abe. Coarsening behavior of lath and its effect on creep rates in tempered martensitic 9Cr-2W steels. *Materials Science and Engineering: A*, 387-389:565–569, December 2004.

[16] E. Cerri, E. Evangelista, S. Spigarelli, and P. Bianchi. Evolution of microstructure in a modified 9Cr-1Mo steel during short term creep. *Materials Science and Engineering A*, 245(2):285–292, May 1998.

[17] Vani Shankar, M. Valsan, K. Bhanu Sankara Rao, R. Kannan, S.L. Mannan, and S.D. Pathak. Low cycle fatigue behavior and microstructural evolution of modified 9Cr-1Mo ferritic steel. *Materials Science and Engineering: A*, 437(2):413–422, November 2006.

[18] P. J. Ennis and A. Czyrska-Filemonowicz. Recent advances in creep resistant steels for power plant applications. *OMMI*, 1(1), 2002.

[19] J. Pešička, A. Aghajani, Ch. Somsen, A. Hartmaier, and G. Eggeler. How dislocation substructures evolve during long-term creep of a 12% cr tempered martensitic ferritic steel. *Scripta Materialia*, 62(6):353–356, March 2010.

[20] J. Hald. Creep strength and ductility of 9 to 12 chromium steels. *Materials at High Temperatures*, 21(1):41–46, 2004.

[21] G. Eggeler, J.C. Earthman, N. Nilsvang, and B. Ilschner. Microstructural study of creep rupture in a 12% chromium ferritic steel. *Acta Metallurgica*, 37(1):49–60, January 1989.

[22] C. G. Panait, A. Zielinska-Lipiec, T. Koziel, A. Czyrska-Filemonowicz, A.-F. Gourgues-Lorenzon, and W. Bendick. Evolution of dislocation density, size of subgrains and MX-type precipitates in a P91 steel during creep and during thermal ageing at 600°c for more than 100,000 h. *Materials Science and Engineering A*, 527 (16-17):4062–4069, June 2010.

[23] B. Josefsson, A. Kvist, and H. O. Andrén. Atom probe microanalysis of weld metal in a submerged arc welded chromium-molybdenum steel. *Le Journal de Physique Colloques*, 48(C6):435–440, 1987.

[24] B. Fournier. *Fatigue-fluage des aciers martensitiques à 9-12%Cr : comportement et endommagement.* PhD thesis, Ecole des MINES ParisTech, 2007. `http://tel.archives-ouvertes.fr/tel-00203753/fr/`.

[25] J. Z. Briggs and T. D. Parker. The super 12 percent Cr steels. 1965.

[26] H. Newell. *Metal Progress*, pages 51–55, 1936.

[27] J. Hald. Metallurgy and creep properties of new 9-12% cr steels. *Steel research*, 67 (9):369–374, 1996.

[28] ASME Code Case 1943. Seamless modified 9Cr-1Mo. 1983.

[29] F. Masuyama. page 811, Chiba, Japan, 1992.

[30] H. Naoi, T. Fujita, H. Mimura, M. Ohgami, H. Morimoto, T. Takana, Y. Yazaki, and T. Fujita. New steels for advanced plant up to 620°C. In *Proceedings of the EPRI Conference*, pages 8–29, USA, 1995. Ed. E. Metcalfe, London, May 1995.

[31] ASME code case 2179: Seamless 9Cr-2W material. August 1994.

[32] R. Blum and J. Hald. Benefit of advanced steam power plants. In *Proceedings of the 6th Liege Conference on Materials for advanced power engineering*, pages 1009–1016, 1998.

[33] A.A. Tavassoli, I. Le Naour, and I. Tournié. Mechanical properties of 9Cr ferritic steels developed for steam generators. Note Technique NT SRMA 92-1968, CEA Saclay - Division SRMA, 1992.

[34] Framatome ANP. Approvisionnement de tôles et fabrication de joints soudés en acier de nuance z10 CDV nb 9-1 pour le CEA saclay. Note technique, Framatome ANP, 2002.

[35] ASTM Standard A387. *Specification for Pressure Vessel Plates, Alloy Steel, Chromium-Molybdenum.* ASTM International, PA, 1999.

[36] *RCC-MRx : Règles de Conception et de Construction des Matériels Mécaniques des Installations Nucléaires.* AFCEN, 2012.

[37] F. Masuyama. History of power plants and progress in heat resistant steels. *iSiJ international*, 41(6):612–625, 2001.

[38] R. L. Klueh and Donald R. Harries. *High-chromium ferritic and martensitic steels for nuclear applications.* ASTM International, July 2001. ISBN 9780803120907.

[39] J. Orr, D. Burton, and C. Rasche. Sensitivity of microstructure and mechanical properties of steel 91 to initial heat treatments. *Ironmaking and Steelmaking (UK)*, 20(6):415–423, 1993.

[40] V. Foldyna and Z. Kubon. In A. Strang, editor, *Conference Proceedings: Performance of Bolting Materials in High Temperature Plant Applications - York 1994*, London, 1995. Institute of Materials.

[41] Z Kubon, V Foldyna, and V Vodarek. Analysis of strengthening mechanisms in 9 to 12% chromium steels. *Microstructural Stability of Creep Resistant Alloys for High Temperature Plant Applications*, (2):257–269, 1998.

[42] G. Eggeler, N. Nilsvang, and B. Ilschner. Microstructural changes in a 12-percent chromium steel during creep. *Steel Research*, 58(2):97–103, 1987.

[43] H. Kitahara, R. Ueji, N. Tsuji, and Y. Minamino. Crystallographic features of lath martensite in low-carbon steel. *Acta Materialia*, 54(5):1279–1288, 2006.

[44] J. C. Brachet. *Alliages martensitiques 9Cr-1Mo : effets de l'addition de l'azote, du niobium et du vanadium sur la microstructure, les transformations de phase et les propriétés mécaniques.* PhD thesis, Université de Paris-Sud, Orsay, 1991.

[45] D. Guttmann. *Etude du revenu de la martensite dans les aciers faiblement alliés à 2% de manganèse, Influence de l'antimoine.* PhD thesis, Université de Nancy, Nancy, 1974.

[46] Y. de Carlan and L. Guetaz. Analyse morphologique et cristallographique de la structure martensitique dans l'acier eurofer. Technical Report Ref. CEA/DEN/DMN/SRMA 00-2400, CEA Saclay/ SRMA, Gif-sur-Yvette, France, 2000.

[47] M. Igarashi, S. Muneki, H. Kutsumi, T. Itagaki, N. Fujitsuna, and F. Abe. A new concept for strengthening of advanced ferritic steels for usc power plant. In *Proceedings of the fifth international Charles Parsons turbine conference*, pages 334–347, 2000.

[48] G. Kurdjumov and G. Sachs. Uber den mechanismus der stahlhartung. *Zeitschrift fur Physik*, 64:225, 1930.

[49] Z. Nishiyama. *Martensite transformation.* Maruzen, Tokyo, 1971.

[50] V. Randle and O. Engler. *Introduction to Texture Analysis: Macrotexture, Microtexture and Orientation Mapping.* Amsterdam, 2000.

[51] B. Sonderegger, S. Mitsche, and H. Cerjak. Martensite laths in creep resistant martensitic 9-12% Cr steels–Calculation and measurement of misorientations. *Materials Characterization*, 58(10):874–882, October 2007.

[52] G. Eggeler and A. Dlouhy. Boron segregation and creep in ultra-fine grained tempered martensite ferritic steels. *Zeitschrift fur Metallkunde*, 96(7):743–748, 2005.

[53] H. Brillet. Comportement en fatigue d'un acier à 9%Cr à 550°c. Technical Report Ref. CEA/DEN/DMN/SRMA 2003-2525, CEA/ SRMA, Gif-sur-Yvette, France, 2003.

[54] J. Pešička, A. Dronhofer, and G. Eggeler. Free dislocations and boundary dislocations in tempered martensite ferritic steels. *Materials Science and Engineering A*, 387-389:176–180, December 2004.

[55] P.R. Jemian, J.R. Weertman, G.G. Long, and R.D. Spal. Characterization of 9Cr-1MoVNb steel by anomalous small-angle x-ray scattering. *Acta Metallurgica et Materialia*, 39(11):2477–2487, November 1991.

[56] B. Gieseke, C. Brinkman, and P. Maziasz. The influence of thermal aging on the microstructure and fatigue properties of modified 9cr-1mo steel. In *Microstructures and mechanical properties of aging material*. TMS The Minerals, Metals & Materials Society, 1993.

[57] G. Eggeler. The effect of long-term creep on particle coarsening in tempered martensite ferritic steels. *Acta Metallurgica*, 37(12):3225–3234, December 1989.

[58] S. Spigarelli, E. Cerri, P. Bianchi, and E. Evangelista. Interpretation of creep behaviour of a 9Cr-Mo-Nb-V-N (T91) steel using threshold stress concept. *Materials Science and Technology*, 15:1433–1440, December 1999.

[59] K. Sawada, K. Kubo, and F. Abe. Creep behavior and stability of MX precipitates at high temperature in 9Cr-0.5Mo-1.8W-VNb steel. *Materials Science and Engineering A*, 319-321:784–787, December 2001.

[60] R. Lim, M. Sauzay, F. Dalle, I. Tournié, P. Bonnaillie, and A.-F. Gourgues-Lorenzon. Modelling and experimental study of the tertiary creep stage of grade 91 steel. *International Journal of Fracture*, 169:213–228, February 2011.

[61] JC Vaillant, B Vandenberghe, B Hahn, H Heuser, and C Jochum. T/P23, 24, 911 and 92: New grades for advanced coal-fired power plants-Properties and experience. *International Journal of Pressure Vessels and Piping*, 85(1-2):38–46, February 2008.

[62] R. Bonadé, P. Spätig, R. Schäublin, and M. Victoria. Plastic flow of martensitic model alloys. *Materials Science and Engineering A*, 387-389:16–21, December 2004.

[63] B. Gieseke, C. Brinkman, and P. Maziasz. The influence of thermal aging on the microstructure and fatigue properties of modified 9cr-1mo steel. In *First International Conference on Microstructures and Mechanical Properties of Aging Materials*, pages 107–115, 1993.

[64] B. Fournier, M. Sauzay, M. Mottot, H. Brillet, I. Monnet, and A. Pineau. Experimentally based modelling of cyclically induced softening in a martensitic steel at high temperature. In *International conference on Creep and Fracture in High Temperature Components - Design and Life Assessment Issues*, London, 2005. ECCC.

[65] N. J. Hoff. The necking and the rupture of rods subjected to constant tensile loads. *Journal of Applied Mechanics*, 20(1):105–108, 1953.

[66] K. Kimura, H. Kushima, F. Abe, and K. Yagi. Inherent creep strength and long term creep strength properties of ferritic steels. *Materials Science and Engineering A*, 234-236:1079–1082, August 1997.

[67] E.W. Hart. Theory of the tensile test. *Acta Metallurgica*, 15(2):351–355, February 1967.

[68] S. Dumoulin, L. Tabourot, C. Chappuis, P. Vacher, and R. Arrieux. Determination of the equivalent stress-equivalent strain relationship of a copper sample under tensile loading. *Journal of Materials Processing Technology*, 133(1-2):79–83, February 2003.

[69] B.A. Senior, F.W. Noble, and B.L. Eyre. Development of microstructure and strengthening in ferritic steel x20crmov 12 1 at 823k during long-term creep tests and during annealing. *VGB Kraftwerkstechnik*, 73(8):646–653, 1993.

[70] A. Orlová, J. Buršík, K. Kuchařová, and V. Sklenička. Microstructural development during high temperature creep of 9% cr steel. *Materials Science and Engineering A*, 245(1):39–48, April 1998.

[71] K. Sawada, M. Takeda, K. Maruyama, R. Ishii, M. Yamada, Y. Nagae, and R. Komine. Effect of w on recovery of lath structure during creep of high chromium martensitic steels. *Materials Science and Engineering A*, 267(1):19–25, July 1999.

[72] V. Gaffard, J. Besson, and A.F. Gourgues-Lorenzon. Creep failure model of a tempered martensitic stainless steel integrating multiple deformation and damage mechanisms. *International Journal of Fracture*, 133(2):139–166, 2005.

[73] V. Sklenička, K. Kuchařová, M. Svoboda, L. Kloc, J. Buršík, and A. Kroupa. Long-term creep behavior of 9-12%Cr power plant steels. *Materials Characterization*, 51 (1):35–48, August 2003.

[74] F. Matsuda and T. Fujkawa. Reference stress approach for estimation creep strain of tapered cylindrical vessels. In *International Conference on Engineering Aspects of Creep Vol 2*, page 51.

[75] Lloyd, GJ, BSc, and DPhil. The relation between creep crack growth rates and creep-fatigue crack growth rates in austenitic type 316 steel. In *International Conference on Engineering Aspects of Creep Vol. 1*, pages 239–248. Mechanical Engineering Publications Limited, 1980.

[76] Q. Auzoux. *Reheat cracking of austenitic stainless steels - influence of work hardening on intergranular damage*. PhD thesis, MINES ParisTech and CEA Saclay, 2004. `http://tel.archives-ouvertes.fr/tel-00273520/fr/`.

[77] J. Čadek, V. Šustek, and M. Pahutová. An analysis of a set of creep data for a 9Cr1Mo0.2V (P91 type) steel. *Materials Science and Engineering A*, 225(1-2): 22–28, April 1997.

[78] K Kimura, H Kushima, and K Sawada. Long-term creep deformation property of modified 9Cr-1Mo steel. *Materials Science and Engineering A*, 510-11:58–63, June 2009.

[79] F. Abe. Stress to produce a minimum creep rate of 10-5%/h and stress to cause rupture at 105 h for ferritic and austenitic steels and superalloys. *International Journal of Pressure Vessels and Piping*, 85(1-2):99–107, 2008.

[80] B.A. Senior, F.W. Noble, and B.L. Eyre. The nucleation and growth of voids at carbides in 9Cr-1Mo steel. *Acta Metallurgica*, 34(7):1321–1327, July 1986.

[81] P. W. Bridgman. The stress distribution at the neck of a tension specimen. *Transactions of ASME*, 32:553–574, 1944.

[82] C. J. Middleton. Reheat cavity nucleation and nucleation control in bainitic creep-resisting low-alloy steels. *Metal Science*, 15(4):154–167, April 1981.

[83] H. R. Tipler, L. H. Taylor, and B. E. Hopkins. Some direct observations on the metallography of Creep-Cavitated grain boundaries. *Metal Science*, 4:167–170, January 1970.

[84] N. G. Needham. Report of British steel corporation to the Commission of the European Communities. Technical Report Contract No. 7210.MA/802, 1983.

[85] G. Eggeler. Microstructural parameters for creep damage quantification. *Acta Metallurgica et Materialia*, 39(2):221–231, February 1991.

[86] N. G. Needham and T. Gladman. Nucleation and growth of creep cavities in a type 347 steel. *Metal Science*, 14(2):64–72, February 1980.

[87] T. G. Nieh and W. D. Nix. The formation of water vapor bubbles in copper and their effect on intergranular creep fracture. *Acta Metallurgica*, 28(5):557–566, 1980.

[88] S. E. Stanzl, A. S. Argon, and E. K. Tschegg. Diffusive intergranular cavity growth in creep in tension and torsion. *Acta Metallurgica*, 31(6):833–843, 1983.

[89] B. F. Dyson and D. McLean. A new method of predicting creep life. *Metal Science*, 6(1):220–223, January 1972.

[90] B. F. Dyson and D. Mclean. Creep of nimonic 80A in torsion and tension. *Metal Science*, 11(2):37–45, February 1977.

[91] B.F. Dyson. Continuous cavity nucleation and creep fracture. *Scripta Metallurgica*, 17(1):31–37, January 1983.

[92] J. Koplik and A. Needleman. Void growth and coalescence in porous plastic solids. *International Journal of Solids and Structures*, 24(8):835–853, 1988.

[93] R. Raj and M.F Ashby. Intergranular fracture at elevated temperature. *Acta Metallurgica*, 23(6):653–666, June 1975.

[94] M. Volmer and A. Weber. *Physik Chem.*, 119:277, 1925.

[95] R. Becker and W. Döring. Kinetic treatment of grain formation in supersaturated vapors. *Ann. Physik*, 24:719–752, 1935.

[96] J. Frenkel. A general theory of heterophase fluctuations and pretransition phenomena. *The Journal of Chemical Physics*, 7(7):538, 1939.

[97] J. B. Zeldovich. *Acta Physicochim. URSS*, 18:1, 1943.

[98] D. Turnbull. Phase changes. In *Solid State Physics: Advances in Research and Applications*, volume 3, page 268. F. Seitz and D. Turnbull, New York, academic press inc. publishers edition, 1956.

[99] R. Raj. Nucleation of cavities at second phase particles in grain boundaries. *Acta Metallurgica*, 26(6):995–1006, June 1978.

[100] P.J. Clemm and J.C. Fisher. *Acta Metallurgica*, 3:70, 1955.

[101] D. Turnbull. Transient nucleation. *Tans. Met. Soc. AIME*, 175:774–783, 1948.

[102] A. Kantrowitz. Nucleation in very rapid vapor expansions. *The Journal of Chemical Physics*, 19(9):1097, 1951.

[103] R. F. Probstein. Time lag in the Self-Nucleation of a supersaturated vapor. *The Journal of Chemical Physics*, 19(5):619, 1951.

[104] R Fleck, D Taplin, and C Beevers. An investigation of the nucleation of creep cavities by 1 MV electron microscopy. *Acta Metallurgica*, 23(4):415–424, April 1975.

[105] D. Hull and D.E. Rimmer. The growth of grain-boundary voids under stress. *Philosophical Magazine*, 4(42):673–687, 1959.

[106] J. R. Rice. Constraints on the diffusive cavitation of isolated grain boundary facets in creeping polycrystals. *Acta Metallurgica*, 29(4):675–681, April 1981.

[107] H. Riedel. Continuous nucleation of grain boundary cavities in creep rupture. *Z. Metallkd.*, 76(10):669–675, 1985.

[108] I-W. Chen and A. S. Argon. Diffusive growth of grain-boundary cavities. *Acta Metallurgica*, 29(10):1759–1768, October 1981.

[109] J. R. Rice. Time dependent fracture of materials at elevated temperature. In *US Department of Energy Report CONF*, volume 790236, page 130, 1979.

[110] A. Needleman and J.R Rice. Plastic creep flow effects in the diffusive cavitation of grain boundaries. *Acta Metallurgica*, 28(10):1315–1332, October 1980.

[111] B. Budiansky and R. J. O'connell. Elastic moduli of a cracked solid. *International Journal of Solids and Structures*, 12(2):81–97, 1976.

[112] C. Herring. Diffusional viscosity of a polycrystalline solid. *Journal of Applied Physics*, 21(5):437–445, May 1950.

[113] D. François, A. Pineau, and A. Zaoui. *Mechanical Behaviour of Materials: Viscoplasticity, damage, fracture, and contact mechanics.* Springer, November 1998. ISBN 9780792348955.

[114] M.E. Kassner and T.A. Hayes. Creep cavitation in metals. *International Journal of Plasticity*, 19(10):1715–1748, 2003.

[115] B. F. Dyson. Constraints on diffusional cavity growth rates. *Metal Science*, 10(10): 349–353, October 1976.

[116] B. J. Cane. Interrelationship between creep deformation and creep rupture in 2.25Cr-1Mo steel. *Metal Science*, 13(5):287–294, May 1979.

[117] E. Van Der Giessen, M.W.D. Van Der Burg, A. Needleman, and V. Tvergaard. Void growth due to creep and grain boundary diffusion at high triaxialities. *Journal of the Mechanics and Physics of Solids*, 43(1):123–165, January 1995.

[118] H. Riedel. *Fracture at high temperatures.* Springer-Verlag, Berlin ;New York, 1987. ISBN 9780387172712.

[119] F. Barcelo and B. Fournier. Déterminer l'orientation cristallographique des grains ou blocs de lattes entourant les cavités de fluage. Technical Report Ref. FdE 2008/06-1BF, CEA Saclay - Division SRMA, 2008.

[120] A. M. Huntz, P. Guiraldenq, M. Aucouturier, and P. Lacombe. Relation entre les phénomènes de diffusion du fer et du chrome radioactifs dans les alliages fer-chrome de 0 à 15% de chrome et leur transformation $\alpha \leftrightarrows (\alpha + \gamma)$. *Mémoires Scientifiques de la Revue de Métallurgie*, 66(2):85–104, 1969.

[121] A. M. Huntz. Influence de la teneur en chrome et de la teneur en impuretés interstitielles (carbone et azote) sur la diffusion volumique et intergranulaire du fer 59* dans les alliages fer-chrome de 0 à 15% de chrome. Relations avec les transformations $\alpha \leftrightarrows (\alpha + \gamma)$. *Mémoires Scientifiques de la Revue de Métallurgie*, 70(2): 81–101, 1973.

[122] F. Chaix and A. M. Huntz. Mesure des coefficients de diffusion en volume et intergranulaire du fer radioactif dans des alliages fer-chrome monophasés α et de teneur proche de celle du minimum de la boucle γ. Relations avec les transformations de phase $\alpha \leftrightarrows (\alpha + \gamma)$. *Mémoires Scientifiques de la Revue de Métallurgie*, 71(2): 115–120, 1974.

[123] H.-J. Jou. Microstructure modeling of third generation disk alloys. Technical Report NASA/CR-2010-216748, NASA, 2010.

[124] Louisette Priester. *Les joints de grains: de la théorie à l'ingénierie.* L'Editeur : EDP Sciences, 2006. ISBN 9782868838728.

[125] O. Diard, S. Leclercq, G. Rousselier, and G. Cailletaud. Distribution of normal stress at grain boundaries in multicrystals: application to an intergranular damage modeling. *Computational Materials Science*, 25(1):73–84, 2002.

[126] O. Diard, S. Leclercq, G. Rousselier, and G. Cailletaud. Evaluation of finite element based analysis of 3D multicrystalline aggregates plasticity: Application to crystal plasticity model identification and the study of stress and strain fields near grain boundaries. *International Journal of Plasticity*, 21(4):691–722, April 2005.

[127] S. Caré and A. Zaoui. Cavitation at triple nodes in α-zirconium polycrystals. *Acta Materialia*, 44(4):1323–1336, April 1996.

[128] R. Desmorat and F.A. Leckie. Singularities in bi-materials: parametric study of an isotropic/anisotropic joint. *European Journal of Mechanics - A/Solids*, 17(1): 33–52, January 1998.

[129] E. Héripré, M. Dexet, J. Crépin, L. Gélébart, A. Roos, M. Bornert, and D. Caldemaison. Coupling between experimental measurements and polycrystal finite element calculations for micromechanical study of metallic materials. *International Journal of Plasticity*, 23(9):1512–1539, September 2007.

[130] M. Berveiller and A. Zaoui. An extension of the self-consistent scheme to plastically-flowing polycrystals. *J. Mech. Phys. Solids*, 26:325–344, 1979.

[131] P. O. Santacreu. Sur la singularité epine engendrée par une discontinuité plastique. *C. R. Acad. Sci. Paris Série IIb*, 318(12):1577–1582, 1994.

[132] H. D. Bui and S. Taheri. La singularité epine dans les bi-matériaux en thermoélastoplasticité. *C. R. Acad. Sci. Paris Série IIb*, 309(16):1527–1533, 1989.

[133] A. Deperrois and K. Dang Van. Inclusions de surface et singularité epine. *C. R. Acad. Sci. Paris Série IIb*, 311(11):1285–1290, 1990.

[134] Robert J. Asaro and Vlado A. Lubarda. *Mechanics of solids and materials.* Cambridge University Press, 2006.

[135] S. Heraud. *Du polycristal au multicristal : Elaboration d'un mésosccope numérique pour une analyse locale en elastoviscoplasticité.* PhD thesis, Ecole Polytechnique, CEA Saclay, 2000.

[136] T. Hoc and S. Forest. Polycrystal modelling of IF-Ti steel under complex loading path. *International Journal of Plasticity*, 17(1):65–85, 2001.

[137] D. Caillard and J.L. Martin. *Thermally activated mechanisms in crystal plasticity.* Elsevier, 2003. ISBN 9780080427034.

[138] A. S. Keh and S. Weismann. *In Electron Microscopy and Strength of Crystals, G. Tomas and J. Washburn (eds.)*, page 231. Interscience, New York, 1963.

[139] D. J. Dever. Temperature dependence of the elastic constants in α-iron single crystals: relationship to spin order and diffusion anomalies. *Journal of Applied Physics*, 43(8):3293–3301, August 1972.

[140] B. Fournier, M. Sauzay, C. Caës, M. Mottot, M. Noblecourt, and A. Pineau. Analysis of the hysteresis loops of a martensitic steel: Part II: study of the influence of creep and stress relaxation holding times on cyclic behaviour. *Materials Science and Engineering: A*, 437(2):197–211, November 2006.

[141] B. K. Choudhary, K. Bhanu Sankara Rao, S. I. Mannan, and B. P. Kashyap.

[142] M. Libert. *Etudes expérimentale et numérique de l'effet des mécanismes de plasticité sur la rupture fragile par clivage dans les aciers faiblement alliés.* PhD thesis, Ecole Centrale de Paris, 2007.

[143] R.A. Lebensohn, O. Castelnau, R. Brenner, and P. Gilormini. Study of the antiplane deformation of linear 2-D polycrystals with different microstructures. *International Journal of Solids and Structures*, 42(20):5441–5459, October 2005.

[144] R. A. Lebensohn, Y. Liu, and P. Ponte Castañeda. On the accuracy of the self-consistent approximation for polycrystals: comparison with full-field numerical simulations. *Acta Materialia*, 52(18):5347–5361, October 2004.

[145] A. Steckmeyer, M. Sauzay, A. Weidner, and E. Hieckmann. Micromechanical modelling of the cyclic stress-strain behaviour of nickel polycrystals. *International Journal of Fatigue*, 2011 (in press).

[146] L. Vincent, M. Libert, B. Marini, and C. Rey. Towards a modelling of RPV steel brittle fracture using crystal plasticity computations on polycrystalline aggregates. *Journal of Nuclear Materials*, 406(1):91–96, November 2010.

[147] L. Vincent, L. Gelebart, R. Dakhlaoui, and B. Marini. Stress localization in BCC polycrystals and its implications on the probability of brittle fracture. *Materials Science and Engineering: A*, 528(18):5861–5870, July 2011.

[148] M. Sauzay. Cubic elasticity and stress distribution at the free surface of polycrystals. *Acta Materialia*, 55(4):1193–1202, February 2007.

List of Figures

1.1 Courbe de fluage des métaux (Figure issue de [4]). 16
1.2 Loi de Monkman-Grant pour l'acier Grade 91 à des températures comprises entre 500 et 625°C et pour des durées de vie jusqu'à 200 × 10^3h [7]. . . . 16
1.3 Variation de contraintes de fluage (σ^{eng}) en fonction des durées de vie (t_f) d'après [7](CEA) et [8–11]. Figure issue de [7]. 17
1.4 Striction observée sur une éprouvette de Grade 92 à un instant précédant la rupture en traction monotone à la vitesse de déformation de 2.5×10^{-4}s^{-1} à 550°C [13]. 17
1.5 Réduction de la section en zone de striction mesurée à la rupture pour l'acier Grade 91 d'après [4, 7]. Figure issue de [7]. 18
1.6 Baisse de la dureté de l'acier Grade 91 (noté « BM-Crept ») selon la durée de vie et la température de fluage [14]. 18
1.7 Cavités de fluage intergranulaires observées en microscopie optique dans un acier martensitique à 12%Cr pour une déformation $\varepsilon^{eng} = 5\%$ durant un essai de fluage à 650°C et 80 MPa [21]. Les cavités sont situées le long des anciens joints de grains austénitiques et des joints de blocs d'après [21]. 19

2.1 Evolution de la composition chimique des aciers à 9-12%Cr [27, 29]. . . . 22
2.2 Evolution de la dureté d'un acier à 12%Cr le long du revenu [42]. 24
2.3 Microstructure de l'acier Grade 91 à l'état de réception observée en (a) microscopie optique, (b) microscopie électronique à balayage (MEB ou SEM) et (c) microscopie électronique à transmission (MET ou TEM) [24]. 25
2.4 Schéma de la microstructure de l'acier Grade 91 à l'état de réception [43]. 26
2.5 Observations des sous-grains et des dislocations dans l'acier Grade 91 à l'état de réception [24]. La distribution spatiale des dislocations est hétérogène. 27
2.6 Module d'Young de l'acier Grade 91 [36] 29
2.7 Essais de traction sur l'acier Grade 91 (a) à 625°C à des vitesses de déformation comprises entre 10^{-5} et 5×10^{-2}s^{-1} et (b) à trois températures, à la même vitesse de 10^{-3}s^{-1} [4]. 29

3.1 Schematic diagram showing the sectioning procedure and zones for FEG-SEM observations. 39

3.2 Ratio of the time spent in tertiary creep stage to total creep lifetime for Grade 91 steel at 500-600°C (CEA/SRMA) and at 625°C [72], Grade 92 steel at 600°C [73], A5052-0 aluminium alloy at 150°C [74], IN100 nickel-based alloy at 1000°C [3], 316 austenitic stainless steel at 625°C [75], and 316L(N) austenitic stainless steel at 600°C [76]. 40
3.3 True strain rate evaluated using numerical derivation from creep curves (engineering strain vs. time) at 500°C. 41
3.4 True strain rate evaluated using numerical derivation from creep curves (engineering strain vs. time) at 550°C. 41
3.5 True strain rate evaluated using numerical derivation from creep curves (engineering strain vs. time) at 600°C. 42
3.6 Norton power-law fit at 500-600°C (CEA/SRMA) and at 625°C [72]. . . . 42
3.7 Softening slope versus minimum creep rate for Grade 91 steel, according to the date given by CEA/SRMA and [8, 72]. 43
3.8 Reduction of area measured after fracture as a function of minimum creep rate [7, 72]. 44
3.9 FEG-SEM observations of long-term creep damage on longitudinal cross-sections far from the necking area for creep tests on Grade 91 steel at (a) 500°C for 160×10^3 h and (b) 600°C for 94×10^3 h. 44
3.10 Multiple loading-unloading creep test at 350 MPa and 500°C on Grade 91 steel. Unloading and further loading parts of the curve are not indicated. 45
3.11 Evolution of necking during creep at 350 MPa and 500°C. 45
3.12 Diameter profile of the P91 creep specimen during creep test at 350 MPa and 500°C. 46
3.13 Experimental and predicted engineering strain evolution with the homogeneous deformation approach and either (1) the Norton power-law or (2) the modified power-law including the material softening effect, for creep tests at 500°C. 48
3.14 Experimental and predicted engineering strain evolution with the homogeneous deformation approach and either (1) the Norton power-law or (2) the modified power-law including the material softening effect, for creep tests at 550°C. 48
3.15 Experimental and predicted engineering strain evolution with the homogeneous deformation approach and either (1) the Norton power-law or (2) the modified power-law including the material softening effect, for creep tests at 600°C. 49
3.16 Specimen at onset of necking. 50
3.17 Longitudinal section of the specimen after the onset of necking. 51
3.18 Lifetime predicted by the necking model using (a) the Norton power-law and integration formulation and (b) the modified power-law including the softening effect for various values of the initial diameter variation, δD. . . 53
3.19 Predicted evolutions of the necking section with time. Symbols : experimental fracture surfaces, dotted lines : Norton law and Hart Eq. (3.18), dashed lines : Norton power-law and time integration formulation Eq. (3.17), and solid lines : modified power-law including the softening effect. Initial diameter variation $\delta D = 20$ µm. 53

3.20 Experimental results and lifetimes predicted with the necking model using either the Norton power-law or the modified power-law including the softening effect, for $\delta D = 20$ µm. 54
3.21 Experimental results and evolution of cross-section versus time predicted with the necking model taking into account the creep-induced material softening, for the creep test performed at 500˚C and 350 MPa. 55
3.22 Experimental results and lifetimes predicted by the upper and lower bounds for a large number of tempered martensitic materials at temperatures between 500 and 700˚C (CEA/SRMA and [4, 8, 10, 59, 73, 79]. 56

4.1 Nucleation and growth of cavities in 12%Cr steel during a creep test carried out at 650˚C and 80 MPa from [21]. 66
4.2 Optical micrographs of cavitated 12%Cr-Mo-V steel after a 5% creep elongation at 650˚C under 80 MPa after [21]. 67
4.3 SEM micrograph of a typical cavity after a creep elongation of 5% at 650˚C under an applied stress of 80 MPa [21]. 68
4.4 (a) Cavity number over cross-section fields of 214×286 µm^2 and (b) area fraction of cavities measured in [4]. $D/D_0 = 1$ for cross-sections located in the homogeneous parts of creep specimens and $D/D_0 < 1$ for cross-sections located in the necking region. 69
4.5 Microcracks following FAGB or block boundary segments perpendicular to the loading axis, observed in a cross-section near the fracture surface, after a creep lifetime of 7000 h at 625˚C [4]. 69
4.6 Ductile cavities lying on (a) a Lave phase, (b) on M_23C_6 carbides, and forming at a triple point, observed in a cross-section near the fracture surface after a creep lifetime of 7000 h at 625˚C [4]. 70
4.7 Voids formed either (a) at grain boundary junctions or (b) at inclusions located at grain boundaries. Replotted after [93]. 71
4.8 Reference (1) and new (2) states of the system as a result of the introduction of a grain boundary cavity [99]. 73
4.9 Contribution of the volume energy term and surface energy term to the total change in free energy with increasing radius of the cavity [99]. . . . 74
4.10 The volume of the critical cavity for a fixed value of r_c for (a) homogeneous and (b-d) three types of heterogeneous nucleation. The one with the smallest volume will have the highest nucleation probability. Replotted after [99]. 75
4.11 Nucleation rate normalised by N_a^{max} as a function of tensile stress in pure copper. The threshold stress refers to the stress for which the normalised nucleation rate is equal to 1 s^{-1}m^{-2}. Replotted after [99]. 76
4.12 Experimental nucleation times in a commercial copper alloy [104] compared with (1) the predicted incubation time given in Eq. (4.17) and (2) the lower bound of the nucleation time given in Eq. (4.18) [99], taking into account the grain boundary diffusion and the coefficient of pure copper. . 78
4.13 (a) Growth of isolated cavities by grain boundary diffusion modelled by Raj and Ashby [93], (b) resolved normal stress along grain boundary [93]. 80

4.14 Schemata representing (a) uniform and (b) heterogeneous cavitation at (especially) grain boundaries under vertical loading replotted after [114]. The latter one leads to constrained cavity growth. 82
4.15 Cavity growth rates predicted using an unconstrained cavity growth model (dashed lines) and a constrained cavity growth model [107](solid lines), compared with experimental measurements in bainitic steels [84]. Redrawn in [114]. 85
4.16 Predicted fracture lifetime taking into account unconstrained cavity growth (dashed lines) and constrained cavity growth (solid lines) with either continuous or instantaneous nucleation [107]. The predictions are compared with the measured lifetimes of $2\frac{1}{4}$Cr-1Mo steel in over-heated condition [116]. Redrawn in [114]. 85

5.1 Creep cavities in Grade 91 steel subjected to creep at 500°C under 230 MPa, after a lifetime of 160×10^3h. FEG-SEM observations by Bonnaillie and Haney [7] using a magnification of 1000. 90
5.2 Creep cavities in Grade 91 steel subjected to creep at 600°C under 90 MPa, after a lifetime of 94×10^3h. FEG-SEM observations by Bonnaillie and Haney [7] using a magnification of 500. 90
5.3 Creep cavities in grade 91 steel subjected to creep at 500°C under 250 MPa, after a lifetime of 59×10^3h. FEG-SEM observations using a magnification of 1000 at Ecole des MINES with A.-F. Gourgues-Lorenzon and A. Laurent. 91
5.4 Creep cavities in Grade 91 steel subjected to creep at 600°C under 125 MPa, after a lifetime of 5×10^3h. FEG-SEM observations using a magnification of 1000 at Ecole des MINES with A.-F. Gourgues-Lorenzon and A. Laurent. 91
5.5 Sizes distribution of creep cavities (equivalent circular diameter) in Grade 91 steel represented by (a) probability and (b) cumulative probability after a creep lifetime of 160×10^3 h at 500°C (230 MPa). Magnification: 1000, minimum size of detectable cavities: 0.2 µm. 94
5.6 Size distribution of creep cavities (equivalent circular diameter) in Grade 91 steel represented by (a) probability and (b) cumulative probability after a creep lifetime of 94×10^3 h at 600°C (90 MPa). Magnification: 500, minimum size of detectable cavities: 0.5 µm. 94
5.7 A cavity located at a triple junction of block boundaries of Grade 91 steel subjected to the creep test at 600°C and 90 MPa (94 kh), identified using (a) SEM observations and (b) SEM EBSD analysis [119]. 95
5.8 cavities located (a) at a packet or block boundary (size of 290 nm), (b) at a carbide-matrix interface - type A (size of 320 nm), (c) at the triple junction of a carbide and a boundary of the matrix - type B (size of 160 nm) and (d) at a matrix boundary between two carbides (size of 90 nm). Creep lifetime: 59×10^3h, temperature: 500°C, applied stress: 250 MPa. 96
5.9 Cavities located at (a) a triple junction of block boundaries (a size of 120 nm) and (b) at Laves phase-matrix interface (size of 80 nm). Creep lifetime: 5×10^3h, temperature: 600°C, applied stress: 125 MPa. 96

5.10 Diffusion coefficients in function of contents in Cr for (a) grain boundary diffusion and (b) volume diffusion given from [120–122]. 98

5.11 Comparison between cavity diameter predicted using the Rice length ($2L_R$) and the measured maximum and average diameters of cavities. 99

5.12 Comparison between experimental lifetime at 500°C (CEA) and times to failure predicted using the Raj and Ashby model and using the Riedel bounds. The values of L and $\dot{N}_0$ were evaluated from the observations of the specimen loaded at 500°C and 230 MPa (the values are slightly different at 500°C and 250 MPa). 101

5.13 Comparison between experimental lifetime at 600°C, after creep experiments at CEA and ones reported in [4,8,73], and times to failure predicted using the Raj and Ashby model and using the Riedel bounds. The values of L and $\dot{N}_0$ were evaluated from the observations of the specimen loaded at 600°C and 90 MPa (the values are slightly different at 600°C and 125 MPa). 101

5.14 Comparisons between the measured maximum and average values of diameter and the diameter predicted using the Raj and Ashby model and using the Riedel bounds. (a) 230 MPa at 500°C and (b) 90 MPa at 600°C. Corrected experimental values to take into account 3D shape of cavities (measured 2D size times a factor $4/\pi$). 102

5.15 Comparisons between the experimental size distributions and the ones predicted using the Riedel bounds for the creep tests at (a) 230 MPa at 500°C and (b) 90 MPa at 600°C. Mean experimental diameter: $\overline{d}^{exp}$, maximum experimental diameter: d^{exp}_{max}, mean diameter predicted using respectively the Riedel lower and upper bounds: $\overline{d}^{RL}$, $\overline{d}^{RU}$ 103

5.16 Incubation times predicted using the Raj model given by Eq. (4.17), for spherical shapes with $F_v = \frac{4\pi}{3}$. 106

5.17 Axial stress distribution given in Pa. Horizontal loading axis. Stress: 90 MPa, temperature: 600°C, creep time: 94×10^3h. 108

6.1 Cavity located at a polycrystalline triple point of a Zr alloy observed by Caré and Zaoui [127] at a tensile strain of 24% and room temperature. Many slip bands are observed and the strain field is heterogeneous around the triple point [127]. 117

6.2 (a) Microstructure of zirconium built using EBSD measurements (the Schmidt factor is high in white grains and low in black grains) [129]. (b) Axial strain fields measured using microextensometry at a macroscopic strain of 2.5% at room temperature [129]. (c) Superposition of both experimental results [129]. The loading direction is horizontal. 118

6.3 (a) Voronoï polycrystalline aggregate containing 100 grains meshed by tetrahedral finite elements [125]. (b) Normal stress averaged along different grain boundaries in a Zr alloy subjected to a tensile test at a strain rate of 10^{-5}s^{-1} at room temperature, compared with an analytical model assuming uniform stress field in the whole polycrystal (upper curve) [125]. 119

6.4 (a) Voronoï polycrystalline aggregate containing 2197 grains meshed by cubic elements. (b) Normal stress averaged along different grain boundaries and standard deviations, in a Zr alloy subjected to a tensile test at strain rate of $2 \times 10^{-4} s^{-1}$ at 350°C [126]. 119
6.5 Kinematic model of elastoplastic transformation at the single crystal scale after [134]. 120
6.6 Obstacle profile in the framework of thermal activation. 122
6.7 Evolution of critical resolved shear on slip systems $\{110\}\langle111\rangle$ and $\{112\}\langle111\rangle$ in Fe-α after [138]. 123

7.1 Polycrystalline aggregate containing 125 blocks of random orientations. Issued from [145]. 127
7.2 Boundary conditions, six degrees of freedom of rigid body motion are blocked. 128
7.3 Experimental loading stages of the creep tests at 500°C and 600°C before reaching their final creep engineering stress (σ^{eng}) which are respectively 230 MPa and 90 MPa. Similar loading curves are used for applying the boundary conditions during the starting of the finite element computations. 129
7.4 Effect of the number of finite elements per block on the macroscopic engineering strain vs. time curve for the creep test at 600°C and 90 MPa. The material parameters are given in Tables 6.2 and 7.1. For each number of blocks, only one set of random crystal orientations is chosen. 130
7.5 Predicted creep engineering strain vs. time curves of the creep test at 600°C and 90 MPa, using one aggregate of 5^3 blocks meshed by 4^3 FEs per block and four independent sets of crystal orientations. The used crystal elastoviscoplasticity parameters are reported in Tables 6.2 and 7.1. 132
7.6 Predicted evolution of the macroscopic engineering strain during creep at 600°C under 90 MPa using four numbers of blocks for the polycrystalline aggregate. The aggregate is meshed by 4^3 FEs per block. The used crystalline elastoviscoplasticity parameters are reported in Tables 6.2 and 7.1. 133
7.7 Evolution of the macroscopic engineering strain during creep at 500°C under 230 MPa predicted using two values for the parameter V^*. The polycrystalline aggregate contains 5^3 block and is meshed by 4^3 FEs per block. The values of the parameters ΔG_0 and τ_0 at 500°C are reported in Table 7.1. 134
7.8 Sensitivity of predicted engineering strains of creep at 500°C under 230 MPa due to mesh refinement for two V^* values. Polycrystalline aggregates of 5^3 blocks and the same values of the parameters ΔG_0 and τ_0 at 500°C reported in Table 7.1 are used. 134
7.9 Distributions of (a) axial stress fields, (b) axial strain fields after a creep time of 30×10^3 h at 600°C and 90 MPa, given at the surface of the polycrystalline aggregate constituted of 5^3 blocks using the following parameter values: $\Delta G_0 = 3.3$ eV, $\tau_0 = 27$ MPa and $V = 400b^3$. 136
7.10 Distribution of the mean values per block of $\langle\sigma\rangle_{xx}^{block}$ and $\langle\sigma\rangle_{eq}^{block}$ after 30×10^3 h of creep at 600°C under a creep stress of 90 MPa. 137
7.11 Triaxiality of each block in the polycrystalline aggregate of 5^3 blocks for creep at 600°C and 90 MPa. 138

7.12 Distributions of the mean values of (a) $\langle\varepsilon\rangle_{xx}^{block}$ and (b) $\langle\varepsilon_{eq}^{v}\rangle^{block}$ after 30×10^3 h of creep time at 600˚C and 90 MPa. Both distributions seem to be described by a periodicity of 25 blocks, number of blocks comprised in each layer of the aggregate of 5^3 blocks perpendicular to the loading axis. 139

7.13 Ratios $\langle\sigma\rangle_{xx}^{block}/\Sigma_{xx}$ at an engineering strain of 2.3% (after 50×10^3h) during the creep test at 600˚C and 90 MPa on the grade 91 steel, compared with the bound values computed by Diard et al. [125] at an engineering strain of 3% during a tensile test carried out on a Zr alloy at room temperature and at a strain rate of 1×10^{-5}s^{-1}. 140

7.14 Effect of creep time on the cumulative probability distributions of the average mechanical fields per block during the creep test at 600˚C and 90 MPa. A polycrystalline aggregate constituted of 5^3 blocks meshed by 4^3FEs/block is used. The crystal viscoplasticity parameter values are given in Table 7.1. 141

7.15 Influence of the number of blocks on the distributions of $\langle\sigma\rangle_{xx}^{block}$, $\langle\varepsilon\rangle_{xx}^{block}$, $\langle\epsilon_{eq}^{v}\rangle^{block}$ and $\langle\sigma\rangle_{eq}^{block}$ after 30×10^3h of creep test at 600˚C and 90 MPa. All polycrystalline aggregates are meshed by 4^3 FEs/block. the crystal viscoplasticity parameter values reported in Table 7.1 are used. 142

7.16 Effect of mesh refinement on the distributions of $\langle\sigma\rangle_{xx}^{block}$ and $\langle\epsilon\rangle_{xx}^{block}$ after 30×10^3h of creep test at 600˚C and 90 MPa, using a polycrystalline aggregate of 5^3 blocks and one set of random crystal orientations. 144

7.17 Effect of the V^* value choice on the distributions of $\langle\sigma\rangle_{xx}^{grain}$ and $\langle\epsilon\rangle_{xx}^{grain}$ after 50×10^3h of creep test at 500˚C and 230 MPa. A polycrystalline aggregate of 5^3 blocks is used and meshed by 4^3 FEs/block. 145

8.1 Meshing of the triple point area including one triple point and their boundaries. The thickness of the model is equal to the size of finite elements located at the triple junction (0.4, 0.1 or 0.05 units). 148

8.2 Effect of mesh refinement on the normal stress field along block boundary L2 during creep at 600˚C and 90 MPa for one set of random crystal orientations. The length of block boundary L2 is 10 length units. The triple point is located at distance 0 and the middle of block boundary L2 at distance of 5 units. 150

8.3 Time evolution of normal stress fields at block boundary L2 close to the triple junction. Average value and amplitudes using 20 sets of random crystal orientations. 152

8.4 Normal stress profiles along a half length of block boundary L2 after 50×10^3h of creep at 500˚C under $\sigma^{eng}=230$ MPa computed using 20 sets of ransom crystal orientations. The triple junction corresponds to distance 0. The total length of block boundary L2 is 10 units. 153

8.5 Normal stress profiles along a half length of block boundary L2 after 30×10^3h of creep at 600˚C under $\sigma^{eng}=90$ MPa computed using 20 sets of random crystal orientations. The triple junction corresponds to distance 0. The total length of block boundary L2 is 10 units. 154

8.6 Effect of the block softness on the normal stress distribution (in Pa) for two sets of random crystal orientations, after 30 × 10^3h of creep at 600°C under $\sigma^{eng} = 90$ MPa. 155
8.7 Time evolution of the normal stress at block boundary L2 at two locations during creep at 500°C under 230 MPa. 156
8.8 Time evolution of the normal stress averaged along the half length of block boundary L2 during creep at 500°C under 230 MPa. Symbols are related to the individual sets of blocks 157
8.9 Microstructure of grade 91 steel after the creep test at 500°C under 230MPa before and after meshing. The loading axis is horizontal. The EBSD map contains a high number of non-indexed pixels which could lead to an uncertainty of microstructure filling. 159
8.10 Microstructure of grade 91 steel after the creep test at 600°C under 90MPa before and after meshing. The loading axis is vertical. The EBSD map contains a high number of non-indexed pixels which could lead to an uncertainty of microstructure filling. 159
8.11 Distribution of the axial stress and strain fields after 50 × 10^3h of creep time at 500°C and 230 MPa computed using the microstructure in Fig. 8.9 surrounded by a homogeneous matrix (10 times larger). The loading direction is horizontal. 160
8.12 Distribution of the axial stress and strain fields after 30 × 10^3h of creep time at 600°C and 90 MPa computed using the microstructure in Fig. 8.10 surrounded by a homogeneous matrix (10 times larger). The loading direction is vertical. 161
8.13 Normal stress profiles along block boundaries belonging to two triple points (Fig. 8.9b) after 50 × 10^3h at 500°C and 230MPa. The triples points correspond to the distance equal to 0. 163
8.14 Normal stress profiles along block boundaries belonging to two triple points (Fig. 8.10b) after 50 × 10^3h at 600°C and 90MPa. The triples points correspond to the distance equal to 0. 164

9.1 Comparisons between experimental creep lifetimes after CEA creep tests and [6, 73] and the predictions using either the upper bound of the necking model including material creep softening (UNS), or the Riedel lower bound and Dyson law (LC) or the Riedel upper bound and Dyson law (UC). One creep test at 600°C has reached the end of the secondary stage 50 kh ago is still in progress at CEA/SRMA. Its estimated experimental lifetime is noted by "est.exp". 176

List of Tables

2.1 Composition chimique exprimée en pourcentage massique de l'acier Grade 91 selon ASTM Standard A387 - Gr 91 [35](minimum/maximum), et des deux tôles en acier Grade 91 étudiées et fabriquées à Creusot-Marrel (CM) [33] et Usinor [34]. 23
2.2 Traitements thermiques des deux tôles de Grade 91 fabriquées à Creusot-Marrel [33] et Usinor [34]. 23
2.3 Tailles moyennes des anciens grains austénitiques (d_g), des blocs (d_{bl}) et des sous-grains (d_{sg}) pour l'acier Grade 91, obtenus grâce à des traitements thermiques de type de ceux décrits dans la Table 2.2. 24
2.4 Densité totale de dislocations pour les aciers à 9-12%Cr. 27
2.5 Densité de dislocations mobiles pour les aciers à 9-12%Cr. 27
2.6 Tailles des précipités $M_{23}C_6$ et MX présents dans les aciers à 9-12%Cr. . 28

3.1 Chemical composition of both materials under study expressed in wt.%. . 37
3.2 Heat treatments of both materials under study. 37
3.3 Database of creep tests carried out at CEA/SRMA on the Grade 91 steel. T : temperature, σ^{eng} : engineering stress, t_f : lifetime. 38
3.4 Creep test carried out at 500°C and 350MPa on Grade 91 steel at CEA/SRMA, interrupted at three engineering strain levels (ε^{eng}) before fracture. 38
3.5 Norton law parameters. 40
3.6 Predictions of the onset of necking. 51

4.1 Observations of cavity nucleation after [21, 80, 82]. 65

5.1 Characteristics of the creep tests considered for studying creep cavitation in Grade 91 steel. 87
5.2 Statistics parameters of the quantitative study of creep cavities in Grade 91 steel. 89
5.3 Smallest sizes of creep cavities in Grade 91 steel. 92
5.4 Summary on the quantification of creep cavities after observations at 500°C (CEA data), 600°C (CEA data) and 625°C [4]. N_m is the 2D number density of cavities measured from polished cross-section, $\overline{d}$ is the average 2D cavity diameter by considering circular areas. The used observation parameters are given in Table 5.2. 92
5.5 Characteristic size and average distance between cavities in the considered Grade 91 steel using the observation parameters in Table 5.2. d_{min} is the lower cut-off value of the size distribution. 93

5.6 Ahrrenius parameters for self-diffusion coefficients along grain boundaries and in the bulk for tempered martensitic steels [120–122]. 97
5.7 Sensitivity of predictions of lifetime and cavity size to the values of model parameters. Reference values: $\overline{\omega}_f = 0.1$, $2L = 25$ µm at 500˚C and 67 µm at 600˚C, $\dot{N}_0 = 2.8$ m^{-2}s^{-1} at 500˚C and 0.65 m^{-2}s^{-1} at 600˚C , $D_b\delta$ determined from Table 5.6 (for diffusion of Fe in 9.1%Cr steel). The studied creep tests: (1) at 500˚C under 230 MPa and (2) at 600˚C under 90 MPa. (3): Riedel lower bound, (4) Riedel upper bound. 105
5.8 Comparison between cavity densities measured after creep tests and predictions using Eq. (4.14) and the adjusted values of the geometry factor F_v. 106
5.9 Computed normal stress at the precipitate-matrix interface with respect to the applied engineering stress. $\sigma^{eng} = 90$ MPa, temperature: 600˚C, creep time: 94×10^{3}h. 107

6.1 Easy slip systems in the bcc structure [136, 137]. 121
6.2 Independent elastic constants of Fe-α single crystals [139]. 123

7.1 Parameter values for the crystal viscoplastic constitutive equations. . . . 130
7.2 Computed minimum creep strain rate depending on the meshing parameters. The material parameters are given in Tables 6.2 and 7.1. One set of random crystal orientations is assigned to each polycrystalline aggregate. 131

8.1 Ajusted parameter values for the creep flow rule described by Eqs. (8.1) and (8.2), using creep data at 500˚C for σ^{eng} ranging between 210 and 270 MPa (see Table 3.3) and at 600˚C for σ^{eng} ranging between 70 and 125 MPa (see Table 3.3). 149
8.2 Amplitude of variation of the normal stress at block boundary L2 with respect to the macroscopic stress due to random orientations. The minimum creep strain rate corresponds to creep times of 30 × 10^{3}h for the first creep test and of 50 × 10^3 of the second one. Twenty microstructure configurations are considered (Fig. 8.1). 158
8.3 Predictions of nucleation rates using the Raj nucleation model and taking into account the maximum tensile stress concentration factor of 2 obtained by the triple point model. $\dot{N}_{a0} = \frac{4\pi\gamma_s D_b\delta}{\Omega^{4/3}\sigma_n} N_a^{max} \exp\left(\frac{\sigma_n\Omega}{k_bT}\right)$, $\frac{\Delta G_c}{k_bT} = \frac{4{\gamma_s}^3 F_v}{{\sigma_n}^2 k_bT}$ and $\dot{N}_a = \dot{N}_{a0} \exp\left(-\frac{\Delta G_c}{k_bT}\right)$ from Eq. (4.14). $\gamma_s = 1.42$ Jm^{-2} [118], $\gamma_b = 1.7$ Jm^{-2} [124], $\gamma_I = 1.1$ Jm^{-2} [123], $\gamma_{Ib} = 1$ Jm^{-2} [124], $Q_b = 254$ kJmol^{-1} [120], $D_{b0}\delta = 1.88$ m^{2}s^{-1} [120], $k_b = 1.3806488 \times 10^{-23}$ JK^{-1} and $\Omega = 1.18 \times 10^{-29}$m^3. 166

Simulation numérique et étude expérimentale du fluage de l'acier Grade 91 à haute température

RESUME : L'acier grade 91 serait un candidat approprié pour des éléments de structures du circuit secondaire et du générateur de vapeur des réacteurs nucléaires de génération IV. Leur durée de vie sera prolongée jusqu'à 60 ans. Cela nécessite de considérer les mécanismes actifs durant de très longs temps de fluage afin de proposer des prédictions de durées de vie plus fiable que de simples extrapolations.

La striction est le mécanisme de ruine principal pour des durées de vie jusqu'à 160 kh à 500°C et 94 kh à 600°C. Une simulation de la striction tenant compte de l'adoucissement du matériau conduit à deux lois de bornes qui encadrent les durées de vie expérimentales d'un grand nombre d'aciers martensitiques revenus jusqu'à 200 kh à température 500-700°C. Des cavités intergranulaires observées en FEG-SEM à deux durées de vie longues affectent faiblement la vitesse de déformation.

Une prédiction du développement des cavités permettrait d'extrapoler les durées de vie hors du domaine expérimental. Leur germination et croissance, supposées associées à la diffusion des lacunes, sont modélisées grâce à deux modèles classiques. Le premier tient compte d'une germination instantanée (Raj et Ashby) et le second d'une germination continue - Dyson. Le second, plus stable par rapport à ses paramètres que le premier, conduit à des prédictions des tailles finales de cavités en accord raisonnable avec les mesures en FEG-SEM. La vitesse de germination identifiée expérimentalement est requise dans ce modèle.

La germination continue des cavités par diffusion est modélisée grâce au modèle classique de Raj. Ce modèle ne permet pas des prédictions de densité de cavités en accord avec les mesures, même en tenant compte de la germination aux interfaces matrice / précipités, observée au MEB-FEG et d'un facteur maximal de concentration de contrainte locale de 2. Ce dernier a été obtenu grâce à des calculs par éléments finis en déformations planes du fluage de microstructures simulées ou réelles, comprenant des points triples ou des précipités/phases de Laves.

L'utilisation de la loi de germination de Dyson permet de proposer des prédictions au-delà de 200kh. La durée de vie prédite par le modèle de Riedel d'un essai à basse contrainte semble être en accord avec la durée expérimentale estimée de l'essai (toujours en cours) et actuellement en stade tertiaire, basée sur la fraction de la durée de vie habituellement consommée par le stade tertiaire.

Mots clés : fluage, grade 91, striction, adoucissement, cavitation, diffusion, point triple

Numerical and experimental study of creep of Grade 91 steel at high temperature

ABSTRACT: Grade 91 steel is a suitable candidate for structural components of the secondary and the vapour of generation IV nuclear reactors. Their in-service lifetime will last for 60 years. It is necessary to consider the mechanisms involved during long-term creep to propose reliable predictions of creep lifetimes.

Necking is the main failure mode for creep lifetimes up to 160 kh at 500°C and 94 kh at 600°C. Necking modelling including the material creep softening leads to two bound equations including experimental lifetimes of a large number of tempered martensitic steels loaded up to 200 kh at temperature 500-700°C. The observed creep intergranular cavities are shown to affect very weekly creep strain rate.

The prediction of the cavity evolution will allow estimating creep lifetimes out of experimental data domain. Their nucleation and growth, supposed to be associated to vacancy diffusion, are modelled using two classical models. The first one considers instantaneous nucleation (Raj and Ashby) and the second one continuous nucleation obeying the Dyson law (Riedel). The second one leads to two bound equations, more stable with respect to the parameter values. It allows predicting final size of cavities in reasonable agreement with measured ones. Yet, the nucleation rate should still be estimated from measured cavity densities.

Nucleation of cavities by diffusion is simulated using the Raj model. This model does not allow predicted final cavity densities in agreement with the measured ones, even by considering cavity nucleation at precipitates/Laves interfaces experimentally observed and the maximum local stress concentration of a factor 2 computed using finite element calculation in a 2D plane strain hypothesis based on either simulated or real microstructures containing triple points or precipitates/Laves phases.

The use of the Dyson model allows us to propose predictions of long-term creep lifetimes. Lifetime predicted using the diffusion-induced growth model of one creep test under low stress still in progress is approximately in agreement with the experimental lifetime estimated based on the fraction of tertiary stage.

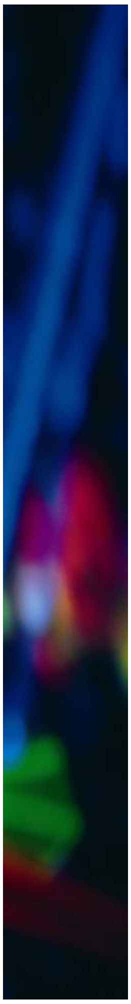Keywords : creep, grade 91, necking, softening, cavitation, diffusion, triple point